# Quantitative states of the in-situ stress of the Canadian Duvernay Formation and deterministic analysis on the regional fault stability

by

Luyi Shen

A thesis submitted in partial fulfillment of the requirements for the degree of

Doctor of Philosophy

in
Geophysics

Department of Physics
University of Alberta

## Abstract

Maps of the in-situ stress directions and magnitudes at the depth of the Duvernay Formation within the Alberta Energy Regulator's (AER) Kaybob assessment area (centered on the town of Fox Creek), East Shale basin (centered on the city of Red Deer) and Willesden Green oil field are constructed from multiple sets of oriented borehole images, density logs, and static and dynamic wellbore-pressure tests collected from nearby boreholes that targeted the Duvernay Formation.

Azimuths of borehole breakouts and drilling-induced tensile fractures interpreted from borehole image logs reveal that the orientation of maximum horizontal compressive stress ($S_H$) in the studied area is dominantly northeast-southwest, mainly in agreement with the typical stress directions throughout much of the Alberta Basin. Vertical-stress magnitudes ($S_V$) come from estimates of the overburden pressures obtained by integrating more than 1000 smoothed density logs. Dynamic borehole-pressurization tests variously referred to as minifrac, microfrac, and diagnostic fracture injection test (DFIT), were reanalyzed. A consistent procedure is adapted to find the fracture-closure pressure ($P_{FC}$), which is here taken to be equal to the minimum horizontal compression ($S_h$). Pore pressures ($P_P$) were also estimated from the pressurization tests. Stress inversion of the focal mechanism solutions for the earthquakes nearby validated the assumed Andersonian stress regime and provided the shape-ratio of the stress. Combined with borehole breakout observations, we constrained the magnitudes of $S_H$ that completes the Andersonian stress tensor.

It is shown that the ambient pore pressures of the nearby Duvernay unconventional reservoirs can provide enough $P_f$ triggering fault movement. The local fluid pressures acting on

the fault can be readily increased above the critical value if a hydraulic connection exists between the fault and a propagating hydraulic fracture within which pressures in excess of the minimum compression exist. The critical pressure necessary to induce slip is estimated using a probabilistic model that incorporates uncertainties of stress and fault's mechanical properties. These critical pressures are greater than expected hydrostatic pressure but less than the nearby unconventional reservoirs' pore pressures.

We further build another 3D stress model for the areas of Red Deer, which had also been historically seismic quiescent but experienced recent high profile induced earthquakes. A susceptibility map, built on the basis of faulting planes' slip tendency, shows that the HF-induced clusters geographically overlap with the zones of higher susceptibility. High ambient pore pressure does not correlate with high susceptibility, and large deviatoric stress is needed to cause HF-induced earthquakes.

## Preface

**Chapter 3** is adapted from a version that is also published as a report submitted to the Alberta Geological Survey as 'Shen, L., Schmitt, D.R. and Haug, K., 2018. Measurements of the states of in situ stress for the Duvernay Formation near Fox Creek, west-central Alberta. Alberta Energy Regulator/Alberta Geological Survey, AER/AGS Report, 97, p.29.' The data reported in this work is published as the companion dataset 'Shen, L., Schmitt, D.R., and Haug, K., 2018. In-Situ Stress Measurements for the Duvernay Formation, Alberta (tabular data, tab-delimited format); Alberta Energy Regulator / Alberta Geological Survey, AER/AGS Digital Data 2018-0013.' Luyi W. Shen was responsible for the investigation, original manuscript writing, code developing, visualization of the data, and editing of the final documents. D. Schmitt supervised this work, formatted the concept, made a significant contribution to the writing of the original manuscript, and editing of the final paper. K. Haug assisted in the data collection.

**Chapter 4** has been published as 'Shen, L.W., Schmitt, D.R. and Haug, K., 2019. Quantitative constraints to the complete state of stress from the combined borehole and focal mechanism inversions: Fox Creek, Alberta. Tectonophysics, 764, pp.110-123.' Luyi W. Shen was responsible for the investigation, original manuscript writing, code developing, visualization of the data, and editing of the final documents. D. Schmitt supervised this work, formatted the concept, made a significant contribution to the writing of the original manuscript, and editing of the final paper. K. Haug assisted in the data collection.

**Chapter 5** has been published as 'Shen, L.W., Schmitt, D.R. and Schultz, R., 2019. Frictional stabilities on induced earthquake fault planes at Fox Creek, Alberta: A pore fluid

pressure dilemma. Geophysical Research Letters, 46(15), pp.8753-8762.' Luyi W. Shen was responsible for the investigation, original manuscript writing, code developing, visualization of the data, and editing of the final documents. D. Schmitt supervised this work, formatted the concept, made a significant contribution to the writing of the original manuscript, and editing of the final paper. R. Schultz assisted in the editing of the final document and provided the focal mechanism solutions of the earthquakes.

**Chapter 6** has been recently revised and currently under consideration for publication in the *Journal of Geophysical Research: Solid-Earth*. Luyi W. Shen was responsible for the investigation, original manuscript writing, code developing, visualization of the data, and editing of the final documents. D. Schmitt supervised this work, formatted the concept, made a significant contribution to the writing of the original manuscript and editing of the final paper. R. Wang provided partially the data analyzed and assisted in the writing of the original manuscript. T. Hauck assisted in the writing of the geology component of the paper, data visualization, and also generally the editing of the paper.

The raw well testing data studied here were submitted by industry operators to the Alberta Energy Regulator (AER) as required by AER Directive 59. These data are available for public access through AER's data distribution and dissemination system (DDS). Well log information is retrieved from Alberta Geological Survey's well log database disseminated through IHS Markit's Petra$^{TM}$ log analysis software. No confidential data, nor any information derived from the confidential data, is included in this thesis.

## Acknowledgement

The work presented in this thesis is developed under the supervision of Prof. D. Schmitt. Prof. D. Schmitt made critical contributions to the development of this thesis and my scientific skills. He is a good mentor and friend.

This journey is certainly not lacking in moments that I was frustrated enough to want to quit, but I'm glad I didn't. If a survey was sent to me asking if I agree that doing this degree is worthwhile, I would say yes I strongly agree 10/10.

I thank my wife for supporting me during these five years. I'm glad she didn't try to divorce me but instead gave birth to my son.

I also thank Alberta Energy Regulator for sending me paychecks every two weeks. Unlike other fellow graduate students who live with minimum wage, I had a very comfortable middle-class life and didn't get the complete experience of a Ph.D. student life.

Further, the committee members (both internal and external) are thanked for taking their time to review this work and provide useful feedbacks. I understand slogging through this 200+ pages thesis is soul-sucking and I'm sure they have better things (like finishing real papers) to do.

## Table of Contents

**Abstract**……..ii
**Preface**……iv
**Acknowledgement** ..... vi
**List of Tables** ..... x
**List of Figures** ..... xii
**List of Symbols and Acronyms** ..... xxii
**Chapter 1: Motivation and context** ..... 1
**1.1 background** ..... 1
**1.2 Thesis outline** ..... 5
**References** ..... 7
**Chapter 2: Geomechanical principles and definitions** ..... 11
**2.1 Cauchy stress tensor and Anderson's assumption** ..... 11
**2.2 Law of friction and effective stress** ..... 15
**2.3 Deterministic Fault slip tendency analysis** ..... 19
**References** ..... 20
**Chapter 3: Borehole measurements of in-situ stress** ..... 22
**3.1 Stress States of Earth's Upper Crust** ..... 22
**3.2 Prior Stress Information in Alberta** ..... 25
**3.3 Stress measuring methods** ..... 28
3.3.1 Determination of Vertical Stress ($S_V$) ..... 28
3.3.2 Determination of Minimal Horizontal Stress ($S_h$) ..... 30
3.3.3 Determination of Formation Pore Pressure ($Pp$) ..... 44
3.3.4 Determination of Directions and Magnitudes of $S_H$ ..... 54
**3.4 Conclusion** ..... 57
**References** ..... 58
**Chapter 4 Quantitative constraints to the complete state of stress from the combined borehole and focal mechanism inversions: Fox Creek, Alberta** ..... 65
**4.1 Introduction** ..... 65
4.1.1 Study Area ..... 66

4.1.2 Geological Structure ..... 68
4.1.3 Fox Creek Induced Seismicity ..... 69
4.1.4 Prior Knowledge of Stress State ..... 70
**4.2 Data and Methods** ..... 71
4.2.1 $S_H$ Orientations $\phi$ ..... 73
4.2.2 Vertical Stress $S_V$ ..... 80
4.2.3 Minimum Horizontal Compression $S_h$ ..... 84
4.2.4 Formation Pore Pressure $P_P$ ..... 88
4.2.5 Greatest Horizontal Compression $S_H$ ..... 89
**4.3 Discussion** ..... 94
4.3.1 $S_H$ Directions ..... 94
4.3.2 $P_P$ and $S_h$ Gradients ..... 96
4.3.3 Validity of Stress Inversion and Andersonian Assumption ..... 97
4.3.4 3D Stress Model ..... 100
**4.4 Conclusion** ..... 102
**4.5 Appendix** ..... 103
**References** ..... 104
**Chapter 5. Frictional Stabilities on Induced Earthquake Fault Planes at Fox Creek, Alberta: A Pore Fluid Pressure Dilemma** ..... 117
**5.1 Introduction** ..... 117
**5.2 Slip Tendency Analysis** ..... 119
**5.3 Fox Creek, Alberta, Events** ..... 120
**5.4 Triggering of fault slip with increasing $P_f$** ..... 126
**5.5 Conclusion** ..... 131
**5.6 Appendix 5A. Summary of earthquakes analyzed in this study** ..... 132
**5.7 Appendix 5B. Methodology** ..... 133
5.7.1 Analyses on seismic attributes derived lineaments ..... 134
5.7.2 Expectations for $C$ and $\mu$ ..... 136
5.7.3 Monte-Carlo Simulation of $SNR$ for different $P_f$ (for Figure 5.4a) ..... 138
5.7.4 Monte-Carlo Simulation of $P_f$ required to initiate slip (for Figure 5.4b) ..... 139
**References** ..... 139

**Chapter 6. States of in-situ stress in the Duvernay East Shale Basin and Willesden Green of Alberta, Canada: variable in-situ stress states effect fault stability** ..... 149
**6.1 Introduction** ..... 149
**6.2 Geological background and induced earthquakes** ..... 153
6.2.1 Regional seismicity: natural and induced ..... 153
6.2.2 Regional geology ..... 157
6.2.3 Regional state of stress ..... 161
**6.3 Stress measurements and fault stability** ..... 164
6.3.1 Data and Quantitative 3D Stress Model ..... 164
6.3.2 Stability analysis for the $M_W$ 3.8 earthquake (Event A) ..... 178
6.3.3 Assess regional susceptibility ..... 182
**6.4 Discussion** ..... 184
6.4.1 Comparison of $S_h$ and $P_P$ with Fox Creek area. ..... 184
6.4.2 Relation to other seismicity in the area ..... 186
6.4.3 What triggered the $M_W$ 3.8 earthquake (Event A) ..... 187
6.4.4 Areal constraints on stability and factors controlling IS ..... 191
**6.5 Conclusions** ..... 195
**References** ..... 196
**Chapter 7: Conclusions and directions for future research** ..... 213
**7.1 Contributions of Work Described Here** ..... 213
**7.2 Suggestions for future research** ..... 214
**References** ..... 216
**Bibliography** ..... 217

## List of Tables

**Table 5A-1.** A total of 11 earthquakes recorded by the regional seismometer network with well resolved focal mechanisms are analyzed in this study. The abbreviated column names stand for $M_W$ – Magnitudes, Lat – Latitude (deg), Lon – Longitude (deg), Dep – Depth (km), S – Strike Angle N-E (deg), D – Dip angle (deg), R – Rake angle (deg).

**Table 5A-2.** States of in-situ stress at the epicentral locations of the earthquakes. The abbreviated column names stand for $M_W$ – Magnitudes, $S_H$ AZ – N-E orientation of maximum horizontal compressional stress (deg), $S_h$ – Minimum horizontal stress (MPa), $S_V$ – Vertical stress (MPa), $S_H$ - Maximum horizontal stress (MPa) constrained using the shape-ratio evaluated through stress inversion technique. $S_H$ max – Maximum $S_H$ constrained with borehole observation. $P_P$ – Apparent pore pressures of the unconventional shale oil/gas reservoir nearby.

**Table 5B-3.** A summary of previous friction test on rocks with mineral composition related to this study (Chapter 5)

**Table 5B-4.** Mineral composition (in percentage by weight) of the Duvernay shale determined through Xray-Diffraction analysis. The abbreviated column names stand for: Q – Quartz, C – Calcite, A – Anorthite, O – Orthoclase, K – Kaolinite, P-Pyrite, A2 – Ankerite, D – Dolomite, M – Muscovite/Illite, A3- Albite

**Table 6.1.** Significant Seismic Events in the Area and Relation to stress field modelled in this study (Chapter 6)

**Table 6.2**. Comparison of calculated stress and pore pressure gradients between the Fox Creek and Red Deer study areas.

# List of Figures

**Figure 2.1.** stress components of the Cauchy tensor (Eqn 2.1) in $x_1$–$x_2$-$x_3$ coordinate system. Retrieved from Wikimedia Commons under the CC BY-SA 3.0 license.

**Figure 2.2.** Graphic illustration of the Andersonian stress with $S_V$, $S_H$ and $S_h$ as principal components. After *Bell et al*. [1990]

**Figure 2.3.** Traction vector decomposed into normal and shear components on a plane with the state of stress described by an Andersonian stress tensor. Adapted from *Schmitt* [2014]

**Figure 2.4.** a) A graphic illustration on the traction force $T$ on a faulting plane with fluid pressures $P$. b) the stability and instability states described by Amonton's friction law. Adapted from *Schmitt* [2014]

**Figure 3.1.** Anderson's faulting theory and stress regimes: a) strike-slip fault movement, when $S_H > S_V > S_h$; b) reverse or thrust fault movement, when $S_H > S_h > S_V$; and c) normal fault movement, when $S_V > S_H > S_h$.

**Figure 3.2.** Extent of the Duvernay Formation described by *Rokosh et al*., [2012] in west-central Alberta, summary of information available in existing compilations of the directions of $S_H$ from the World Stress Map [*Reiter et al*., 2014; *Heidbach et al*., 2016], and $S_h$ gradients and locations of measurements [coloured contours and red dots; *Haug and Bell*, 2016] in Alberta and northeastern British Columbia.

**Figure 3.3.** a) Example of a density log retrieved during this study; blue curve represents the original log, and the orange one represents the smoothed results for $S_V$ modelling. b) Computed $S_V$

from the density log shown in part a; density at depth <500 m is assumed to be equal to the smallest value from the smoothed density recordings (orange line in part a). Red lines show the boundaries of some geological units penetrated by the well.

**Figure 3.4.** Different phases of fluid flow during the diagnostic fluid-injection test: pre–shut-in (blue), pre-closure (pink), and post-closure (brown).

**Figure 3.5.** Four near-wellbore fluid-flow regimes proposed by *Cinco-Ley* [1981]: a) fracture linear flow, with fluid flowing in the direction of fractures; b) bilinear flow, with fluid flowing in the direction of fractures and also leaking into the nearby formation; c) formation linear flow, with fluid flowing from the fractures to the nearby formation rocks in a direction perpendicular to that of the fractures; and d) radial flow, with fluid flowing outwards radially from the wellbore to the nearby formations.

**Figure 3.6.** Transformations of the diagnostic fluid-injection test (DFIT) pressure history for use in constraining fracture-closure pressure ($P_{FC}$): a) fall-off curve of the wellbore pressure following the shut-in; b) $\sqrt{t}$ plot assuming Carter leak-off; c) *G-function* plot initially proposed by *Nolte* [1979]; and d) *log(t)* versus *log($P_w$)* plot.

**Figure 3.7.** Diagnostic fluid-injection test (DFIT) data and analysis from well 01-11-034-24W4, with pressures recorded by a pressure gauge at surface: a) recorded pressure history from the DFIT, showing the moment when the well is shut in after the hydraulic fractures are created; inset shows the entire injection/shut-in history; the shut-in period is many times longer than the injection period to allow wellbore pressure to reduce to fracture-closure pressure and close to pore pressure of the surrounding formation rocks; b) log*($P_w$) versus* log*(t)* plot constraining $P_{FC}$ at ~22.9 MPa; c) $P_w$ *versus log(t)* plot constraining $P_{FC}$ at 22.0–23.1 MPa; d) $\sqrt{t}$ plots estimate the $P_{FC}$ at 22.9 MPa, the left axis showing the values of $dp/d(\sqrt{t})$ and the right axis showing the corresponding pressures at

the same time; e) *G-function* plots estimate $P_{FC}$ at 22.9 MPa, the left axis showing the values of GdP/dG and the right axis showing the corresponding pressures at the same time.

**Figure 3.8.** Conceptual illustration showing the superposed fluid flow in the borehole: a) schematic showing the flow and buildup phases of the test and the principle of superposition; following the shut-in of the well, it is assumed that the wellbore fluid will continue to flow out (dashed line) and an injection of fluid at the same rate will result in a net zero flow rate; b) step function for varying flow rate, the solid line representing the flow rate that can be numerically represented by a step function (red dashed line).

**Figure 3.9.** Sample analysis of a flow-buildup test: a) recorded pressure history during the test; and b) extrapolated pressures with the linear-flow and radial-flow assumptions using the superposition principle.

**Figure 3.10.** Sample post-closure analysis to extrapolate the formation pore pressure: a) using Nolte's approach with assumptions for both linear (blue line) and radial (orange line) flow regimes, respectively; black lines show the extrapolated final wellbore pressure following these two assumed flow regimes; b) using the Soliman-Craig approach (blue and orange lines for linear and radial flow, respectively) with the same assumptions as part a; large plot shows the last part of the measurement when the linear extrapolation is evaluated, with the entire analysis shown in the inset.

**Figure 3.11.** Sample Ultrasonic Borehole Imager (UBI$^{TM}$) wellbore images with identifiable a) borehole breakouts (BOs), and b) drilling-induced tensile fractures (DITFs).

**Figure 4.1.** a) Map of Alberta with lines giving $S_H$ directions in the WSM, red dots showing locations of $S_h$ magnitude measurements, and contours representing the estimated $S_h$-to-depth ratio as compiled by *Haug and Bell* [2016]. The gray zone shows the areal extent of the Duvernay

Formation. The black dashed lines enclose the area investigated in this study. b) An expanded view of the study area including epicentres and focal mechanism solutions for the felt earthquakes from 2013 to 2017 compiled by *Schultz et al.* [2017]. The orange arrows indicate the $S_H$ orientations in the study area recorded by WSM. c) The cross-section of the stratigraphy [*Branscombe et al*., 2018] in the study area from A to A' as shown in b). The black dots along the Duvernay Formation represent the projection of earthquakes shown in b) assuming the earthquakes happen within the Duvernay Formation [*Eaton et al*., 2018; *Schultz et al*., 2017]

**Figure 4.2.** The measurements utilized for this study. The surfaces rendered from top to bottom include 30-m resolution shuttle radar topography, and the Mississippian Unconformity [*Branscombe et al*., 2018], and the tops of the Duvernay Formation extracted from a commercial database and the Neoproterozoic Basement as interpolated from [*Peterson*, 2017]. Red dots and yellow circles indicate the positions of $S_h$ and $P_P$ measurements respectively and many of which are obtained from the same transient pressure record. b) The top-down overview of the study region and the measurement points. Red dots and yellow circle show the locations of $S_h$ and $P_p$ measurements as in a). The black arrows represent the $S_H$ azimuth reveavled by borehole failures intepreted from image logs located within the study area, reported in *Shen et al.,* [2018b]. The solid black circles indicate the epicentral positions of suspected induced events [*Schultz et al*., 2016] as shown in Figure 2.1. White areas indicate disruption of the Duvernay Formation by the coeval Leduc Reefs.

**Figure 4.3.** Examples of depth segments of high-quality ultrasonic amplitude reflectivity image log data from well UWI 12-11-64-27W5 showing zones with (a and, (b BOs, and without (c and, (d BOs.

**Figure 4.4.** a) The complete set of 20 observations of reported in *Shen et al.,* [2018b], plotted versus depth and colour-coded by each borehole. b) Rose diagram histogram distribution of $S_h$ orientation measurements $\phi$ for the entire set of final average $\phi$ for all the boreholes (including those reported in WSM) used. c) The von Mises circular distribution for the full set of azimuths from a) with the maximum occurring at $\phi = 43°$.

**Figure 4.5.** a) Map of averaged $S_H$ azimuths $\phi$ determined using IDW. Black arrows represent stress orientation measurements reported by *Shen et al*., [2018b]. Small white arrows represent those from WSM. The cyan dashes represent directly the modelled $\phi$ at grid points in the study area while the background colour is the smoothed model for $\phi$ over the area. The red arrows and dots show the strikes of the faulting planes revealed by earthquakes' focal mechanism solutions and the epicentral locations. b) The search radius of each prediction point for IDW. c) Confidence in the $S_H$ azimuth prediction. Values close to zero represent high confidence and values close to one stand for low confidence.

**Figure 4.6.** a) The lithostatic pressures of the upper section of the model. b) The topographic impact on the $S_V$ at the tops of the Duvernay Formation evaluated through the GFM. c) The difference between the topographic impact and lithostatic pressures of the upper section of the model. d) The vertical stress $S_V$ mapped into the middle depth point of the Duvernay Formation from the elevation corrected model and e) its corresponding uncertainty. The black crosses represent the wellbores with density logs. f) The stress to depth ratio for $S_V$.

**Figure 4.7.** Magnitudes of a) $S_h$ and b) $P_p$ versus depth with error bars representing uncertainties. Black lines show the best linear fit for each case.

**Figure 4.8.** Projections to the top of the Duvernay Formation of a) the modelled $S_h$ value. b) The uncertainty of the modelled $S_h$. c) the spatial perturbation of $S_h$ calculated by subtracting the modelled $S_h$ value with the linear trend of Eqn. 4.4. d) The difference between $S_h$ and $S_V$. In all panels the white dashed line represents the contour with an uncertainty of 3 MPa. Empty spaces indicate the engulfed Leduc reefs. Red crosses show the locations of the $S_h$ observations.

**Figure 4.9.** 3D projections to the top of the Duvernay Formation of a) the modelled $P_P$ value. b) The uncertainty of the modelled $P_P$. c) The spatial perturbation of $P_P$ calculated by subtracting the modelled $P_P$ value with the linear trend of Eqn. 2.5. d) The difference between $P_P$ and hydrostatic fluid pressures. In all panels, the white dashed line represents the contour with an uncertainty of 7 MPa. Empty spaces indicate the engulfed Leduc Reefs. Red circles show the locations of the $P_P$ observations.

**Figure 4.10.** histogram of the shape-ratio R from stress inversion with red line represents the nonparametric kernel-smoothing distribution fit (Bowman and Azzalini, 1997) that include a) all inversion results regardless of the $\sigma_2$ dip; or only those results with $\sigma_2$ dip angles b) greater than 80° c) greater than 85°; d) greater than 88°

**Figure 4.11.** $S_h$ measurements and calculated $S_H$ from SB with $S_V$ and $S_H$ modelled in this study at the location of the $S_h$ measurements. The Whisker-Box plot of $S_H$ denotes the range of possible values of $S_H$. The blue boxes confine 25$^{th}$ and 75$^{th}$ percentile of the CDF of $S_H$, and red dashes present the most probable value of $S_H$. Whiskers represent the minimum and maximum values of $S_H$. Black crosses represent the magnitudes of $S_H$ initially estimated by SA.

**Figure 4.12.** Axes of $\sigma_1, \sigma_2, \sigma_3$ from the recorded earthquake's focal mechanism solutions and stress inversion. Contours represent densities of $\sigma_1, \sigma_2, \sigma_3$ solutions from stress inversion. Red

circles and small blue crosses represent the P/T axes from the input focal mechanism solutions. Black symbols show the most probable orientation of the in-situ stress by stress inversion. Blue squares and lines indicate the orientations of $S_H$ predicted from the stress model at each of the earthquake's epicentral locations shown in **Figure 4.5.**

**Figure 4.13.** $S_h$ measurements reported in *Woodland and Bell,* [1989], *Haug and Bell,* [2016] and SB. The dashed line represents the linear regression results on SB data (see Eqn. 4.3)

**Figure 5.1.** a) Focal mechanisms of the earthquakes analyzed in this paper. The black dots show the epicentres of each earthquake. The coloured background shows the depth of the Duvernay Formation that is cotemporaneous with Leduc reefs (white areas). Blue and orange arrows show the direction of $S_H$ determined by borehole observations from WSM [*Heidbach et al.*, 2016] and *Shen et al*., [2019]. Dashed line box indicates area of the directly measured stress tensor components shown as interpolated maps at the top of the Duvernay Formation in panels b-e. In these panels the black dots indicate the epicenters and the associated black arrows the slip direction determined from focal mechanisms. b) $S_H$ trend azimuth $\phi$ shown both as the colormap and on select grid points as cyan arrows c) vertical total compressive stress $S_V$, d least horizontal total compressive stress $S_h$ and e) formation pore pressure $P_P$. The greatest horizontal total compressive stresses are described by a statistical distribution at each grid point and are not shown.

**Figure 5.2.** Stereonet plot with *SNR* shown in nonlinear colormap for the poles of any arbitrarily oriented faulting planes in the at the epicenters of the well-oriented $M_W$ 3.6 and 4.1 events with the Andersonian model stresses $S_h$ = 65 MPa; $S_V$ = 84 MPa, $S_H$ = 124 MPa with $\phi$ = 41° using a) $P_f$ = *0,* b) Hydrostatic $P_H$ = 33 MPa, and c) $P_f$ = measured $P_P$ 62 MPa; and for the poorly oriented $M_W$ 3.9 event d) $P_f$ = *0,* e) Hydrostatic $P_H$ = 33 MPa, and f) $P_f$ = measured $P_P$ 57 MPa. See text for details.

**Figure 5.3.** Increasing slip tendency (*SNR*) of the fault with rising $P_f$ for a) $M_W$ 4.1 and b) 3.9 events. The *SNR* of the earthquake's faulting plane at different fluid pressures. The red and green regions represent the SNR distributions setting, respectively, for $C = 0$ and $C = 5$ MPa. The width of the stripe represents the uncertainty of *SNR* due to different $S_H$, and the black lines show the calculation with the most confident value for $S_H$. Gray box highlights the range of *SNR* (0.4- 0.8).

**Figure 5.4.** Monte-Carlo calculations versus angle $\psi$ of a) *SNR* distributions on the fault planes calculated assuming $P_f = 0$ (blue) and $P_f = P_P$ (green), boxes indicate the 25$^{th}$ and 75$^{th}$ percentile limits of the probability density functions, and the red lines indicate the most probable SNR value for each case, plotted versus the angle $\psi$ bisecting each events local $S_H$ direction $\phi$ and the fault plane strike. b) The distributions fluid pressures needed to activate the faults, boxes indicate the 25$^{th}$ and 75$^{th}$ percentile limits of the probability density functions, and the red lines indicate the most probable critical $P_f$ value. Black dashed lines represent the fracture closure pressure (equal to $S_h$), measured virgin $P_P$ and depth-dependent normal hydrostatic pressure $P_H$. Shaded gray zones in both panels indicate suggested *SNR* and optimal orientation angle ranges.

**Figure 5B-1.** Fault inferred through reflection seismic survey with background colours represent the attributes used for seismic interpretation. a) Black lines represent the HF wells trajectories. Coloured lines represent lineaments interpreted as faults with. b) Beach balls show the resolved focal mechanisms for earthquakes $M_W$ 3.6 and $M_W$ 4.1. In both a) and b) dashed black arrows represent the orientation of $S_H$.

**Figure 6.1**. **a)** Overview of the study area in Alberta, Canada with West Shale Basin (WSB) and East Shale Basin (ESB), respectively, that are separated by the Rimbey-Meadowbrook reef trend. **b)** Bedrock stratigraphy of western central Alberta with elements from the cross-section shown in **c)** for the line A-A' in a). Vertical depth in c) is exaggerated by 50 times.

**Figure 6.2. a)** Map of major geographic features associated with the Duvernay Formation, including the WSB and the ESB. **b)** Detail map of epicenters within the study area, the background color indicates depths from sea level to the tops of the Duvernay Formation. Outlined brown squares: three major earthquakes designated A, B, and C with FM resolved (details Table 6.1) **c)** 3D view of the study area, comprising in stratigraphically descending order, the surface topography, sub-Cretaceous unconformity

**Figure 6.3**. Geological features of our study are with a) map of the tectonic provinces mapped by *Ross et al.,* [1991] with their boundary lines reproduced in *Gu and Shen,* [2015].

**Figure 6.4.** Spatial maps for the states of stress in the center of the Duvernay Formation of our study area. **a)** the orientation of $S_H$ and **b)** normalized uncertainty A (from 0 - 1). **c)** the magnitudes of $S_V$ and **d)** uncertainty. **e)** magnitudes of $S_h$ and **f)** the uncertainties. **g)** and **h)** shows the $P_P$ and the uncertainties. White contours in e) to h) show the enclosed areas with uncertainties of less than 5 MPa for $S_h$ and 4.5 MPa for $P_P$. Gray lines enclose the areal extent of the Duvernay Formation engulfed by the Leduc reefs.

**Figure 6.5.** Reported measurements (with their respective uncertainties) and linear regression results for **a)** $S_h$ and **b)** $P_P$ from different sources.

**Figure 6.6.** Estimated maximum stress $S_H$ from borehole breakouts. The width of the polygons mark the $25^{th}$ to $75^{th}$ percentile of the cumulative probability density functions for $S_H$, computed using Monte-Carlo methods, and the black lines stand for median values of $S_H$.

**Figure 6.7. a)** The distribution of shape factor $R$ computed for both conjugate fault planes from the earthquake's ($M_W$ 3.8/$M_L$ 4.2) focal mechanism solution, and **b)** inverted $S_H$ with the predicted

$S_h$ and $S_V$ at the epicenter, using the $R$ distribution from conjugate plane 1, assuming an Andersonian strike-slip stress regime.

**Figure 6.8**. Stereonets of the *SNR* on all possible planes at *Event* A*'s* focus calculated assuming vanishing cohesion $C$ with a) no fluid pressure $P_f = 0$, b) normal hydrostatic pressure $P_f = P_H$, and c) Duvernay Formation pore pressure $P_f = P_P$. Blue and red dots are the poles of the two conjugate planes of the event's FM. Black dots indicate the poles for hypothetical optimally oriented planes. Blue and white contours delineate *SNR* = 0.8 and 0.4.

**Figure 6.9.** Monte Carlo distributions of **a)** shear traction, **b)** normal clamping traction and **c)** critical $P_f^c$ required for slip on either *of Event* A*'s* conjugate planes.

**Figure 6.10**. Required critical pressure $P_f^c$ to activate hypothetical faults across the study area for **a)** hypothetical faults across the region oriented parallel to the conjugate plane 1 for the Red Deer earthquake listed in Table 6.1, and **b)** assumed faults oriented optimally to slip. **c)** and **d)** are the corresponding pressure difference $\Delta P$ ($= P_f^c - P_P$) shown in a) and b). **e)** The study area in *Schultz and Wang* [2020], with earthquake locations and nearby HF wells.

**Figure 6.11.** The slip tendency of the **a)** conjugate faulting plane 1, **b)** 2 of the FM solutions for the *Event* A, and **c)** a hypothetical fault oriented optimally (assuming $\mu = 0.6$) for slip initiation. Red and green stripes represent the range of values calculated for the constrained bounds of $S_H$ (75 – 106 MPa, median 84 MPa) account for either $C = 0$, or 5 MPa. Gray box denotes the expected range of $\mu$ between 0.4 and 0.8.

## List of Symbols and Acronyms

| | |
|---|---|
| $\sigma_{i,j}$ | Cauchy stress tensor in Einstein notation |
| $\sigma_1$, $\sigma_2$, $\sigma_3$ | Principal components of a stress tensor |
| $S_h$, $S_V$, $S_H$ | Andersonian minimum horizontal stress, vertical stress, maximum horizontal stress, in MPa |
| $P_p$ | Formation rock pore pressure, in MPa |
| $P_w$ | Drilling mud pressure, in MPa |
| $P_f$ | Fluid pressure in the gap of fault, in MPa |
| $P_f^c$ | Critical fluid pressure above which the fault slips, in MPa |
| $P_H$ | Hydrostatic pressure, in MPa |
| $\phi$ | Azimuth of the direction of $S_H$ as measured clockwise looking down from North in degrees, stress orientation |
| $\rho$ | Rock density, in kg/m$^3$ |
| $R$ | Shape-ratio of stress |
| $\psi$ | Friction angle of rock, in degrees |
| $\mu$ | Coefficient of friction |
| $C_o$ | Unconfined Compressive Strength, in MPa |
| $\boldsymbol{T}$ | Traction vector describe the forces on an arbitrary plane caused by the stress field |
| $\tau_i$ | Shear projection of the traction vector on an arbitrary plane in Einstein notation |
| $\boldsymbol{t}$ | Vector consists of 5 elements describing the deviatoric part of a normalized stress tensor |

| | |
|---|---|
| $A$ | Kernel matrix describing linear relationship between in-situ stress and fault's slipping direction. |
| $\boldsymbol{s}$ | Unit vector describing slipping direction of fault |
| $\boldsymbol{N}$ | Unit vector normal to the fault |
| $\sigma_i$ | Normal pressure vector in Einstein notation |
| $M_W$ | Moment magnitude scale |
| $M_L$ | Richter local magnitude |
| $SNR$ | Shear-to-normal ratio of the traction force on a faulting plane |
| $FM$ | Focal Mechanism |
| WSM | World Stress Map |
| WG | Willesden Green oil field |
| WSB | West shale basin |
| ESB | East shale basin |
| RHMSZ | Rocky mountain house seismic zone |
| CDF | Cordillera Deformation Front |

# Chapter 1: Motivation and context

## 1.1 background

Material deformations are governed by its constitutive model and the states of stress. As such, studies on the mechanics of geological materials in the Earth's interior requires quantitative knowledge of the state of in-situ stress. Having such knowledge is important for a number of practical and societally relevant purposes as regards a wide range of engineering projects that include hydrocarbon and geothermal energy exploitation, greenhouse gas and waste fluid geological sequestration, deep subsurface mining, earthquake hazard assessment, and subsurface space engineering as well as more basic scientific investigations related to large scale geodynamic processes and the physical processes driving fault slip. Consequently, having a fuller appreciation of the actual magnitudes and directions of stress in the earth before, during, and long after humans disrupt the subsurface is increasingly important.

This thesis focuses on one particular issue of anthropogenically induced earthquakes where the need for better knowledge of in-situ stress is further emphasized as this will directly impact issues related to public safety, economic viability, and societal permission. Human activities have been linked to earthquakes at least since the 1960s, and there have been a few key examples prominent more generally worth reviewing [see *Suckale*, 2009; *Van der Baan and Calixto*, 2017; *Zang et al*., 2014; *Schultz et al*., 2020]. One area of concern focused on earthquakes associated with the crustal loading of large surface reservoirs that altered the state of stress and pore fluid pressures in the crust in their vicinity with the 1967 Koynanagar earthquake, Maharashtra, India near the recently commissioned Koyna Dam [*Gupta et al*., 1969] that led to at least 177 deaths.

The injection of waste fluids beginning in 1962 into a deep borehole (3671 m) drilled into cratonic rocks beneath at the Rocky Mountain Arsenal, Denver, USA was linked to a series of earthquakes [*Healy et al*., 1968; *Evans,* 1966]. These latter events led to the only controlled tests in which seismicity was intentionally induced by changing subsurface fluid pressures at a remote site near Rangeley, Colorado that demonstrated a link between elevated pore pressures and seismicity [*Raleigh et al*., 1976]. This work even led to a great deal of speculation as to whether or not large earthquakes might actually be tamed. The topic did not receive as much attention again until the late 2006 startup of a geothermal project at Basel, Switzerland, led to a flurry of small events, almost all only instrumentally detectable, with a few up to $M_L$ 3.4 led to the shut-down of the project [*Deichmann and Giardini*, 2009; *Giardini*, 2009] – the seismicity slowly after lessened stopping the water injection. Both scientific, regulatory, and public interest in the topic accelerated greatly; however, with the damaging $M_w$ 5.6 Prague, OK earthquake in late 2011 combined with greatly elevated levels of seismicity that began in 2009 that were linked to large volumes of waste brines as a byproduct of hydrocarbon production. Correlative studies [*Keranen et al*., 2013; *Elsworth*, 2013] linked the elevated levels of seismicity to the volumes of the fluid re-injected in disposal wells.

Since then, interest in induced seismicity had become a global phenomenon with a large number of studies being motivated (see examples above). However, prior to this series of work, the investigations are primarily statistical in nature, attempting to establish spatial-temporal correlations.

More locally, the Western Canada Sedimentary Basin has largely been aseismic, although part of the reason for this could be related to the paucity of seismometers over the large areas. That

said, there were a number of events linked to hydrocarbon production or disposal of waste fluids prior to 2000. The 1970 Snipe Lake event (M ~= 5.1) was suspected to be linked to nearby enhanced oil recovery operations that inject fluid into the subsurface. The later Rocky Mountain House earthquakes (up to M 3.4) were better located, owing to the close CNSN seismometer network [*Wetmiller*, 1986], with a strong spatial-temporal correlation to the enhanced hydrocarbon recovery in the nearby Strachan gas field [*Rebollar et al.*, 1982; 1984]. Significant earthquakes were also recorded (M up to 4.1) from 1984 to 1993 near the Fort St. John, British Columbia *[Horner et al.* 1994 ], associated with injection of fluids.

Though some success had been reported, seismic susceptibility analysis developed solely on the basis of statistical correlation (e.g., Probabilistic Seismic Hazard Analysis, PSHA) had shown strong misprediction in the areas that had been mapped as relatively 'low risk' but later with large, devastating earthquake happened in the premise [e.g., Tohoku earthquake, M 9.1, 2011, Wenchuan earthquake, M 7.9, 2008, Haiti earthquake, M 7.0, 2010, see details in *Stein et al.*, 2012]. Retrospectively speaking, this discrepancy is not surprising as the statistical modeling requires the input of historical earthquake records that can be easily biased by the seismometer network's detection limit and, in the context of induced earthquakes, the presence or absence of industrial activities.

Industrial activity-induced seismicity has been widely reported and commonly associated with unconventional hydrocarbon exploitation [*Elsworth*, 2013]. However, most of the USA's reported events are due to the injection of wastewater [*Keranen et al*., 2013; 2014]. Often, a sufficient amount of water and a long window of time allows the states of in-situ stress and fluid pressures to be adequately altered to favor fault activation. Though similar wastewater injection-

induced earthquakes had also been reported in the Western Canada Sedimentary Basin [e.g., *Schultz et al*., 2014], more to be highlighted is the hydraulic fracturing (HF) induced earthquakes [*Schultz et al*., 2020], particularly in the province of Alberta, the ones near the town of Fox Creek and later near the city of Red Deer. In the Horn River Basins of British Columbia, hydraulic fracturing activities were also suspected to be the cause of the increasing seismicities [*Farahbod et al*., 2015].

HF operations inject much smaller amounts of water into the subsurface but at a higher, burst rate to create fractures up to the lengths of a few hundred meters. These fractures alter the geological materials' hydraulic properties that allow fluids to flow more efficiently through the targeted hydrocarbon reservoir.

It is particularly worth considering that only a small fraction of HF wells (< 2% of the multi-stage horizontal wells, *Atkinson et al*., 2016, much less if vertical wells are to be included) are linked to earthquakes that are larger (M > 2) than the more commonly seen 'microseismicity'. The latter is considered a normal phenomenon that acoustic energies are emitted when hydraulic stimulation fractures the rock. Literature published prior to this work [e.g., *Atkinson et al*., 2016] loosely attribute these wells as 'seismogenic' without further detailed explanation on the physical controlling factors. Statistical modeling had been employed to explore the sensitivities of different geological factors to the seismic susceptibilities [*Pawley et al*., 2018]; however, the work published before the Red Deer ($M_W$ 3.8) events mapped the area to be low risk, highlighting the deficiencies in such statistical modeling approach and a need for physical, deterministic analysis.

In this thesis, we aim to deterministically analyze the faults' slip tendency for two areas where the Devonian Duvernay Formation is heavily targeted for HF operations. We collected and

processed raw borehole records to obtain the complete stress tensor as a function of spatial locations. Two 3D stress models, which are the key components of this thesis, are constructed and can be accessed through [*Shen*, 2019; *Shen and Schmitt*, 2020].

## 1.2 Thesis outline

The thesis is arranged as follows.

In **Chapter 2** we provide some essential theoretical background to understanding stress and resolved tractions of planes in the earth, and the basic definitions of the parameters used in the thesis are discussed. Frictional stability is discussed in terms of effective stress laws.

In **Chapter 3** we review tools earlier workers had adapted for the purpose of quantitatively determining states of stress and pore fluid pressure using borehole measurements. The methods we adopted processing the raw wellbore test results and borehole logs are presented in this chapter too. Some of the data that are later incorporated in Chapters 3 and 5 are presented and discussed. Much of the material in this chapter is part of the internally reviewed published report of Alberta Geological Survey (see the preface for details).

In **Chapter 4**, We develop a quantitative predictive model for the state of stress of a volume of crust encompassing the Duvernay Formation with a spatial extent of over 150 km × 150 km centered near the municipality of Fox Creek, Alberta. An average direction of the maximum horizontal compression $S_H$ of N43°E is determined from the analysis of 20 borehole image logs. A model of the vertical stress $S_V$, corrected for topographic variations, is provided from the integration of a 3D density volume constructed from 1125 density logs. The minimum horizontal compression $S_h$ and pore pressure $P_P$ are evaluated through analysis of 57 well tests carried out

within the Duvernay Formation; 3D models developed by kriging of the observed values. Stress inversion of the focal mechanism solutions for the earthquakes nearby validated the assumed Andersonian stress regime and provided the shape-ratio of the stress which further allowed estimation of maximum horizontal compression $S_H$. A program is provided allowing the user to calculate the full set of components necessary to describe the states of in-situ stress for a location of interest near the Duvernay formation within our study area. The material in this Chapter is published in *Tectonophysics* (see the preface for details)

In **Chapter 5**, with the knowledge of the stress state developed in Chapter 3, we physically model the slip-tendencies on the faulting planes of eleven earthquakes that are linked to hydraulic fracturing stimulations of an unconventional hydrocarbon reservoir in a historically aseismic area of NE Alberta using a recently constructed quantitative model for in-situ stresses and pore pressures. It is shown that the ambient pore pressures of the nearby Duvernay unconventional reservoirs can provide enough $\Delta P_f$ triggering fault movement. The local fluid pressures acting on the fault could readily be increased above the critical value if a hydraulic connection exists between the fault and a propagating hydraulic fracture within which pressures in excess of the minimum compression exist. The critical pressures necessary to induce slip, is estimated using a probabilistic model that incorporates uncertainties of stress and fault mechanical properties. These critical pressures are greater than expected hydrostatic pressure but less the pore pressures of nearby unconventional reservoirs. The material in this chapter is published in *Geophysical Research Letters* (see the preface for details).

In **Chapter 6**, we start by quantitatively constraining the magnitudes and orientations of minimum ($S_h$), maximum ($S_H$) horizontal stresses, vertical stress ($S_V$) utilizing both borehole

measurements and earthquake's focal-mechanism (FM) solutions for a study area where a newly emerging swarm of HF induced earthquakes are reported (near the city of Red Deer, Canada). The pore pressures ($P_P$) are also assessed through several transient well testing results targeting the unconventional reservoirs. This knowledge allows the fault stabilities for the HF induced Red Deer ($M_L$ 4.2/$M_W$ 3.8) earthquake to be assessed. The N-S (or E-W) aligned fault, revealed by the FM solution, appears to be stable at a hydrostatic fluid pressure but unstable when fluid pressure is increased to the level of ambient unconventional reservoir pore pressures. The slip-tendency of the faults in the region studied is assessed by calculating the required fluid pressures to activate hypothetical faults; we find that the HF-induced clusters geographically overlap with the zones of higher susceptibility. High ambient pore pressure does not correlate with high susceptibility, and large deviatoric stress is needed to cause HF-induced earthquakes. The final version of this chapter may be different as the manuscript has been revised and is currently in the review process of the *Journal of Geophysical Research: Solid-Earth*.

Finally, Chapter 7 provides a summary of the contribution made through **Chapters** 3 – 6. A number of caveats that were not adequately accounted for in this study are discussed, and future improvements are suggested.

As may be seen from the above, the core of this thesis is in the format of a compilation of published manuscripts, and as such, there will unavoidably be some repeated themes. The author asks for the reader's forbearance of this unescapable review through the three key chapters.

## References

Atkinson, G.M., Eaton, D.W., Ghofrani, H., Walker, D., Cheadle, B., Schultz, R., Shcherbakov, R., Tiampo, K., Gu, J., Harrington, R.M. and Liu, Y., 2016. Hydraulic fracturing and

seismicity in the Western Canada Sedimentary Basin. *Seismological research letters*, *87*(3), pp.631-647.

Deichmann, N. and Giardini, D., 2009. Earthquakes induced by the stimulation of an enhanced geothermal system below Basel (Switzerland). *Seismological Research Letters*, *80*(5), pp.784-798.

Ellsworth, W.L., 2013. Injection-induced earthquakes. *Science*, *341*(6142).

Evans, D.M., 1966. The Denver area earthquakes and the Rocky Mountain Arsenal disposal well. *The Mountain Geologist*.

Farahbod, A.M., Kao, H., Walker, D.M. and Cassidy, J.F., 2015. Investigation of regional seismicity before and after hydraulic fracturing in the Horn River Basin, northeast British Columbia. *Canadian Journal of Earth Sciences*, *52*(2), pp.112-122.

Giardini, D., 2009. Geothermal quake risks must be faced. *Nature*, *462*(7275), pp.848-849.

Gupta, H., Narain, H., Rastogi, B.K. and Mohan, I., 1969. A study of the Koyna earthquake of December 10, 1967. *Bulletin of the Seismological Society of America*, *59*(3), pp.1149-1162.

Horner, R.B., Barclay, J.E. and MacRae, J.M., 1994. Earthquakes and hydrocarbon production in the Fort St. John area of northeastern British Columbia. *Can. J. Explor. Geophys.*, *30*(1), pp.39-50.

Healy, J.H., Rubey, W.W., Griggs, D.T. and Raleigh, C.B., 1968. The Denver earthquakes. *Science*, *161*(3848), pp.1301-1310.

Keranen, K.M., Savage, H.M., Abers, G.A. and Cochran, E.S., 2013. Potentially induced earthquakes in Oklahoma, USA: Links between wastewater injection and the 2011 Mw 5.7 earthquake sequence. *Geology*, *41*(6), pp.699-702.

Keranen, K.M., Weingarten, M., Abers, G.A., Bekins, B.A. and Ge, S., 2014. Sharp increase in central Oklahoma seismicity since 2008 induced by massive wastewater injection. *Science*, *345*(6195), pp.448-451.

Pawley, S., Schultz, R., Playter, T., Corlett, H., Shipman, T., Lyster, S. and Hauck, T., 2018. The geological susceptibility of induced earthquakes in the Duvernay play. *Geophysical Research Letters*, *45*(4), pp.1786-1793.

Raleigh, C.B., Healy, J.H. and Bredehoeft, J.D., 1976. An experiment in earthquake control at Rangely, Colorado. *Science*, *191*(4233), pp.1230-1237.

Rebollar, C.J., Kanasewich, E.R. and Nyland, E., 1982. Source parameters from shallow events in the Rocky Mountain House earthquake swarm. *Canadian Journal of Earth Sciences*, *19*(5), pp.907-918.

Rebollar, C.J., Kanasewich, E.R. and Nyland, E., 1984. Focal depths and source parameters of the Rocky Mountain House earthquake swarm from digital data at Edmonton. *Canadian Journal of Earth Sciences*, *21*(10), pp.1105-1113.

Schultz, R., Stern, V. and Gu, Y.J., 2014. An investigation of seismicity clustered near the Cordel Field, west central Alberta, and its relation to a nearby disposal well. *Journal of Geophysical Research: Solid Earth*, *119*(4), pp.3410-3423.

Schultz, R., Skoumal, R.J., Brudzinski, M.R., Eaton, D., Baptie, B. and Ellsworth, W., 2020. Hydraulic fracturing-induced seismicity. *Reviews of Geophysics*, *58*(3), p.e2019RG000695.

Shen, L., 2019. Data for: Quantitative constraints to the complete state of stress from the combined borehole and focal mechanism inversions: Fox Creek, Alberta, Mendeley Data, V1, doi: 10.17632/nxhs4ppcdf.1

Shen, L., and Schmitt, D., 2020. Data for: States of in-situ stress in the Duvernay East Shale Basin and Willesden Green of Alberta, Canada: variable in-situ stress states effect fault stability, Mendeley Data, V1, doi: 10.17632/tgmxx5vkjx.1

Stein, S., Geller, R.J. and Liu, M., 2012. Why earthquake hazard maps often fail and what to do about it. *Tectonophysics*, *562*, pp.1-25.

Suckale, J., 2009. Induced seismicity in hydrocarbon fields. In Advances in geophysics. Vol. 51, pp. 55-106. Elsevier. 3

Van der Baan, M. and Calixto, F.J., 2017. Human-induced seismicity and large-scale hydrocarbon production in the USA and C anada. *Geochemistry, Geophysics, Geosystems*, *18*(7), pp.2467-2485.

Wetmiller, R.J., 1986. Earthquakes near Rocky Mountain House, Alberta, and their relationship to gas production facilities. *Canadian Journal of Earth Sciences*, *23*(2), pp.172-181.

Zang, A., Oye, V., Jousset, P., Deichmann, N., Gritto, R., McGarr, A., Majer, E. and Bruhn, D., 2014. Analysis of induced seismicity in geothermal reservoirs–An overview. *Geothermics*, *52*, pp.6-21.

# Chapter 2: Geomechanical principles and definitions

In this chapter we provide some of the basic definitions and background theories. This includes sections that discuss basic and commonly accepted assumptions on the states of stress for upper crust, the concept of effective stress and laws of friction. These principles are essential for the analysis that are going to be presented in the later chapters.

## 2.1 Cauchy stress tensor and Anderson's assumption

We include here a brief review on the basic elements of solid mechanics that are relevant to this work, as indicated in its title, the stability of fault. Briefly, the work here uses the concept of traction forces due to a state of stress on a given planar surface within a solid continuum. Stress is defined as the traction force divided by the area of the surface. If one considers an infinitesimal cube within the medium aligned with an $x_1$-$x_2$-$x_3$ co-ordinate frame, one can then find the 18 tractions on each of the cube's 6 faces. Assuming a body that is composed of many infinitesimal cuboids, the stress, as a function of the coordinate ($x_1$, $x_2$, $x_3$, Figure 2.1) describes the 6 traction forces applied on such cube's surfaces. A total of 18 shear and normal components are needed to describe the stress completely. However, for the body to remain static (i.e., not moving nor rotating), the opposing tractions must balance leading to 6 independent stresses expressed as the symmetric Cauchy tensor

$$\boldsymbol{\sigma} = \begin{bmatrix} \sigma_{11} & \sigma_{12} & \sigma_{13} \\ \sigma_{12} & \sigma_{22} & \sigma_{23} \\ \sigma_{13} & \sigma_{23} & \sigma_{33} \end{bmatrix} \tag{2.1}$$

which, when provided with respect to the co-ordinate frame, completely describes the states of stress at the point in the medium.

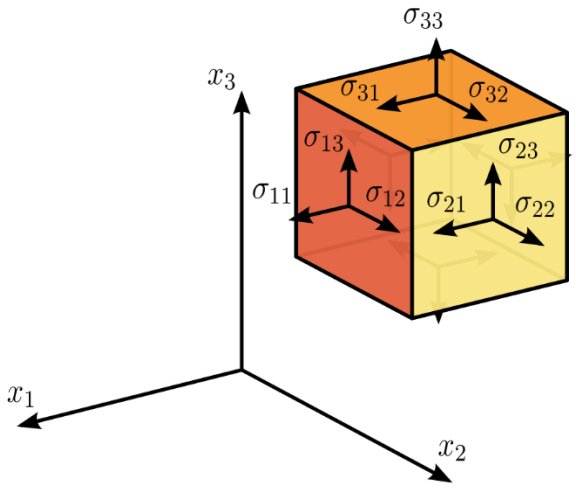


**Figure 2.1.** stress components of the Cauchy tensor (Eqn 2.1) in $x_1$–$x_2$-$x_3$ coordinate system. Retrieved from Wikimedia Commons under the CC BY-SA 3.0 license.

In Eqn 2.1, each of the stress component $\sigma_{ij}$ is described under the coordinate system shown in Figure 2.1. The subscript *i*, denotes the normal direction of the surface and *j* denotes the direction of traction force. As such, $\sigma_{ii}$ represents the traction pressure parallel to the normal direction and $\sigma_{ij}$ represents the shear stress. For different reference coordinate systems, the tensor $\boldsymbol{\sigma}$ can be rotated by multiplying with a rotation matrix [see example in *Mavern*, 1969]. Among the infinite number of ways a stress tensor can be rotated, there exists one special coordinate frame where all the shear stresses equal vanish leaving only the normal stress  In this coordinate system, the three normal components ($\sigma_{11}$, $\sigma_{22}$, $\sigma_{33}$) are called the principal stresses. There is no loss of information during the stress tensor rotation; these three principal components and the definition of the reference coordinate system can completely describe the states of stress at a point.

Owing to the technical difficulties and economic challenges, some simplification on the states of stress for Earth's crust is necessary. Commonly accepted and referred to as the Andersonian [1905] stress states, the in-situ stress is assumed to have one of the principal components parallel to gravity (Figure 2.2). This assumption allows some immediate constraints on the stress state: first, the vertical principal component ($S_V$) can be reasonably approximated by the pressure generated by a column of rock from Earth's surface to the depth point; second, the other two principal components (minimum horizontal stress $S_h$, maximum horizontal stress $S_H$) must be orthogonal to the gravity vector and each other. The latter point is of particular importance as it allows the direction of the stress tensor to be described by a scalar angle between one of the horizontal principal stress directions and a geographic axis. Here, following conventions used in the World Stress Map project [WSM, *Heidbach et al*., 2016) the stress field orientation is simply described by the single azimuthal angle ($\phi$) between the geographic North and the direction of $S_H$. As such, the stress tensor is completed as:

$$\boldsymbol{\sigma} = \begin{bmatrix} S_H & 0 & 0 \\ 0 & S_h & 0 \\ 0 & 0 & S_V \end{bmatrix}. \tag{2.2}$$

Please note that as we have $S_H$, $S_h$ and $S_V$ as the principal components of $\boldsymbol{\sigma}$, the shear components are automatically equal to zero.

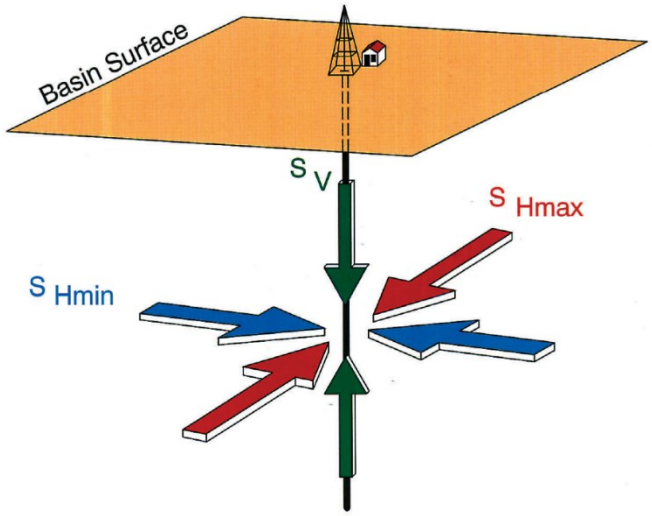


**Figure 2.2.** Graphic illustration of the Andersonian stress with $S_V$, $S_H$ and $S_h$ (denoted as $S_{Hmin}$ in the figure) as principal components. After *Bell et al*. [1990]. In this study, we used the positive-compression sign that was adopted in many other geomechanics analyses.

Though Anderson's assumption is generally well accepted, many have reported that $S_V$ may deviate from the actual principal stress direction, particularly in areas with rapidly varying surface topography and locations where sharp material discontinuities (e.g., fault, folding) exist. However, Anderson's assumption remains a pillar for most geomechanical analysis on Earth's upper crust in layered sedimentary basins with gentle surface topography; we adopt this assumption here too, but we also provide a brief discussion on the caveats and compatibility to the actual stress states (see section 4.2.5 and 4.3.1).

At the time of this writing, a technique that can measure the complete stress state at depth from the surface does not exist, although various creative techniques [see review in *Schmitt et al*., 2012] had been employed to allow proxies measurements that can infer for the state of stress. With more details available in Chapter 3, the horizontal stress magnitudes can be constrained through

transient well fluid pressure tests and the shape of drilled, originally circular, borehole allow determination of stress orientation.

Another important parameter that much be accounted for is the pore fluid pressure. Though often assumed to be hydrostatic, the gradient of subsurface fluid pressure varies. This pressure acts on within the rock's pore spaces and joints and alters the 'effective' stress. We will briefly talk more about this in section 2.3 in the context of how the states of stress and fluid pressures impact the fault's slip tendency, following a brief overview of methods to determine the stress components and fluid pressures are presented in the section below.

## 2.2 Law of friction and effective stress

It has already been noted that at a fundamental level the Cauchy stress components on a given surface are derived from the tractions. This of course can be reverted in that knowledge of the complete stress tensor readily allows a traction vector $\boldsymbol{T}$ to be found on any arbitrarily oriented plane within the material according to

$$\boldsymbol{T} = \boldsymbol{\sigma} \cdot \boldsymbol{n}, \tag{2.3}$$

where $\boldsymbol{n}$ is a unit vector normal to the plane (Figure 2.3). This equation allows assessment of the mechanical states that is readily applicable for a faulting plane. The traction vector $\boldsymbol{T}$ can be further decomposed to normal and shear tractions on the faulting plane where the normal traction $\sigma_N$ is parallel to $\boldsymbol{n}$ and shear traction $\tau$ is parallel to the plane (see Figure 2.3).

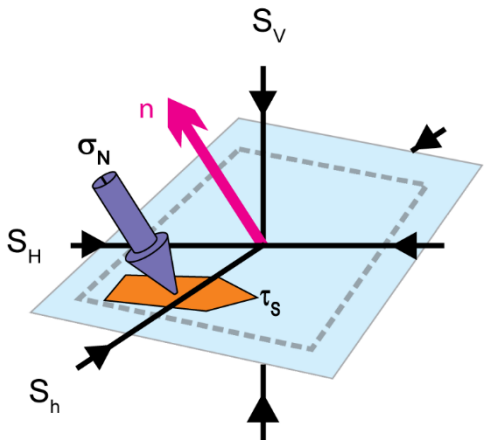


**Figure 2.3.** Traction vector decomposed into normal and shear components on a plane with the state of stress described by an Andersonian stress tensor. Adapted from *Schmitt* [2014]

Consider a fault that slips to cause an earthquake to be a planar feature whose orientation is described by its normal ***n***. If the state of stress in known and the fault remains locked, the normal and shear tractions on that plane are readily determined using Eqn 2.3 – the tractions on each of the two sides are equal as long as the fault remains still. These two scalars can sufficiently describe the condition of the frictional balances of a fault incipient for movement (Figure 2.4).

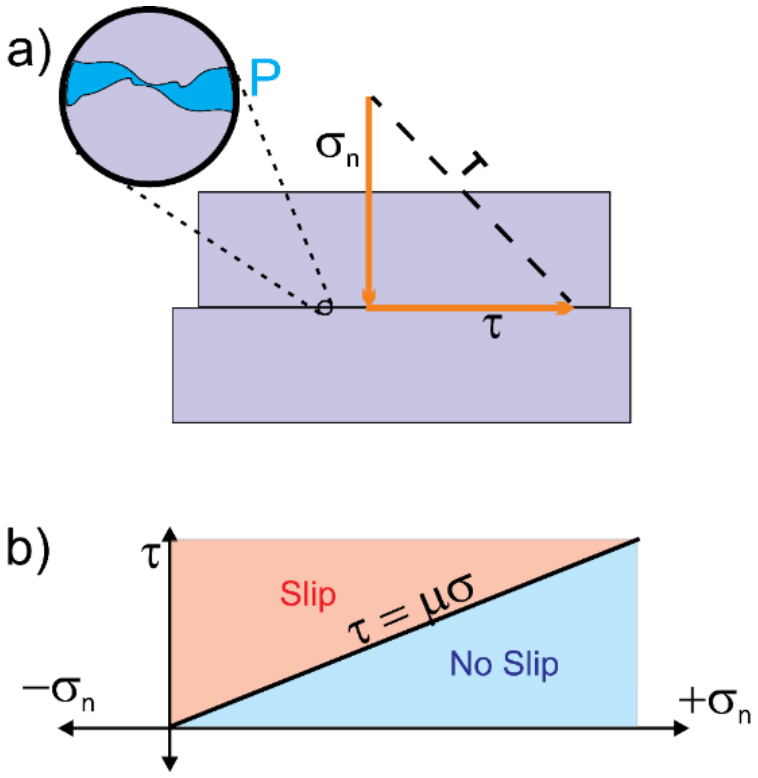


**Figure 2.4.** a) A graphic illustration on the traction force *T* on a faulting plane with fluid pressures *P*. b) the stability and instability states descrbied by Amonton's friction law. Adapted from *Schmitt* [2014]

Though more often referred to as Coulomb's friction law, Guillaume Amontons first proposed that the maximum friction forces at which slip first occurs from a static position are proportional to the normal traction [Amontons' first law of friction, *Amontons*, 1699] and, further, that these are independent of the area of contact [Amontons' second law of friction, *Amontons*, 1699]. Charles de Coulomb [*Coulomb*, 1784] furthered Amontons' law and proposed that the ratio between friction and the normal force is controlled by the contacting materials' properties described by an empirical frictional coefficient $\mu$. This completes Coulomb's friction law that for two contacting surfaces to remain not sliding, the following equation must be satisfied:

$$\tau \geq \mu\sigma_N, \tag{2.4}$$

where $\mu$ is the frictional coefficient. More directly, Eqn. 2.4 says that frictional forces will lock the two opposing sides together until the shear traction equals or exceeds a threshold that depends on the frictional quality of the surface, the normal traction, and an initial cohesive resistance

One complicating factor in the Earth, however, is that we expect that fluids, be they liquid or gas or a combination, ubiquitously reside within any open void space. These fluids, too, will be pressurized to varying degrees and this 'pore pressure' $P_P$ must be considered as it also (Figure 2.4) will affect levels at which rock failure, or slip along surfaces, will occur. The fluid pressure is usually accounted through the Terzaghi effective stress concept in which, essentially, the magnitude of the normal traction $\sigma_N$ acting on the plane is reduced by the magnitude of the pore fluid pressure

$$\tau \geq \mu(\sigma_N - P_P), \tag{2.5}$$

The Terzaghi effective stress concept is widely discussed in the soil and rock mechanics literature and the reader may find more details in numerous texts (e.g., Jaeger et al, 2007). There are two important points arising out of the effective stress law however. The first is apparent in Eqn. 2.5 in which a normal traction is diminished by the pore fluid pressure while the shear traction remains unchanged. The second is the failure behavior of the material is essentially controlled not by the $\sigma_N$ itself but by the variable $\sigma_N - P_P$; that is, as long as the value of $\tau$ remains constant we would expect failure to occur once $\sigma_N - P_P$ reached the threshold.

As noted by Eqn. 2.5, slip will be expected to occur once the shear traction $\tau$ exceeds the frictional normal traction $\sigma_N$-dependent constraint. This can be accomplished two ways, either by perturbing the state of stress directly (changes $\sigma_N$ and $\tau$) or by changing the fluid pressure. The

former can be achieved through the poroelastic deformation and the latter requires change the fluid pressure level of the fault. However, the poroelastic effect of HF operation is expected to be secondary considering the smaller amount of injected fluid.

It is also worth noting that in some work, a cohesion $C$ is included to account for the initial shear strength of rock joints and that transforms Eqn. 2.4 to:

$$\tau \geq \mu(\sigma_N - P_P) - C, \tag{2.6}$$

The choices of $C$ and $P_P$ vary in different analysis pending on the geological/engineering conditions and are, in many cases without the support of strong physical evidence, heavily impacted by authors' reasoning and interpretation. However, consensus exist on the choice of the important friction coefficient $\mu$. Following the work of *Byerlee* [1978] that $\mu$ should be constrained between 0.6 to 0.8, many geomechanical analysis adopted the assumption that $\mu \approx 0.6$ [*Zoback*, 2010]. Meta-analysis on reported laboratory experiments [*Shen et al*., 2019] also show that it is reasonable to constrain $\mu$ between 0.4 to 0.8. Though $\mu$ is also known to vary when the fault starts slipping at different rate, for studies concerning the fault's slip tendency a static $\mu$ applied in Eqn. 2.6 should suffice.

## 2.3 Deterministic Fault slip tendency analysis

The concepts discussed in this chapter are the foundations of studies concerning the fault stabilities and, by its extensions, the mechanics of earthquakes. Though the principal seems straightforward, in practice, actual quantitative determination of the stress tensor $\boldsymbol{\sigma}$ is rather difficult, even with Anderson's simplification. Particularly, determination of the magnitudes and orientations of the horizontal stress remain challenging, owing to the engineering difficulty and

the resultant monetary investment related to drilling of wells. Further, while the methods to obtain $S_h$ and $S_V$ are relatively well established, finding the magnitude of $S_H$ remains to this day unresolved. As such, despite the growing need from the hydrocarbon energy and mining industries, publicly available stress information for Earth's crust remains difficult to obtain.

In this work, we aggregated a moderate amount of borehole stress measurements that allow us to develop two fully quantitative 3D stress models for the Duvernay Formation near in the areas near the town of Fox Creek and city of Red Deer – these two areas were seismically quiescent but with HF induced earthquakes reported recently. Using the principles from section 2.2, we deterministically assessed the slip tendencies of the faults that are responsible for the earthquakes. The critical fluid pressures that is needed to satisfy Eqn. 2.6 are calculated and compared with the natural ambient pore pressures of the Duvernay unconventional reservoir. The 3D stress model near the city of Red Deer also allowed a comparison for areas that experienced high or low level of seismicities.

## References

Amontons, G., Moyen de substituer commodement l'action du feu a la force des hommes et des chevaux pour mouvoir les machines. *Académie Royale de Paris*, *1699*, p.143.

Anderson, E.M., 1905. The dynamics of faulting. *Transactions of the Edinburgh Geological Society*, *8*(3), pp.387-402.

Bell, J.S., Price, P.R. and McLellan, P.J., 1990. In-situ stress in the western Canada Sedimentary Basin. *Bulletin of Canadian Petroleum Geology*, *38*(1), pp.157-157.

Byerlee, J., 1978. Friction of rocks. In *Rock friction and earthquake prediction* (pp. 615-626). Birkhäuser, Basel.

Coulomb, C.A., 1784. Recherches théoriques et expérimentales sur la force de torsion: & sur l'élasticité des fils de métal: application de cette théorie à l'emploi des métaux dans les arts & dans différentes expériences de physique: construction de différentes balances de torsion, pour mesurer les plus petits degrés de force: observations sur les loix de l'élasticité & de la coherence.

Heidbach, O., Rajabi, M., Reiter, K., Ziegler, M. and Wsm Team, 2016. World stress map database release 2016. *GFZ Data Services*, *10*.

Malvern LE. Introduction to the Mechanics of a Continuous Medium. 1969.

Schmitt, D.R., Currie, C.A. and Zhang, L., 2012. Crustal stress determination from boreholes and rock cores: Fundamental principles. *Tectonophysics*, *580*, pp.1-26.

Schmitt, D.R., 2014. Basic geomechanics for induced seismicity: A tutorial. *CSEG Rec*, *39*(11), pp.24-9.

Zoback, M.D., 2010. *Reservoir geomechanics*. Cambridge University Press.

# Chapter 3: Borehole measurements of in-situ stress

## 3.1 Stress States of Earth's Upper Crust

At sufficient depths in a sedimentary basin with gently varying topography, it is commonly assumed that one of the principal components of the stress tensor is vertical with magnitude equal to the overburden pressure. This vertically directed principal stress is denoted $S_V$. Under this assumption, the directions of the two other orthogonal principal stresses must then lie in the horizontal plane and are called the maximum ($S_H$) and minimum ($S_h$) horizontal stress. Additionally, if we express the state of stress using the Cauchy stress tensor ($\sigma$), there must exist at least one orthogonal coordinate system in which the full tensor of the stresses can be expressed as

$$\sigma = \begin{bmatrix} S_H & 0 & 0 \\ 0 & S_h & 0 \\ 0 & 0 & S_v \end{bmatrix}. \tag{3.1}$$

The assumption that one of the principal stresses is vertical simplifies orientation of the stress tensor because the three principal stresses must be orthogonal to one another, so only one horizontal direction needs to be specified [*Zoback*, 2007]. All stress directions provided in this report are the angle of $S_H$ in degrees measured clockwise from geographic north.

*Anderson* [1905] synthesized three basic scenarios to describe a fault's movement at different stress states (Figure 3.1). A fault will slip normally when $S_V > S_H > S_h$, and such a stress regime is considered 'normal.' Similarly, stress regimes that allow strike-slip fault movement ($S_H > S_V > S_h$) and reverse (or thrust) fault movement ($S_H > S_h > S_V$) are categorized as strike-slip and reverse stress states. The determination of the vertical stress is often considered easier for the

upper crust compared with its horizontal counterparts. The magnitude of $S_V$ of a point in the relatively deep subsurface is equal to the total overburden pressure at that depth, which, in most of the Alberta Plains, can be calculated by integrating the density-dependent gravitational weight of the rocks overlying that depth. Evaluations of the magnitudes of in situ horizontal stresses are often subject to challenges and can only be reliably accomplished by drilling a borehole. Additionally, the uppermost crust is often saturated with fluid (i.e., groundwater, hydrocarbon). The fluid in the pore spaces within the rock will result in a non-zero pore pressure and will subsequently alter the effective stresses in the rock's matrix. Therefore, in studying stress states, it is also essential to have knowledge of the pore pressure ($P_P$), as this, via the concept of effective stress, influences the stress-dependent physical properties of rock in situ and is a significant factor in controlling rock failure and slip along pre-existing planes of weakness (see review in Schmitt et al., 2012). The reference hydrostatic pressure ($h(z)$) describes the variation in pore-fluid pressure with depth ($z$) expected in the crust when rocks are fully water saturated from the surface downwards. The depth-dependent pressure head is given by

$$h(z) = -g\rho_w z\,, \tag{3.2}$$

where $g$ is the acceleration due to gravity (assumed to be 9.8 m/s$^2$ in this case), $\rho_w$ is the density of water (most commonly considered to be 1000 kg/m$^3$ , with temperature and pressure effects ignored), and $z$ is the depth below the surface. The reservoir is said to be overpressured or underpressured if the pore pressure at the specified depth exceeds or is less than $h(z)$, respectively.

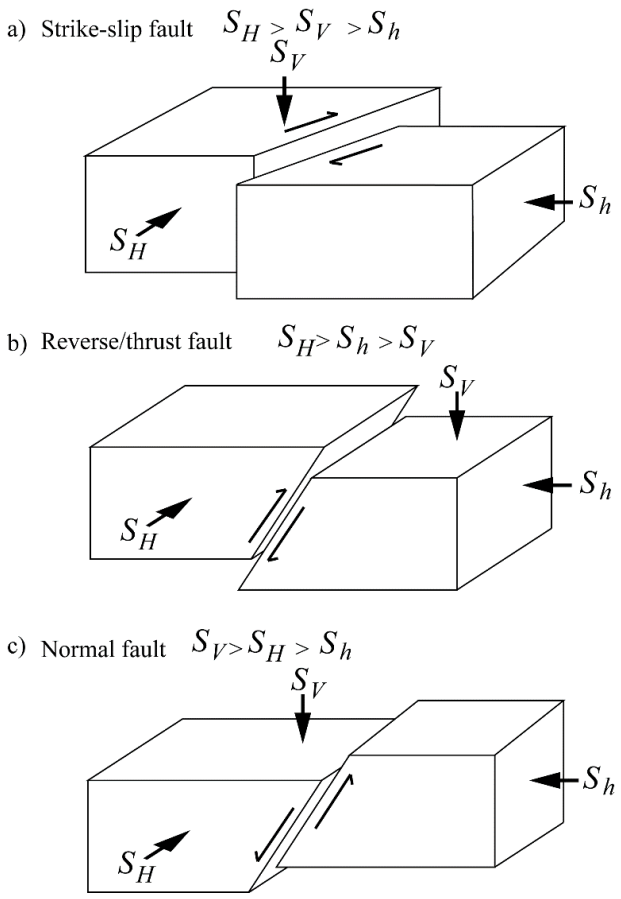


**Figure 3.1.** Anderson's faulting theory and stress regimes: a) strike-slip fault movement, when $S_H > S_V > S_h$; b) reverse or thrust fault movement, when $S_H > S_h > S_V$; and c) normal fault movement, when $S_V > S_H > S_h$.

All stress and pressure magnitudes are expressed using the SI unit 'pascal' (Pa, $N/m^2$), with kPa and MPa equating to $10^3$ Pa and $10^6$ Pa, respectively. Further, in line with standard practice in the geosciences, we assume the convention with compressive stresses and pressures having a positive sign and tensile stresses having a negative sign. Note that quantitative stress magnitudes and pore pressures are often reported in practice as gradients with their corresponding depth *z*. Some care must be taken with the 'gradients' as provided because they are almost always calculated from the ratio of a single measured value to the depth at which the measurement was

made and, as such, can be misleading for practitioners when used to estimate real absolute values at other locations or depths. For example, the $S_h$ gradient merely is $S_h/z$, which presumes that $S_h = 0$ at the surface ($z = 0$). If this assumption is incorrect, then the extension of these results to different locations will result in incorrect estimation of the values. This approach can be more problematic should certain formations concentrate stresses based on the rock's mechanical properties [e.g., *Plumb et al.,* 1991]. In such a case, use of the gradient alone could lead to significant error when applied to formations whose depths differ from that where the measurement is made initially. To avoid this problem, we report directly all values of observed stress magnitudes and the depths from which the values originate in the accompanying digital datasets.

### 3.2 Prior Stress Information in Alberta

The earliest developments in the analysis of borehole breakouts as indicators of in situ stresses came from the pioneering studies of geophysicist D.I. Gough at the University of Alberta and geologist J.S. Bell at the Geological Survey of Canada [*Bell and Gough,* 1979; *Gough and Bell,* 1981, 1982; *Fordjor et al.,* 1983; *Bell and Babcock,* 1986; *Woodland and Bell,* 1989]. They used the orientations from four-arm dip-meter logs from boreholes, some of which lie within the study area. These early studies stimulated a great deal of research, much of which is compiled within the current World Stress Map [*Heidbach et al.,* 2016], although only stress directions are usually available. *Morin* [2017] provided a recent review of the stress determination literature in Alberta that begins with these early studies.

*Bell et al*., [1994] published the first comprehensive accumulation of the state of stress in the WCSB. In addition to stress directions obtained, at that time primarily from oriented dip-meter logs, they added analyses of a number of minifracture tests obtained across the WCSB to constrain

the magnitude of the $S_h$. Bell and coauthors updated this work periodically [*Bell and Bachu*, 2003; *Bell and Grasby*, 2012], with the final compilation available for his data [*Haug and Bell*, 2016] including a total of 106 $S_h$ measurements for northwestern B.C. and Alberta. The average $S_h$ 'gradient' ($S_h$ to depth ratio) for the Alberta Basin is estimated to be 19 kPa/m from the *Haug and Bell* [2016, Figure 3.2] dataset. The vertical stress $S_V$ 'gradient' ($S_V$ to depth ratio), on the other hand, is often considered to range roughly between 20 and 25 kPa/m in sedimentary rocks. The stress regime in Alberta is therefore assumed to be either strike-slip or normal.

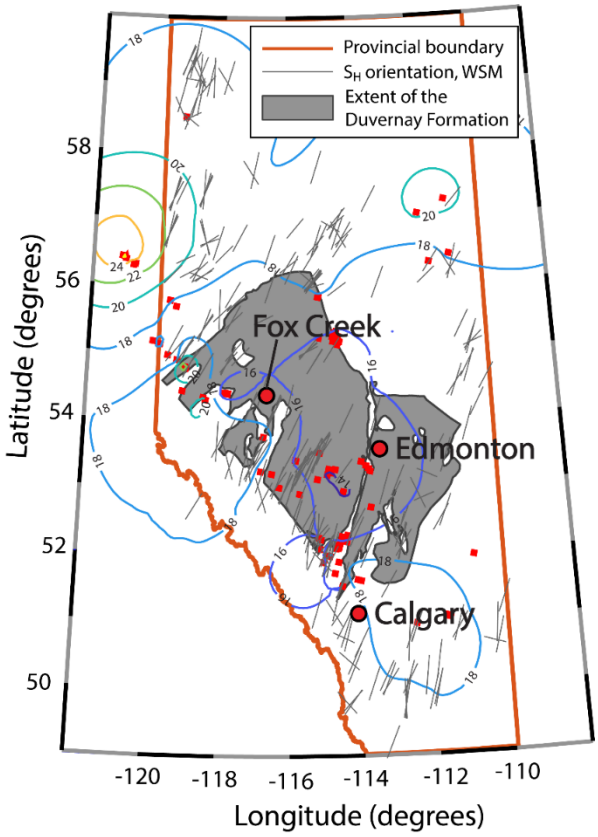


**Figure 3.2.** Extent of the Duvernay Formation described by *Rokosh et al*., [2012] in west-central Alberta, summary of information available in existing compilations of the directions of $S_H$ from the World Stress Map [*Reiter et al*., 2014; *Heidbach et al*., 2016], and $S_h$ gradients and locations of measurements [coloured contours and red dots; *Haug and Bell*, 2016] in Alberta and northeastern British Columbia.

On top of the dataset compiled by Bell and others, researchers have also attempted to provide additional data aimed at better constraining the regional stress orientations. The most recent version of the World Stress Map (WSM, Figure 3.2) provides a snapshot for the orientation of the stress tensor for most of the North American continent [*Reiter et al*., 2014; *Heidbach et al*., 2016], with most of the measurements recorded for the Alberta Basin obtained from older, oriented dip-meter logs [*Babcock*, 1978] arising from oil/gas exploration activities. A brief snapshot of the $S_h$ 'gradient' is provided in a recent study by *Fox and Soltanzadeh* [2015], although the details of that analysis and the actual stress magnitudes were not made available for public access.

The orientation of $S_H$ near Fox Creek is observed to be ~30–50°. Recent analysis of earthquakes recorded near Fox Creek shows dominant patterns of strike-slip faulting mechanisms, in agreement with previous $S_h$ and $S_V$ observations [*Wang et al*., 2016, 2017; *Schultz et al*., 2017]. These focal mechanisms, together with aftershocks, suggest that the fault planes strike nearly north-south (i.e., 0° or 180°), indicating that the conjugate $S_H$ orientation should be either 330° or 030°, assuming a frictional coefficient of 0.6. Similar angles of plate motion were also reported by *Zoback and Zoback* [1991] and *Henton et al*., [2006]. Combining the findings from the previous studies, the in-situ stress near Fox Creek is in the strike-slip stress regime, with $S_H$ orientation of roughly 30°–50°.

The existing compilations in the WSM [*Reiter et al*., 2014] and the *Haug and Bell* [2016] report are useful and important. However, these datasets still lack the full set of components necessary for more informed interpretation of the stress state within the sector of the Kaybob assessment area near Fox Creek. In this report, we attempt to provide quantitative measures of the

magnitudes of $P_P$, $S_V$, and $S_h$, and the horizontal-stress directions. A preliminary constraint on the magnitude of $S_H$ is also briefly discussed here.

## 3.3 Stress measuring methods

### *3.3.1 Determination of Vertical Stress ($S_V$)*

As noted earlier, it is widely accepted that the vertical stress ($S_V$) at depths sufficiently below the influence of variations in the surface topography is nearly the overburden pressure and can be estimated by integration using the overlying rock densities $\rho(z)$ down from the surface to depth $z$ as

$$S_V = g \int_0^z \rho(z) dz \,. \tag{3.3}$$

Geophysical density logs are commonly obtained for oil/gas exploration and development wells. The method relies on the attenuation of gamma rays originating from radioactive cesium; more information on density logging is available in *Ellis and Singer* [2007]. The litho-density is used primarily to provide an estimate of the rock porosity and secondarily as a lithology indicator. Here we use the logged density measurements directly to estimate vertical stress.

Despite the simplicity of Equation 3.3, two issues arise that complicate the use of such logs to estimate vertical stress:

1) Because the instrument used to determine density must be in contact with the borehole wall rock, the quality of such logs can vary depending on borehole conditions. The density of the sedimentary rocks in the study area could range broadly from about 2000 kg/m$^3$ for a highly porous, water-saturated Cretaceous sandstone to 2700 kg/m$^3$ for a nonporous Paleozoic limestone. For example, the poor-quality, raw density log shown by the blue lines in Figure 3.3a

indicates a range of densities from <1500 $kg^3$ to >3000 $kg/m^3$; such extreme values are not reasonable and are likely due to rough borehole geometry that interferes with proper log operation. We overcame this limitation using a two-step process in which unreasonable outliers were first removed and then a 50 m wide, running-average smoothing filter was applied (orange line in Figure 3.3a). We estimated $S_V$ magnitudes of ~90 MPa at 3500 m (Figure 3.3b). This process was applied to density logs retrieved from more than 600 boreholes within the study area.

2) Density logs are often obtained only for depth intervals near the target formation, and only rarely are complete density logs available from the surface to the depth of interest. Significant gaps in the measured $\rho(z)$ along sections are often present in individual wells—particularly in the shallower depths (<500 m). This problem was partially overcome by using the available density logs, scattered both laterally and in depth, to create a final function that constructs a simple one-dimensional $\rho(z)$ using a statistical approach. For the sake of simplicity, we assumed that $\rho$ is a function of $z$ only. Hence, at any given depth, the associated value of $\rho$ is obtained from kriging of all smoothed log $\rho$ available from the same depth.

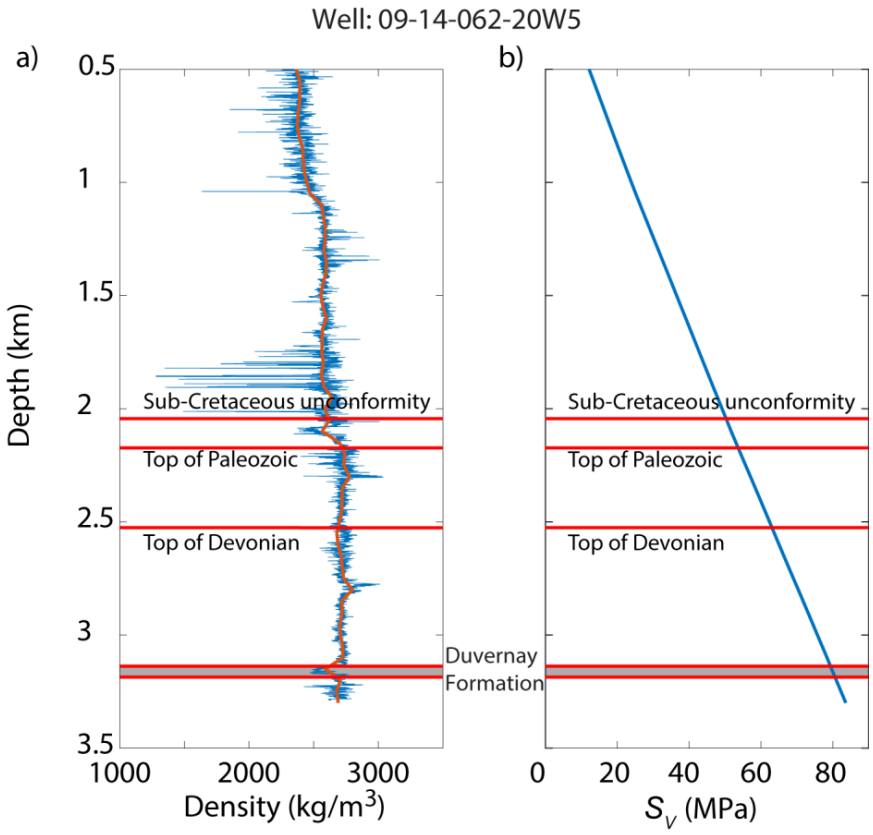


**Figure 3.3.** a) Example of a density log retrieved during this study; blue curve represents the original log, and the orange one represents the smoothed results for $S_V$ modelling. b) Computed $S_V$ from the density log shown in part a; density at depth <500 m is assumed to be equal to the smallest value from the smoothed density recordings (orange line in part a). Red lines show the boundaries of some geological units penetrated by the well.

### *3.3.2 Determination of Minimal Horizontal Stress ($S_h$)*

Operators will often invest in a pressure-transient well test that involves the creation of a small hydraulic fracture to constrain various geomechanical and reservoir parameters. Ideally, the pressure history of the section of an open borehole within which the fracture is created is isolated using pressurized packers to provide information that is useful in the design of the more robust hydraulic-fracture stimulation program. Briefly, the interval between the packers is pressurized

until a fracture is created at the borehole wall. Pumping to the interval continues to extend the fracture into the formation. After pumping ceases, the interval is 'shut in' and the pressure $P_w(t)$ is allowed to decline naturally as the fluid in the borehole interval and the fracture permeates naturally into the formation. In principle, this decline curve may be interpreted to provide a host of geometric and flow-related parameters [*Nolte*, 1979; *Schmitt and Haimson*, 2017]. Here, we focus solely on the interpretation of such tests to obtain measures of the fracture-closure pressure ($P_{FC}$) and the formation-pore pressure ($P_P$).

The tests go by many names, such as microfrac, minifrac, and diagnostic fracture-injection test (DFIT). Currently in industry, the term DFIT is used widely but loosely, being applied to a wide variety of different wellbore-pressure tests significantly outside the scope of the proper multicycle pressure test. It is therefore important to know exactly how such tests were carried out. In this study, we include a number of DFITs carried out within a limited depth interval along the borehole that is isolated either by inflatable packers in an open hole or by perforations in a cased hole. Interpretation of the latter can be affected by restricted-flow effects through the perforations and by a potentially larger volume of fluid within the borehole, both of which lead to decreased ability to detect small changes in $P_w(t)$.

Figure 3.4 illustrates different time segments of an ideal $P_w(t)$ record, and fluid volume flowing into and out of the isolated interval. This process, and the interpretation of the decline curve $P_w(t)$, were described in detail by *Schmitt and Haimson* [2017], so only a brief overview is given here. Figure 3.4 is meant only to illustrate various time segments during the DFIT testing and is not drawn to proper scale with respect to pressure or time. These segments are as follows:

- The initial pressure $P_{EQ}$ within the sealed interval is assumed to be at equilibrium before the test. Pressurization of the interval commences with pressure increasing until a tensile fracture from the interval into the rock mass initiates at $P_{FI}$, followed by unstable-fracture propagation into the formation at the breakdown pressure ($P_b$), which we here take to be the reference time $t_0$.

- Pumping of fluids to the interval may continue to extend further the induced fracture. This fracture-propagation pressure ($P_{FP}$) may be controlled by numerous factors, such as fluid viscosity and whether the measurement is carried out in an open borehole or through perforations in a cased borehole. Pumping stops and the interval and open fracture are shut in at $t_1$, with the pressure dropping rapidly to the shut-in pressure $P_{SI}$ (see blue section in Figure 3.4).

- In the post–shut-in period immediately following time $t_1$, it is assumed that the induced fracture remains propped open by the interval pressure $P_w(t)$. However, $P_w(t)$ declines during this shut-in period due to 'leak-off' flow to the formation from the still-open induced fracture and, in open-hole situations, the sealed borehole interval (see pink section in Figure 3.4).

- At time $t_2$, the fracture-closure pressure ($P_{FC}$) is reached. It is usually assumed that $P_{FC}$ is the lowest pressure required to keep the hydraulic fracture open; as such, it is equal to the magnitude for minimum principal stress $\sigma_3$, although Detournay et al. (1989) suggested, based on consideration of poroelastic effects, that $P_{FC} > \sigma_3$. Consequently, accurate determination of $P_{FC}$ is a key goal in the DFIT $P_w(t)$ analyses (see brown section in Figure 3.4).

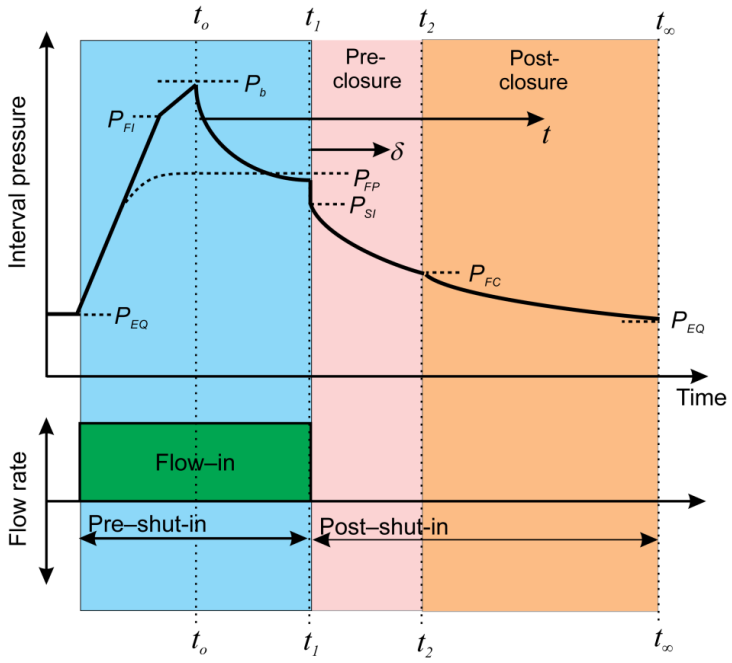


**Figure 3.4.** Different phases of fluid flow during the diagnostic fluid-injection test: pre–shut-in (blue), pre-closure (pink), and post-closure (brown).

The post-closure leak-off continues after $t_2$, with $P_w(t)$ continuing to decline until it eventually, given sufficient time, equilibrates with the pore pressure $P_{EQ}$ within the formation. Furthermore, the pressure-drawdown curve can be extrapolated to estimate the wellbore pressure at the infinite shut-in time. The extrapolated reservoir pressures from DFITs, on the other hand, provide constraints on the pore pressure of the rocks near the wellbore.

Different plotting strategies, in which the dependent and independent axes are various functions, transformations, or derivatives of $P_w(t)$ versus $t$, respectively, have been developed to identify the point at which the fluid pressure $P_{FC}$ is barely large enough to keep the fractures open. Some of these strategies are reviewed in *Schmitt and Haimson* [2017] and *Craig et al.* [2017]. *Barree et al*. [2009] and *Craig et al*. [2017] further re-examined available field and laboratory $P_w(t)$ determinations and suggested that a 'holistic' combination of *G-function* derivative [*Nolte*,

1979], square-root time, and log-log plotting be employed, which they illustrated with some examples. Recently, questions have also been raised regarding the validity of the *G-function* and its underlying assumptions in the low–leak-off shale formations such as the Duvernay [*Zanganeh et al*., 2018]. Obtaining consistent measures for $P_{FC}$ from these various visualization-enhancement methods lends credence to a proper interpretation. Fluid flow through the wellbore into the hydraulically induced fractures can be divided into pre-closure and post-closure phases, as previously discussed. There is still debate regarding how flow regime would change in response to fracture closure and the corresponding impacts on the recorded pressure history in the wellbore. Most researchers have come to agree that one could, in principle, identify fracture closure through the slope change in the pressure history. Plotting pressure history in either *log(t)* versus *log* $(p_w)$ or *log (t)* versus $p_w$, which amplifies such slope change, has been successfully applied to the interpretation of downhole flow phases [*Doe et al*., 1981; *Haimson and Rummel*, 1982].

*Cinco-Ley* [1981] further proposed that the fluid flow near the wellbore can be categorized into four regimes (Figure 3.5). Assuming that fluid leak-off in the fractures is minimal in tight and impermeable formation rocks, Cinco-Ley's flow regimes can be essentially reduced to only linear (Figure 3.5a) and radial flows (Figure 3.5d), and the pressure drop and time follows the relationship $log\ t \propto log\ \Delta p$ [*Barree et al*., 2009]. It is possible to delineate $P_{FC}$ using plots of $log[P_w(t)]$ versus *log(t)* or $P_w(t)$ *versus log(t)*. One could, in principle, obtain a measure of $P_{FC}$ by finding where the $log[P_w(t)]$ versus *log[t]* plot deviates from this slope (or one near it).

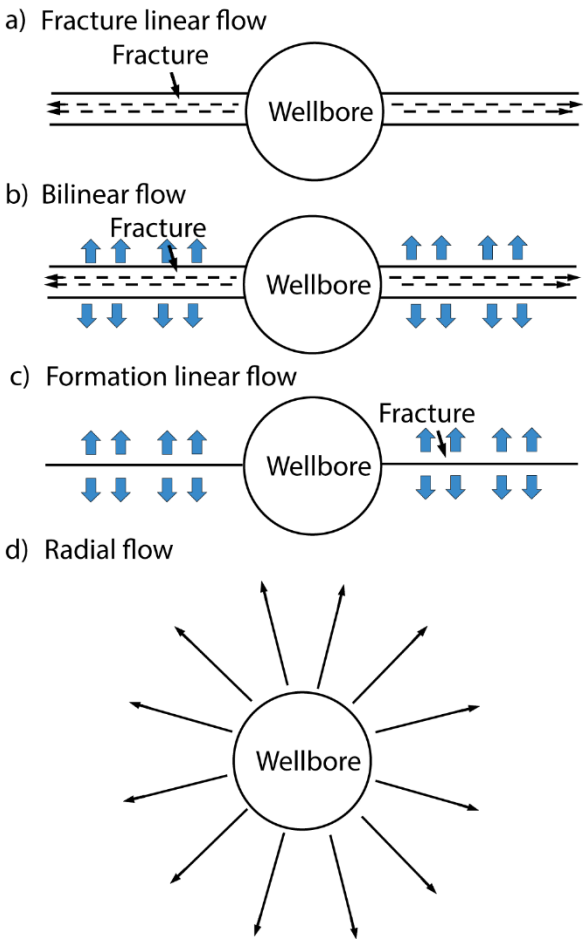


**Figure 3.5.** Four near-wellbore fluid-flow regimes proposed by *Cinco-Ley* [1981]: a) fracture linear flow, with fluid flowing in the direction of fractures; b) bilinear flow, with fluid flowing in the direction of fractures and also leaking into the nearby formation; c) formation linear flow, with fluid flowing from the fractures to the nearby formation rocks in a direction perpendicular to that of the fractures; and d) radial flow, with fluid flowing outwards radially from the wellbore to the nearby formations.

The downhole fluid flow becomes much more complicated for more permeable formation rocks when fracture growth and pressure-dependent fluid leak-offs happen with comparable magnitudes. Following the assumptions laid out by R.D. Carter [see *Howard and Fast*, 1957], namely that 1) the fractures have a uniform width, and 2) the flow in the fracture is linear in the direction perpendicular to the fracture face, the Carter leak-off is widely assumed by industry

practitioners to describe the flow rate as being inversely proportional to $\sqrt{t}$ where $t$ is the total injection time. In Howard and Fast (1957), it is further assumed that fluid velocity is uniform across the fracture, so the 'Carter' leak-off equation can be presented as

$$q(t) = C_L/\sqrt{t}\,, \tag{3.4}$$

where $q$ is the fluid-loss rate and $C_L$ is the fracturing-fluid coefficient that describes the resistance for the fluid leaking off to the formations. $C_L$ is commonly referred as 'Carter's leak-off coefficient' by industry. The analyses below incorporate this underlying assumption.

The first transformation of the pressure draw-down (Figure 3.6a), resulting from fluid leak-off from the borehole, is predicated on the assumption of a linear flow regime, following *Cinco-Ley* [1981], in which $P_w(t)$ changes proportionally to $\sqrt{t}$. Consequently, the locus of $P_w(t)$ versus $\sqrt{t}$ would be a straight line (Figure 3.6b), the point of deviation from which would indicate $P_{FC}$. *Barree et al*. [2009] noted that use of this criterion in practice leads to an early pick of fracture closure (overestimated $P_{FC}$) and suggested the use of the inflection point that may more readily be found from the derivative $dP_w(t)/d\sqrt{t}$ plot. This behaviour is further enhanced in the semilog derivative $\sqrt{t}\, dP_w(t)/d\sqrt{t}$ curve, with $P_{FC}$ declared at the point of departure of its trajectory from the initial linear increase.

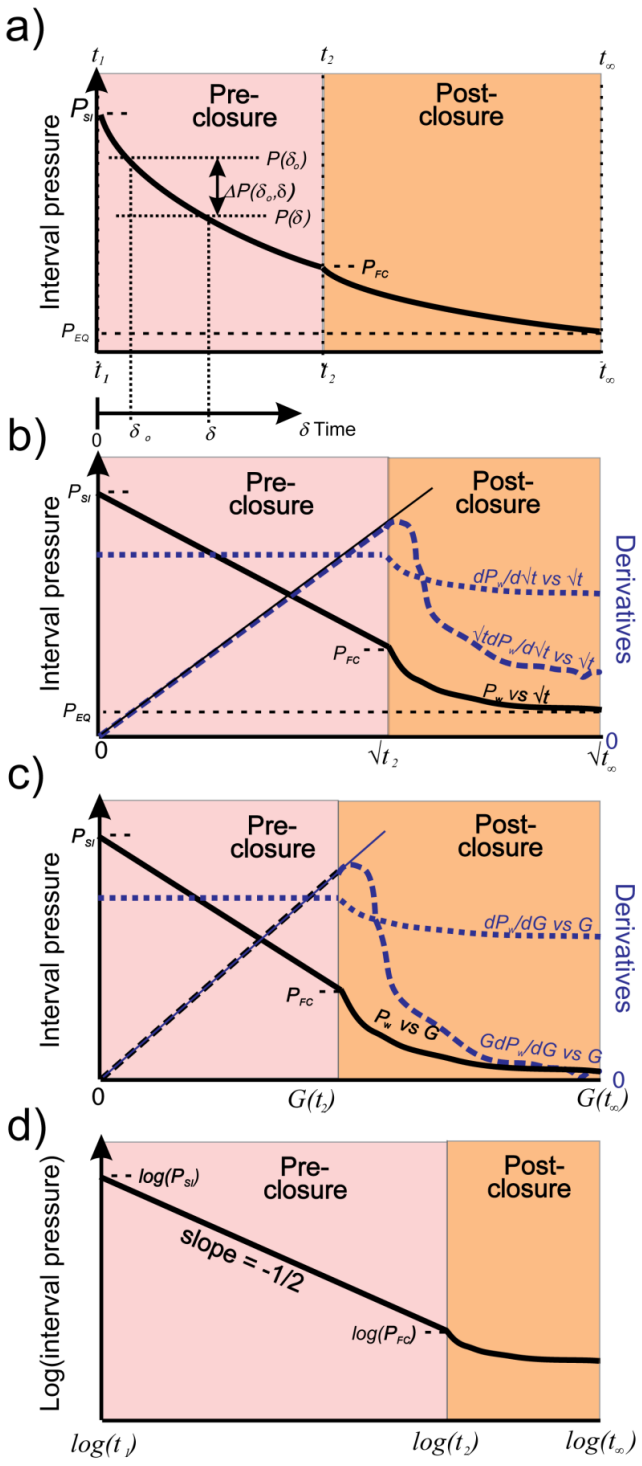


**Figure 3.6.** Transformations of the diagnostic fluid-injection test (DFIT) pressure history for use in constraining fracture-closure pressure ($P_{FC}$): a) fall-off curve of the wellbore pressure following the shut-

in; b) $\sqrt{t}$ plot assuming Carter leak-off; c) *G-function* plot initially proposed by Nolte (1979); and d) *log(t)* versus $log(P_w)$ plot.

*Nolte* [1979] further extended Carter's assumption with a fixed vertical height of fracture and described a linear relationship between pressure and a dimensionless shut-in time using the proposed *G function*. In Nolte's formulation, Carter leak-off is modified to account for the horizontal growth of the fracture. Nolte assumed the fracture would grow linearly with time during the pumping stage, so the Carter leak-off coefficient would be proportionally dependent on the pumping time. Pressure-dependent leak-off is also considered in Nolte's formulation.

Consequently, the second important standard procedure (Figure 3.6c) employed to estimate $P_{FC}$ relies on what is referred to as *G-function* analysis. The relationship between time and wellbore pressure is given in terms of a dimensionless shut-in time $\delta = [t - t_1]/t_1$ for $t > t_1$ [*Nolte*, 1979]. Time ($t$) accumulates only after the fracture is created at a time $t_0$, presumed to be the initiation of fracture propagation [*Barree et al*., 2009]. The use of such forms of dimensionless times follows from earlier work by *Horner* [1951]:

$$\Delta P(\delta_o, \delta) = P * G(\delta_o, \delta), \tag{3.5}$$

where $P$ is the 'Nolte match pressure' [*Castillo*, 1987], which is a constant depending on a variety of parameters that control the loss of fluids from the fracture, fracture geometry, the fracture's 'age' (i.e., $t_1 - t_o$), and normalized pressures within the fracture [*Nolte*, 1979; *Castillo*, 1987]. $\Delta$ refers to the change in the pressure $P$. We mostly ignored the effect of these in this study, as the determination of $P_{FC}$ depends more on the details of the behaviour of the pressure-decline curve, but we note that analysis of the decline curves can conversely provide some of this information.

Indeed, *Nolte*'s [1979, 1986] original intent was to deduce the fracture geometry, and flow constraints from the post–shut-in pressure-decline curve, using knowledge of $P_{FC}$ obtained using other methods [*Nolte*, 1979]. More germane to the current discussion, the time-dependent *G-function* is

$$G(\delta_o,\delta)=\frac{4}{\pi}\left[g(\delta)-g(\delta_o)\right]. \tag{3.6}$$

The function for the limiting case with small leak-off into the growing fracture during its growth in the pressurization period is

$$g(\delta)=\frac{4}{3}\left[(1+\delta)^{3/2}-\delta^{3/2}-1\right] \tag{3.7}$$

or

$$g(\delta)=(1+\delta)\arcsin\left[\frac{1}{(1+\delta)^{1/2}}\right]+\delta^{1/2}. \tag{3.8}$$

For the case where there is substantial leak-off in more permeable formations, Barree et al. (2009) used $\delta_o = 0$ at $t = t_1$. Both of the intermediate functions (high leak-off and low leak-off) in reality give similar results, and here we use the low leak-off form (Equation 3.7), given the expected low permeability within the Duvernay Formation.

*Castillo* [1987] exploited the linearity of Equation 3.5, noting that a plot of $P_w(t))$ versus $G(\delta_o,\delta)$ is a line during the post-closure fluid leak-off period in Figure 3.6b, with a slope equal to $P^*$ and an intercept of $P_{SI}$. Consequently, he suggested that this plot would deviate from a line at $P_{FC}$. Detection of this point is further enhanced in the plot of $dP_w(t)/dG$ versus $G(\delta_o,\delta)$, which

would remain at the constant value of $P^*$ during the decline period and change slope after closure. As with the $\sqrt{t}$ plotting, the initial section of the plot of the semilog derivative $GdP_w(t)/dG$ should be a line passing through the origin, with $P_{FC}$ declared at the point where $GdP_w(t)/dG$ leaves this line [*Barree* et al., 2009].

Finally, curves related to log[$P_w(t)$] versus log[$t$] may also be employed to delineate $P_{FC}$. For the ideal case, pressure decline for a fracture linear flow in the post–shut-in period, the slope of this curve is expected to be –½ (Figure 3.7d). Again, one could in principle obtain a measure of $P_{FC}$ by finding where the log[$P_w(t)$] versus log[$t$] plot deviates from this slope (or one near it). In practice, this is not so easily accomplished [e.g., *Barree et al*., 2009] and here we employ the linear portion of this curve to initially limit the range of possible values for $P_{FC}$.

The procedure used to constrain $P_{FC}$ in this study is illustrated in Figure 3.7, which begins with a plot of $P_w(t)$ versus $t$ (Figure 3.7a) for 180 hours for the test in well 01-11-034-24W4 at 2157.5 m depth. The operational procedures of this test were not detailed in the report submitted to the Alberta Energy Regulator by the operators. Because of this, assumptions were made that the injection begins when the wellbore fluid pressure starts rising, as recorded by the pressure gauge at 0 h. The well is considered shut-in when a sudden pressure drop is observed at ~0.09 h (see Figure 3.7a).

The curves in the *log[$P_w(t)$]* versus *log[t]* plot (Figure 3.7b) and the [$P_w(t)$] versus *log[t]* plot (Figure 3.7c) display a linear section that we interpret to correspond to the fracture linear flow (see Figure 3.7a). This linear fit of the log-scale curve corresponds to a $P_{FC}$ between 21.9 and 23.0 MPa (see Figure 3.7b and c) at ~4 hours after shut-in. With the constraint range of $P_{FC}$ obtained through the *log(t)*-based plots, the *G-function* and $\sqrt{t}$ plots (Figure 3.7d and e) are

investigated to further refine the timing of fracture closure. In this example, the estimated $P_{FC}$ through *G-function* analysis is 22.9 MPa, which falls within the range constraint of $P_{FC}$ obtained through the *log*(t)-based plots. The $\sqrt{t}$ plot shows a $P_{FC}$ of 22.9 MPa , roughly the same (these numbers are rounded) as was estimated through the *G-function* analysis (22.9 MPa), indicating a minimal amount of fluid leak-off, as expected for this low-permeability formation. The consistency in the constraining $P_{FC}$ using various methods provides credence for our approach. The success of this approach can be at least partially attributed to the fact that the low permeability of the Duvernay Formation limits the amount of pressure-dependent leak-off, which could present challenges for more permeable formations.

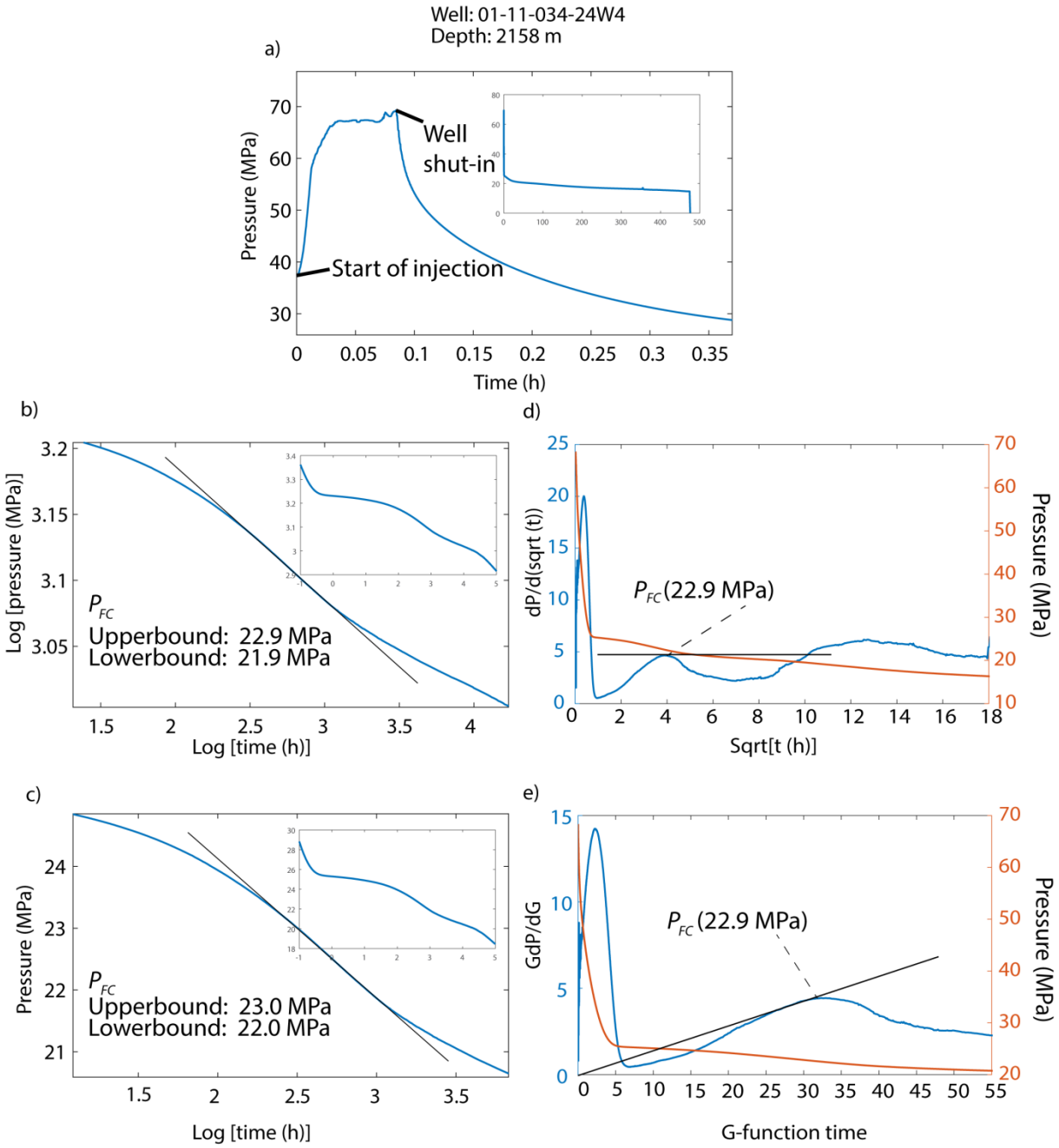


**Figure 3.7.** Diagnostic fluid-injection test (DFIT) data and analysis from well 01-11-034-24W4, with pressures recorded by a pressure gauge at surface: a) recorded pressure history from the DFIT, showing the moment when the well is shut in after the hydraulic fractures are created; inset shows the entire injection/shut-in history; the shut-in period is many times longer than the injection period to allow wellbore pressure to reduce to fracture-closure pressure and close to pore pressure of the surrounding formation

rocks; b) log*($P_w$) versus* log*(t)* plot constraining $P_{FC}$ at ~22.9 MPa; c) $P_w$ *versus log(t)* plot constraining $P_{FC}$ at 22.0–23.1 MPa; d) √t plots estimate the $P_{FC}$ at 22.9 MPa, the left axis showing the values of dp/d(√t) and the right axis showing the corresponding pressures at the same time; e) *G-function* plots estimate $P_{FC}$ at 22.9 MPa, the left axis showing the values of GdP/dG and the right axis showing the corresponding pressures at the same time.

In some cases, the pressure history is recorded with a pressure gauge at the surface, so the actual downhole pressure can be estimated as $P_w = P + P_h$, where $P_h$ is the hydrostatic pressure at the depth of measurement. When a detailed description of fluid properties was not provided in an operator's report, we assumed that the wellbore fluid had a specific weight of 9.8 kN/m$^3$. Therefore, the minimum horizontal stress is constrained between 43.0 and 44.2 MPa. One could also, in principle, estimate the breakdown pressure from the maximum value of the recorded pressure history and then estimate the maximum horizontal stress. However, without detailed knowledge of the operations of this test and the mechanical properties of the formation rocks, such an estimate would only be speculative.

Ideally, the DFIT should be conducted in 'open-hole' conditions immediately after the borehole is drilled. Nevertheless, operators may conduct the DFITs through perforated casing that has already been installed for engineering-practicality reasons. In principle, the interpretations of the 'cased-hole' DFITs follow the same procedures as the 'open-hole' test. The cased-hole test results may be more uncertain due to complications caused by restrictions in fluid flow through the casing and cement. According to the submitted industry reports, all of the DFITs that provided data for this study were carried out in 'open-hole' conditions.

*3.3.3 Determination of Formation Pore Pressure (Pp)*

Formation pore pressure can be constrained by a number of well-testing techniques, including static-gradient tests, flow/buildup tests, and post-closure DFIT analysis. The fluid flow from or into the wellbore is driven by the pressure difference between the wellbore and the fluid/pore pressures in the surrounding rocks. The formation-fluid pressure can be indirectly determined by measuring the wellbore pressure and fluid-flow rate. That being said, there are arguments for and against the use of these well-testing techniques in different circumstances. In this section, we briefly discuss the measurement of pore pressure using each of these methods.

Static-gradient surveys assume that the flow from the reservoir to the borehole has reached a steady state after a sufficiently long time ($t_\infty$), such that an equilibrium $P_w(t) \rightarrow P_{EQ} = P_P$ has been attained. Such an assumption may be valid if the flow rate is meager, with only a small amount of fluid extracted from the reservoir, and reservoir pressure near the wellbore is not affected by the fluid extraction. A static-gradient survey is often performed by placing a pressure gauge downhole to obtain the fluid pressure at a certain depth. This type of survey is regularly conducted in cased holes, so linear extrapolation with assumed or calculated fluid density is needed to estimate the fluid pressure at the depth of the perforations, where the borehole fluid pressure is considered equivalent to that of the surrounding geological formation. The pressure calculated for the mid-point of perforations (MPP) is typically considered a loose constraint for the fluid pressure in the nearby geological formations. The static-gradient test will often be performed at multiple points along a cased wellbore, primarily because it can be done easily, to obtain the averaged MPP pressure through linear extrapolation.

The static-gradient survey is often followed by a transient pressure test to obtain a more reliable constraint on formation-fluid pressure. Flow and build-up tests often start with lowering the pressure $P_w(t)$ by extracting fluid from the wellbore for a period of time. The wellbore is then shut in to allow reservoir fluids to flow back in with a corresponding increase in $P_w(t)$ that depends on the pressure differentials and the reservoir fluid mobility. In principle for a reservoir of infinite extent, the wellbore fluid pressure $P_w(t)$ will in infinite time approach the limiting reservoir pressure $P_P$. In practice, the time allowed for such tests is restricted by practical considerations and, to overcome this problem, workers instead have developed methods to extrapolate an observed $P_w(t)$ to estimate the $P_P$.

Analytical solutions for the pressure-time functions of different flow regimes can be derived and compared with the wellbore-pressure history to extrapolate the reservoir pressures. The pressure-time functions of borehole fluid flow for different flow regimes are usually presented in the following form:

$$P - P_w = C * F(t)\,, \tag{3.9}$$

where $t$ is the 'equivalent flow time', which is a function of the flow time of the testing well, and $F$ is an arbitrary function of time. For a buildup test, the equivalent flow time should approach a constant limit when the actual shut-in time is infinitely large, in order for $P_w$ to approach $P$. Plotting the wellbore pressure against the equivalent time allows extrapolations of the pressure history approaching such a limit and therefore provides an estimation of wellbore pressures at an infinitely long shut-in time. Estimation of fluid pressure using linear and radial fracture-flow assumptions, which are the two most extreme scenarios, will provide range constraints for the actual formation-fluid pressure.

For an unfractured wellbore, radial fluid flow dominates (Figure 3.7d) and, assuming a flow rate of $q$, the wellbore's fluid pressure will take the following form:

$$P_w = P - q * B * log\,(t)\,, \tag{3.10}$$

where $q$ is the flow rate and $B$ is a constant that depends on wellbore geometry, fluid properties, and formation permeability. *Horner* [1951] proposed an approach to predict the wellbore pressure after borehole shut-in using the superposition of fluid flow. It is assumed that, after the shut-in, a fluid injection with a rate equal to that of the flow-out rate before shut-in is introduced while the fluid is still flowing out of the wellbore at the same rate. The total fluid-flow rate in the wellbore remains equal to zero, and the pressure changes in the borehole will be equal to the superposed pressure change from the fluid flow out and the fluid injection (Figure 3.8a). An approximate solution for the fluid-pressure change in the wellbore can therefore be established as

$$P_w = P - qBlog(\Delta t) + qBlog\left(t_p + \Delta t\right), \tag{3.11}$$

where $\Delta t$ is the shut-in time or the injection time for the hypothetical injection flow and $t_p$ is the flow-out time before the injection. The so-called 'Horner time' [*Horner*, 1951] can therefore be defined as

$$F_H = log\left(\frac{t_p+\Delta t}{\Delta t}\right), \tag{3.12}$$

where $t_p$ is the production time before well shut-in and $\Delta t$ is the time elapsed after shut-in.

Following the Horner equation [*Horner*, 1951] and assuming a radial wellbore flow, the wellbore pressure at the infinitely long shut-in time can be obtained by identifying the linear trend in the Horner plot at the end of the buildup stage and extrapolating it to intercept with the t = 1

point, where $\Delta t = \infty$. If the formation surrounding the wellbore is fractured, linear fracture flow needs to be considered instead of radial flow, so the linear flow equation [Equation 3.11; *Ahmed and McKinney*, 2011] would be applied to extrapolate the final wellbore shut-in pressure using the similar superposition principle

$$P_w = P_{initial} - qB\left[\sqrt{\Delta t} - \sqrt{t_c + \Delta t}\right], \tag{3.13}$$

in which $qB\sqrt{\Delta t}$ accounts for the hypothetical injection flow and $qB\sqrt{t_c + \Delta t}$ represents the pressure change due to fluid flow out. Subsequently, the equivalent time for linear fracture flow can be expressed as

$$F_H = -\sqrt{\Delta t} + \sqrt{t_c + \Delta t}\,. \tag{3.14}$$

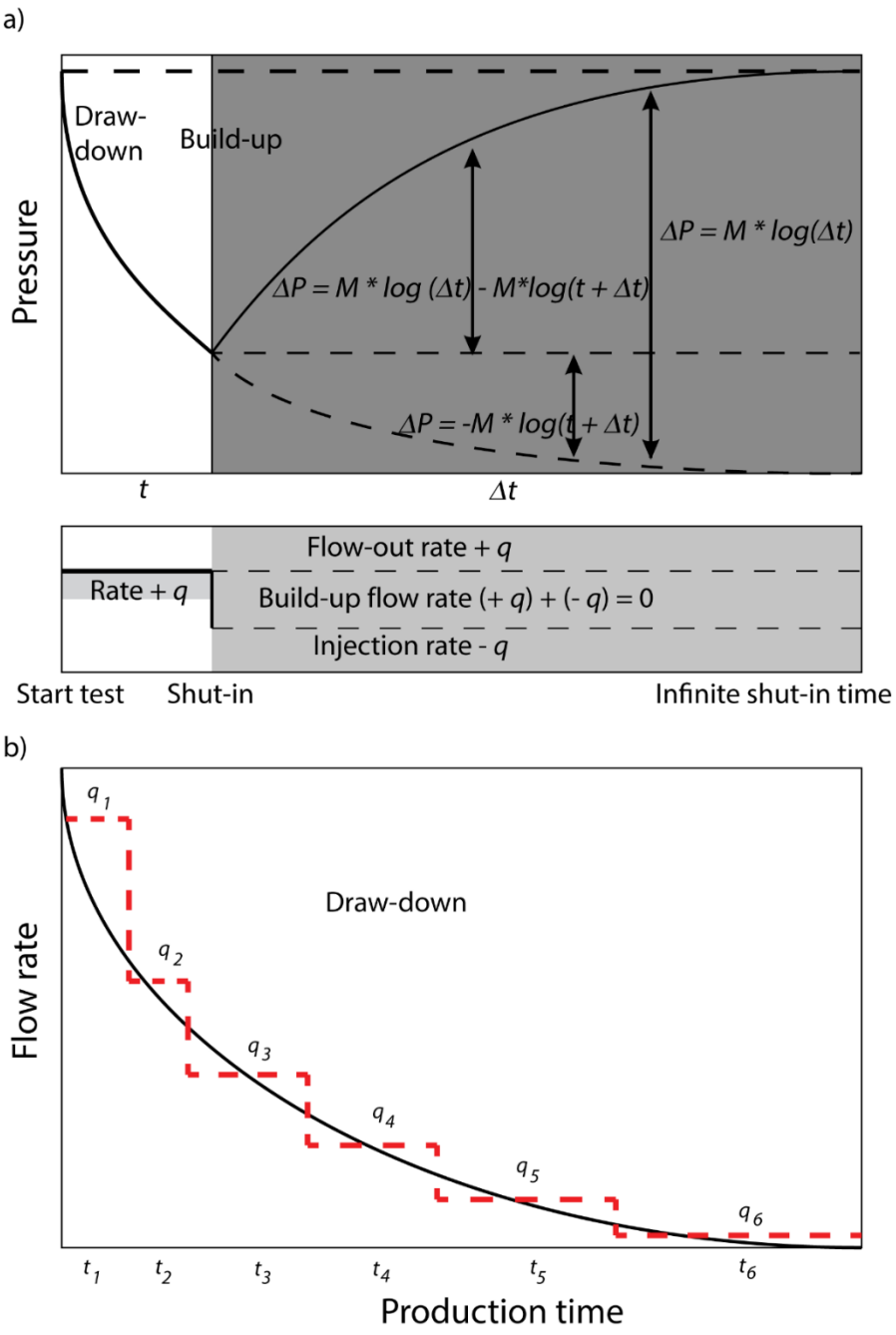


**Figure 3.8.** Conceptual illustration showing the superposed fluid flow in the borehole: a) schematic showing the flow and buildup phases of the test and the principle of superposition; following the shut-in of the well, it is assumed that the wellbore fluid will continue to flow out (dashed line) and an injection of fluid at the same rate will result in a net zero flow rate; b) step function for varying flow rate, the solid line representing the flow rate that can be numerically represented by a step function (red dashed line).

In this case, $F_H$ is linearly proportional to the wellbore pressure ($P_w$). The linear fracture Horner time also approaches 0 at the infinitely long shut-in time. Following a similar approach, the initial formation pressure can be estimated by extrapolating the linear trends in the linear Horner time plot and finding its intercept with t = 0.

Equations 3.11 and 3.13 assume that the flow rate in a wellbore is constant. In case the flow rate is not constant, the flow history can be divided into a step function of many segments of time within which the flow rate is constant (Figure 3.8b). Equations 3.11 and 3.13 can therefore be rearranged to represent the superposition of the multiple steps with different flow rates as

$$t_h = \sum_{j=1}^{n} \frac{q_j - q_{j-1}}{q_n} \sqrt{t - t_{j-1}} \tag{3.15}$$

for linear flow and

$$t_h = \sum_{j=1}^{n} \frac{q_j - q_{j-1}}{q_n} log\ (t - t_{j-1}) \tag{3.16}$$

for radial flow. In Equations 3.15 and 3.16, $q_j$ represents the flow rate at each step; $t_j$ is the corresponding flow time; $t_h$ is the superposed linear or radial time; and $q_n$ is proposed to be the final flow rate in the wellbore before shut-in, although it does not mathematically impact the extrapolated eventual shut-in pressure. In this study, the superposed time plots are used when the flow rate is reported for the well testing. In cases when the flow rate is not available, a constant flow rate is assumed from when the well starts flowing until shut-in.

An example (well 08-32-046-09W5, TVD 3140 m) is provided here for identifying formation-fluid pressure using the superpositioned linear- and radial-flow assumptions. Figure 3.9a shows the pressure history recorded for the flow-buildup test, with the final wellbore pressure

recorded at 47.5 MPa. The extrapolated $P_w(t)$ at the infinite shut-in time is estimated to be between 48.9 and 51.3 MPa.

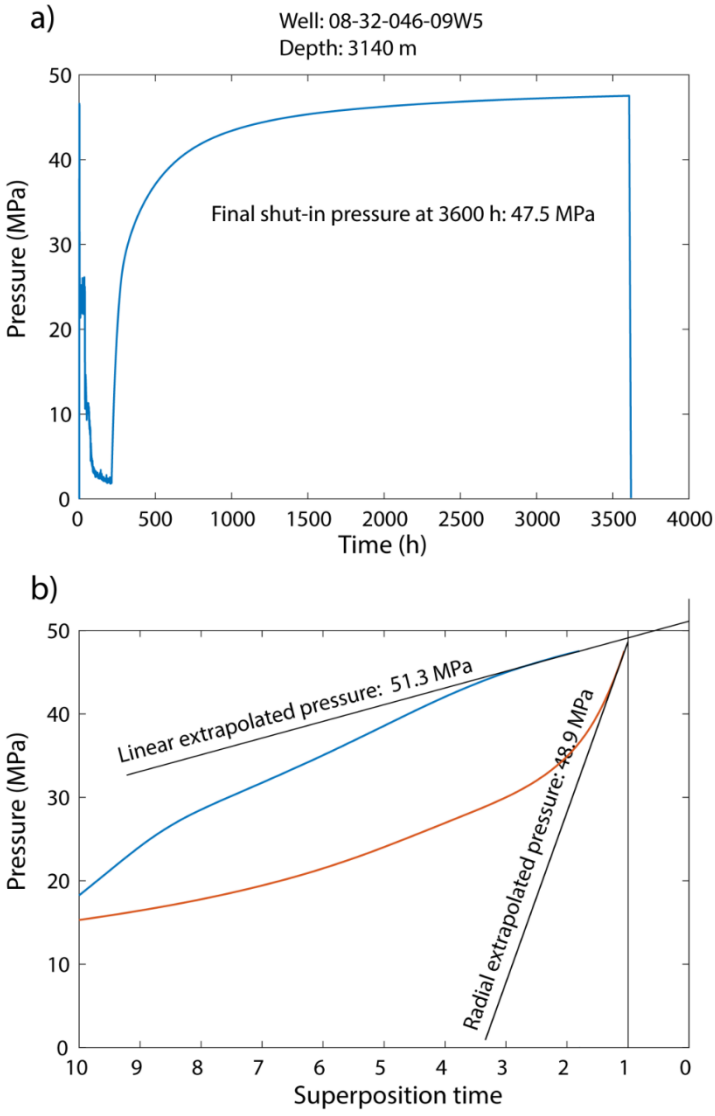


**Figure 3.9.** Sample analysis of a flow-buildup test: a) recorded pressure history during the test; and b) extrapolated pressures with the linear-flow and radial-flow assumptions using the superposition principle.

Similar to the flow-buildup test, the pressure history of the DFIT after fracture closure provides an indication of the reservoir pressure. Notably, the extrapolations of Nolte (1979) and

Soliman et al. (2005) are commonly used to determine the theoretical wellbore pressure ($P_w$) for the infinitely long shut-in time, which should be equal to the initial undisturbed formation-fluid pressure.

*Soliman* et al. [2005] proposed that, if the flow is radial, the wellbore pressure can be expressed as

$$P_w = P_i + M * \frac{1}{t_p+\Delta t} \tag{3.17}$$

and, for linear fracture flow, as

$$P_w = P_i + M * \sqrt{\frac{1}{t_p+\Delta t}}, \tag{3.18}$$

where $t_p$ is the production/injection time and $\Delta t$ represents the time elapsed after shut-in.

For both scenarios, the equivalent time is bounded between 1 (well shut-in time) and 0 (infinite time after shut-in). Linear extrapolations of the $P_w$ linear/radial equivalent time to intercept with the time axis at 0 yields an estimation of initial reservoir/formation pressure.

Nolte (1979) also proposed the relationships

$$P_w = P_i + M * log(1 + \frac{16}{\pi^2} * t_c/(t - t_c)) \tag{3.19}$$

for radial flow and

$$P_w = P_i + M * (\sqrt{1 + \pi^2 * \frac{t-t_c}{16t_c}} - \sqrt{\pi^2 * \frac{t-t_c}{16t_c}}) \tag{3.20}$$

for linear fracture flow. Where $t_c$ stands for the fracture closure time and t is the cumulative test time.

A linear relationship between the proposed equivalent time $F$ and wellbore pressure can be established, using Soliman-Craig or Nolte's approach, respectively, as

$$F_L = \frac{1}{t_p + \Delta t} \text{ or } F_L = \sqrt{1 + \pi^2 * \frac{t - t_c}{16 t_c}} - \sqrt{\pi^2 * \frac{t - t_c}{16 t_c}} \tag{3.21}$$

for linear fracture flow and

$$F_R = \sqrt{\frac{1}{t_p + \Delta t}} \text{ or } F_L = log(1 + \frac{16}{\pi^2} * t_c/(t - t_c)) \tag{3.22}$$

for radial flow. Extrapolation of the linear trends of $F_L$ versus $P_w$ or $F_R$ versus $P_w$ and finding their intercept with F = 0 (infinite shut-in time) allows reservoir fluid pressures of the undisturbed state to be constrained.

Figure 3.10 shows an example of a well-testing result (well 01-11-034-24W4) at a depth of 2158 m, with the eventual shut-in pressures estimated by Nolte and Soliman-Craig linear/radial plots. The eventual shut-in pressure recorded by surface pressure gauge for this test is constrained between 12.5 and 14.5 MPa using Nolte's approach and between 12.1 and 14.6 MPa using the Soliman-Craig solutions. As mentioned earlier, the pressure history for this test was recorded by surface pressure gauges, so the actual downhole pressures at the measurement depth need to be computed by adding the hydrostatic pressures. Assuming a water density of 1000 kg/m$^3$ and gravitational acceleration of 9.8 m/s$^2$, the results from this test constrained the formation pressure to between 33.2 and 34.7 MPa. The kinks near the ends of both pressure-history curves in Figure

3.10 can be caused by operators pulling off the pressure gauges at the end of testing, causing artifacts at the end of the curves.

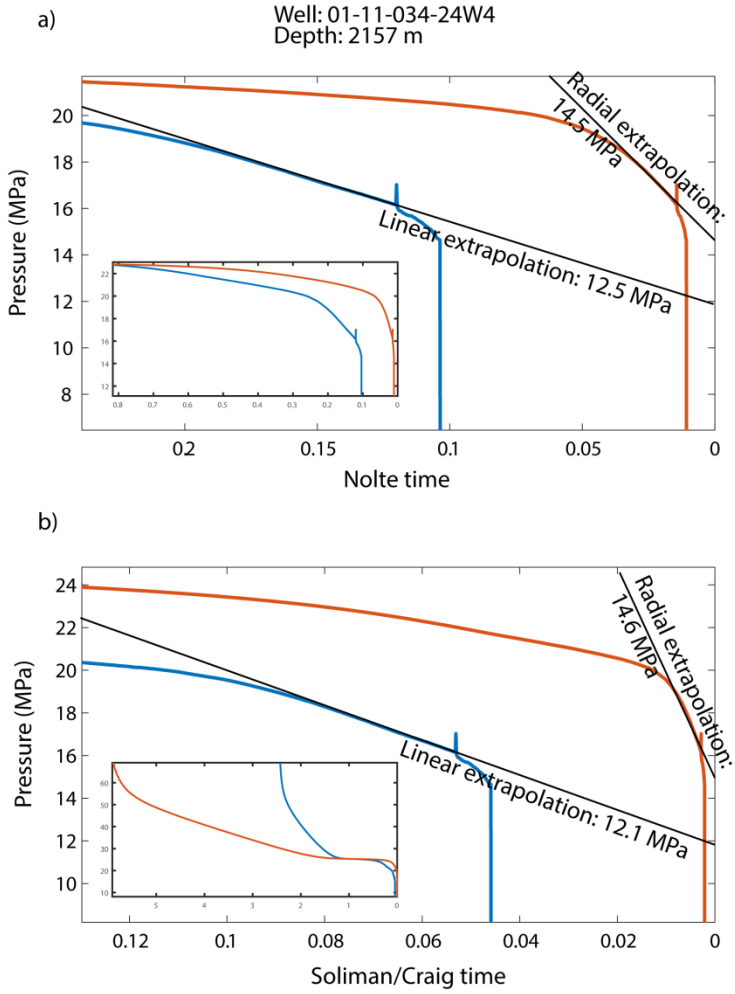


**Figure 3.10.** Sample post-closure analysis to extrapolate the formation pore pressure: a) using Nolte's approach with assumptions for both linear (blue line) and radial (orange line) flow regimes, respectively; black lines show the extrapolated final wellbore pressure following these two assumed flow regimes; b) using the Soliman-Craig approach (blue and orange lines for linear and radial flow, respectively) with the same assumptions as part a; large plot shows the last part of the measurement when the linear extrapolation is evaluated, with the entire analysis shown in the inset.

In this study, we recorded the pore pressure extrapolated using the Soliman-Craig and Nolte methods for each of the DFITs collected. Horner linear and radial extrapolations were applied to the analysis for the flow and buildup tests, and both results estimated assuming linear fracture flow and radial flow. Note that the actual fluid flow in the wellbore is more complicated than the assumptions laid out above. To accurately determine the real reservoir pressure, adequate modelling and history matching are needed; however, due to the limitation of time and resources, we do not extend our discussion to the modelling of wellbore fluid flow. That being said, the actual pore pressure of the nearby formation rocks is constrained by the results estimated based on the assumption of flow regimes being linear or radial. In the accompanying datasets, pore-pressure estimates from the methods described above are recorded for each test analyzed in this study.

### *3.3.4 Determination of Directions and Magnitudes of $S_H$*

*Bell and Gough* [1979] and *Gough and Bell* [1981] first noticed, from examination of oriented dip-meter logs, that the elongation of the cross-sections of deep vertical boreholes in western Alberta is consistently oriented northeast-southwest. They surmised that these features originated from the azimuthal variations of the horizontal-stress concentrations ($S_H$ and $S_h$), causing shear compressive failure of the borehole wall centred on the borehole's spring line pointing in the $S_h$ direction. This failure leads to spalling of the rock from the borehole wall elongating the borehole's radius in this direction; these elongations are now commonly referred to as borehole breakouts. Consequently, determining the horizontal-stress directions is done relatively simply by finding the azimuths of the borehole breakouts (BO) using oriented calipers or image logs.

Similarly, the hoop stresses on borehole spring-line azimuths aligned with $S_H$ are most prone to pure tensile failure; this can result in drilling-induced tensile fractures (DITF) being created on the borehole wall. If these exist, their azimuth will likewise directly indicate the $S_H$ direction.

Although controversial, the existence and dimensions of BOs and DITFs are often used to constrain stress magnitudes. To do this, one requires knowledge of the rock strengths, which are often difficult to obtain, particularly in the absence of core for direct measurements. *Barton et al.* [1988] provided a formula that combines the observed angular width Θ of a breakout with knowledge of the rock's unconfined compressive strength (UCS) and an independently determined measure of the magnitude of $S_h$ (usually from the fracture-closure pressure [$P_{FC}$] determined in the pressure-decline analyses described earlier) to constrain the magnitude of $S_H$:

$$S_H = \frac{UCS + P_P + P_W - S_h(1-2cos\Theta)}{1+2cos\Theta}. \quad (3.23)$$

We will employ this formula later to estimate $S_H$. Note, however, that to simplify the number of variables required, Equation 3.23 does not correctly incorporate a true Mohr-Coulomb failure criterion, thus biasing the results.

In this study, oriented wellbore-image logs are analyzed to constrain the orientation of horizontal stresses. The borehole images used for this study are logged using either an ultrasonic borehole televiewer or a microresistivity imaging device (e.g., Ultrasonic Borehole Imager [UBI$^{TM}$] or Fullbore Formation Microimager [FMI$^{TM}$]). Both tools have proven useful in determining the geometry of boreholes in order to identify BOs and DITFs. An example of a portion of an ultrasonic-image log containing both BOs and DITFs is given in Figure 3.11. Further

details on the theory of the formation and interpretation of such features can be found in *Schmitt et al*. [2012].

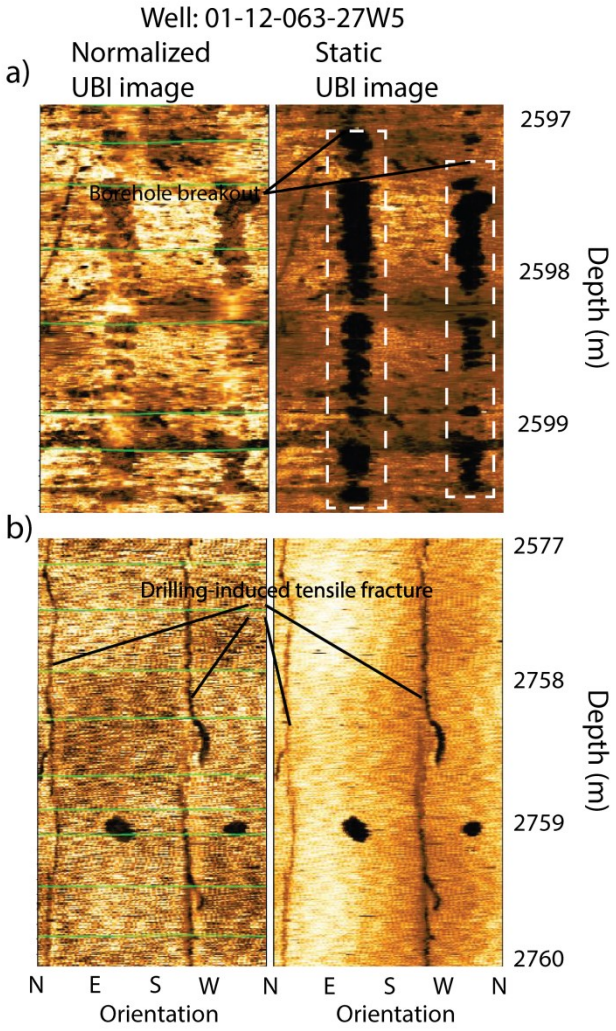


**Figure 3.11**. Sample Ultrasonic Borehole Imager (UBI$^{TM}$) wellbore images with identifiable a) borehole breakouts (BOs), and b) drilling-induced tensile fractures (DITFs).

Note that the example given in Figure 3.11 is one of the higher quality logs. There are noticeable cases where breakouts are often mimicked by other phenomena, so care must be taken in the interpretation of these features. Damage to the borehole wall during drilling or reaming can

often be mistakenly interpreted. Also, natural fractures or large cavities may produce responses similar to those expected from BOs and DITFs. To ensure the accuracy of the BO and DITF identification, we employed the following assessment criteria:

1) The identified BOs and DITFs should be roughly aligned with the expected stress orientation of ~N45°E in this part of Alberta, compiled in the World Stress Map [*Heidbach et al*., 2016] with recent additions [*Reiter et al*., 2014].

2) The BO and DITF directions should be consistent along the length of the borehole. A certain amount of variation in the stress orientation is expected, although the stress orientation should generally be roughly consistent in any given location because Alberta is generally considered tectonically stable.

3) The orientations of BOs and DITFs in a given location must be approximately 90° apart from each other because they represent the directions of $S_h$ and $S_H$, which must be 90° apart to fulfill the required symmetry of the stress tensor.

4) Only pairs of BOs or DITFs appearing along the same spring line through the borehole (i.e., 180° apart) are acceptable.

## 3.4 Conclusion

This chapter detailed the methods we adopted in analyzing transient well testing results and borehole images. The borehole data analyzed using these methods allowed the development of the results that will be presented in chapters 4 to 6.

## References

Ahmed, T. and McKinney, P. (2011): Advanced Reservoir Engineering (revised); Elsevier, 424 p.

Anderson, E.M. (1905): The dynamics of faulting; Transactions of the Edinburgh Geological Society, v. 8, no. 3, p. 387–402.

Atkinson, G.M., Eaton, D.W., Ghofrani, H., Walker, D., Cheadle, B., Schultz, R., Shcherbakov, R., Tiampo, K., Gu, J., Harrington, R.M. and Liu, Y. (2016): Hydraulic fracturing and seismicity in the Western Canada Sedimentary Basin; Seismological Research Letters, v. 87, no. 3, p. 631–647.

Babcock, E.A. (1978): Measurement of subsurface fractures from dipmeter logs; AAPG Bulletin, v. 62, no. 7, p. 1111–1126.

Barree, R.D., Barree, V.L. and Craig, D. (2009): Holistic fracture diagnostics: consistent interpretation of prefrac injection tests using multiple analysis methods; SPE Production & Operations, v. 24, no. 3, p. 396–406.

Barton, C.A., Zoback, M.D. and Burns, K.L. (1988): In-situ stress orientation and magnitude at the Fenton geothermal site, New Mexico, determined from wellbore breakouts; Geophysical Research Letters, v. 15, no. 5, p. 467–470.

Bell, J.S. and Babcock, E.A. (1986): The stress regime of the Western Canadian Basin and implications for hydrocarbon production; Bulletin of Canadian Petroleum Geology, v. 34, no. 3, p. 364–378.

Bell, J.S. and Bachu, S. (2003): In situ stress magnitude and orientation estimates for Cretaceous coal-bearing strata beneath the plains area of central and southern Alberta; Bulletin of Canadian Petroleum Geology, v. 51, no. 1, p. 1–28.

Bell, J.S. and Gough, D.I. (1979): Northeast-southwest compressive stress in Alberta evidence from oil wells; Earth and Planetary Science Letters, v. 45, no. 2, p. 475–482.

Bell, J.S. and Grasby, S.E. (2012): The stress regime of the Western Canadian Sedimentary Basin; Geofluids, v. 12, no. 2, p. 150–165.

Bell, J.S., Price, P.R. and McLellan, P.J. (1994): In-situ stress in the Western Canada Sedimentary Basin; Chapter 29 *in* Geological Atlas of the Western Canada Sedimentary Basin, G.D. Mossop and I. Shetsen (ed.), Canadian Society of Petroleum Geologists, Calgary, Alberta and Alberta Research Council, Edmonton, Alberta, p. 439–446.

Castillo, J.L. (1987): Modified fracture pressure decline analysis including pressure-dependent leakoff; Low-Permeability Reservoirs Symposium, Denver, Colorado, May 18–19, 1987, Paper SPE 16417, https://doi.org/10.2118/16417-MS.

Cinco-Ley, H. (1981): Transient pressure analysis for fractured wells; Journal of Petroleum Technology, v. 33, no. 9, p. 1–749.

Craig, D.P., Barree, R.D., Warpinski, N.R. and Blasingame, T.A. (2017): Fracture closure stress: re-examining field and laboratory experiments of fracture closure using modern interpretation methodologies; Society of Petroleum Engineers, Annual Technical Conference and Exhibition, October 9-11, San Antonio, Texas, Paper SPE-187038-MS, https://doi.org/10.2118/187038-MS.

Davis, M. and Karlen, G. (2013): A regional assessment of the Duvernay Formation; a world-class liquids-rich shale play; extended abstract of presentation at CSPG/CSEG/CWLS GeoConvention 2013, (Integration: Geoscience Engineering Partnership), Calgary, Alberta, May 6-12, 2013, Search and Discovery Article #10638 (2014), URL

<http://www.searchanddiscovery.com/pdfz/documents/2014/10638davis/ndx_davis.pdf.html> [August 2018].

Detournay, E., Cheng, A.D., Roegiers, J.C. and McLennan, J.D. (1989): Poroelasticity considerations in in situ stress determination by hydraulic fracturing; International Journal of Rock Mechanics and Mining Sciences & Geomechanics Abstracts, v. 26, no. 6, p. 507–513.

Doe, T., Ingevald, K., Strindell, L., Haimson, B. and Carlsson, H. (1981): Hydraulic fracturing and overcoring stress measurements in a deep borehole at the Stripa test mine, Sweden; American Rock Mechanics Association, 22nd U.S. Symposium on Rock Mechanics (USRMS), June 29–July 2, 1981, Cambridge, Massachusetts, Paper ARMA-81-0373, URL <https://www.onepetro.org/conference-paper/ARMA-81-0373> [August 2018].

Ellis, D.V. and Singer, J.M. (2007): Well Logging for Earth Scientists (Second Edition); Springer, Dordrecht, 692 p., https://doi.org/10.1007/978-1-4020-4602-5.

Fordjor, C.K., Bell, J.S. and Gough, D.I. (1983): Breakouts in Alberta and stress in the North American plate; Canadian Journal of Earth Sciences, v. 20, no. 9, p. 1445–1455.

Fox, A.D. and Soltanzadeh, M. (2015): A regional geomechanical study of the Duvernay Formation in Alberta, Canada; paper presented at GeoConvention 2015, *Geoscience: New Horizons*, May 4–8, 2015, Calgary, Alberta.

Gough, D.I. and Bell, J.S. (1981): Stress orientations from oil well fractures in Alberta and Texas; Canadian Journal of Earth Sciences, v. 18, p. 638–645.

Gough, D.I., and Bell, J.S. (1982): Stress orientation from borehole wall fractures with examples from Colorado, east Texas, and northern Canada; Canadian Journal of Earth Sciences, v. 19, p. 1358–1370.

Green, D.G. and Mountjoy, E.W. (2005): Fault and conduit controlled burial dolomitization of the Devonian west-central Alberta Deep Basin; Bulletin of Canadian Petroleum Geology, v. 53., no. 2, p. 101–129.

Haimson, B.C. and Rummel, F. (1982): Hydrofracturing stress measurements in the Iceland research drilling project drill hole at Reydarfjordur, Iceland; Journal of Geophysical Research: Solid Earth, v. 87, no. B8, p. 6631–6649.

Haug, K. and Bell, J.S. (2016): Compilation of in situ stress data from Alberta and northeastern British Columbia (tabular data, tab delimited); Alberta Energy Regulator, AER/AGS Digital Data 2016-0040, URL <https://ags.aer.ca/publications/DIG-2016-0040.html> [August 2018].

Heidbach, O., Rajabi, M., Reiter, K., Ziegler, M. and WSM Team (2016): World Stress Map Database Release 2016; GFZ Data Services, http://doi.org/10.5880/WSM.2016.001.

Henton, J.A., Craymer, M.R., Dragert, H., Mazzotti, S., Ferland, R. and Forbes, D.L. (2006): Crustal motion and deformation monitoring of the Canadian landmass; Geomatica, v. 60, no. 2, p. 173–191.

Horner, D.R. (1951): Pressure build-up in wells; 3rd World Petroleum Congress, May 28–June 6, 1951, The Hague, Netherlands, Paper WPC-4135, URL <https://www.onepetro.org/conference-paper/WPC-4135> [August 2018].

Howard, G.C. and Fast, C.R. (1957): Optimum fluid characteristics for fracture extension; American Petroleum Institute, *Drilling and Production Practice*, January 1, 1957, New York, New York, Paper API-57-261, https://www.onepetro.org/conference-paper/API-57-261 [August 2018].

Morin, M.L. (2017): Natural and drilling induced fractures in the Grosmont Formation, Alberta: implications for the state of stress; M.Sc. thesis, University of Alberta, Edmonton, Alberta, 108 p.

Nolte, K.G. (1979): Determination of fracture parameters from fracturing pressure decline; Society of Petroleum Engineers, Annual Technical Conference and Exhibition, September 23–26, Las Vegas, Nevada, Paper SPE-8341-MS, https://doi.org/10.2118/8341-MS.

Nolte, K.G. (1986): A general analysis of fracturing pressure decline with application to three models; SPE Formation Evaluation, v. 1, no. 6, p. 571–583.

Pawley, S., Schultz, R., Playter, T., Corlett, H., Shipman, T., Lyster, S. and Hauck, T. (2018): The geological susceptibility of induced earthquakes in the Duvernay play; Geophysical Research Letters, v. 45, no. 4, p. 1786–1793.

Plumb, R.A., Evans, K.F. and Engelder, T. (1991): Geophysical log responses and their correlation with bed-to-bed stress contrasts in Paleozoic rocks, Appalachian Plateau, New York; Journal of Geophysical Research: Solid Earth, v. 96, no. B9, p. 14509–14528.

Preston, A., Garner, G., Beavis, K., Sadiq, O. and Stricker, S. (2016): Duvernay reserves and resources report: a comprehensive analysis of Alberta's foremost liquids-rich shale resource; Alberta Energy Regulator, AER report, 83 p., <https://www.aer.ca/documents/reports/DuvernayReserves_2016.pdf> [August 2018].

Reiter, K., Heidbach, O., Schmitt, D., Haug, K., Ziegler, M. and Moeck, I. (2014): A revised crustal stress orientation database for Canada; Tectonophysics, v. 636, p. 111–124, http://dx.doi.org/10.1016/j.tecto.2014.08.006.

Rokosh, C.D., Lyster, S., Anderson, S.D.A., Beaton, A.P., Berhane, H., Brazzoni, T., Chen, D., Cheng, Y., Mack, T., Pana, C. and Pawlowicz, J.G. (2012): Summary of Alberta's shale- and siltstone-hosted hydrocarbon resource potential; Energy Resources Conservation Board, ERCB/AGS Open File Report 2012-06, 327 p.

Schmitt, D.R. (2014): Basic geomechanics for induced seismicity: a tutorial, CSEG Recorder, v. 39, no. 11, p. 24–29.

Schmitt, D.R. and Haimson, B.C. (2017): Hydraulic fracturing stress measurements in deep holes; Chapter 6 *in* Rock Mechanics and Engineering, Volume 1: Principles, X-T. Feng (ed.), CRC Press, p. 183–225.

Schmitt, D.R., Currie, C.A. and Zhang, L. (2012): Crustal stress determination from boreholes and rock cores: fundamental principles; Tectonophysics, v. 580, p. 1–26, http://dx.doi.org/10.1016/j.tecto.2012.08.029.

Schultz, R., Wang, R., Gu, Y.J., Haug, K. and Atkinson, G. (2017): A seismological overview of the induced earthquakes in the Duvernay play near Fox Creek, Alberta; Journal of Geophysical Research: Solid Earth, v. 122, no. 1, p. 492–505.

Shen, Luyi (2019), "Data for: Quantitative constraints to the complete state of stress from the combined borehole and focal mechanism inversions: Fox Creek, Alberta", Mendeley Data, V1, doi: 10.17632/nxhs4ppcdf.1

Shen, L., and D. Schmitt (2020), Data for: States of in-situ stress in the Duvernay East Shale Basin and Willesden Green of Alberta, Canada: variable in-situ stress states effect fault stability, Mendeley Data, V1, doi: 10.17632/tgmxx5vkjx.1

Soliman, M.Y., Craig, D.P., Bartko, K.M., Rahim, Z. and Adams, D.M. (2005): Post-closure analysis to determine formation permeability, reservoir pressure, residual fracture properties; Society of Petroleum Engineers, Middle East Oil and Gas Show and Conference, March 12–15, 2005, Kingdom of Bahrain, Paper SPE-93419-MS, https://doi.org/10.2118/93419-MS.

Wang, R., Gu, Y.J., Schultz, R., Kim, A. and Atkinson, G. (2016): Source analysis of a potential hydraulic-fracturing-induced earthquake near Fox Creek, Alberta; Geophysical Research Letters, v. 43, no. 2, p. 564–573.

Wang, R., Gu, Y.J., Schultz, R., Zhang, M. and Kim, A. (2017): Source characteristics and geological implications of the January 2016 induced earthquake swarm near Crooked Lake, Alberta; Geophysical Journal International, v. 210, no. 2, p. 979–988.

Woodland, D.C. and Bell, J.S. (1989): In situ stress magnitudes from mini-frac records in western Canada; Journal of Canadian Petroleum Technology, v. 28, no. 5, 11 p., https://doi.org/10.2118/89-05-01.

Zanganeh, B., MacKay, M.K., Clarkson, C.R. and Jones, J.R. (2018): DFIT analysis in low leakoff formations: a Duvernay case study; Society of Petroleum Engineers, SPE Canada Unconventional Resources Conference, March 13–14, 2018, Calgary, Alberta, Paper SPE-189826-MS, https://doi.org/10.2118/189826-MS.

Zoback, M.D. (2007): Reservoir Geomechanics; Cambridge University Press, Cambridge, United Kingdom, 489 p.

Zoback, M.D. and Zoback, M.L. (1991): Tectonic stress field of North America and relative plate motions; Neotectonics of North America, v. 1, p. 339–366.

# Chapter 4 Quantitative constraints to the complete state of stress from the combined borehole and focal mechanism inversions: Fox Creek, Alberta

## 4.1 Introduction

Usually, the key limiting factor in carrying out stability analyses is the lack of quantitative information on the stress state. In this work, we aim to develop a complete quantitative Andersonian [*Anderson*, 1951] stress state model with consisting of the magnitudes of the vertical $S_V$, least horizontal $S_h$ and greatest horizontal $S_H$ principal stresses, and the $S_H$ orientation $\phi$ in an area that has recently experienced earthquakes induced by hydraulic fracturing operations.

$S_V$ is commonly assumed to be given by integration of the overlying gravitational load [*McGarr and Gay*, 1978]. In certain areas, the stress orientation $\phi$ of the greatest horizontal compression $S_H$ may be inferred from existing compilations such as the World Stress Map [*Heidbach et al*., 2010]. Finding the magnitudes of both $S_H$ and the least horizontal compression $S_h$ is difficult, and usually researchers make various assumptions based on extrapolations of quantitative results [*Schwab et al*., 2017; *Weides et al*., 2014], consistency with local earthquakes [*Chang et al*., 2010; *Morris et al*., 2017], frictional limits [*Çiftçi,* 2013; *Schwab et al.*, 2017], constraints from various well tests [*Chang et al*., 2010; *Konstantinovskaya et al*., 2012], extrapolated empirical relationships [*Adewole and Healy*, 2017; *Williams et al*., 2016], or borehole stabilities [*Peška and Zoback*, 1995; *Williams et al*., 2016; *Valley and Evans*, 2019]. As most of these authors indicate, the lack of proper measurements of the horizontal stress magnitudes, particularly with regards to $S_H$ for which direct measurement remains elusive, is the most significant source of uncertainties in their stability analyses.

Most stress compilations, too, have focused on tectonic stress directions over large areas. Regional studies that focus not only on stress directions but include quantitative determination of stress magnitudes from a representative number of boreholes remain rare [*Bailey et al*., 2016; *Konstantinovskaya et al*., 2012; *Nelson et al*., 2007; *Streit and Hillis*, 2004]. Here, we focus on the development of a quantitative model for the magnitudes and directions of the stress tensor in an area of 150 km × 150 km centred at the municipality of Fox Creek, Alberta (Figure 4.1a and b). The need to understand better the conditions leading to earthquakes that appear to have been produced by hydraulic fracturing of the unconventional Duvernay Formation in NW Alberta motivated our effort to develop a model allowing quantitative assessment of the states of in-situ stress. We extract magnitudes of $S_V$, $S_h$, and $P_p$ from geophysical well logs and transient pressure tests. Estimates of $\phi$ are obtained by interpretation of borehole deformation features and supported by stress inversion performed with reported focal mechanism solutions of nearby earthquakes. Subsequently, we constrain the range of $S_H$ by combining the shape-ratio $R$ determined from the stress inversion with the previously obtained $S_V$ and $S_h$. The dense measurements utilized in this sudy allows the development of a model which can be used to predict the quantitative stress values and $P_p$ in a crust volume encompassing the Duvernay formation and the epicenters of induced earthquakes.

### *4.1.1 Study Area*

The study area from 53.5° to 55°N latitude and -118.5° to -115.5°W longitude (see Figure 4.1a) includes the epicentres of felt earthquakes (see Figure 4.1b) induced by hydraulic fracturing operations near the municipality of Fox Creek, Alberta [*Schultz et al*., 2018; *Schultz et al*., 2015; *Schultz et al*., 2017; *Wang et al*., 2016; *Wang et al*., 2017].

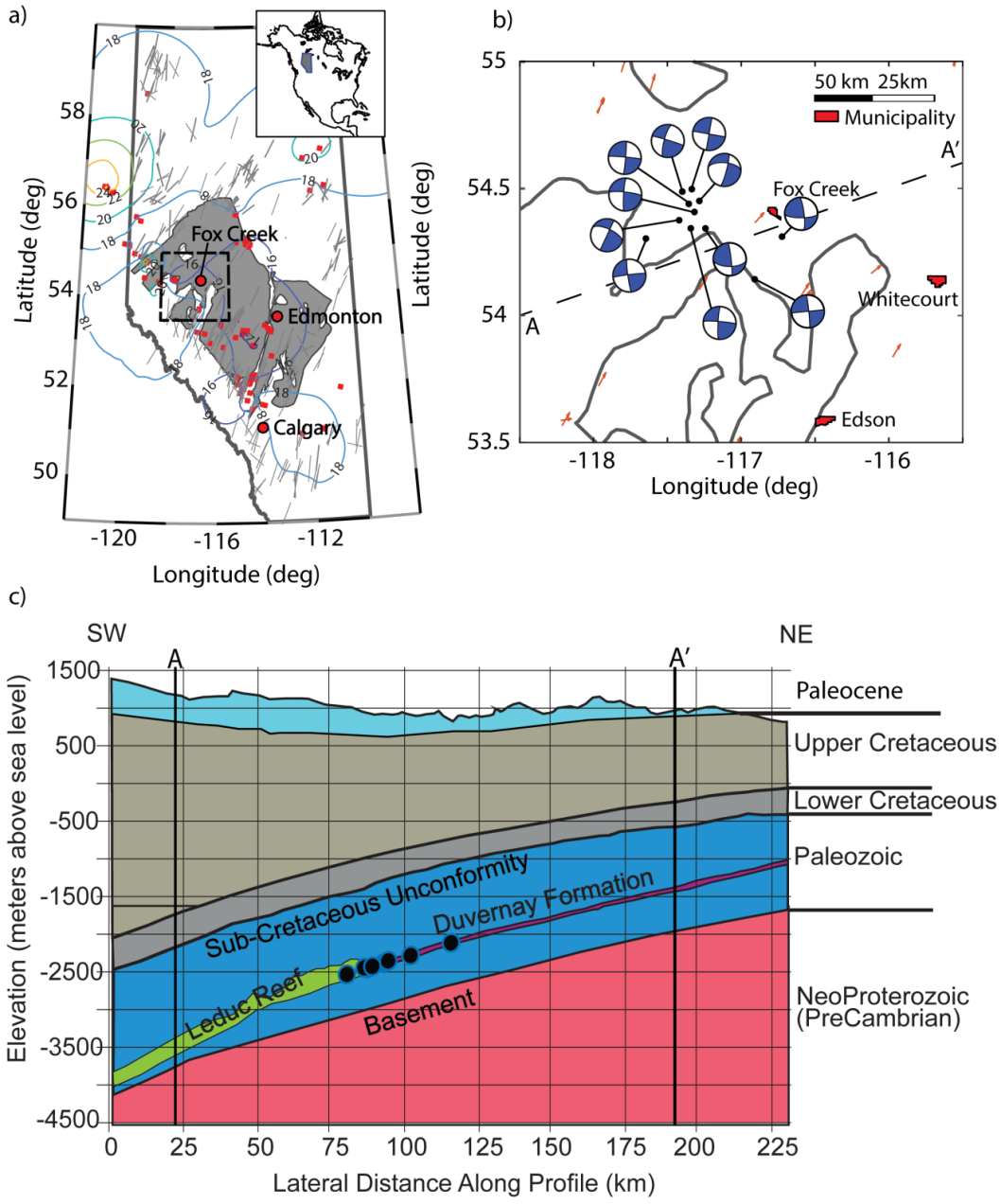


**Figure 4.1** a) Map of Alberta with lines giving $S_H$ directions in the WSM, red dots showing locations of $S_h$ magnitude measurements, and contours representing the estimated $S_h$-to-depth ratio as compiled by *Haug and Bell*, [2016]. The gray zone shows the areal extent of the Duvernay Formation. The black dashed lines enclose the area investigated in this study. b) An expanded view of the study area including epicentres and focal mechanism solutions for the felt earthquakes from 2013 to 2017 compiled by *Schultz et al*., [2017].

The orange arrows indicate the $S_H$ orientations in the study area recorded by WSM. c) The cross-section of the stratigraphy [*Branscombe et al*., 2018] in the study area from A to A' as shown in b). The black dots along the Duvernay Formation represent the projection of earthquakes shown in b) assuming the earthquakes happen within the Duvernay Formation [*Eaton et al*., 2018; *Schultz et al*., 2017]

### *4.1.2 Geological Structure*

The study area contains distinct packages of Neoproterozoic-Paleozoic and Phanerozoic sediment deposited, respectively, in a passive margin and foreland basin settings. These sediments overlie the stable North American cratonic basement constructed of Proterozoic crystalline rock (Figure 4.2c). The Paleozoic portion of the sediments consists mostly of evaporites, carbonates, and shales deposited in open-marine environments, also including Frasnian age Leduc reef complexes contemporaneous with the Duvernay Formation that is a prominent target of hydraulic fracturing operations [*Lyster et al*., 2017]. Development of the Alberta Foreland Basin commenced in the Late Jurassic-Early Cretaceous from the successive loading of overthrust sheets [*Cant and Stockmal*, 1989] with the basin filling with siliciclastics. In the study area, these siliciclastics were deposited onto the Paleozoic unconformity surface referred to as the Mississippian, or Sub Cretaceous Unconformity in the study region, and upwards of 2 km of these sediments may have since been removed by erosion [*Wu*, 1991]. The craton and Paleozoic sediments display significant inclination; the top of the Duvernay Formation, for example, drops from ~ -1400 m below surface level (mbsl) in the NE to < -3000 mbsl in the SW of the study area (see Figure 4.2c) while the top of the craton elevation declines from ~ -1800 mbsl to ~ -4000 mbsl (see Figure 4.2c). In contrast, the surface elevation increases from ~750 mbsl to >2000 mbsl as it includes portions of the disturbed belt east of the Rocky Mountains.

The Paleozoic sediments burial subjected the organic-rich shale to conditions favourable for the formation of light hydrocarbon, most of which migrated eastward sourcing the many conventional carbonates and clastic hydrocarbon fields within the Western Canada Sedimentary Basin. Economic quantities of light hydrocarbons remain locked within the low permeability rock matrix of the organic-rich formations, and this has encouraged hydraulic fracturing activities in the Duvernay Formation [*Preston et al*., 2016], some of which are associated with induced seismicity.

Some faults have been seen in reflection seismic profiles more regionally outside the study area [*Richards et al*., 1994; *Weides et al*., 2014] or inferred from the structural mapping of geological tops [*Green and Mountjoy*, 2005]. Analysis of textural seismic attributes of 3D seismic volumes at undisclosed locations in the region has hinted at the existence of subsurface lineaments that are possibly interpreted as faults [*Chopra et al*., 2017; *Eaton et al*., 2018] but to our knowledge most of these lineaments, many of which are not optimally oriented for slipping, have not been linked to any of the felt induced earthquakes.

### *4.1.3 Fox Creek Induced Seismicity*

From December 2013 to 2016 more than 250 earthquakes with magnitudes $M_W > 2.5$ have been temporally correlated with hydraulic fracturing operations within Fox Creek Duvernay Formation [*Schultz et al*., 2017]. All of these have occurred from ~15% of the wells within a relatively confined area of the administrative Kaybob assessment area [*Schultz et al*., 2018]. It is also worth noting hydraulic fracturing operations within the Duvernay Formation about 200 km to the south (Willesden Green Field) have not induced any felt seismicity. Detailed reasons for this are as yet unknown, but spatial associations to possible basement faults associated with well

mapped Devonian reef complexes [*Schultz et al*., 2016] or high pore pressures [*Eaton*, 2017; *Eaton and Schultz*, 2018; *Fox and Soltanzadeh*, 2015] were implicated. Statistical analyses further suggest that the volume of fluid injected during a given stimulation is a contributing factor, particularly when it is noted that no induced seismicity by hydraulic fracture operations before the first event in 2013 was detected [*Schultz et al*., 2018].

*Schultz et al*. [2017] provide a recent summary of the induced seismicity from 2013 to 2016 detailing about 250 events within 17 distinct clusters. The event's focal mechanism conjugate planes strike N-S/E-W predominantly and indicate strike-slip displacement with P-axis vectors pointing at an azimuth of 45° ± 5° consistent with expected regional horizontal stress directions [[*Bell and Grasby*, 2012; *Reiter et al*., 2014] with the source mechanisms being largely double-couple. The earthquake epicentres are located with an accuracy of < 1 km, but the hypocenter depths remain poorly constrained at ~5±2 km [*Schultz et al*., 2017].

### *4.1.4 Prior Knowledge of Stress State*

The first efforts at mapping stress directions near the study area occurred in deep boreholes drilled in western Alberta. The analysis of borehole breakouts (BOs), using oriented calliper logging tools (dip-meters) by *Bell and Gough* [1979]. *Bell et al*. [1994] gathered new BO stress direction measurements supplemented with a few quantitative estimates of $S_h$ magnitudes from a variety of well tests. This work has been periodically updated [*Bell and Bachu*, 2003; *Bell and Grasby*, 2012]; with the final raw compilation recently available [*Haug and Bell*, 2016]. Additional stress directions were also found within the literature, too, expanded information on stress orientations [*Reiter et al*., 2014] that mainly indicate NE-SW compression across Alberta; this

direction is not necessarily always perpendicular to the disturbed belt of the Canadian Rocky Mountains as is often presumed.

Prior to the present study, there were 64 reported stress directions from *Reiter et al*. [2014] and included in the latest version of Word Stress Map [WSM, *Heidbach et al*., 2016] nearby (see supplementary material); 19 of these measurements are directly within the study area (see Figure 4.2a). A small number of fracture closure (presumed to represent $S_h$) and $P_P$ [*Woodland and Bell*, 1989] are reported near the study area, these data were incorporated into *Haug and Bell*'s [2016] compilation which spatially covers the entire Alberta Basin. Sections of the Duvernay Formation appear to be highly over-pressured [*Fox and Soltanzadeh*, 2015]. *Shen et al*. [2018a] attempted constraining the $S_H$ through the recorded width of borehole breakouts interpreted from image logs. However, this attempt is subject to some drawbacks including lack of knowledge on the rock mechanical parameters and $P_P$ at the rocks near the wellbore. Most of the borehole breakouts utilized in *Shen et al*. [2018a] are recorded in the segments above the Duvernay Formation. As such the full set of components of the in-situ stress, which are necessary for comprehensive characterization of the states of in-situ stress within our area of interests near Fox Creek, is still lacking. This lack of information motivates our study to constrain, as quantitatively as possible, the full stress tensor in the vicinity of the induced earthquakes.

## 4.2 Data and Methods

This study focuses on developing models for the directions and magnitudes that allow for extrapolation of the stress tensor to any points of interest within the study area. $P_P$, and $S_h$ magnitudes interpreted from a variety of borehole pressure tests (e.g., diagnostic fracture injection

test (DFIT), static gradient survey, and flow/build up test) and values of $\phi$ extracted from image logs.

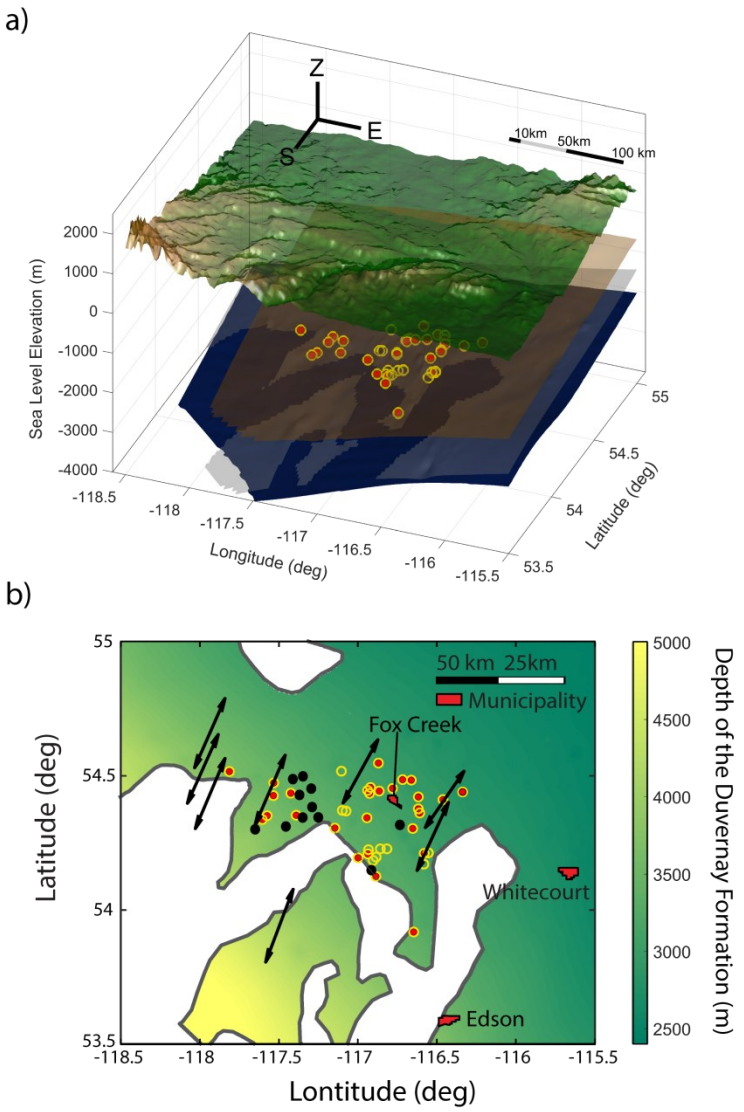


**Figure 4.2** The measurements utilized for this study. The surfaces rendered from top to bottom include 30-m resolution shuttle radar topography, and the Mississippian Unconformity (Branscombe et al., 2018), and the tops of the Duvernay Formation extracted from a commercial database and the Neoproterozoic Basement as interpolated from [*Peterson*, 2017]. Red dots and yellow circles indicate the positions of $S_h$ and $P_P$ measurements respectively and many of which are obtained from the same transient pressure record.

b) The top-down overview of the study region and the measurement points. Red dots and yellow circle show the locations of $S_h$ and $Pp$ measurements as in a). The black arrows represent the $S_H$ azimuth revealed by borehole failures intepreted from image logs located within the study area, reported in *Shen et al*., [2018b]. The solid black circles indicate the epicentral positions of suspected induced events [*Schultz et al*., 2016] as shown in Figure 4.1. White areas indicate disruption of the Duvernay Formation by the coeval Leduc Reefs.

These data are already publicly available [*Shen et al*., 2018a, b], together with detailed descriptions of the methodologies used to extract this information. Hereafter for brevity we shorten these reports' citations to SA and SB, respectively. We further attempt here to constrain $S_H$ magnitudes utilizing the measurements recorded in SB and focal mechanism solutions for the earthquakes reported within our study area. To avoid confusion, here 'depth' $z$ refers to the true vertical depth (TVD) defined as the vertical distance from the measurement point in the Earth to the drilling rig's Kelly Bushing reference as corrected by any borehole deviation. Elevations $h$ are measured in meters relative to sea level with positive and negative values representing heights respectively above and below sea level. We use the compression positive sign convention that compressive stress, pore pressure, and rock strength all have positive values. Fig. 4.2a and b shows the positions of the various measurements relative to the epicentres of the major induced earthquakes and important stratigraphic markers.

### *4.2.1 $S_H$ Orientations $\phi$*

We employ the orientations of BOs [*Bell and Gough*, 1979] and DITFs [*Aadnoy*, 1990; *Aadnoy and Bell*, 1998; *Brudy and Zoback*, 1999] reported in SB the spring-lines of which strike, respectively, perpendicular and parallel to the $S_H$ azimuth $\phi$ [*Schmitt et al*., 2012; *Zoback*, 2007;

*Zoback et al*., 2003]. The model developed here uses a two-step process in which the statistics of the directions from a given borehole are first defined with these results then spatially interpolated to estimate the stress direction across the study area.

We employed both oriented ultrasonic borehole televiewer and micro-resistivity imaging logs in the analysis; with examples of typical ultrasonic image log data given in Fig. 4.3. Values of $\phi$ were obtained in the analysis of over 2000 m of borehole image logs taken from 20 boreholes both within (8 boreholes, see Figure 4.2b) and close to the study area. The depth extents and directions are tabulated in SB according to quality control assessment criteria described in SA, the analysis here includes four additional logs over those that were available for SB, these new data and a summary of the SB results are included in the supplementary material with WSM quality ranks calculated for reference. It is worth noting that sections of the boreholes interpreted in SB deviate significantly from vertical; in the analysis here, however, almost all log information used is from nearly vertical boreholes with any data obtained at inclinations more than 30° excluded. Clear images of BOs or DITFs are scarce in the segments of the Duvernay Formation and most recorded stress orientations in SB are from the overlying formations. Interpolation of these directions using an inverse distance weight scheme described below provides the final stress direction map.

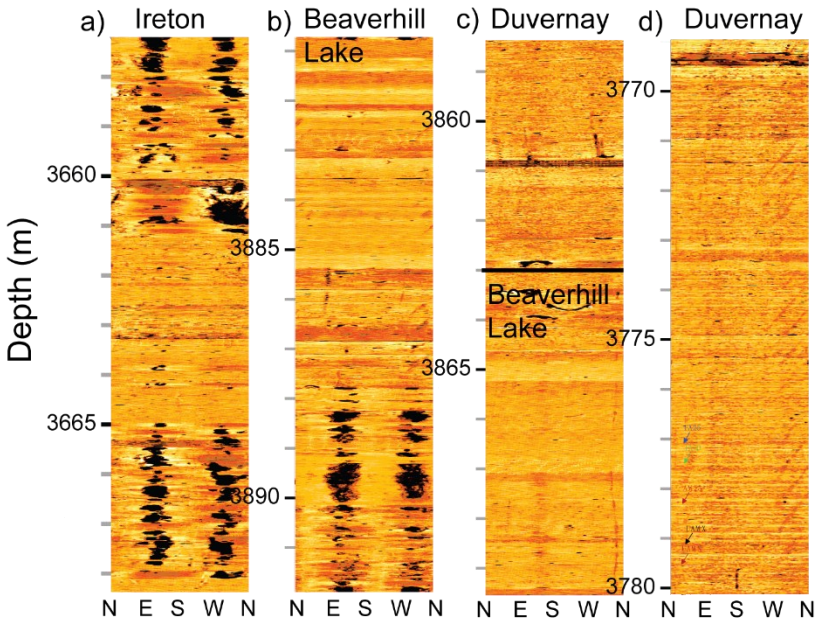


**Figure 4.3.** Examples of depth segments of high-quality ultrasonic amplitude reflectivity image log data from well UWI 12-11-64-27W5 showing zones with (a and, (b BOs, and without (c and, (d BOs.

The final value of $\phi$ reported at the location of each borehole is the weighted average of its the set of $\phi$ observations as colour-coded in Fig. 4.4a. This is accomplished using available CircStat software toolbox [*Berens*, 2009] that calculates the average of a set of complex numbers in Euler form with phase angles and amplitudes equal to the observed $\phi$ and their quality index weights, respectively. This averaging procedure was further adapted to account for the fact that $\phi$ exists only over the azimuth range of $0° \leq \phi \leq 180°$ sufficiently describes the $S_H$ directions by simply adding into the data suite each value's appropriately weighted symmetric counterpart at azimuth $\phi' = \phi + \pi$. The final direction for that data set occurs at the orientation with the maximum probability of the corresponding von Mise's circular probability distribution [*Mardia and Jupp*, 1999]. We illustrate by application to the entire final set of average $\phi$, including those wellbores located outside of our study region, as shown in an equal area rose diagram of the dispersion (Fig.

4.4b) and the corresponding von Mise's probability distribution (Fig. 4.4c) with the peak at $\phi$ = 43°.

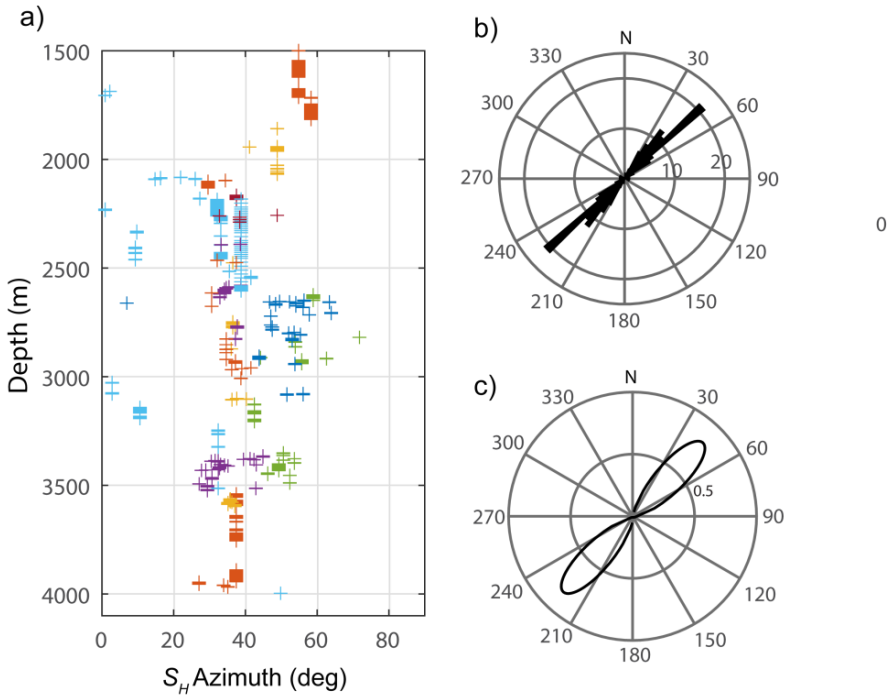


**Figure 4.4.** a) The complete set of 20 observations of $\phi$, reported in SB, plotted versus depth and colour-coded by each borehole. b) Rose diagram histogram distribution of $S_h$ orientation measurements $\phi$ for the entire set of final average $\phi$ for all the boreholes (including those reported in WSM) used. c) The von Mises circular distribution for the full set of azimuths from a) with the maximum occurring at $\phi$ = 43°.

Many researchers have attempted to develop maps that highlight areal trends in $\phi$ by calculating spatial averages from scattered individual $\phi$ determinations using a variety of averaging methods that have been applied at regional or global scales using earthquake focal mechanisms [*Hardebeck and Hauksson*, 2001] or stress indicators [*Heidbach et al*., 2010; *Reiter et al*., 2014]. Given the sparsity of data, these methods usually search over areas with dimensions of 100's of km in order to determine a set of data for averaging. The situation here differs somewhat here that

the total study area is more confined with areal dimensions significantly less than the wavelengths of these larger scale studies. For this reason, we take a different approach in which the borehole averaged $\phi$ values are interpolated using an adaptation of the Inverse Distance Weighting (IDW) method with the results shown in Fig. 4.5a. In order to estimate the $\phi$ at a given point in the map, each neighboring observation '$i$' is weighted $W_i$ according to the ratio of its assigned quality index $Q_i$ to its distance $D_i$

$$W_i = Q_i/D_i \tag{4.1}$$

We note that although one must assign a low WSM quality ranking to these BOs and DITF as they are discontinuous, within a given borehole the orientations generally do remain consistent lending more confidence than the formal quality ranking might suggest. That said, the quality of the image logs also varied, and to account for this a numerical quality weight $Q_i$ was assigned to each average $\phi$ semi-quantitatively (see supplementary material). $Q_i \equiv 1$ only for those clear image logs displaying long BO and DITF. $Q_i \equiv 0.75$ for lower quality image logs that still exhibited clear BOs or DITFs that were either of limited extent or perturbed by natural fractures resulting in greater estimated $\phi$ uncertainties. Finally, $Q_i \equiv 0.25$ for those values provided by the WSM primarily because these measures were beyond our control; we do not intend that this necessarily reflects those earlier measurements validity.

Essentially, to obtain a representative value of $\phi$ at a given point in the map the algorithm searches over circles of increasingly larger radii until the sum of all of the $Q_i$ within the circle reaches a threshold value of 3. Once this threshold is exceeded, the IDW weighted average $\phi$ is then calculated using CircStat. The search radius of each of the prediction points in our study area are shown in Fig. 4.5b. In order to avoid a 'bulls-eye' effect in the averaging from proximate data

points, a minimum distance $D_i$ = 2 km is enforced although this situation is rare as the distances between the boreholes are mostly larger. The ratio between the weighted standard deviation of measurements $\sigma$ within the search radius to the sum of the corresponding weights

$$A = \frac{\sigma}{\sum w_i} \tag{4.2}$$

This confidence measure $A$ (Figure 4.5c) accounts for the consistency, the quality, and the proximity of the input measurements relative to the prediction point. Points with high confidence have $A \rightarrow 0$. The confidence of IDW $\phi$ is poor in the SW due to conflicting stress directions at some of the boreholes.

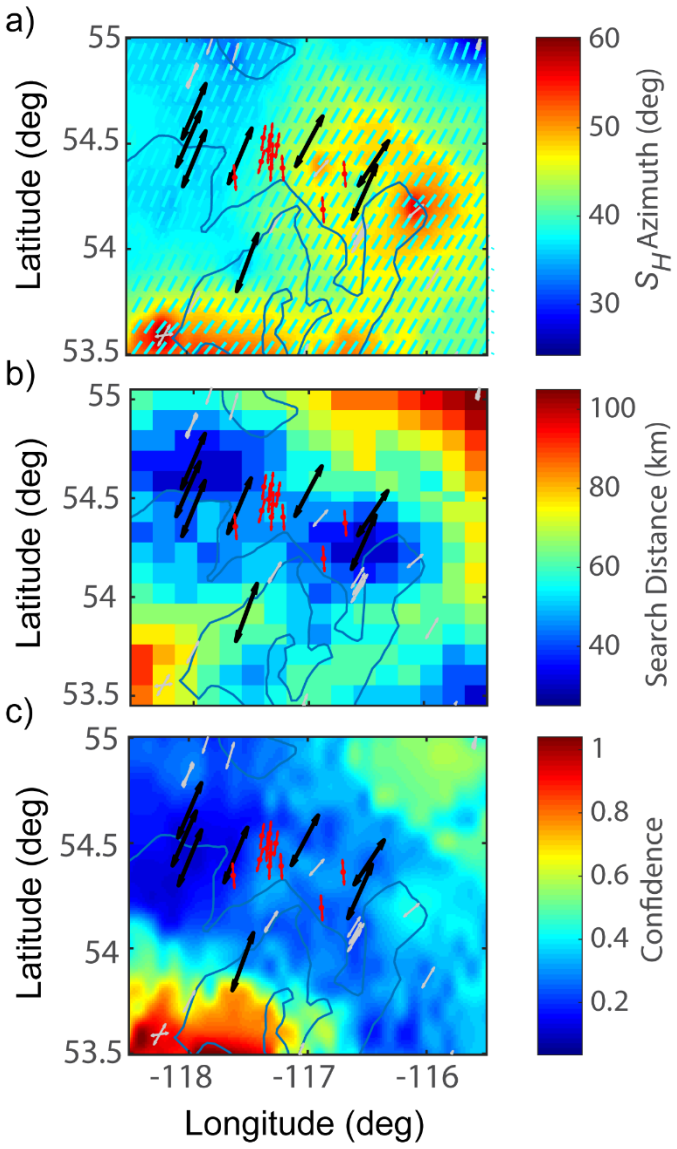


**Figure 4.5.** a) Map of averaged $S_H$ azimuths $\phi$ determined using IDW. Black arrows represent stress orientation measurements reported by SB. Small white arrows represent those from WSM. The cyan dashes represent directly the modelled $\phi$ at grid points in the study area while the background colour is the smoothed model for $\phi$ over the area. The red arrows and dots show the strikes of the faulting planes revealed by earthquakes' focal mechanism solutions and the epicentral locations. b) The search radius of each prediction point for IDW. c) Confidence in the $S_H$ azimuth prediction. Values close to zero represent high confidence and values close to one stand for low confidence.

*4.2.2 Vertical Stress $S_V$*

It is often assumed and generally accepted that the vertical stress $S_V$ is one of the principal direction of the subsurface stress tensor at sufficient depth and that its magnitude is given by overburden pressure due to the weight of the overlying rock mass with density $\rho(z)$. We incorporate 1125 digital $\rho(z)$ logs, with 694 located directly within the study area (Fig. 4.6e), through the IHS$^{TM}$ digital log database. However, some issues require careful consideration in its practical application. First, the data quality in these logs is often suspect when for example the sensor loses contact with the formation rock in rugose boreholes. Specific procedures used to overcome noise and to incorporate uncertainty from such data were implemented and described in detail in SA. Second, the $\rho(z)$ logs are often only collected over intervals immediately surrounding the zone of economic interest. Measured densities in the topmost 500 m are rare. In order to overcome these restrictions, a 3D density model was constructed by kriging over constant elevations. These calculations were implemented with the adaptation of mGstat [*Hansen*, 2004], a Matlab$^{TM}$ wrapper for the geostatistical modelling program Gstat (Pebesma and Wesseling, 1998), and variogramfit by *Schwanghard* [2010] with details provided in SA.

Another issue in the development of a model for SV is that the surface topography varies across the study area. It is well known that topography perturbs both the stress directions and magnitudes [*McTigue and Mei*, 1981; *Miller and Dunne*, 1996; *Savage and Swolfs*, 1986; *Schmitt and Li*, 1993], particularly near the surface. We adapted the 3D Green's function methods (GFM) developed by *Liu and Zoback* [1992] who needed to account for severe topographic expression near the Cajon Pass scientific drilling project.

Briefly, we separate the crust volume within the study area into a lower elastic halfspace overlain by a layer whose topmost surface matches the topography. The method uses as Green's functions the solutions to the Boussinesq and Cerruti problems that, respectively, give the stress states induced by applying a vertical or a horizontal point load onto the surface of an elastic halfspace. The topographic load stresses are then given as a convolution of these Green's functions with the topographic loads expected at the top of the halfspace. The vertical and horizontal loads applied to the halfspace are determined from the densities and thicknesses of the upper section.

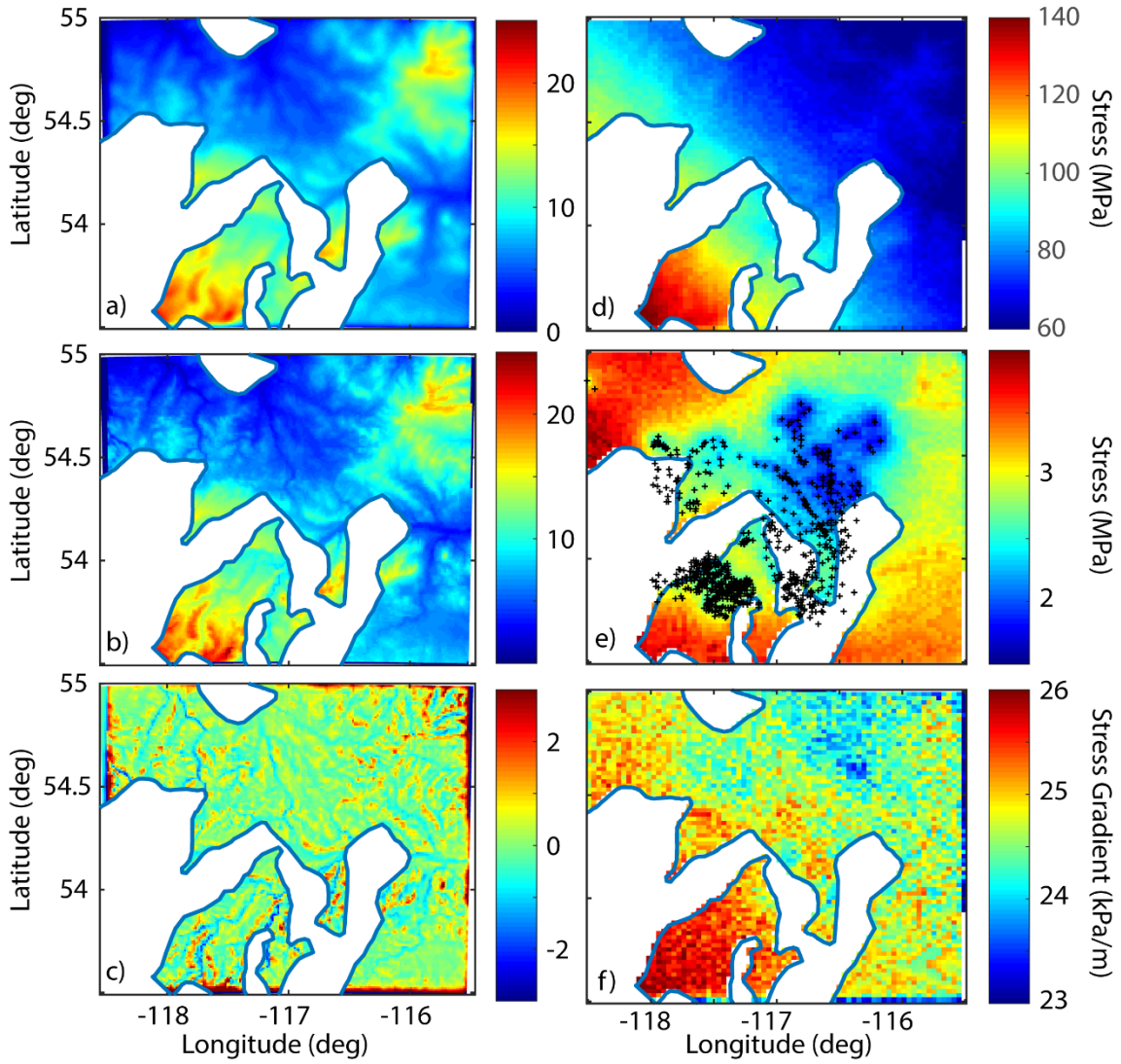


**Figure 4.6.** a) The lithostatic pressures of the upper section of the model. b) The topographic impact on the $S_V$ at the tops of the Duvernay Formation evaluated through the GFM. c) The difference between the topographic impact and lithostatic pressures of the upper section of the model. d) The vertical stress $S_V$ mapped into the middle depth point of the Duvernay Formation from the elevation corrected model and e) its corresponding uncertainty. The black crosses represent the wellbores with density logs. f) The stress to depth ratio for $S_V$.

An elevation $h$ = 558 m that is ~20 meters below the lowest surface elevation over the study area separates the upper section and lower halfspace. The summation of the topographic

impact from the upper section and the lithostatic pressures of the lower halfspace is an approximation of the actual $S_V$ [*Liu and Zoback*, 1992]. To overcome the limits of the sparse density logging information at shallow depth, we gathered the boreholes with density logs with elevation 100 meters below the top of lower halfspace (elevation > 458m). The average densities of these boreholes are then adapted to make the 2D near surface topography density map through kriging. The lithostatic pressures of the lower halfspace are calculated using the 3D density volume.

Fig. 4.6a shows the topographic impact component of the $S_V$ at the tops of the Duvernay Formation with a comparison to the lithostatic pressures (Fig. 4.6b) and a noticeable difference is observed (Fig. 4.6c) The GFM suppresses the short-wavelength topographical features while the influence of the long-wavelength, regional topographical variations remain at the depth of the Duvernay Formation. Evaluating the $S_V$ only considering the densities of rocks can result in an error of up to 1.5 MPa at the depth of the Duvernay Formation, at vicinities where topography varies rapidly. Gaps in the boundaries of the figure are the artifacts caused by the conversion of the input graticular coordinates to a Cartesian coordinate for faster calculation of distances.

We project the final modelled $S_V$ magnitude (Fig. 4.6d) and its uncertainty as determined through the propagation of errors (Fig. 4.6e) onto the tops of the Duvernay Formation. The uncertainties for $S_V$ range from 2 MPa to 5 MPa and primarily reflect the local concentration of available density log data (see Fig. 4.6e). The secant gradient of $S_V$ (Figure 4.6f), which is merely the ratio of the calculated value of $S_V$ to the depth used widely in industry to allow for simple estimation of stress, is roughly 24-26 kPa/m.

### *4.2.3 Minimum Horizontal Compression $S_h$*

We interpreted 30 selected well pressure tests, variously referred to as micro-frac, mini-frac, or in this case, Diagnostic Fracture Injection Tests (DFITs) in order to provide estimates of $S_h$ magnitudes with the details of the methods employed provided in SA and the results in SB. All of the measurements analyzed for this paper were carried out within the Duvernay Formation, but we also include in the supplementary material some earlier values from the overlying Cretaceous section provided by *Woodland and Bell* [1989]. Briefly, the raw data used is from time series of the wellbore pressure $P_w(t)$ measured during testing. A series of repeated pressurizations and fracture re-openings with controlled pressure declines are preferred for stress measurement [*Bell et al*., 1994; *Schmitt and Haimson*, 2016], but standard industry practice employs only one single pressurization and decline cycle in tests that can run for many days in the low permeability formations. Typically, an interval of the borehole is sealed using packers. This interval is then rapidly pressurized until $P_w(t)$ drops indicating the creation of a fracture in the formation. Pumping to the formation may continue in order to extend the fracture into the formation further. This fracture is presumed to grow in the direction of $S_H$ and perpendicular to the minimum horizontal compression. When deemed appropriate by the operator pumping ceases and the interval is 'shut-in' allowing $P_w(t)$ to evolve as fluid diffuses from the induced fracture that is assumed to still be open into the formation. $P_w(t)$ eventually decays to the $S_h$ magnitude at which point the fracture closes and the $P_w(t)$ decline behaviour changes. Hence, finding this fracture closure pressure $P_{fc}$ at this point of departure allows $S_h$ to be estimated.

Four different approaches, described in detail in SA, were used on each available $P_w(t)$ record providing a range of values allowing a level of uncertainty to be assessed. Due to the lack

of information we have not considered instrumental error as being important as typical errors for pressure gauges used in such studies are small relative to the pressures observed, and further, this information is not generally provided in the records available to us. More serious deviations could come from the fact that pressures within the 'closed' interval may, in many instances, be measured at the surface and as such the values reported at depth here may be corrected for hydrostatic head differences that are sensitive to the pressure and temperature variations of the borehole fluid. We further assume that the TVD values provided are correct. In a small number of cases only already interpreted values of $P_{fc}$ were available as $P_w(t)$ was not provided by the operator; these are arbitrarily assigned a higher uncertainty of 5% as we were unable to assess the original quality of the data.

When plotted with respect to depth, irrespective of spatial location, the $S_h$ magnitudes generally increase (Figure 4.8a) although with some scatter may reflect the heterogeneity of the stress field. Linear regression of the $S_h$ - $z$ depth relation gives directly

$$S_h(z) = 32.1(\pm 3.1)\ \frac{kPa}{m} z - 41.8(\pm 10.2)\ MPa \tag{4.3}$$

to 95% confidence.

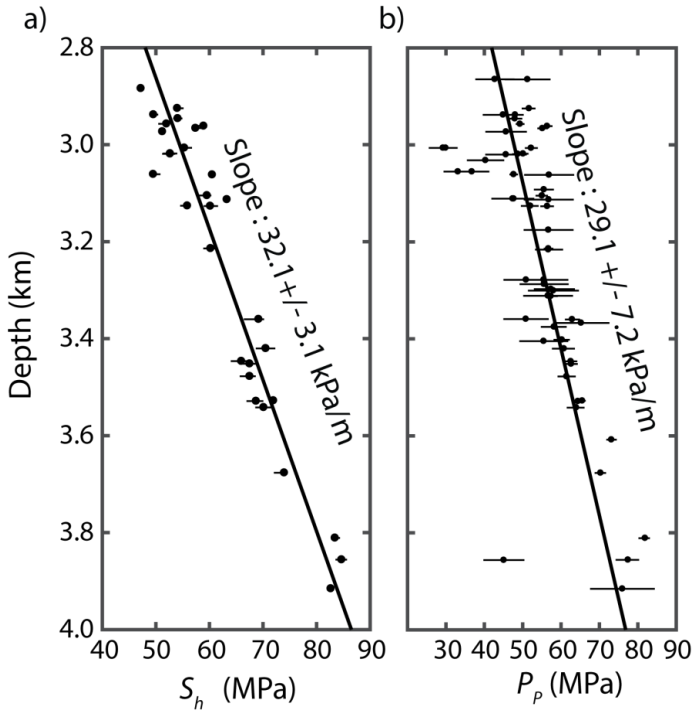


**Figure 4.7.** Magnitudes of a) $S_h$ and b) $P_p$ versus depth with error bars representing uncertainties. Black lines show the best linear fit for each case.

The regression analysis above provides some capacity for $S_h$ prediction, but it cannot include any spatial variations in the stress field. We account for such variability in a second model for $S_h$ established by kriging of the available measurements. In order to do this, before interpolation, we first removed the depth-dependent trend by shifting the observed $S_h$ to the same depth using the tangent gradient $\Delta S_h/\Delta z$ = 32.1 kPa/m ± 3.1 kPa/m from Eqn. 4.3. These interpolated data were then corrected down to the depth at the top of the Duvernay Formation to provide the spatially varying model $S_h(x,y)$ shown in Figure 4.8a. The spatial model for *Sh* with its associated uncertainty (Fig. 4.8b) is available in the supplementary materials.

The differences between this interpolated model and the more straightforward linear trend of Eqn. 4.3 (Figure 4.8c) show a maximum spatial difference of ~10 MPa from the highest to

lowest values. These differences do not appear random. For example, the modelled values exceed those of the linear trend over an E-W band from about -117° to -116.5° near the center of the study area. We compare the $S_h$ and $S_V$ by subtracting model $S_v$ (Figure 4.8d) from the corresponding model $S_h$ (see Figure 4.8a). The result (see Figure 4.8d) suggests that the difference between the two decreases with depth.

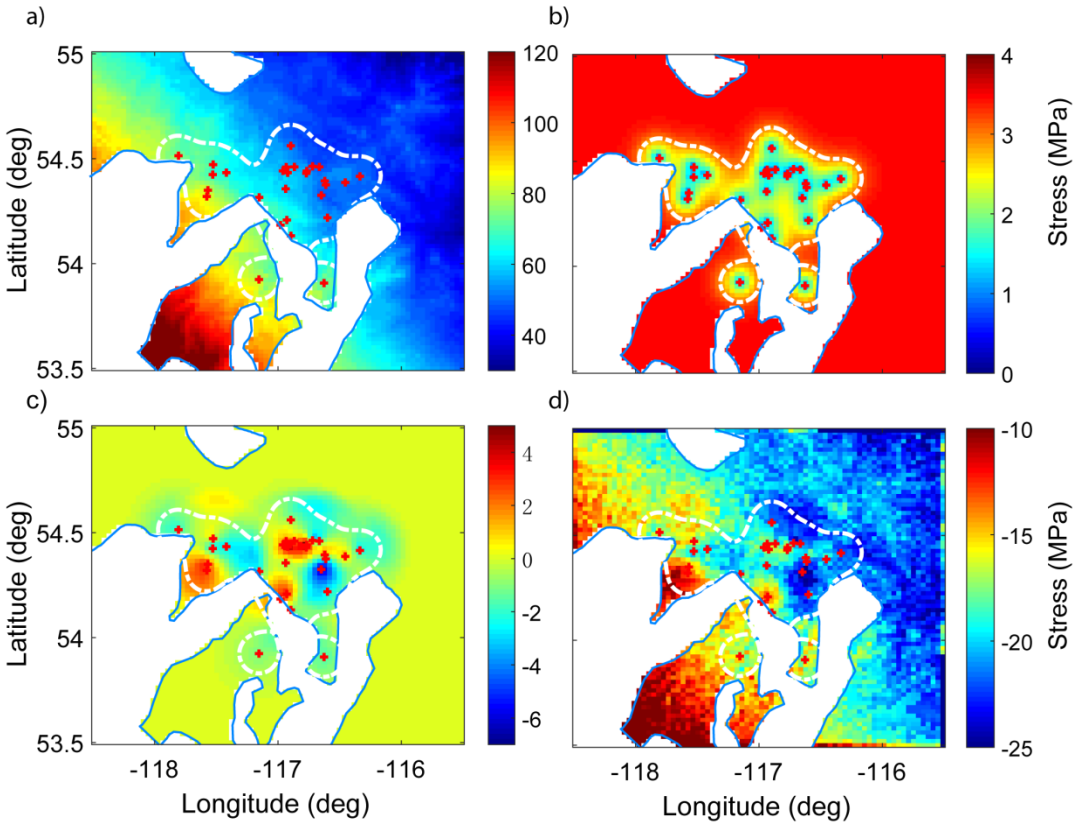


**Figure 4.8.** Projections to the top of the Duvernay Formation of a) the modelled $S_h$ value. b) The uncertainty of the modelled $S_h$. c) the spatial perturbation of $S_h$ calculated by subtracting the modelled $S_h$ value with the linear trend of Eqn. 4.3. d) The difference between $S_h$ and $S_V$. In all panels the white dashed line represents the contour with an uncertainty of 3 MPa. Empty spaces indicate the engulfed Leduc reefs. Red crosses show the locations of the $S_h$ observations.

### *4.2.4 Formation Pore Pressure $P_P$*

We also include 57 measurements of fluid pressure as indicated by various techniques including i) asymptotic extrapolations of the decline in $P_w(t)$ after fracture closure in the tests just described, ii) static pressure gauge tests, and iii) flow/build up tests (see SA for additional details). We note that these are values that are obtained usually within a section of the cased but perforated borehole after relatively long periods (sometimes days) once the cased well has been opened. They represent the equilibrium pressure or its estimate measured within the borehole that is presumed to indicate a uniform virgin pore fluid pressure within the rock mass.

Regression of these observed $P_P$ with depth (Figure 4.7b) gives a trend

$$P_P(z) = 29.1(\pm 7.2)\frac{kPa}{m}z - 39.6(\pm 23.4)\ MPa \tag{4.4}$$

with a tangent slope $\Delta P_P/\Delta z$ = 29.1 kPa/m ± 7.2 kPa/m. Using the same methodology as applied in the development of the $S_h(x,y)$ map above, a spatially interpolated map of $P_P$ was calculated by kriging (Figure 4.9a) with these interpolated values provided in the supplementary material. Despite having a larger number of measurement points, the uncertainty in $P_P$ (Figure 4.9b) is nearly double that of $S_h$. Such uncertainty primarily arises from the errors inherent in attempting to extend the slowly dissipating $P_w(t)$ to infinite time, and the greater uncertainties assessed the static values.

The observed and modelled $P_P$ significantly exceeds what is expected for a normal hydrostatic gradient, assuming a groundwater specific weight of 9.8 kN/m$^3$ (Figure 4.9d). However, there appear to be coherent zones where the modelled $P_P$ is significantly diminished relative to the trend of Eqn. 4.4 (Figure 4.9c) that may be related to the contacts at the Duvernay Formation and the Leduc reefs.

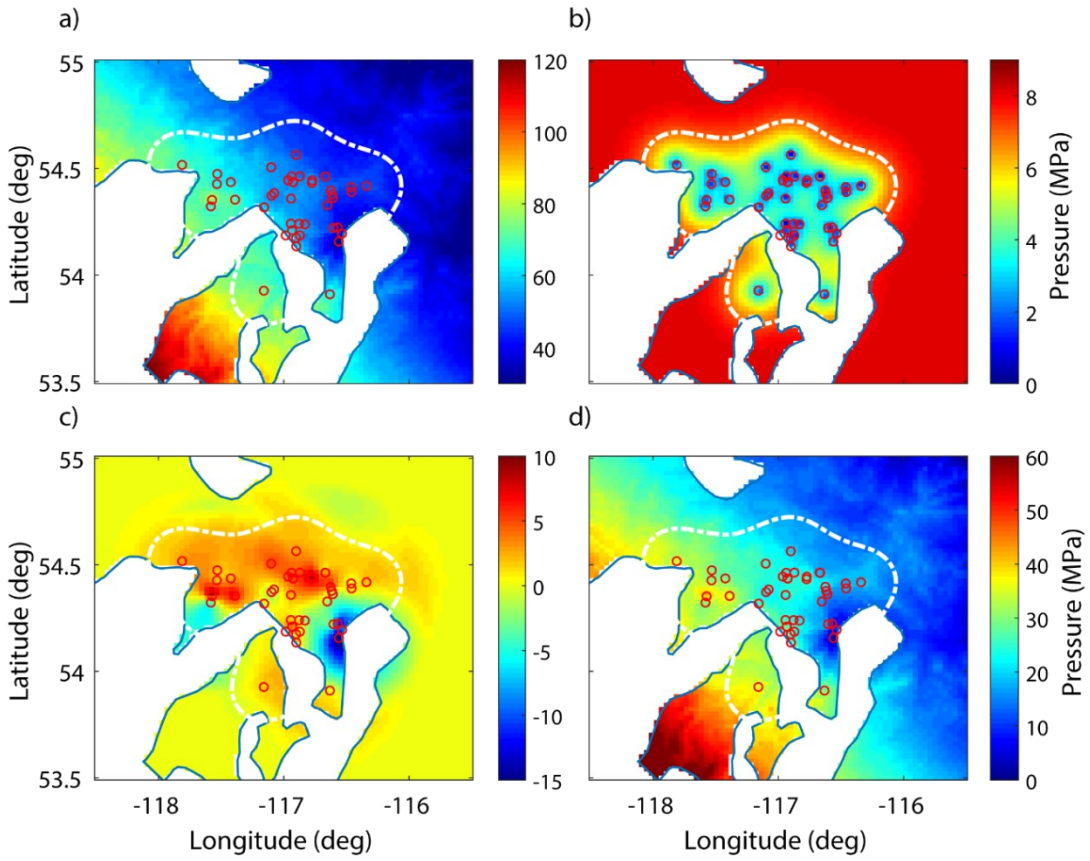


**Figure 4.9.** 3D projections to the top of the Duvernay Formation of a) the modelled $P_P$ value. b) The uncertainty of the modelled $P_P$. c) The spatial perturbation of $P_P$ calculated by subtracting the modelled $P_P$ value with the linear trend of Eqn. 4.4. d) The difference between $P_P$ and hydrostatic fluid pressures. In all panels, the white dashed line represents the contour with an uncertainty of 7 MPa. Empty spaces indicate the engulfed Leduc Reefs. Red circles show the locations of the $P_P$ observations.

### *4.2.5 Greatest Horizontal Compression $S_H$*

Unlike $S_h$, the determination of the magnitudes of $S_H$ remains challenging as the direct measurement from deep boreholes is technically difficult and cost prohibitive. In SA, assessment of $S_H$ is provided using the formulation had been previously applied for the KTB borehole [*Barton et al.*, 1988], assuming the negligible difference between the formation $P_P$ and drilling fluid

pressures. However, such calculated $S_H$ values are subject to significant uncertainties as results of the mostly unknown input $P_p$, $S_h$ and rock strength at the depths of the observed BO, which are often more than one-thousand meters shallower than the depths of the Duvernay Formation. We did initially attempt to directly constrain the $S_H$ magnitudes exploiting observed DITF and BO widths from the segments of image logs from the Duvernay Formation. However, unacceptably high uncertainties primarily due to the high values of $P_p$ led us to abandon this approach.

Alternatively, the $S_H$ magnitudes were constrained by the inversion of the induced earthquakes focal mechanisms in a manner similar to that employed recently by *Terakawa and Hauksson* [2018]. The methodologies for stress inversion are well developed [Gephart, 1990; Jones, 1988; Kastrup et al., 2004; Montone et al., 2004], with a brief synoposis included in the appendix. This method provides a single measure of the principal stress magnitudes $\sigma_1 \geq \sigma_2 \geq \sigma_3$ via a shape factor $R$:

$$R = \frac{\sigma_1 - \sigma_2}{\sigma_1 - \sigma_3} \tag{4.5}$$

Notably, one disadvantage of such approaches is that they presume the uniformity of the regional stress field throughout the volume of crust studied regardless of position, depth, or lithology. As such, the ability to obtain an independent measure of a local stress magnitude directly, as might be hoped for from a borehole, is sacrificed. However, stress field homogeneity may be a reasonable assumption given the consistency in $\phi$ and the behaviour of $S_h$ with depth (see Eqn. 4.3).

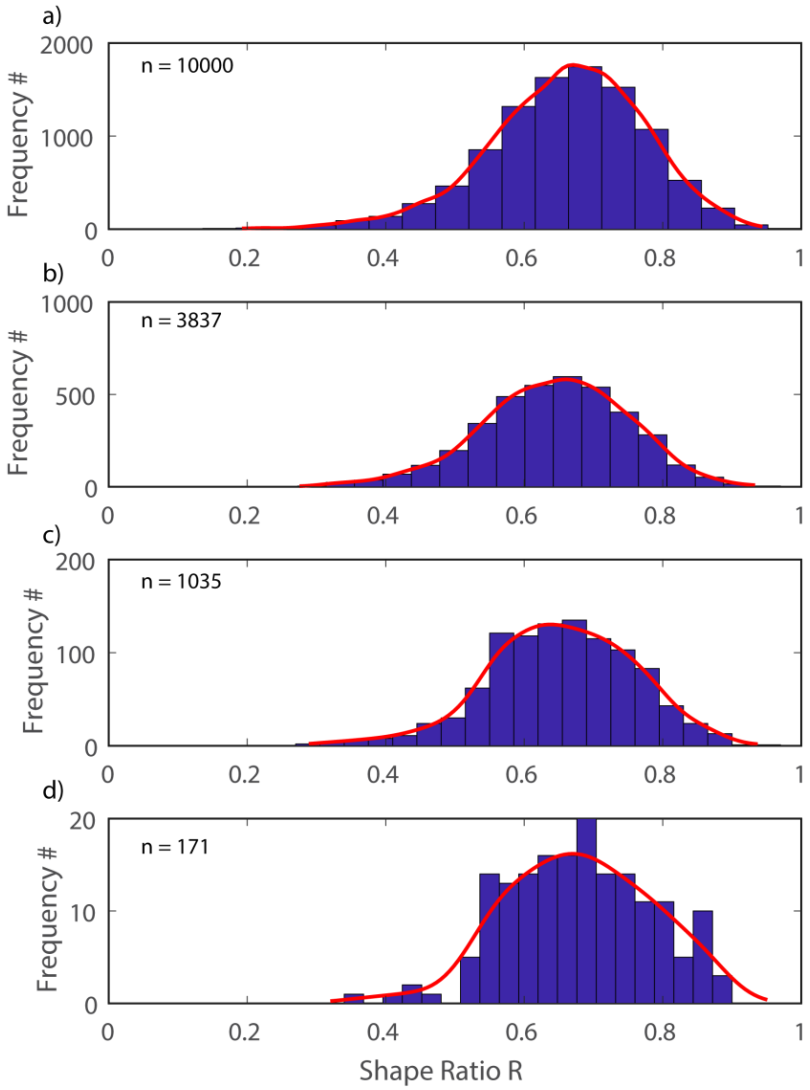


**Figure 4.10.** histogram of the shape-ratio R from stress inversion with red line represents the nonparametric kernel-smoothing distribution fit [*Bowman and Azzalini*, 1997] that include a) all inversion results regardless of the $\sigma_2$ dip; or only those results with $\sigma_2$ dip angles b) greater than 80° c) greater than 85°; d) greater than 88°

The ambiguity between the fault and the auxiliary plane is problematic when focal mechanisms are used. Following the Mohr-Coloumb frictional faulting criteria (Eqn. 4.1), *Lund and Slunga* [1999] sought the correct plane by testing which was the least stable and hence

expected to slip. *Vavryčuk* [2014] iteratively applied this criterion to *Michael*'s [1984] inversion; this necessitates a range of values of $\mu$ to be input in addition to the slip and fault plane estimates provided from the suite of observed focal mechanisms. In this study, we used the *Vavryčuk*'s [2014] stress inversion program in which the focal mechanism strikes, rakes, and dips (see supplementary material) for the ensemble of earthquakes (see Figure 4.1b) are used, to both provide an *R* value and to better determine which nodal planes best represent the faults. A broad range of $0.2 \leq \mu \leq 1.2$ for friction is used given there are no laboratory constraints on rock friction. Mean random errors of 10° were assigned to the input values for the $\boldsymbol{n_k}$ taken from the focal mechanisms.

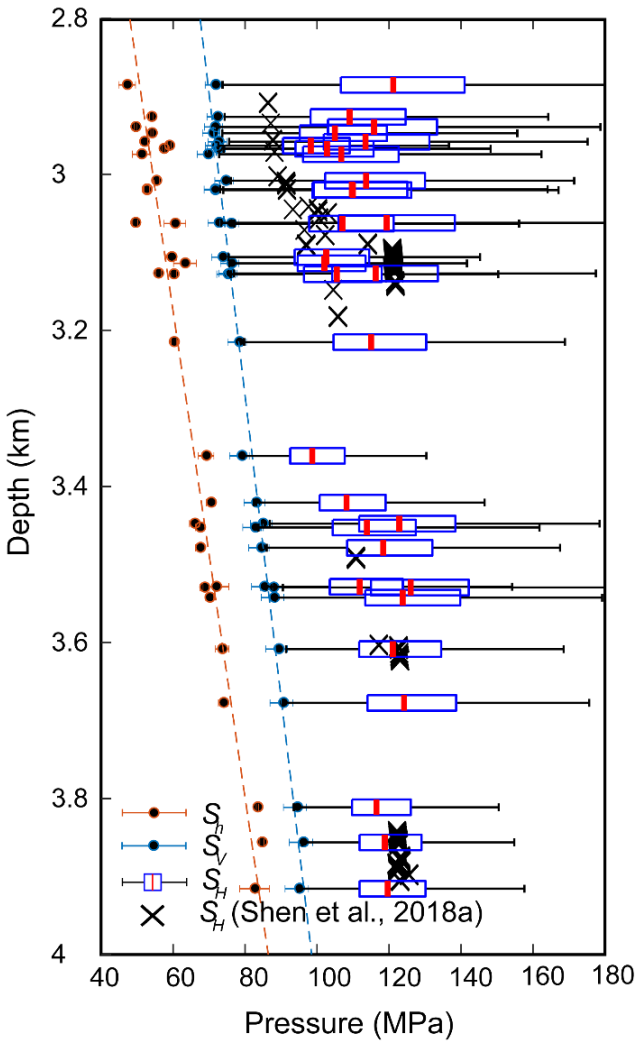


**Figure 4.11.** $S_h$ measurements and calculated $S_H$ from SB with $S_V$ and $S_H$ modelled in this study at the location of the $S_h$ measurements. The Whisker-Box plot of $S_H$ denotes the range of possible values of $S_H$. The blue boxes confine 25th and 75th percentile of the CDF of $S_H$, and red dashes present the most probable value of $S_H$. Whiskers represent the minimum and maximum values of $S_H$. Black crosses represent the magnitudes of $S_H$ initially estimated by SA.

Ten-thousand realizations with these differing parameters were inverted from the 11 earthquake focal mechanism solutions (see Figure 4.1b) producing a distribution of $R$ values (Figure 4.10a). The Probability Density Function (PDF) fit to this distribution using nonparametric

kernel-smoothing distribution fit indicates the most probable value for $R$ is 0.67 with 90% probability of falling in the range $0.46 < R < 0.84$.

The statistical distribution of $R$ is further utilized to calculate the probability distribution of $S_H$ through a Monte-Carlo simulation using 5000 realizations assuming that $S_h$ and $S_V$ are coaxial to $\sigma_3$ *and* $\sigma_2$ respectively, in accordance with the strike-slip focal mechanisms. More discussion on the justification of such assumption is provided in section 3.3. We account for the uncertainties of $S_h$ ($\sigma_3$) and $S_V$ ($\sigma_2$) by assuming a uniform distribution of random noise based on their assessed observational uncertainties (see section 4.2.2 and 4.2.3). Figure 4.11 shows the constrained $S_H$ values and probability distributions at the locations of each $S_h$ observation with the statistical distribution of $R$ shown in Figure 4.10a.

## 4.3 Discussion

### *4.3.1 $S_H$ Directions*

The map for the $S_H$ direction (see Figure 4.5a) shows that $\phi$ is reasonably uniform across the study area and consistent with the earlier studies indicating the general NE-SW compression that appears to persist within the Western Canada Sedimentary Basin [*Bell and Gough*, 1979; *Reiter et al*., 2014]. The N43°E average $\phi$ determined here is close to the ~N45°E found using a broader search area with a radius of ~500 – 1000 km [*Reiter et al*., 2014]. Stress inversion performed on the focal mechanism solutions of the earthquakes within the region (see Figure 4.2) yields a most probable $\phi$ of ~N55° E (Figure 4.12) with a probability distribution varying from N40° E – N60° E, slightly higher than our predicted $\phi$ , using solely borehole observations, at the locations of the earthquakes between N39°E to N45°E (see Figure 4.5a and Figure 4.12). Irregular

geological features, in particular, the Leduc reefs hypothesized to have nucleated along faults, do not appear to perturb the stress directions. Moreover, we do not observe stress rotation at vicinities near the epicentres of the reported earthquakes.

The predominantly strike-slip focal mechanisms observed for the Fox Creek earthquakes [*Bao and Eaton*, 2016; *Schultz et al*., 2017; *Wang et al*., 2016; *Zhang et al*., 2016] are consistent with fault slip on vertical planes that strike early N-S. $S_H$, with $\phi$ ~39-45° at the regions of near the epicentres of these earthquakes, acts to the inferred fault plane that in turn leads to a frictional angle $\psi = 14 - 52°$. These friction angles correspond to reasonable estimates for the coefficient of friction $\mu \sim 0.3$ or higher. If the regional average (~43°) or the longer-wavelength modelling result (~45°) are to be used [*Reiter et al*., 2014], the frictional angles are subsequently decreased to $\psi \sim 0 - 7°$ with correspondingly very low coefficient of frictions < 0.1. Though, care must be taken with this simplified analysis as it does not fully account for the possible combinations of fluid pressures and stresses resolved onto the fault plane. A more complete analysis is currently underway.

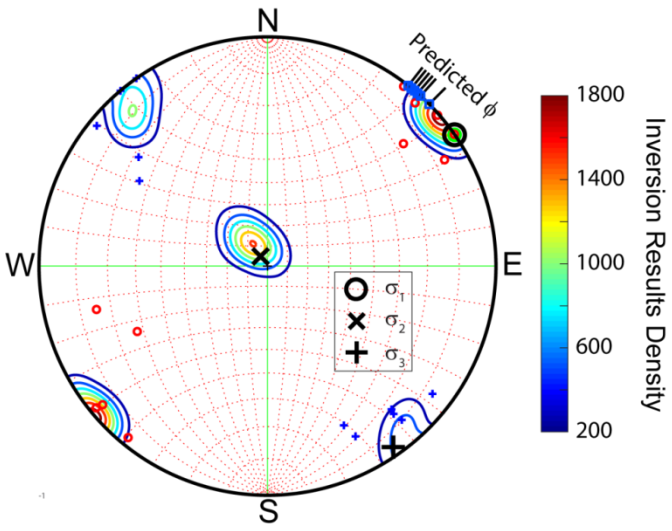


**Figure 4.12.** Axes of $\sigma_1, \sigma_2, \sigma_3$ from the recorded earthquake's focal mechanism solutions and stress inversion. Contours represent densities of $\sigma_1, \sigma_2, \sigma_3$ solutions from stress inversion. Red circles and small blue crosses represent the P/T axes from the input focal mechanism solutions. Black symbols show the most probable orientation of the in-situ stress by stress inversion. Blue squares and lines indicate the orientations of $S_H$ predicted from the stress model at each of the earthquake's epicentral locations shown in Figure 4.5

### *4.3.2 $P_P$ and $S_h$ Gradients*

The observed $P_P$ all substantially exceed those anticipated from a normal hydrostatic (water) gradient of ~9.8 kPa/m that assumes continuous hydraulic conductivity from depth to the surface; and, indeed, even exceed the expected wellbore fluid pressure $P_w$ with gradients bounded below ~14 kPa/m due to high mud densities reported. Using our data, the 'secant' $P_P$ gradient that is usually given in standard industry practice as the simple ratio of pore pressure to depth ranges from 12.3 kPa/m to 20.3 kPa/m. This mostly agree with the simpler secant gradients to the Duvernay Formation in the areas recently published [*Eaton and Schultz*, 2018; *Lyster et al*., 2017] and to values ranging 16 kPa/m to 22 kPa/m more globally from other researchers [*Bell and Grasby*, 2012; *Haug and Bell*, 2016; *White and Foxall*, 2016; *Yerkes et al*., 1990].

However, these simple secant $P_P$ gradients underestimate the much higher local 'tangent' gradient $\Delta P_P/\Delta z$ ranging between 28.8 kPa/m ± 3.9 kPa/m determined from the linear regression with the depth of the $P_P$ observed within the Duvernay Formation within the study area as indicated by Eqn. 4.4. This is particularly worth noting as it exceeds the tangent gradient of ~26 kPa/m expected for lithostatic gravitational load $S_V$ within the Paleozoic section. The corresponding $S_h$ secant gradients range from 16.1 kPa to 21.9 kPa that, similarly, is significantly less than the tangent $S_h$ gradient $\Delta S_h/\Delta z$ = 32.4 kPa/m ± 4.2 kPa/m (Eqn. 4.3). Before this study, workers [*McGarr*, 1988] have argued that lithostatic pressure provides an appropriate reference stress state [*Zang and Stephansson*, 2010]; and consequently, the higher rate of increase of the pore pressure over the vertical stress observed here is unexpected [*Swarbrick and Osborne*, 1998]. The approach of $P_P \rightarrow S_h$, too, may be meaningful and may suggest a linkage between pore pressures and tectonic loading. Conversely, within the shallower overlying Cretaceous formations, the $P_P/S_h$ ratio is significantly lower *Woodland and Bell* [1989] although these values may have been compromised by earlier hydrocarbon production [*Bell et al*., 1994].

### *4.3.3 Validity of Stress Inversion and Andersonian Assumption*

We constrain the magnitudes of $S_H$ through stress inversion on the focal mechanism solutions of the earthquakes recorded within our study area and near the depth of the Duvernay Formation. The stress inversion using multiple earthquakes' focal mechanism solutions fundamentally relies on two assumptions affecting its validity: 1. the slip direction and the shear traction on the faulting plane are parallel; and 2. The stress field in the rock mass encompassing these epicentral locations is uniform [*Pollard et al*., 1993]. Assumption #1, alternatively known

as the Wallace-Bott hypothesis [*Bott*, 1959; *Wallace*, 1951], is generally accepted for mid-upper crustal earthquakes [*Célérier et al*., 2012].

The validity of assumption #2 is often questioned [*Faulkner et al*., 2006; *Pollard and Segall*, 1987; *Zoback et al*., 1989] and it is critical to determine whether it can reasonably apply here particularly given that we do see variations in the stress field. Some researchers have attempted to overcome stress field heterogeneities by dividing their regions into subzones with similar focal mechanisms over which the stress field is assumed consistent [*Hardebeck and Michael*, 2006; *Hicks et al*., 2000; *Kastrup et al*., 2004; *Levandowski et al*., 2018]. The subzones in these studies are usually much larger than our current study area, and although we observe noticeable spatial variations of the stress field, there is no evidence for stress concentration or rotation near the epicentres of the observed earthquakes. Further, the focal mechanisms used in the stress inversions also appear to be reasonably uniform. Few earthquakes were reported in our study area before the recently induced seismicity [*Atkinson et al*., 2016; *Schultz et al*., 2017] and this too might suggest that more localized stress concentrations along and at the ends of slip zones are not complicating the stress field. Finally, the good agreement between the stress orientations determined from the borehole image logs with those arising from the inversion further suggests a uniformity of at least the stress directions.

The stress inversion itself cannot provide quantitative stress magnitudes directly. Values of the two principal components must be known in order to calculate the magnitudes of the remaining one. So far, we developed our stress model under the assumption of an Andersonian stress regime in which $S_H$, $S_V$, $S_h$ are equal to $\sigma_1$, $\sigma_2$, $\sigma_3$ respectively. It is questionable whether such an assumption is valid as the stress orientation revealed by stress inversion shows, small but

noticeable, deviation from vertical and horizontal axes (see Figure 4.12). To test the sensitivity of our $R$ to the deviation of the stress tensor, we plotted the histograms of $R$ from all randomly simulated results (see Figure 4.10a), along with $R$ corresponding to stress tensor with $\sigma_2$ deviated 10° (Figure 4.10b), 5° (Figure 4.10c) and 2° (Figure 4.10d) from vertical. The fitted PDFs for each of the plotted histograms are stochastically identical, suggesting that our assessed $R$ is not impacted.

Also, the most probable stress orientation revealed by the stress inversion, honouring the requirement that stress axes are orthogonal to each other, remains nearly Andersonian with a deviation of $\sigma_2$ from vertical of less than 5°. Additionally, the 'uncertainty' of $R$, assessed through stress inversion, reflects the spatial variation of states of crustal stress on top of the mathematical errors. Very generous uncertainties (10° for each component) are given for the input focal mechanisms to account for errors in seismological recordings resulting conservative assessment on the range of $R$ and possibly contribute to the deviation of stress axes. Thus, we conclude with confidence that our assumption of Andersonian stress regime and the subsequently constrained ranges of $S_H$, assuming that $S_h$ and $S_V$ are parallel to $\sigma_3$ and $\sigma_2$, are valid.

It is also worth noting that, though drawbacks of $S_H$ assessed through borehole failures (see section 2.4.2.5) results in rather large uncertainties, the ranges of $S_H$ constrained in this study is consistent with the values from SA calculated with borehole observations. However, without detailed rock mechanics and hydrogeological knowledge for the formations where the BOs are observed in SA, we cannot say if such an agreement is a coincidence.

Because of the uniformity to the stress field imposed by the inversion, the depth and spatial variation $S_H$ assessed through this approach is only a reflection of the varying $S_V$ and $S_h$. We cannot

produce a spatial map or vertical profile of $R$ or subsequently $S_H$**,** given the uncertainties of on the depths and focal mechanism solutions of the earthquakes mixed up with spatial variation.

### *4.3.4 3D Stress Model*

The primary purpose of this study is to develop a model that allows for the states of in-situ stress within and near the Duvernay Formation to be quantitatively estimated. For a given input location (in terms of latitude and longitude) and depth, the Matlab™ program, 3D_stress_duvernay, provides the Andersonian stress magnitudes [$S_H$, $S_V$, $S_h$], the pore pressure $P_p$, and the stress orientation $\phi$ with conservative estimates of uncertainty. The model incorporates the 2D interpolated values $\phi$, $S_V$, $S_h$ and $P_P$ of the data used to make the maps shown respectively in Figs. 4.5, 4.6, 4.8 and 4.9 as well as the datum depth at the tops of the Duvernay Formation (see Fig. 4.2). These values are laterally refined by cubic spline interpolation based on the latitude and longitude of the point of interest. We assume that $\phi$ remains unchanged with depth. The datum depth values for $S_h$ and $P_P$ are corrected to the depth of interest using the tangent slopes of Eqns. 4.4 and 4.5 accounting for the uncertainties. A similar method is used to estimate $S_V$ with conservative tangent lithostatic gradients (23.5 kPa/m – 27.4 kPa/m) based on rock densities from 2400 kg/m$^3$ to 2800 kg/m$^3$. A distribution for $S_H$ is then determined using a number of random Monte-Carlo simulations, with updated values of $S_h$ and $S_V$, through the probability distribution function for $R$ (see Fig. 4.10a).

One issue with the current model is that all of the $S_h$ and $P_P$ measurements obtained originated from well testing solely within the Duvernay Formation; and our prediction of states of stress nearby relies upon their linear extrapolation from that depth. Stress relaxation, often caused by faulting [*Hergert et al*., 2015; *Vernik and Zoback*, 1992] or time-dependent viscous deformation

[*Sone and Zoback*, 2014], could perturb the stress field with time resulting in lower than expected horizontal stress magnitudes [*Plumb et al*., 1991]. *Sone and Zoback* [2013] reported a series of laboratory experiments describing the viscous deformation of shale and suggested considerate stress relaxation over the geological time. That being said, opposed to the samples tested in their reported work, the Duvernay shale generally consists of low clay averaging at 26% [*Hammermaster et al*., 2012]. Such mineral composition generally results in less creep potential [*Sone and Zoback*, 2013]. Ultrasonic and static strain anisotropy measurements show high stiffness in the direction parallel to layering that is similar to a pore-free quartzite [*Ong et al*., 2016]. As such we do not expect significant stress relaxation within it.

There is no data, to our knowledge, regarding time-dependent behaviour of the surrounding formations. However, we argue that this local extrapolation still adequately predicts the states of stress within a reasonable depth range of about ±200m from the Duvernay Formation). Figure 4.13 shows that the linear depth relationship established with $S_h$ measurements exclusively obtained from the Duvernay Formation remains valid when compared with measurements obtained from overlaying formations across the Alberta basin. The gradients of the $S_h$ from these two data sets become smaller at the depth shallower than 2.5 km probably because these shallower measurements are primarily within the lower density Cenozoic siliclastics. However, the gradients and linearity trend of the *Haug and Bell* [2016] data below 2.5 km depth is consistent with the present Duvernay Formation measurements. Combined regression of the current data with that below 2.5 km from *Haug and Bell* [2016] gives a tangent slope of 31.5 kPa/m ± 2.5 kPa/m, close to the gradient of 32.1 kPa/m ± 3.8 kPa from Eqn. 4.3, which was calculated using exclusively SB data. For context, the shallowest measurement from SB is measured at a depth of 2.9 km. Accounting the uncertainties associated with the *Haug and Bell* [2016] measurements, we are

confident the linear relationship described by Eqn. 4.3is applicable to the depths reasonably close to the Duvernay Formation.

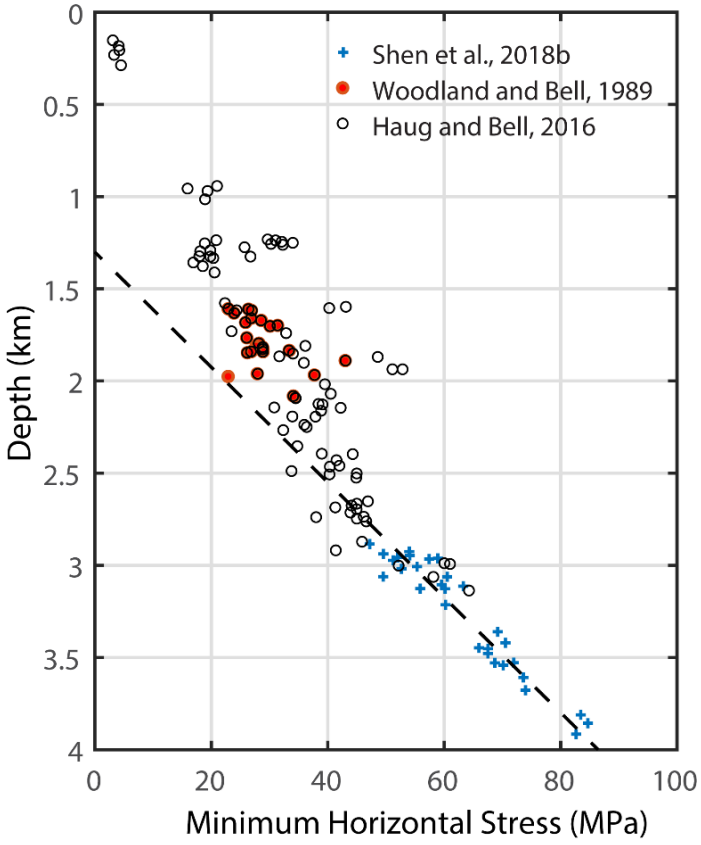


**Figure 4.13.** $S_h$ measurements reported in *Woodland and Bell* [1989], *Haug and Bell* [2016] and SB. The dashed line represents the linear regression results on SB data (see Eqn. 4.3)

## 4.4 Conclusion

We developed a model to predict the full set of stress components describing the Cauchy stress tensors for the states of in-situ stress within the Duvernay Formation, in a locale subject to a number of earthquakes induced by hydraulic fracturing operations. This type of model is only

possible because of the density of direct stress measurements from hydrocarbon development boreholes in the study area and to our knowledge, unique.

Transient well testing results provided measurements on the $S_h$ and $P_p$ allowed us to extrapolate for crustal volumes nearby. The large quantity of density logs from oil/gas operations facilitated our efforts of establishing a 3D density model and allowed the calculation of $S_V$. We performed stress inversion on 11 well resolved focal mechanisms from earthquakes recorded in the center of our study region. The stress inversion results supported the assumed Andersonian stress regime and enabled estimation of $S_H$.

The compiled stress measurements further enabled a predictive model allowing assessment of states of stress within our study area, at depths reasonably close to the Duvernay Formation. Full set of the components describing the Cauchy tensor of the in-situ stress can be obtained, through the provided program 3D_stress_duvernay, for the given location and depth within our study area. Such a model is useful for analyzing the source mechanism of the recent nearby earthquakes. As we recognize that the model is imperfect, we further attempt to include estimates of uncertainty. The heterogeneity of the stress gradient and $S_H$, though not directly accounted in our model, is captured within our uncertainty ranges.

## 4.5 Appendix

*Synoposis for inversion of earthquake's focal mechnism solutions for constraints on $S_H$*

The ensemble of faults with different known orientations used in the inversion are all presumed to be subject to a uniform stress field $\sigma_{ij}$. A traction vector $\boldsymbol{T_k}$ calculated from this stress field acts on each fault plane; and it is resolved into a normal $\boldsymbol{\sigma_k}$ and a shear $\boldsymbol{\tau_k}$ component, with

the direction of the latter described by unit vector $\boldsymbol{N_k} = N_{k1}\boldsymbol{x_1} + N_{k2}\boldsymbol{x_2} + N_{k3}\boldsymbol{x_3}$. *Angelier* [1979] obtained the former from the faults' dips and strikes and the latter from the corresponding slickenslide rakes $\boldsymbol{s_k} = s_{k1}\boldsymbol{x_1} + s_{k2}\boldsymbol{x_2} + s_{k3}\boldsymbol{x_3}$ presuming it and $\boldsymbol{\tau}$ are co-axial [*Bott*, 1959; *Wallace*, 1951]. This same information is obtained from earthquake focal mechanisms, although the ambiguity of the fault and auxiliary planes must be considered. *Michael* [1984] further made the problem tractable by 1) by assuming that $|\boldsymbol{\tau_k}|$ takes the same value on each fault in the ensemble; 2) by normalizing $|\boldsymbol{\tau_k}| = 1$, and; 3) by considering only the deviatoric part of the stress tensor $\hat{\sigma}_{ij}$. This last assumption necessarily provides an additional useful constraint because $\mathrm{tr}(\hat{\sigma}_{ij}) \equiv 0$ allowing the deviatoric stress tensor to be represented by only five components expressed in a vector $\boldsymbol{t} = [\hat{\sigma}_{11}\ \hat{\sigma}_{12}\ \hat{\sigma}_{13}\ \hat{\sigma}_{22}\ \hat{\sigma}_{23}]^T$. Taken together with $\boldsymbol{a_k}$ being a $3 \times 5$ matrix comprised of 15 $\boldsymbol{n_k}$ dependent elements Michael (1984) stacked these for the ensemble of $m$ faults

$$\begin{bmatrix} \boldsymbol{s}_1 \\ \boldsymbol{s}_2 \\ \vdots \\ \boldsymbol{s}_m \end{bmatrix} = \boldsymbol{S} = \begin{bmatrix} \boldsymbol{a}_1 \\ \boldsymbol{a}_2 \\ \vdots \\ \boldsymbol{a}_m \end{bmatrix} \boldsymbol{t} = \boldsymbol{A}\boldsymbol{t} \tag{4.6}$$

that may then be solved inversely to find $\boldsymbol{t}$. The resulting normalized deviatoric stress components in $\boldsymbol{t}$ cannot reveal the actual stress magnitudes but do yield both the stress tensor's orientation and R value.

## References

Aadnoy, B.S., 1990. In-situ stress directions from borehole fracture traces. Journal of Petroleum Science and Engineering 4, 143-153.

Aadnoy, B.S., Bell, J.S., 1998. Classification of drilling induced fractures and their relationship to in situ stress directions. The Log Analyst, 27-42.

Adewole, E.O., Healy, D., 2017. Systematic assessment of fault stability in the Northern Niger Delta Basin, Nigeria: Implication for hydrocarbon prospects and increased seismicities. Tectonophysics 699, 227-243.

Anderson, E.M., 1951. The Dynamics of Faulting and Dyke Formation with Applications to Britain, 2nd ed. Oliver and Boyd, London and Edinburgh.

Angelier, J., 1979. Determination of the mean principal directions of stresses for a given fault population. Tectonophysics 56, T17-T26.

Atkinson, G.M., Eaton, D.W., Ghofrani, H., Walker, D., Cheadle, B., Schultz, R., Shcherbakov, R., Tiampo, K., Gu, J., Harrington, R.M., Liu, Y., van der Baan, M., Kao, H., 2016. Hydraulic Fracturing and Seismicity in the Western Canada Sedimentary Basin. Seismological Research Letters 87, 631-647.

Bailey, A.H.E., King, R.C., Holford, S.P., Hand, M., 2016. Incompatible stress regimes from geological and geomechanical datasets: Can they be reconciled? An example from the Carnarvon Basin, Western Australia. Tectonophysics 683, 405-416.

Bao, X.W., Eaton, D.W., 2016. Fault activation by hydraulic fracturing in western Canada. Science 354, 1406-1409.

Barton, C.A., Zoback, M.D., Burns, K.L., 1988. In-situ stress orientation and magnitude at the Fenton Geothermal Site, New Mexico, determined from wellbore breakouts. Geophysical Research Letters 15, 467-470.

Bell, J.S., Bachu, S., 2003. In situ stress magnitude and orientation estimates for Cretaceous coal-bearing strata beneath the plains area of central and southern Alberta. Bulletin of Canadian Petroleum Geology 51, 1-28.

Bell, J.S., Gough, D.I., 1979. Northeast-southwest compressive stress in Alberta evidence from oil wells. Earth and Planetary Science Letters 45, 475-482.

Bell, J.S., Grasby, S.E., 2012. The stress regime of the Western Canadian Sedimentary Basin. Geofluids 12, 150-165.

Bell, J.S., Price, P.R., McLellan, P.J., 1994. Chapter 29 - In-situ stress in the Western Canada Sedimentary Basin, in: Mossop, G.D., Shetsen, I. (Eds.), Geological Atlas of the Western Canada Sedimentary Basin. Canadian Society of Petroleum Geologists and Alberta Research Council,, Edmonton.

Berens, P., 2009. CircStat: a Matlab Toolbox for circular statistics. Journal of Statistical Software 31, 21.

Bott, M.H.P., 1959. The mechanics of oblique slip faulting. Geological Magazine 96, 109-117.

Bowman, A.W., Azzalini, A., 1997. Applied smoothing techniques for data analysis: the kernel approach with S-Plus illustrations. OUP Oxford.

Branscombe, P., MacCormack, K.E., Corlett, H., Hathway, B., Hauck, T.E., Peterson, J.T., 2018. 3D Provincial Geological Framework Model of Alberta, Version 1(dataset, multiple files). Alberta Energy Regulator, Edmonton, Alberta, Canada.

Brudy, M., Zoback, M.D., 1999. Drilling-induced tensile wall-fractures: implications for determination of in-situ stress orientation and magnitude. International Journal of Rock Mechanics and Mining Sciences 36, 191-215.

Cant, D.J., Stockmal, G.S., 1989. The Alberta foreland basin: relationship between stratigraphy and Cordilleran terrane-accretion events. Canadian Journal of Earth Sciences 26, 1964-1975.

Célérier, B., Etchecopar, A., Bergerat, F., Vergely, P., Arthaud, F., Laurent, P., 2012. Inferring stress from faulting: From early concepts to inverse methods. Tectonophysics 581, 206-219.

Chang, C., Lee, J.B., Kang, T.-S., 2010. Interaction between regional stress state and faults: Complementary analysis of borehole in situ stress and earthquake focal mechanism in southeastern Korea. Tectonophysics 485, 164-177.

Chopra, S., Sharma, R.K., Ray, A.K., Nemati, H., Morin, R., Schulte, B., D'Amico, D., 2017. Seismic reservoir characterization of Duvernay shale with quantitative interpretation and induced seismicity considerations—A case study. Interpretation 5, T185-T197.

Çiftçi, N.B., 2013. In-situ stress field and mechanics of fault reactivation in the Gediz Graben, Western Turkey. J. Geodyn. 65, 136-147.

Eaton, D., 2017. Dynamics of fault activation from hydraulic fracturing in overpressured shales, 79th EAGE Conference and Exhibition 2017-Workshops Date. EAGE, Paris, p. 4.

Eaton, D., Schultz, R., 2018. Increased likelihood of induced seismicity in highly overpressured shale formations. Geophysical Journal International 214, 751-757.

Eaton, D.W., Igonin, N., Poulin, A., Weir, R., Zhang, H., Pellegrino, S., Rodriguez, G., 2018. Induced Seismicity Characterization during Hydraulic-Fracture Monitoring with a Shallow-Wellbore Geophone Array and Broadband Sensors. Seismological Research Letters 89, 1641-1651.

Faulkner, D., Mitchell, T., Healy, D., Heap, M., 2006. Slip on'weak'faults by the rotation of regional stress in the fracture damage zone. Nature 444, 922.

Fox, A., Soltanzadeh, M., 2015. A Regional Geomechanical Study of the Duvernay Formation in Alberta, Canada, Geoconvention 2015. Canadian Society of Petroleum Geologists, Calgary, p. 4. pp.

Gephart, J.W., 1990. Stress and the direction of slip on fault planes. Tectonics 9, 845-858.

Green, D.G., Mountjoy, E.W., 2005. Fault and conduit controlled burial dolomitization of the Devonian west-central Alberta Deep Basin. Bulletin of Canadian Petroleum Geology 53, 101-129.

Hammermaster, K., Schmidt, G., Dunn, L., Brown, M., Bernard, R., Wen, E., Befus, R. and Gardiner, S., 2012. The Duvernay Formation (Devonian): an emerging shale liquids play in Alberta. In Canada: Expanded Abstracts, CSPG Conferences Abstract Archive.

Hardebeck, J.L., Hauksson, E., 2001. Crustal stress field in southern California and its implications for fault mechanics. Journal of Geophysical Research-Solid Earth 106, 21859-21882.

Hardebeck, J.L., Michael, A.J., 2006. Damped regional-scale stress inversions: Methodology and examples for southern California and the Coalinga aftershock sequence. Journal of Geophysical Research: Solid Earth 111.

Haug, K., Bell, J.S., 2016. Compilation of in situ stress data from Alberta and Northeastern British Columbia (tabular data, tab delimited). Alberta Energy Regulator, Edmonton.

Heidbach, O., Tingay, M., Barth, A., Reinecker, J., Kurfeß, D., Müller, B., 2010. Global crustal stress pattern based on the World Stress Map database release 2008. Tectonophysics 482, 3-15.

Heidbach, Oliver; Rajabi, Mojtaba; Reiter, Karsten; Ziegler, Moritz; WSM Team (2016): World Stress Map Database Release 2016. GFZ Data Services. http://doi.org/10.5880/WSM.2016.001

Hergert, T., Heidbach, O., Reiter, K., Giger, S., Marschall, P., 2015. Stress field sensitivity analysis in a sedimentary sequence of the Alpine foreland, northern Switzerland. Solid Earth 6, 533.

Hicks, E.C., Bungum, H., Lindholm, C.D., 2000. Stress inversion of earthquake focal mechanism solutions from onshore and offshore Norway. Norsk Geologisk Tidsskrift 80, 235-250.

Hubbert, M.K., Rubey, W.W., 1959. Role of Fluid Pressure in Mechanics of Overthrust Faulting .1. Mechanics of Fluid-Filled Porous Solids and Its Application to Overthrust Faulting. Geol. Soc. Am. Bull. 70, 115-166.

Jaeger, J., Cook, N., Zimmerman, R., 2007. Fundamentals of rock mechanics. Wiley-Blackwell, New York.

Jones, L.M., 1988. Focal mechanisms and the state of stress on the San Andreas fault in southern California. Journal of Geophysical Research: Solid Earth 93, 8869-8891.

Kastrup, U., Zoback, M.L., Deichmann, N., Evans, K.F., Giardini, D., Michael, A.J., 2004. Stress field variations in the Swiss Alps and the northern Alpine foreland derived from inversion of fault plane solutions. Journal of Geophysical Research: Solid Earth 109.

Konstantinovskaya, E., Malo, M., Castillo, D.A., 2012. Present-day stress analysis of the St. Lawrence Lowlands sedimentary basin (Canada) and implications for caprock integrity during CO2 injection operations. Tectonophysics 518-521, 119-137.

Levandowski, W., Herrmann, R.B., Briggs, R., Boyd, O., Gold, R., 2018. An updated stress map of the continental United States reveals heterogeneous intraplate stress. Nature Geoscience, 1.

Liu, L., Zoback, M.D., 1992. The effect of topography on the state of stress in the crust: Application to the site of the Cajon Pass Scientific Drilling Project. Journal of Geophysical Research 97, 5095-5108.

Lund, B., Slunga, R., 1999. Stress tensor inversion using detailed microearthquake information and stability constraints: Application to Ölfus in southwest Iceland. Journal of Geophysical Research: Solid Earth 104, 14947-14964.

Lyster, S., Corlett, H., Berhane, H., 2017. Hydrocarbon Resource Potential of the Duvernay Formation in Alberta – Update. Alberta Energy Regulator, Edmonton, p. 44.

Mardia, K., Jupp, P., 1999. Directional Statistics. Wiley.

McGarr, A., 1988. On the State of Lithospheric Stress in the Absence of Applied Tectonic Forces. Journal of Geophysical Research: Solid Earth 93, 13609-13617.

McGarr, A., Gay, N.C., 1978. State of Stress in the Earth's Crust. Annual Review of Earth and Planetary Sciences 6, 405-436.

McTigue, D.F., Mei, C.C., 1981. Gravity-Induced Stresses near Topography of Small Slope. Journal of Geophysical Research 86, 9268-9278.

Michael, A.J., 1984. Determination of stress from slip data: faults and folds. Journal of Geophysical Research: Solid Earth 89, 11517-11526.

Miller, D.J., Dunne, T., 1996. Topographic perturbations of regional stresses and consequent bedrock fracturing. Journal of Geophysical Research: Solid Earth 101, 25523-25536.

Montone, P., Mariucci, M.T., Pondrelli, S., Amato, A., 2004. An improved stress map for Italy and surrounding regions (central Mediterranean). Journal of Geophysical Research: Solid Earth 109.

Morris, A.P., Ferrill, D.A., Walter, G.R., Price, A.M., Smart, K.J., Skoumal, R.J., Brudzinski, M.R., Currie, B.S., 2017. Lessons learned from the Youngstown, Ohio induced earthquake sequence from

January 2011 to January 2012. Journal of Rock Mechanics and Geotechnical Engineering 9, 783-796.

Nelson, E.J., Chipperfield, S.T., Hillis, R.R., Gilbert, J., McGowen, J., Mildren, S.D., 2007. The relationship between closure pressures from fluid injection tests and the minimum principal stress in strong rocks. International Journal of Rock Mechanics and Mining Sciences 44, 787-801.

Ong, O.N., Schmitt, D.R., Kofman, R.S., Haug, K., 2016. Static and dynamic pressure sensitivity anisotropy of a calcareous shale. Geophys. Prospect. 64, 875-897.

Pebesma, E.J., Wesseling, C.G., 1998. Gstat: a program for geostatistical modelling, prediction and simulation. Computers & Geosciences 24, 17-31.

Peška, P., Zoback, M.D., 1995. Compressive and tensile failure of inclined well bores and determination of in situ stress and rock strength. Journal of Geophysical Research: Solid Earth 100, 12791-12811.

Peterson, J., 2017. Subcrop extents of geological units at the sub-Cretaceous unconformity, west-central Alberta (gridded data, ASCII format), in: Regulator, A.E. (Ed.), AER/AGS Digital Data. Alberta Energy Regulator, Edmonton.

Plumb, R.A., Evans, K.F., Engelder, T., 1991. Geophysical log responses and their correlation with bed-to-bed stress contrasts in Paleozoic rocks, Appalachian Plateau, New York. Journal of Geophysical Research: Solid Earth 96, 14509-14528.

Pollard, D., Saltzer, S., Rubin, A.M., 1993. Stress inversion methods: are they based on faulty assumptions? Journal of Structural Geology 15, 1045-1054.

Pollard, D., Segall, P., 1987. Fracture mechanics of rock.

Preston, A., Garner, G., Beavis, K., Sadia, O., Strickler, S., 2016. Duvernay Reserves and Resources Report:A Comprehensive Analysis of Alberta's Foremost Liquids-Rich Shale Resource. Alberta Energy Regulator, Calgary, p. 83.

Reiter, K., Heidbach, O., Schmitt, D., Haug, K., Ziegler, M., Moeck, I., 2014. A revised crustal stress orientation database for Canada. Tectonophysics 636, 111-124.

Richards, B., Barclay, J., Bryan, D., Hartling, A., Henderson, C., Hinds, R., 1994. Carboniferous strata of the Western Canada sedimentary basin, in: Mossop, G.D., Shetsen, I. (Eds.), Geological atlas of the Western Canada Sedimentary Basin. Canadian Society of Petroleum Geologists and Alberta Research Council, Calgary.

Savage, W.Z., Swolfs, H.S., 1986. Tectonic and gravitational stress in long symmetric ridges and valleys. Journal of Geophysical Research: Solid Earth 91, 3677-3685.

Schmitt, D., Li, Y., 1993. Influence of a stress relief hole's depth on induced displacements: application in interferometric stress determinations, International journal of rock mechanics and mining sciences & geomechanics abstracts. Elsevier, pp. 985-988.

Schmitt, D.R., Currie, C.A., Zhang, L., 2012. Crustal stress determination from boreholes and rock cores: Fundamental principles. Tectonophysics 580, 1-26.

Schmitt, D.R., Haimson, B.C., 2016. Hydrualic fracturing stress measurements in deep holes, in: Feng, X.-T. (Ed.), Rock Mechanics and Engineering. CRC Press, Raton, pp. 183-225.

Schultz, R., Atkinson, G., Eaton, D.W., Gu, Y.J., Kao, H., 2018. Hydraulic fracturing volume is associated with induced earthquake productivity in the Duvernay play. Science 359, 304-308.

Schultz, R., Corlett, H., Haug, K., Kocon, K., MacCormack, K., Stern, V., Shipman, T., 2016. Linking fossil reefs with earthquakes: Geologic insight to where induced seismicity occurs in Alberta. Geophysical Research Letters 43, 2534-2542.

Schultz, R., Stern, V., Novakovic, M., Atkinson, G., Gu, Y.J., 2015. Hydraulic fracturing and the Crooked Lake Sequences: Insights gleaned from regional seismic networks. Geophysical Research Letters 42, 2750-2758.

Schultz, R., Wang, R., Gu, Y.J., Haug, K., Atkinson, G., 2017. A seismological overview of the induced earthquakes in the Duvernay play near Fox Creek, Alberta. Journal of Geophysical Research: Solid Earth 122, 492-505.

Schwab, D.R., Bidgoli, T.S., Taylor, M.H., 2017. Characterizing the Potential for Injection-Induced Fault Reactivation Through Subsurface Structural Mapping and Stress Field Analysis, Wellington Field, Sumner County, Kansas. Journal of Geophysical Research: Solid Earth 122, 10,132-110,154.

Schwanghard, W., 2010. variogramfit. Online web resource. URL https://www.mathworks.com/matlabcentral/fileexchange/25948-variogramfit. Last accessed Jan 2nd, 2018.

Shen, L., Schmitt, D.R., Haug, K., 2018a. Measurements of the states of in situ stress for the Duvernay Formation near Fox Creek, west-central Alberta; Alberta Energy Regulator / Alberta Geological Survey, AER/AGS Report 97, 29 p.

Shen, L., Schmitt, D.R., Haug, K. 2018b. In-Situ Stress Measurements for the Duvernay Formation, Alberta (tabular data, tab-delimited format); Alberta Energy Regulator / Alberta Geological Survey, AER/AGS Digital Data 2018-0013.

Sone, H., Zoback, M.D., 2013. Mechanical properties of shale-gas reservoir rocks—Part 2: Ductile creep, brittle strength, and their relation to the elastic modulus. Geophysics 78, D393-D402.

Sone, H., Zoback, M.D., 2014. Viscous relaxation model for predicting least principal stress magnitudes in sedimentary rocks. Journal of Petroleum Science and Engineering 124, 416-431.

Streit, E.E., Hillis, R.R., 2004. Estimating fault stability and sustainable fluid pressures for underground storage of CO2 in porous rock. Energy 29, 1445-1456.

Swarbrick, R.E., Osborne, M.J., 1998. Mechanisms that generate abnormal, pressures: An overview, in: Law, B.E., Ulmishek, G.F., Slavin, V.I. (Eds.), Abnormal Pressures in Hydrocarbon Environments. Amer Assoc Petroleum Geologists, Tulsa, pp. 13-34.

Terakawa, T. and E. Hauksson., 2018. Absolute Stress Fields in the Source Region of the 1992 Landers Earthquake. Journal of Geophysical Research: Solid Earth 123(10): 8874-8890.

Valley, B. and Evans, K.F., 2019. Stress magnitudes in the Basel enhanced geothermal system. International Journal of Rock Mechanics and Mining Sciences, 118, pp.1-20.

Vavryčuk, V., 2014. Iterative joint inversion for stress and fault orientations from focal mechanisms. Geophysical Journal International 199, 69-77.

Vernik, L., Zoback, M.D., 1992. Estimation of Maximum Horizontal Principal Stress Magnitude from Stress-Induced Well Bore Breakouts in the Cajon Pass Scientific-Research Borehole. Journal of Geophysical Research-Solid Earth 97, 5109-5119.

Wallace, R.E., 1951. Geometry of shearing stress and relation to faulting. The Journal of geology 59, 118-130.

Wang, R., Gu, Y.J., Schultz, R., Kim, A., Atkinson, G., 2016. Source analysis of a potential hydraulic-fracturing-induced earthquake near Fox Creek, Alberta. Geophysical Research Letters 43, 564-573.

Wang, R., Gu, Y.J., Schultz, R., Zhang, M., Kim, A., 2017. Source characteristics and geological implications of the January 2016 induced earthquake swarm near Crooked Lake, Alberta. Geophysical Journal International 210, 979-988.

Weides, S.N., Moeck, I.S., Schmitt, D.R., Majorowicz, J.A., 2014. An integrative geothermal resource assessment study for the siliciclastic Granite Wash Unit, northwestern Alberta (Canada). Environ. Earth Sci. 72, 4141-4154.

White, J.A., Foxall, W., 2016. Assessing induced seismicity risk at CO 2 storage projects: Recent progress and remaining challenges. Int. J. Greenh. Gas Control 49, 413-424.

Williams, J.D.O., Fellgett, M.W., Quinn, M.F., 2016. Carbon dioxide storage in the Captain Sandstone aquifer: determination ofin situstresses and fault-stability analysis. Petrol. Geosci. 22, 211-222.

Woodland, D.C., Bell, J.S., 1989. In-Situ Stress Magnitudes from Mini-Frac Records In Western Canada. Journal of Canadian Petroleum Technology 28, 22-31.

Wu, P., 1991. Flexure of lithosphere beneath the Alberta Foreland Basin: Evidence of an eastward stiffening continental lithosphere. Geophysical Research Letters 18, 451-454.

Yerkes, R., Levine, P., Wentworth, C., 1990. Abnormally high fluid pressures in the region of the Coalinga earthquake sequence and their significance. United States Geological Survey Professional Paper 1487, 235.

Zang, A., Stephansson, O., 2010. Stress Field of the Earths Crust. Springer, Dordrecht.

Zhang, H., Eaton, D.W., Li, G., Liu, Y., Harrington, R.M., 2016. Discriminating induced seismicity from natural earthquakes using moment tensors and source spectra. Journal of Geophysical Research: Solid Earth 121, 972-993.

Zoback, M.D., 2007. Reservoir Geomechanics. Cambridge University Press, Cambridge.

Zoback, M.D., Barton, C.A., Brudy, M., Castillo, D.A., Finkbeiner, T., Grollimund, B.R., Moos, D.B., Peska, P., Ward, C.D., Wiprut, D.J., 2003. Determination of stress orientation and magnitude in deep wells. International Journal of Rock Mechanics and Mining Sciences 40, 1049-1076.

Zoback, M.L., Zoback, M.D., Adams, J., Assumpcao, M., Bell, S., Bergman, E., Blümling, P., Brereton, N., Denham, D., Ding, J., 1989. Global patterns of tectonic stress. Nature 341, 291.

# Chapter 5. Frictional Stabilities on Induced Earthquake Fault Planes at Fox Creek, Alberta: A Pore Fluid Pressure Dilemma

## 5.1 Introduction

The use of hydraulic fracturing (HF), particularly from multiple stages along horizontal boreholes, to access hydrocarbons from low-permeability unconventional and geothermal reservoirs continues to accelerate; and as such it becomes increasingly important that the risks associated with such practices are understood. Essentially, a HF operation consists of rapidly pressurizing a section of a borehole create and propagate new fractures and to disturb natural fracture networks to increase the effective permeability, thus allowing hydrocarbons to flow back to the borehole to be produced. Numerous microseismic events ($M_W < 0$) result, with their locations useful in tracking fracture network growth; but the process by itself in insufficiently energetic to produce larger felt events. Despite this, some larger rare events with $M_W$ possibly up to $M_W$ 4.7 have been temporally and spatially linked to HF operations in Western Canada, the United Kingdom, the United States, and China [*Li et al.*, 2019; *López-Comino et al.*, 2018]. Further study of these events assists in assessing risk levels and may also help understanding of the nucleation of natural earthquakes.

These HF-linked events differ from the significantly greater numbers of earthquakes associated with broader long-term fluid disposal [*Foulger et al.*, 2018]. The circumstances under which they initiate, however, are not universal with some occurring during HF-operations either during either pumping to extend the fracture network or 'flow-back' as the fracture fluids return to the borehole, or some-time after the operations have ceased. The actual hypocenters of these

events with respect to the known injection points, too, remain uncertain making interpretation of the trigger mechanisms difficult. These relationships in time and the ambiguities in location have led to authors variously argue that the events are triggered on pre-existing planes of weakness by either increasing the Coulomb shear stress by poroelastic stress transference [e.g., *Deng et al.*, 2016] or by decreasing the effective stress through transmission of fluid pressures via diffusion or direct hydraulic connection [e.g., *Shapiro and Dinske*, 2009]. However, the true nature of the faults, the fluid communication pathways, and the poroelastic properties of the materials in situ remain unknown, and these hypotheses remain speculative until information only accessible through drilling is obtained.

We do not claim to fully answer this problem here, but we do provide new information on the stability of the fault planes for a number of well-studied events linked to HF operations in the Duvernay Formation in the vicinity of Fox Creek, Alberta. Our analysis relies on a recently developed quantitative model for this area that accurately predicts the state of stress, including pore pressures, at each hypocenter [*Shen et al.*, 2019] subsequently allowing the Mohr-Coulomb stability of each fault plane to be fully evaluated. An unexpected finding is that the fault planes cannot be stable if the pore fluid pressure acting on them is the same as that measured within the reservoir. Conversely, the fluid pressures acting on the faults must be substantially reduced from those within the reservoir rock if the faults are to remain stable, as they appear to have been at least through the historical record prior to 2015.

Below, we begin with a brief review of the Mohr-Coulomb stability criterion used and of the circumstances associated with the Fox Creek events. The stress model is then applied to evaluate the fault stability at the locations of each HF-linked event and this analysis then extended

to delimit the pore fluid pressures required for the faults to become unstable. This analysis leads to suggestions as to the reasons why pore pressures may be diminished on the faults and possible implications for migration of hydrocarbons from the prolific Duvernay source rocks into the overlying siliciclastics conventional reservoirs.

## 5.2 Slip Tendency Analysis

The dynamic behaviour of fault slip is expected to follow empirical rate-state friction laws [*Marone et al.*, 1990; *Ruina*, 1983]. However, the earthquake nucleation still remains poorly understood [*Gomberg*, 2018]. It is often assumed that slip initiates on a pre-existing plane of weakness once the magnitude of its resolved shear traction $|\tau|$ exceeds the frictional restraint, which is proportional to the product of the effective normal traction $\sigma$. Usually, simple Coulomb friction based criteria such as the widely employed Coulomb failure stresses [*Harris*, 1998] or slip tendency *SNR [Morris et al., 1996]* are used to assess the risk that slip will occur. Slip initiation is assumed to be regulated by the static-friction co-efficient $\mu$, the cohesion $C$, and the pore fluid pressure $P_f$ on the slip plane through the Terzaghi effective stress law for shear failure. Accordingly, slip initiates when the ratio of the fault shear $|\tau|$ *to* normal $\sigma$ tractions (the shear to normal ratio *SNR)* resolved onto the fault plane overcomes the fault friction $\mu$:

$$\mu < \frac{|\tau| - C}{\sigma - P_f} \equiv SNR\,. \tag{5.1}$$

Usually, the cohesion $C$ of an already-existing fault plane is assumed small relative to the stresses and is often ignored in such analyses [*Scholz*, 2019; *Zoback*, 2010] including *Morris et al.* [1996] original study. despite evidence of fault healing that has been interpreted as a time dependent friction [*Dieterich*, 1972] or complications associated with separating cohesive and

frictional effects [e.g., *Weiss et al.*, 2016]. If the tectonic stress states that generate the resolved tractions $\tau$ and $\sigma$ as well as the $C$ remain unchanged, then slip along the fault may be triggered by increasing $P_f$, a concept that was first tested by injection of water to a producing oil reservoir at Rangeley, Colorado [*Raleigh et al.*, 1976].

## 5.3 Fox Creek, Alberta, Events

Over the Western Canada Sedimentary Basin, only a small fraction of HF stimulations has been linked to induced earthquakes with $M_W \geq 3$ [*Atkinson et al.*, 2016]. These HF induced earthquakes are geographically clustered, with no induced events detected from the nearby operations targeting the same geological units [*Schultz et al.*, 2017]. Clustering of the seismicity has been statistically related to high pore pressure $P_P$ gradients [*Eaton et al.*, 2018], local geological structure [*Schultz et al.*, 2016], or volumes of injected fluids [*Schultz et al.*, 2018]. Statistical correlations, however, cannot explain the proximate lack of seismicity nor resolve the physical mechanisms. The lack of knowledge of these processes limits the mitigation responses to 'traffic light protocols' during HF operations [*Shipman et al.*, 2018].

Here, we carry out stability analyses using high-quality FM solutions for 11 induced earthquakes (Fig. 5.1a, Table 5A1) linked to HF operations in the Duvernay Formation near Fox Creek, Alberta [*Schultz et al*., 2017]. These analyses rely on a recently developed quantitative model for the full Andersonian tectonic principal stress magnitudes for the greatest SH, least Sh horizontal and the vertical SV compressions, as well the SH azimuth $\phi$ [*Shen et al*., 2019]. Predictive values for each of these components (Fig. 5.1b-e) are obtained through geostatistical modelling using numerous borehole measurements within the Duvernay Formation (Fig. 3.1b). *Shen et al.* [2019] subsequently calculate a range of absolute SH [*Terakawa and Hauksson*, 2018]

from the distribution of stress 'shape factors' determined from FM inversions [*Vavryčuk*, 2014]. The inversion algorithm further provides the three orthogonal principal stress directions that are consistent with both the observed strike-slip mechanisms and with the Andersonian hypothesis that one principal stress is vertical [*Shen et al*., 2019]. When resolved onto the FM inferred fault planes (Table 5A1), these stresses allow us to calculate SNR distributions in order to carry out sensitivity tests on the factors affecting slip initiation with Eqn. 5.1. It is important to note that the pore pressure $P_P$ developed in this model is obtained from direct measurements in numerous boreholes over the area; as will become apparent later we distinguish this from the more general pore fluid pressure of Eqn. 5.1. Further, these measured $P_P$ are often more than double the normal hydrostat and are often more than 90% of the $S_h$ magnitude.

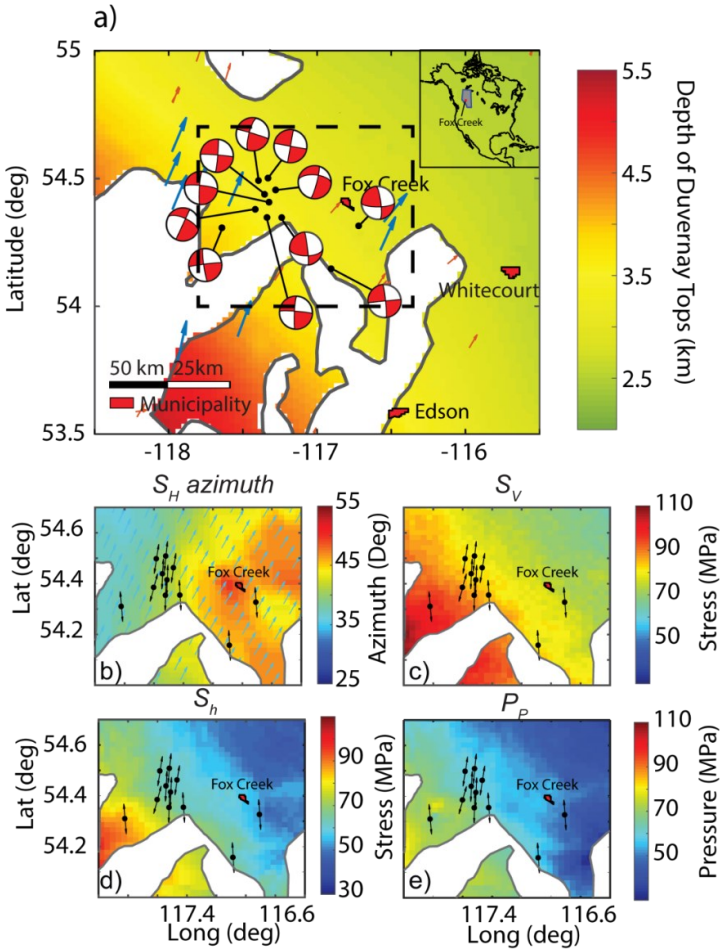


**Figure 5.1.** a) Focal mechanisms of the earthquakes analyzed in this paper. The black dots show the epicenters of each earthquake. The coloured background shows the depth of the Duvernay Formation that is cotemporaneous with Leduc reefs (white areas). Blue and orange arrows show the direction of $S_H$ determined by borehole observations from WSM [*Heidbach et al.*, 2016] and *Shen et al.* [2019]. Dashed line box indicates area of the directly measured stress tensor components shown as interpolated maps at the top of the Duvernay Formation in panels b-e. In these panels the black dots indicate the epicenters and the associated black arrows the slip direction determined from focal mechanisms. b) $S_H$ trend azimuth $\phi$ shown both as the colormap and on select grid points as cyan arrows c) vertical total compressive stress $S_V$, d least horizontal total compressive stress $S_h$ and e) formation pore pressure $P_P$. The greatest horizontal total compressive stresses are described by a statistical distribution at each grid point and are not shown.

Two adjacent HF-induced earthquakes ($M_W$ 3.6, Jan 23, 2015; $M_W$ 4.1, Jan 12, 2016) are selected in part because of the availability of additional active-source seismic attribute images [*Chopra et al.*, 2017, Fig. 5B1] and careful determination of the epicentral locations and depths [*Wang et al.*, 2017]. There, FM indicates strike-slip motion on subvertical N-S striking fault planes. A red traffic light protocol was triggered for one of these events during HF operations [*Shipman et al.*, 2018] and the ground motion was locally felt. Various lines of evidence [*Eaton et al.*, 2018] suggest that the depth of the $M_W$ 4.1 event (and associated cluster) lies at ~3.5 km, coincident with HF of the Duvernay Formation [*Wang et al.*, 2017]. The lateral resolution of the stress model is ~2 km and the values for stress and $P_P$ (Figure 5.1, Table 5A-2) are nearly the same for both events under the assumption they occur within or close to the Duvernay Formation. The slip on these two events is well oriented with respect to the stress field (Figure 5.2a-c) For the sake of comparison, the stability on a third fault plane associated with the Mw 3.9 (Jun 13, 2015) event that less optimally aligned with the stress field (Table 5A-2) is also calculated (Figure 5.2d-f).

Some description of Figure 5.2 is necessary. Following *Morris et al.* [1996] a value for *SNR* is calculated on the entire set of planes possible with its value represented by a color positioned at the point that each plane's pole intersects the hemispherical stereonet projection. These plots are useful in evaluating the range of stable and unstable fault orientations. Further, the *SNR* in Figre 5.2 is calculated (Eqn. 5.1) assuming $C = 0$, using the most probable $S_H$, and with three options of $P_f$ in which it is either omitted, made equal to the normal hydrostatic pressure expected, or assigned the measured value for $P_P$ from the stress model for reasons to become apparent shortly. As points of reference, four black dots on each panel indicate the poles for those planes optimally oriented to the stress field if $\mu = 0.6$. The large red dots are poles to the two well-oriented fault planes (Figure 5.2a-c) and for the more poorly oriented plane (Figure 5.2d-f).

Finally, contour lines of constant *SNR* = 0.4 (grey) or 0.8 (purple) are included representing these two frictional limits according to Eqn. 5.1.

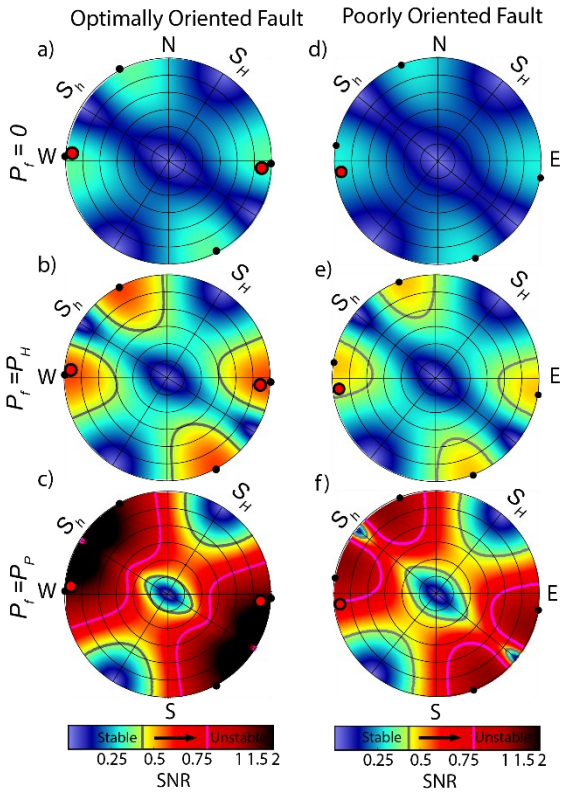


**Figure 5.2.** Stereonet plot with *SNR* shown in nonlinear colormap for the poles of any arbitrarily oriented faulting planes in the at the epicenters of the well-oriented $M_W$ 3.6 and 4.1 events with the Andersonian model stresses $S_h$ = 65 MPa; $S_V$ = 84 MPa, $S_H$ = 124 MPa with $\phi$ = 41° using a) $P_f$ = *0,* b) Hydrostatic $P_H$ = 33 MPa, and c) $P_f$ = measured $P_P$ 62 MPa; and for the poorly oriented $M_W$ 3.9 event d) $P_f$ = *0,* e) Hydrostatic $P_H$ = 33 MPa, and f) $P_f$ = measured $P_P$ 57 MPa. See text for details.

According to Eqn. 5.1, the fault is unstable if *SNR* > $\mu$. To interpret, the areas of the stereonets with values of *SNR* greater than the slip criterion value of $\mu$ chosen represents the set of unstable fault planes. Consequently if $P_f$ = 0 (Figure 5.2a, d) *SNR* reaches a maximum of ~0.3 indicating that the faults could slip only if friction is low; and suggests that the faults would likely

be stable. This situation persists if $P_f$ (Figure 5.2b, e) is at the more normal hydrostatic gradient with low values of *SNR* ~0.5 expected on the faults. However, the situation changes significantly with larger $P_f \approx P_P$ (Figure 5.2c, f) where *SNR* is larger on both fault planes. Indeed, $SNR \geq 2$ for the optimally oriented faults (Fig. 5.2c); barring unexpectedly high friction or cohesion these faults could not remain stable if the formation pore fluid pressure $P_P$ was active on their planes. Alternatively, for the more poorly oriented $M_w$ 3.9 event (Figure 5.2f) $SNR \approx 0.8$.

Within the historical record these faults to the best of our knowledge have appeared to remain clamped (i.e., did not detectably slip). This suggests that the fluid pressure $P_f$ active in the immediate vicinity of the slip planes cannot be the same as the highly overpressured $P_P$ measured from borehole testing within the Duvernay Formation One possible explanation for this is that the planes of weakness are conduits providing transmissive migration pathways for fluids generated within the Duvernay Formation to the overlying and more normally pressured conventional siliciclastics reservoirs. That such pathways may exist is not unexpected given that the Duvernay Formation is believed to be the source rock for much of hydrocarbons within the prolific Western Canada Sedimentary Basin [*Stoakes and Creaney*, 1985]. Fluid pressures within such zones could be relieved via along zones of hydraulic connectivity either continuously or possibly via fault valving mechanisms [*Sibson*, 1990].

As might be expected, regardless of $P_f$ the two earthquakes ($M_W$ 3.6 & 4.1) occur on planes whose poles are close to the maximum *SNR* in Figure 5.2a-c, this seeming agreement warrants further examination. On the one hand, the orientations of the earthquake slip planes are independently given by the focal mechanisms as constructed from the events' radiation patterns. On the other, because the stress state is Andersonian with $S_V$ vertical the orientation of the

maximum *SNR* orientations in the strike-slip environment is entirely controlled by $\phi$, which is also completely independently obtained from examination of borehole image logs. Closer examination of Figure 5.2 shows that here the fault planes strike at angles $\theta = 35°$ and 37° from $\phi$ for the $M_W$ 3.6 and 4.1 events, respectively. This is worth pointing out because the azimuth of focal mechanism *p*-axes, which by definition are 45° from the fault plane, are often taken as a proxy for the stress directions. The smaller angle between the fault plane and $\phi$ is consistent with frictional constraints.

## 5.4 Triggering of fault slip with increasing $P_f$

Carrying out more detailed explorations of the influence of $\mu$, $P_f$, and $C$ on a case by case basis using only slip-tendency plots of Fig. 5.2, or equivalently Mohr stress diagrams, is cumbersome [e.g., *Lele et al.*, 2017]. Instead, in Fig. 5.2 we plot *SNR* as a function of $P_f$ directly on the fault planes for the optimally oriented $M_W$ *4.1* (Fig. 5.3a) and the poorly oriented $M_W$ *3.9* (Fig. 5.3b) using their respective stress tensors (Table 3A-2) but assuming either $C = 0$ (red band) or $C = 5$ MPa (green band). Within Fig. 5.3 at any given $P_f$, the vertical thickness of the band accounts for the uncertainties of the stress tensor at that hypocenter (Table 3A-2) and is primarily controlled by the larger distribution of expected $S_H$ magnitudes. The vertical dashed lines in Fig. 5.3 delineate fluid pressures of the hydrostat $P_H$, the measured Duvernay Formation pore pressure $P_P$, and the measured minimum horizontal compressive stress $S_h$. This latter pore pressure represents an upper limit as once it exceeds $S_h$ natural hydraulic fracturing would be expected. Typically, workers assume $\mu$ ranges from 0.6 to 1.0 in the upper crust [*Byerlee*, 1978]. Here we use the range $0.4 \leq \mu \leq 0.8$, constrained by a variety of experimental friction tests (Table 3B-3) on rocks similar to the clay-poor and stiff Duvernay Formation [*Ong et al.*, 2016], although we

reiterate that there are no direct measurements of the frictional properties of Duvernay Formation rock currently available to our knowledge. Similarly, no direct measures of fault cohesion ($C$) exist; justification for use of these low values is provided in the supplementary materials.

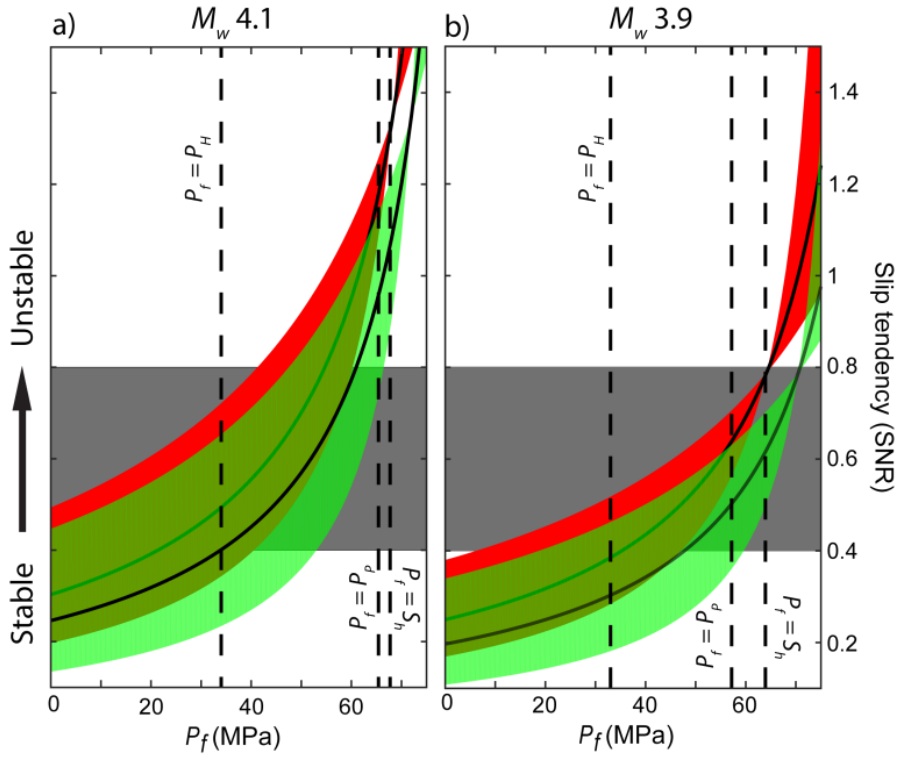


**Figure 5.3.** Increasing slip tendency (*SNR*) of the fault with rising $P_f$ for a) $M_W$ 4.1 and b) 3.9 events. The *SNR* of the earthquake's faulting plane at different fluid pressures. The red and green regions represent the SNR distributions setting, respectively, for $C$ = 0 and $C$ = 5 MPa. The width of the stripe represents the uncertainty of *SNR* due to different $S_H$, and the black lines show the calculation with the most confident value for $S_H$. Gray box highlights the range of *SNR* (0.4- 0.8).

Both fault planes are likely stable if $P_f = P_H$ remains at the normal hydrostat. The poorly oriented fault plane (Figure 5.3b), too, probably remains stable even at pressures exceeding the ambient $P_p$ (57 MPa). In contrast, at the ambient $P_P$ (62 MPa) the optimally oriented fault plane (Figure 5.3a) is already unstable. The historical quiescence of this fault could be interpreted

variously to mean that *i)* it is characterized by unexpectedly high values of $\mu$ or of *C,* or *ii)* that the $P_f$ naturally active on the fault is significantly less than $P_p$. The stabilities on all 11 fault planes are further explored in Figure 5.4a by calculating their individual *SNR* distributions using a Monte-Carlo procedure (see Supplementary Material) that incorporates the uncertainties associated with the three stress magnitudes and depths, and over expected ranges of varying $\mu$ and *C* for two extreme pore fluid pressure cases with $P_f = 0$ (blue) and $P_f = P_P$ (green). Each distribution is shown as a box and whisker format plotted versus the local angle difference $\psi = S - \phi$ between fault strike *S* and the $S_H$ direction (Table 5A-1). $\psi$ can be considered as a proxy measure of how well a given fault plane is oriented with respect to slip with the vertical gray band indicating the range of optimal $\psi$ orientations of 26° to 34° corresponding to the range of $\mu$ between 0.8 to 0.4. The *SNR* distributions of these earthquakes are mostly below 0.4 in the unrealistic case with $P_f = 0$ (Figure 5.4a) reinforcing the expectation that for this extreme case all of the faults would likely remain stable. In contrast, if the faults were perfectly hydraulically connected to the Duvernay Formation such that $P_f = P_P$, almost all the *SNR* distributions shift to values well in excess of 0.8 again indicating that nearly all the faults would be unstable at ambient $P_p$ within the reservoir.

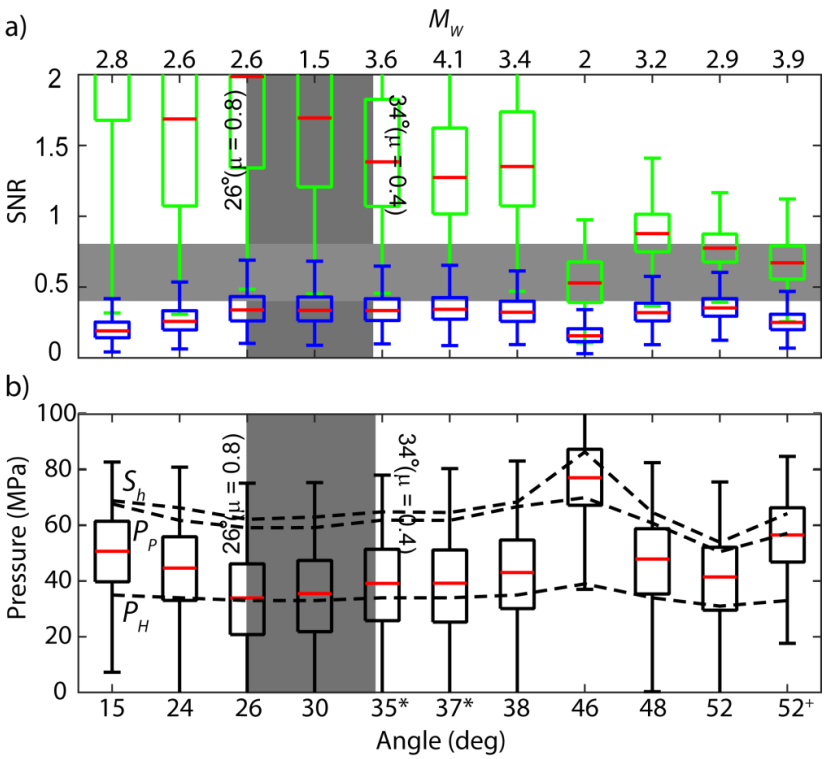


**Figure 5.4.** Monte-Carlo calculations versus angle of a) *SNR* distributions on the fault planes calculated assuming $P_{f=}$ 0 (blue) and $P_f = P_P$ (green), boxes indicate the 25th and 75th percentile limits of the probability density functions, and the red lines indicate the most probable SNR value for each case, plotted versus the angle $\psi$ bisecting each events local $S_H$ direction $\phi$ and the fault plane strike. b) The distributions fluid pressures needed to activate the faults, boxes indicate the 25th and 75th percentile limits of the probability density functions, and the red lines indicate the most probable critical $P_f$ value. Black dashed lines represent the fracture closure pressure (equal to $S_h$), measured virgin $P_P$ and depth-dependent normal hydrostatic pressure $P_H$. Shaded gray zones in both panels indicate suggested *SNR* and optimal orientation angle ranges.

Given that the faults appear unstable under the expected virgin formation $P_P$, distributions of the greatest allowable values for $P_f$ that are necessary to maintain stability (i.e., $SNR \leq \mu$) were further explored using a Monte-Carlo approach for restricted ranges of $\mu$ and $C$ with the individual stress states. For most of the cases, the most probable $P_f$ (Figure 5.4b, see appendix for methods)

required to initiate slip is slightly greater than the local $P_H$ but significantly less than the local $P_P$. This again indicates that the faults are likely not stable under the high ambient formation $P_P$ and suggests that the virgin $P_f$ acting on the faults must be lower.

During hydraulic fracture stimulations, the fluid pressure required to drive a hydraulic fracture into a rock mass must at least exceed the fracture closure pressure (here $S_h$), a value that in practice is readily exceeded by the actual pressures measured in the wellbore $P_w(t)$ at the injection point during stimulation. Consequently, fluid pressures sufficiently high to trigger slip are present within the system during stimulation, although the actual fluid pressures delivered to the fault through the induced fracture network from the borehole remain highly uncertain. Non-double couple focal mechanism components anecdotally suggest fluid inflow into the fault during the earthquake [*Wang et al.*, 2018]. Reportedly, fractures stimulated during the HF well completion extend laterally no more than 400 m with excursions to nearly 900 m from the injection point [*Wilson et al.*, 2018]; and this may provide some insight on the distance fluid pressures could be transmitted during an HF stimulation. That said, model-derived estimates depend on having knowledge of many largely unconstrained factors controlling fracture and fault geometries and fluid transport. Poroelastic stresses, too, may contribute to the stress state on the fault planes at initiation uncertain in these formations but numerical [*Chang and Segall*, 2016] and analytical [*Segall and Lu*, 2015] simulations suggest their influence on the *SNR* is a small fraction relative to $P_f$.

In Figure 5.4, the local angle difference $\psi$ is intentionally chosen as the independent variable to emphasize that the planes of weakness are not necessarily all optimally aligned with the stress field. The suggested range $0.4 \leq \mu \leq 0.8$ delimits the optimal range $34° \geq \psi \geq 26°$

highlighted in Figure 5.4; which almost all of the events fall outside of. This observation could have multiple interpretations. The most likely explanation is that more optimally oriented planes of weakness are absent at these locations; slip instead occurs on those pre-existing faults that are closest to unstable but not perfectly aligned with the stress field. Another interpretation is that the slip does occur on the real fault planes that are optimally oriented, but the FM planes or values of stress (retaining the Andersonian assumption) are uncertain.

## 5.5 Conclusion

The slip-tendencies along faults activated by hydraulic fracture stimulations in a localized area of NW Alberta, Canada were analyzed using a recently developed quantitative model for the full stress tensor and the formation pore fluid pressures $P_p$ within the highly over-pressured Duvernay Formation. Assuming reasonable ranges for fault friction and cohesion, nearly all of the slip-planes studied would be unstable at the measured ambient formation pore fluid pressures $P_p$. This instability persists although most of the slip-planes are not expected to be optimally oriented with respect to the prevailing stress directions. That this area was historically aseismic prior to hydraulic fracturing operations, however, indicates that the natural fluid pressures within the fault zone must be lower unless unexpectedly large frictions or cohesions exist; Monte-Carlo simulations suggest that generally, the most probable critical fluid pressures lie closer to the normal hydrostatic pressure. As hydraulic fracturing stimulations generally attempt to maintain fluid pressures above $S_h > P_p$, the potential to convey in excess of a critical pressure to the surrounding formation exist, although actually quantitatively estimating the critical pressure is difficult. One additional comment arising from is that including even a modest cohesion $C$ does affect the $SNR$ value noticeably; and while omitting $C$ may be useful within the context of engineering risk

assessment better understanding this phenomenon warrants further study. The inferred lower pressures within the faults suggest that they may serve to provide conduits for migration of hydrocarbons out of the low permeability Duvernay Formation to the overlying siliclastic formations and may be consistent with the critically stressed crust hypothesis [*Townend and Zoback*, 2000]. The results here highlight the challenges confronting researchers hoping to understand the physics of earthquake rupture by artificially initiating fault slip [*Savage et al.*, 2017].

## 5.6 Appendix 5A. Summary of earthquakes analyzed in this study

**Table 5A-1.** A total of 11 earthquakes recorded by the regional seismometer network with well resolved focal mechanisms are analyzed in this study. The abbreviated column names stand for $M_W$ – Magnitudes, Lat – Latitude (deg), Lon – Longitude (deg), Dep – Depth (km), S – Strike Angle N-E (deg), D – Dip angle (deg), R – Rake angle (deg).

| $M_W$ | Date | Lat | Lon | Dep | S | D | R |
|---|---|---|---|---|---|---|---|
| 2.8 | 8-Aug-15 | 54.38 | 117.4 | 3.5 | 25 | 90 | -145 |
| 3 | 19-Aug-15 | 54.46 | 117.27 | 3.3 | 15 | 79 | -139 |
| 2.6 | 18-Jan-15 | 54.50 | 117.38 | 3.4 | 195 | 70 | 175 |
| 1.5 | 17-Nov-15 | 54.51 | 117.32 | 3.3 | 10 | 90 | 180 |
| 4.1* | 12-Jan-16* | 54.41 | 117.31 | 3.4 | 184 | 81 | 166 |
| 3.6* | 23-Jan-15* | 54.44 | 117.34 | 3.4 | 5 | 85 | -175 |
| 3.4 | 14-Jan-15 | 54.35 | 117.32 | 3.5 | 183 | 81 | 172 |
| 3.2 | 10-Feb-15 | 54.35 | 117.22 | 3.4 | 354 | 82 | 140 |
| 2.9 | 3-Dec-15 | 54.33 | 116.71 | 3.1 | 353 | 74 | 157 |
| 3.9+ | 13-Jun-15+ | 54.16 | 116.89 | 3.3 | 354 | 85 | -180 |
| 2 | 22-Sep-15 | 54.31 | 117.62 | 3.9 | 172 | 82 | 174 |

*Event analysis shown as examples in Figure 5.2a and 5.3a; +Event analyzed as an example in Figure 5.2b and 5.3b.

**Table 5A-2.** States of in-situ stress at the epicentral locations of the earthquakes. The abbreviated column names stand for $M_W$ – Magnitudes, $S_H$ AZ – N-E orientation of maximum horizontal compressional stress (deg), $S_h$ – Minimum horizontal stress (MPa), $S_V$ – Vertical stress (MPa), $S_H$ - Maximum horizontal stress (MPa) constrained using the shape-ratio evaluated through stress inversion technique. $S_H$ max – Maximum $S_H$ constrained with borehole observation. $P_P$ – Apparent pore pressures of the unconventional shale oil/gas reservoir nearby.

| $M_W$ | $S_H$ AZ $\phi$ | $S_H$ | $S_H$ max | $S_H$ min | $S_h$ | $S_V$ | $P_P$ |
|---|---|---|---|---|---|---|---|
| 2.8 | 40 | 122.5 | 179.0 | 100.4 | 68.5±2.2 | 86.4±2.6 | 67.8±2.2 |
| 3 | 41 | 122.1 | 182.7 | 97.4 | 61.9±2.8 | 81.8±2.5 | 59.2±2.8 |
| 2.6 | 39 | 117.5 | 166.6 | 96.3 | 66.0±2.5 | 83.2±2.4 | 61.8±2.5 |
| 1.5 | 40 | 117.6 | 172.2 | 94.6 | 62.7±2.9 | 80.9±2.5 | 59.2±2.9 |
| 4.1* | 41 | 122.4 | 180.0 | 98.9 | 64.5±2.5 | 83.9±2.7 | 62.5±2.5 |
| 3.6* | 40 | 125.3 | 185.3 | 100.3 | 64.7±2.2 | 84.7±2.7 | 62.1±2.2 |
| 3.4 | 41 | 125.9 | 184.3 | 102.3 | 68.1±2.6 | 87.3±2.7 | 66.7±2.6 |
| 3.2 | 42 | 126.8 | 188.6 | 101.2 | 64.3±2.3 | 85.1±2.1 | 60.9±2.3 |
| 2.9 | 45 | 122.7 | 188.9 | 95.0 | 53.7±1.9 | 76.6±2.3 | 50.5±1.9 |
| 3.9+ | 46 | 112.6 | 163.7 | 92.6 | 63.9±1.6 | 80.1±2.3 | 57.2±1.6 |
| 2 | 38 | 119.9 | 155.2 | 104.9 | 86.0±1.8 | 97.3±2.8 | 70.00±1.8 |

*Event analysis shown as examples in Figure 5.2a and 5.3a; +Event analyzed as an example in Figure 5.2b and 5.3b.

## 5.7 Appendix 5B. Methodology

The slip tendency for an arbitrarily oriented plane is quantified by the value *SNR* of Eqn 5.1. Following [*Morris et al.*, 1996], the *SNR* for all possible fault planes are displayed as contours within a stereonet plot. This necessitates that both the shear $\tau$ and normal $\sigma$ tractions be calculated for the given stress tensor $T$ with known azimuth $\phi$ using well-known equations in continuum mechanics [see review in *Schmitt et al.* 2012].

Examination of Eqn. 5.1 shows that knowledge of both the fluid pressure $P_f$ and the fault cohesion $C$ are required. In Figure 5.2, three stability stereonet plots are calculated for illustrative

cases of $P_p$ = 0, of $P_p$ equal to that expected for the normal hydrostatic pressure at the particular depth, and of $P_p$ that predicted by the model described above. $C$ was set equal to 0 in all cases.

For a given $T$, the Matlab™ code stress_on_plane.m calculates the $\tau$ and $\sigma$ over the range of possible planes with the resulting *SNR* displayed by steronet_plot.m. The *SNR* for each of the presumptive fault planes (Table 2A-1) are also calculated separately versus the fluid pressure $P_f$ for two cases assuming $C = 0$ (red band), or $C = 5$ MPa (green band) and for the range of stress tensors $T$ possible according to the stress model (Figure 5.3).

*5.7.1 Analyses on seismic attributes derived lineaments*

Fig. 5B-1 shows the horizontal slice of the seismic attributes (most-negative curvature), at the depth of the basement, from a 3D seismic survey conducted in an area encompassing two moderate magnitudes earthquakes [*Chopra et al.*, 2017]. The location of Figure 5B-1 was not reported in *Chopra et al.* [2017] and it is inferred that, by cross-referencing with reported earthquake's source mechanisms, these two events marked on Figure 5B-1b are corresponding to the $M_W$ 3.6 and 4.1 events compiled in *Schultz et al.* [2017] and analyzed in Figure 5.2 and 5.3. Authors were informed that the seismic data plotted in Fig. S5 remains proprietary at the moment of this writing. Stability analysis in Fig. 5.2 utilizes the average stress values calculated for these two events with coordinates reported in *Schultz et al.* [2017].

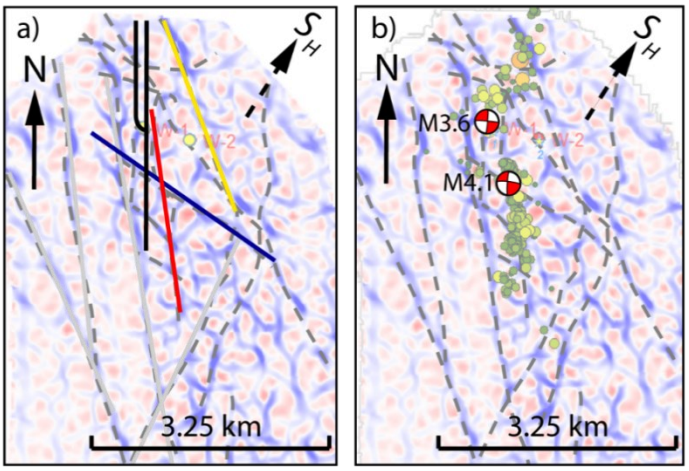


**Figure 5B-1.** Fault inferred through reflection seismic survey with background colours represent the attributes used for seismic interpretation. a) Black lines represent the HF wells trajectories. Coloured lines represent lineaments interpreted as faults with. b) Beach balls show the resolved focal mechanisms for earthquakes $M_W$ 3.6 and $M_W$ 4.1. In both a) and b) dashed black arrows represent the orientation of $S_H$.

Assuming the interpreted lineaments in Figure 3B-1 represent actual faults, of the two dominant transtentional fault orientations (i.e., NNW-SSE and NE-SW, Figure 3B-1), only the NNW-SSE faults appear to be within the spectrum of instability (Fig. 3.2a), while the NE-SW is not. This is in agreement with the reported induced earthquake fault orientations that produced slip nucleation. On the other hand, one fault identified (oriented NWW-SEE), strikes at a stable angle of ~90° from $S_H$, is observed to be non-seismogenic despite proximity to the HF wells. Faults which are more optimally oriented but further away from the seismogenic HF wells are not activated either.

Though the stability analysis provided results in agreement with the observed, or lack of, seismicities, along the lineaments features, it is uncertain if these features represent actual faults within the Duvernay Formation. The interpretation presented by *Chopra et al.* [2017] is made

assuming that the faulting in the sedimentary layers of the study area is basement controlled [*Schultz et al.*, 2017].

*5.7.2 Expectations for C and $\mu$*

In previous studies**,** *C* is often neglected as an earthquake generally reactivates on an existing fault with assumed negligible cohesion. This assumption is supported by most reported lab experiments [*Marone*, 1998]. Though the residual strength of the fault, post shear failure, is measured to be very small, fault regains strength after a period of healing. Earlier researchers debated whether such strength recovery is in forms of friction *[Dieterich, 1972; 1978; Marone and Saffer, 2007]* or cohesion *[Tenthorey and Cox, 2006; Weiss et al., 2016]*. Distinguishing the effects of cohesion and friction as the results of fault healing observed in the lab experiment is also reported to be difficult [*Muhuri et al.,* 2003]. Regardless, measured post shear failure cohesion on clay-rich material is generally small [*Day,* 1992*; Scuderi et al.,* 2017a*; Ikari and Kopf, 2017]*. *Sone and Zoback* [2013] observed that the creep rate of the shale positively correlates with the clay content of the testing sample. Shales from Duvernay and other Paleozoic formations in Western Canada Sedimentary Basin generally has low clay content and would have lesser cohesion than the clay-rich shales. Though larger numbers (>20 MPa) have been reported [*Tenthorey and Cox,* 2006] from fault healing experiment, those numbers are measured at high temperature (> 800 °C) and high-pressure (> 175 MPa) environment. In this study, a conservative range of *C* between 0 – 5 MPa is considered. This admittedly requires more study.

Similarly, values for the in-situ friction static coefficient $\mu$ are not reported. Though a default $\mu$ of 0.6 - 1 is often assumed for many geomechanical studies [*Morris et al.,* 1996*; Zoback,* 2010; *Ellsworth, 2013*], laboratory measurements conducted on the different material composition

of fault gouge at different testing environments observed a wide range of the $\mu$. A brief compilation on the reported $\mu$ known to the authors, and with mineral composition relevant to this study, is provided in the supplementary material (Table S3). X-ray diffraction analysis (Table 3B-4) on five of the samples extracted in-situ from boreholes drilled targeting or through the Duvernay formation shows the significant components of Quartz and Calcite, with a smaller amount of clay. By the friction measurements reported on samples with comparable mineral composition and normal pressures, the $\mu$ of the fault studied in this analysis is selected between 0.4 - 0.8.

**Table 5B-3.** A summary of previous friction test on rocks with mineral composition related to this study

| Author(s) | Mineral composition | Pressure | μ |
|---|---|---|---|
| *Kohli and Zoback* [2013] | Various shale | 10 - 30 MPa | 0.6 -0.79 |
| *Scuderi et al.* [2017b] | Granular quartz powders | 2-18 MPa | 0.56-0.58 |
| *Gu and Wong* [1994] | Quartz | 50-190 MPa | 0.6-0.8 |
| *Crawford et al.* [2008] | Quartz-kaolinite mixtures | 5-50 MPa | 0.5-0.65 |
| *Tembe et al.* [2010] | Quartz and clay | 40 MPa | 0.5-0.75 |
| *Takahashi et al.* [2007] | Quatz and clay | 75 MPa | 0.53-0.68 |
| *Scott et al.* [1994] | Granular quartz | 25 MPa | 0.37 – 0.66 |
| *Ikari et al.* [2011] | Quartz and clay | 20 -50 MPa | 0.6-0.7 |
| *Ikari et al.* [2007] | Quartz and clay | 4-100 MPa | 0.5-0.6 |
| *Morrow et al.* [2000] | Quartz and calcite | 100 MPa | 0.4 -0.85 |
| *Nakatani and Scholz* [2004] | Quartz | 60 MPa | 0.5-0.7 |
| *Marone et al.* [1990] | Quartz | 50-190 MPa | 0.5–0.65 |
| *Logan and Rauenzahn* [1987] | Quartz and clay | 25-70 MPa | 0.5-0.6 |
| *Weeks and Tullis* [1985] | Dolomite marble | 50-75 MPa | 0.56-0.58 |
| *Samuelson and Spiers* [2012] | Quartz and clay | 35 MPa | 0.47-0.61 |

**Table 3B-4.** Mineral composition (in percentage by weight) of the Duvernay shale determined through Xray-Diffraction analysis. The abbreviated column names stand for: Q – Quartz, C – Calcite, A – Anorthite, O – Orthoclase, K – Kaolinite, P-Pyrite, A2 – Ankerite, D – Dolomite, M – Muscovite/Illite, A3- Albite

| Formation | Q | C | A | O | K | P | A2 | D | M | A3 |
|---|---|---|---|---|---|---|---|---|---|---|
| Duvernay | 36.3 | 12.8 | 4.2 | 16.5 | | 1.7 | 10.3 | 6.4 | 11.4 | 2.9 |
| Duvernay | 40.3 | 7.6 | 4.2 | 7.1 | | 0.7 | 9.3 | 16.7 | 10.8 | |

| | | | | | | | | | | |
|---|---|---|---|---|---|---|---|---|---|---|
| Duvernay | 14.1 | 35 | 3.4 | 11.6 | | 3.6 | 3.8 | 22.3 | 6.2 | 6 |
| Duvernay | 40.2 | 12.4 | 6.1 | 10.1 | 0.8 | 2.3 | 6.9 | 5.4 | 9.3 | |
| Beaverhill | 37.9 | 14.2 | 4.1 | 11.8 | | 3.5 | 4.6 | 3.4 | 19.7 | |

*5.7.3 Monte-Carlo Simulation of SNR for different $P_f$ (for Fig. 5.4a)*

The Monte-Carlo calculation used in obtaining the whisker-plot distributions of Figure 4a in the main text are described here. Eqn. 5.1 had defined the SNR which can be calculated with knowledge of the complete stress tensor described by $S_h$, $S_V$, $S_H$, $\phi$ and $P_P$. The Monte-Carlo simulation is excited with a large number of realizations (n = 5000) and ranges of stress components constrained by uncertainties reported [*Shen et al.*, 2019].

Uncertainties caused by varying epicentre's depths are accounted for by assuming a variation of ± 500 m relative to the center of the Duvernay Formation within which the events are most likely to have occurred [*Eaton et al.*, 2018]. In each realization, $S_h$ and $S_V$ are corrected to the randomly selected depth with their tangent slopes discussed earlier. Random $S_H$ finally calculated based on the statistical distribution of the local stress shape-ratio (ranging between 0.46-0.84, [*Shen et al.,* 2019]) and previously generated $S_h$ and $S_V$. We ignore uncertainties in $\phi$ and in the orientations of the focal mechanism solutions due to the lack of reported values. A Matlab™ function monte_carlo_stability.m is provided to perform such analysis. With input parameters for each earthquake shown in Table 2A-1 and stress values in Table 2A-2, this function is adapted in monte_carlo_stability_runit.m to generate the histogram used for plotting Figure 3.4

*5.7.4 Monte-Carlo Simulation of $P_f$ required to initiate slip (for Fig.5.4b)*

Similar to Figure 5.4a, the Monte-Carlo method is adapted to calculate the probability distribution of $P_f$ needed to activate the faults by rearranging Eqn. 5.1:

$$P_f = \sigma - (\tau - C)/\,\mu \tag{5B-1}$$

Calculation of Eqn. 5B-1 utilizes the previously calculated 5000 Shear Stress ($\tau$) and normal pressure ($\sigma$) values along with five-thousand randomly generated $C$ (0 – 5 MPa) and $\mu$ (0.4 – 0.8). The Matlab™ function monte_carlo_stability.m and script monte_carlo_stability_runit.m also perform this analysis.

## References


Anderson, E. M. (1942), The dynamics of faulting and dyke formation with applications to Britain, Oliver and Boyd.

Atkinson, G. M., D. W. Eaton, H. Ghofrani, D. Walker, B. Cheadle, R. Schultz, R. Shcherbakov, K. Tiampo, J. Gu, and R. M. Harrington (2016), Hydraulic fracturing and seismicity in the western canada sedimentary basin, *Seismological Research Letters*, *87*(3), 631-647.

Byerlee, J. (1978), Friction of rocks, *Pure and Applied Geophysics PAGEOPH*, *116*(4-5), 615-626, doi:10.1007/BF00876528.

Chang, K. W., and P. Segall (2016), Injection-induced seismicity on basement faults including poroelastic stressing, *Journal of Geophysical Research: Solid Earth*, *121*(4), 2708-2726, doi:10.1002/2015jb012561.

Chopra, S., R. K. Sharma, A. K. Ray, H. Nemati, R. Morin, B. Schulte, and D. D'Amico (2017), Seismic reservoir characterization of Duvernay shale with quantitative interpretation and induced seismicity considerations—A case study, Interpretation, 5(2), T185-T197.

Crawford, B., D. Faulkner, and E. Rutter (2008), Strength, porosity, and permeability development during hydrostatic and shear loading of synthetic quartz-clay fault gouge, Journal of Geophysical Research: Solid Earth, 113(B3).

Day, R. W. (1992), Effective cohesion for compacted clay, Journal of geotechnical engineering, 118(4), 611-619.

Deng, K., Y. Liu, and R. M. Harrington (2016), Poroelastic stress triggering of the december 2013 crooked lake, alberta, induced seismicity sequence, *Geophysical Research Letters*, *43*(16), 8482-8491, doi:10.1002/2016gl070421.

Dieterich, J. H. (1972), Time-dependent friction in rocks, Journal of Geophysical Research, 77(20), 3690-3697.

Dieterich, J. H. (1978), Time-dependent friction and the mechanics of stick-slip, in Rock Friction and Earthquake Prediction, edited, pp. 790-806, Springer.

Eaton, D. W., N. Igonin, A. Poulin, R. Weir, H. Zhang, S. Pellegrino, and G. Rodriguez (2018), Induced Seismicity Characterization during Hydraulic-Fracture Monitoring with a Shallow-Wellbore Geophone Array and Broadband Sensors, Seismological Research Letters, 89(5), 1641-1651.

Ellsworth, W. L. (2013), Injection-induced earthquakes, Science, 341(6142), 1225942.

Foulger, G. R., M. P. Wilson, J. G. Gluyas, B. R. Julian, and R. J. Davies (2018), Global review of human induced earthquakes, *Earth-Science Reviews*, *178*, 438-514, doi:https://doi.org/10.1016/j.earscirev.2017.07.008.

Gomberg, J. (2018), Unsettled earthquake nucleation, *Nature Geoscience*, *11*(7), 463-464, doi:10.1038/s41561-018-0149-x.

Gu, Y., and T.-f. Wong (1994), Development of shear localization in simulated quartz gouge: Effect of cumulative slip and gouge particle size, pure and applied geophysics, 143(1-3), 387-423.

Harris, R. A. (1998), Introduction to special section: Stress triggers, stress shadows, and implications for seismic hazard, *Journal of Geophysical Research: Solid Earth*, *103*(B10), 24347-24358, doi:10.1029/98jb01576.

Haug, K., and J. S. Bell (2016), Compilation of In Situ Stress Data from Alberta and Northeastern British Columbia (tabular data, tab delimited), edited, Alberta Energy Regulator, AER/AGS Digital Data.

Heidbach, O., M. Rajabi, K. Reiter, M. Ziegler, and W. Team (2016), World Stress Map Database Release 2016, edited by G. D. Services.

Lele, S., T. Tyrrell, G. Dasari, and W. Symington (2017), Geomechanical analysis of hydraulic fracturing induced seismicity at duvernay field in western canada sedimentary basin, in *Geoconvention 2017*, edited, p. 5 pp. , Canadian Society of Petroleum Geologists, Calgary.

Li, L., J. Tan, D. A. Wood, Z. Zhao, D. Becker, Q. Lyu, B. Shu, and H. Chen (2019), A review of the current status of induced seismicity monitoring for hydraulic fracturing in unconventional tight oil and gas reservoirs, *Fuel*, *242*, 195-210, doi:https://doi.org/10.1016/j.fuel.2019.01.026.

Ikari, M. J., and A. J. Kopf (2017), Seismic potential of weak, near-surface faults revealed at plate tectonic slip rates, Science advances, 3(11), e1701269.

Ikari, M. J., D. M. Saffer, and C. Marone (2007), Effect of hydration state on the frictional properties of montmorillonite-based fault gouge, Journal of Geophysical Research: Solid Earth, 112(B6).

Ikari, M. J., C. Marone, and D. M. Saffer (2011), On the relation between fault strength and frictional stability, Geology, 39(1), 83-86.

López-Comino, J. A., S. Cesca, J. Jarosławski, N. Montcoudiol, S. Heimann, T. Dahm, S. Lasocki, A. Gunning, P. Capuano, and W. L. Ellsworth (2018), Induced seismicity response of hydraulic fracturing: Results of a multidisciplinary monitoring at the wysin site, poland, *Scientific Reports*, *8*(1), 8653, doi:10.1038/s41598-018-26970-9.

Kohli, A. H., and M. D. Zoback (2013), Frictional properties of shale reservoir rocks, Journal of geophysical research: solid earth, 118(9), 5109-5125.

Logan, J. M., and K. A. Rauenzahn (1987), Frictional dependence of gouge mixtures of quartz and montmorillonite on velocity, composition and fabric, Tectonophysics, 144(1-3), 87-108.

Marone, C., C. B. Raleigh, and C. Scholz (1990), Frictional behavior and constitutive modeling of simulated fault gouge, *Journal of Geophysical Research: Solid Earth*, *95*(B5), 7007-7025.

Marone, C. (1998), Laboratory-derived friction laws and their application to seismic faulting, Annual Review of Earth and Planetary Sciences, 26(1), 643-696.

Marone, C., and D. M. Saffer (2007), Fault friction and the upper transition from seismic to aseismic faulting, The Seismogenic Zone of Subduction Thrust Faults, 346-369.

Marone, C., C. B. Raleigh, and C. Scholz (1990), Frictional behavior and constitutive modeling of simulated fault gouge, Journal of Geophysical Research: Solid Earth, 95(B5), 7007-7025.

Morris, A., D. A. Ferrill, and D. B. Henderson (1996), Slip-tendency analysis and fault reactivation, Geology, 24(3), 275-278.

Morrow, C., D. E. Moore, and D. Lockner (2000), The effect of mineral bond strength and adsorbed water on fault gouge frictional strength, Geophysical research letters, 27(6), 815-818.

Nakatani, M., and C. H. Scholz (2004), Frictional healing of quartz gouge under hydrothermal conditions: 1. Experimental evidence for solution transfer healing mechanism, Journal of Geophysical Research: Solid Earth, 109(B7).

Ong, O. N., D. R. Schmitt, R. S. Kofman, and K. Haug (2016), Static and dynamic pressure sensitivity anisotropy of a calcareous shale, *Geophysical Prospecting*, *64*(4), 875-897, doi:10.1111/1365-2478.12403.

Raleigh, C., J. Healy, and J. Bredehoeft (1976), An experiment in earthquake control at rangely, colorado, *Science*, *191*(4233), 1230-1237.

Ruina, A. (1983), Slip instability and state variable friction laws, *Journal of Geophysical Research: Solid Earth*, *88*(B12), 10359-10370, doi:10.1029/JB088iB12p10359.

Samuelson, J., and C. J. Spiers (2012), Fault friction and slip stability not affected by CO2 storage: Evidence from short-term laboratory experiments on North Sea reservoir sandstones and caprocks, Int. J. Greenh. Gas Control, 11, S78-S90.

Savage, H. M., J. D. Kirkpatrick, J. J. Mori, E. E. Brodsky, W. L. Ellsworth, B. M. Carpenter, X. Chen, F. Cappa, and Y. Kano (2017), Scientific exploration of induced seismicity and stress (seisms), *Sci. Dril.*, *23*, 57-63, doi:10.5194/sd-23-57-2017.

Schmitt, D. R., C. A. Currie, and L. Zhang (2012), Crustal stress determination from boreholes and rock cores: Fundamental principles, Tectonophysics, 580, 1-26.

Schultz, R., H. Corlett, K. Haug, K. Kocon, K. MacCormack, V. Stern, and T. Shipman (2016), Linking fossil reefs with earthquakes: Geologic insight to where induced seismicity occurs in alberta, *Geophysical Research Letters*, *43*(6), 2534-2542, doi:10.1002/2015gl067514.

Schultz, R., R. Wang, Y. J. Gu, K. Haug, and G. Atkinson (2017), A seismological overview of the induced earthquakes in the Duvernay play near Fox Creek, Alberta, Journal of Geophysical Research: Solid Earth, 122(1), 492-505.

Schultz, R., G. Atkinson, D. Eaton, Y. Gu, and H. Kao (2018), Hydraulic fracturing volume is associated with induced earthquake productivity in the duvernay play, *Science*, *359*(6373), 304-308.

Scholz, C. H. (2019), *The mechanics of earthquakes and faulting*, 3 ed., Cambridge University Press, Cambridge, doi:DOI: 10.1017/9781316681473.

Scott, D. R., C. J. Marone, and C. G. Sammis (1994), The apparent friction of granular fault gouge in sheared layers, Journal of Geophysical Research: Solid Earth, 99(B4), 7231-7246.

Scuderi, M., C. Collettini, and C. Marone (2017a), Frictional stability and earthquake triggering during fluid pressure stimulation of an experimental fault, Earth and Planetary Science Letters, 477, 84-96.

Scuderi, M., C. Collettini, C. Viti, E. Tinti, and C. Marone (2017b), Evolution of shear fabric in granular fault gouge from stable sliding to stick slip and implications for fault slip mode, Geology, 45(8), 731-734.

Segall, P., and S. Lu (2015), Injection-induced seismicity: Poroelastic and earthquake nucleation effects, *Journal of Geophysical Research: Solid Earth*, *120*(7), 5082-5103, doi:10.1002/2015jb012060.

Shapiro, S. A., and C. Dinske (2009), Fluid-induced seismicity: Pressure diffusion and hydraulic fracturing, *Geophysical Prospecting*, *57*(2), 301-310, doi:10.1111/j.1365-2478.2008.00770.x.

Shen, L., D. R. Schmitt, and K. Haug (2018), Measurements of the States of In Situ Stress for the Duvernay Formation near Fox Creek, West-Central Alberta. *Rep.*, 29 pp, Alberta Energy Regulator/Alberta Geological Survey.

Shen, L., D. R. Schmitt, and K. Haug (2019), Quantitative constraints to the complete state of stress from the combined borehole and focal mechanism inversions: Fox Creek, Alberta, Tectonophysics, 764, 110-123.

Shipman, T., R. MacDonald, and T. Byrnes (2018), Experiences and learnings from induced seismicity regulation in alberta, *Interpretation*, *6*(2), SE15-SE21, doi:10.1190/int-2017-0164.1.

Sibson, R. H. (1990), Conditions for fault-valve behaviour, *Geological Society, London, Special Publications*, *54*(1), 15-28, doi:10.1144/gsl.Sp.1990.054.01.02.

Sone, H., and M. D. Zoback (2013), Mechanical properties of shale-gas reservoir rocks—Part 2: Ductile creep, brittle strength, and their relation to the elastic modulusMechanical properties of gas shale—Part 2, Geophysics, 78(5), D393-D402.

Stoakes, F. A., and S. Creaney (1985), Sedimentology of a carbonate source rock: The duvernay formation of alberta, canada

Takahashi, M., K. Mizoguchi, K. Kitamura, and K. Masuda (2007), Effects of clay content on the frictional strength and fluid transport property of faults, Journal of Geophysical Research: Solid Earth, 112(B8).

Tembe, S., D. A. Lockner, and T. F. Wong (2010), Effect of clay content and mineralogy on frictional sliding behavior of simulated gouges: Binary and ternary mixtures of quartz, illite, and montmorillonite, Journal of Geophysical Research: Solid Earth, 115(B3).

Tenthorey, E., and S. F. Cox (2006), Cohesive strengthening of fault zones during the interseismic period: An experimental study, Journal of Geophysical Research: Solid Earth, 111(B9).

Terakawa, T., and E. Hauksson (2018), Absolute Stress Fields in the Source Region of the 1992 Landers Earthquake, Journal of Geophysical Research: Solid Earth, 123(10), 8874-8890.

Townend, J., and M. D. Zoback (2000), How faulting keeps the crust strong, *Geology*, *28*(5), 399-402, doi:10.1130/0091-7613(2000).

Wang, R., Y. J. Gu, R. Schultz, and Y. Chen (2018), Faults and non-double-couple components for induced earthquakes, *Geophysical Research Letters*, *45*(17), 8966-8975, doi:10.1029/2018gl079027.

Wang, R., Y. J. Gu, R. Schultz, M. Zhang, and A. Kim (2017), Source characteristics and geological implications of the january 2016 induced earthquake swarm near crooked lake, alberta, *Geophysical Journal International*, *210*(2), 979-988, doi:10.1093/gji/ggx204.

Vavryčuk, V. (2014), Iterative joint inversion for stress and fault orientations from focal mechanisms, Geophysical Journal International, 199(1), 69-77.

Weeks, J. D., and T. E. Tullis (1985), Frictional sliding of dolomite: A variation in constitutive behavior, Journal of Geophysical Research: Solid Earth, 90(B9), 7821-7826.

Weiss, J., V. Pellissier, D. Marsan, L. Arnaud, and F. Renard (2016), Cohesion versus friction in controlling the long-term strength of a self-healing experimental fault, Journal of Geophysical Research: Solid Earth, 121(12), 8523-8547.

Wilson, M. P., F. Worrall, R. J. Davies, and S. Almond (2018), Fracking: How far from faults?, *Geomechanics and Geophysics for Geo-Energy and Geo-Resources*, *4*(2), 193-199, doi:10.1007/s40948-018-0081-y.

Zoback, M. D. (2010), Reservoir geomechanics, Cambridge University Press.

# Chapter 6. States of in-situ stress in the Duvernay East Shale Basin and Willesden Green of Alberta, Canada: variable in-situ stress states effect fault stability

## 6.1 Introduction

Globally, anthropogenically-induced earthquakes (up to M 5 near densely populated areas) in the past decade had brought much attention to the risk and hazards associated with the injection [e.g., hydraulic fracturing, *R Schultz et al.*, 2020 *Atkinson et al.,* 2020, waste disposal, *Hincks et al.*, 2018, geothermal, *Eberhart‐Phillips and Oppenheimer*, 1984; *Ellsworth et al.,* 2019] and, to a lesser extent, extraction of masses [e.g., *Maury et al.*, 1992; *van Thienen-Visser and Breunese*, 2015; *Wetmiller*, 1986] into/from the subsurface. Extensive efforts had been expended, mainly through the lenses of seismology, with various triggering mechanisms proposed and investigated. Nevertheless, these reports, attempting to forensically correlate earthquakes temporally and spatially with industrial activities, are primarily statistical in nature. There are very few exceptions that are developed on the basis of the deterministic geomechanical observations [e.g., *Deng et al.*, 2016; *McClure and Horne*, 2011; *Shen et al.*, 2019b; *Stork et al.*, 2018; *Ameen* 2016].

Despite the elevated societal concerns, only a small fraction of the HF operations results in moderate earthquakes (M > 2). Loosely, these wells associated with this seismicity are classified as being 'seismogenic' [e.g., *Atkinson et al.*, 2016; *R Schultz et al.*, 2018]; the absence of triggered earthquakes in a majority of other HF wells are attributed to the varying geological conditions. To date, the cause of such discrepancies is not yet well understood, but this is not surprising as statistical correlation requires the input of past earthquake records that would be absent for

aseismic areas. Techniques similar to the Probabilistic Seismic Hazard Analysis (PSHA), which relies on establishing statistical or empirical patterns of reported earthquake events [*Castaños and Lomnitz*, 2002], are adopted to perform susceptibility analysis for large landmasses. Nevertheless, PSHA had demonstrated deficiencies with striking examples of Tohoku earthquake (M 9.1, 2011), Wenchuan earthquake (M 7.9, 2008), Haiti earthquake (M 7.0, 2010) that happened in areas mapped, often owing to their relative prior seismic quiescence, as lower risk [*Stein et al.*, 2012]; these events generated heated debate [e.g., *Frankel*, 2013].

An alternative and more deterministic alternative approach to assessing seismic risk, particularly in areas that historically have been aseismic, is to evaluate the stability of candidate faults under the framework of the Coulomb friction law. Such studies are currently needed for both the purpose of understanding the risk of induced earthquakes and comparing them with statistical susceptibility maps to test the objectivity [*Stein et al.*, 2011]. The growth of deep waste fluid disposal and large-scale hydraulic fracturing for both geothermal and hydrocarbon resources motivates further development of more direct assessments, particularly in areas that are historically aseismic.

The aim of this study is to provide more insights on the area's susceptibility to induced seismicities and and further the controlling geomechanical factors on anthropogenically induced earthquakes overall. Here , we focus on a ~200 km × 200 km study area (Figure 6.1a, 6.2a) includes the city of Red Deer that is a few tens of kilometers to the east of a moderate HF induced earthquake ($M_W$ 3.8/$M_L$ 4.2, [*Schultz and Wang*, 2020]) referred to hereafter as the *Event A* (Table 6.1). In the text below, we start by reviewing the induced activities near the study area with particular attention to the seismic events reported in the East Shale Basin and seismic quiescence

in the nearby Willesden Green oilfield. An overview on the geology and the knowledge, in the public domain, of the states of in-situ stress is included.

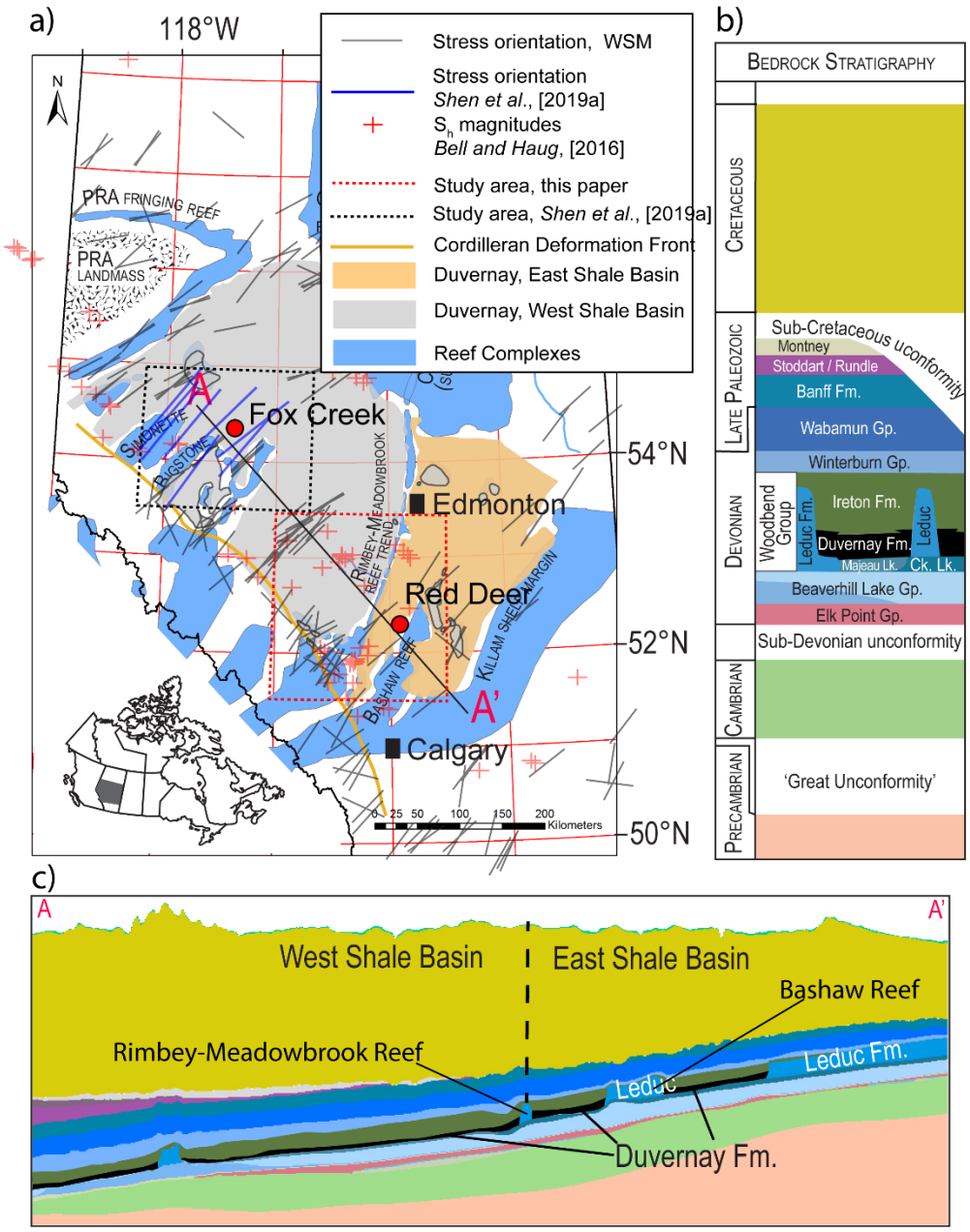


**Figure 6.1. a)** Overview of the study area in Alberta, Canada with West Shale Basin (WSB) and East Shale Basin (ESB), respectively, that are separated by the Rimbey-Meadowbrook reef trend. **b)** Bedrock

stratigraphy of western central Alberta with elements from the cross-section shown in **c)** for the line A-A' in a). Vertical depth in c) is exaggerated by 50 times.

**Table 6.1.** Significant Seismic Events in the Area and Relation to stress field modelled in this study

| | | | Conjugate Plane Orientations | | | | | Andersonian Stress | | | | |
|---|---|---|---|---|---|---|---|---|---|---|---|---|
| | | | | | | | | | Principal Components (MPa) | | | |
| Event | Date<br>$M_W$ | Epicenter<br>Depth | Plane | Strike | Dip | Rake | Azimuth<br>$\phi$ | $S_h$ | $S_V$ | $S_H$ *(Borehole Failure)* | $S_H$ *(FM inversion)* | $P_P$ |
| A* | 03/04/2019<br>$M_W$ 3.8 | N52.20°<br>W114.11°<br>2.5 km | 1 | 101° | 72° | -30° | N47°E | 46 | 61 | 75 – 116 | 65 -106 (median: 84) | 40 |
| | | | 2 | 201° | 62° | -160° | | | | | | |
| B* | 03/10/2019<br>$M_W$ 3.9 | N52.57°<br>W115.26°<br>15 km | 1 | 138° | 49° | 77° | N52°E | - | - | - | - | - |
| | | | 2 | 338° | 42° | 105° | | | | | | |
| C† | 10/19/1996<br>$M_W$ 3.4 | N52.21°<br>W115.25°<br>5.2 km | 1 | 205°<br>*156°* | 44°<br>*44°* | 136° | N50°E | 110 | 132 | 132 - 155 | - | - |
| | | | 2 | 329°<br>*302°* | 61°<br>*51°* | 55° | | | | | | |

*reported in *Schultz and Wang* [2019]

†FM analysis attributed to R. Horner as provided in *Baranova et al*., [1998].

We construct a quantitative model for the state of 3D-stress and formation pore-fluid-pressure for the Duvernay Formation where is targeted for HF operations and overlap with the ranges of earlier reported events' hypocentral depths constrained through geophysical observations

and geological reasonings [*Eaton et al.,* 2018]. Subsequently, we apply such model for a series of fault slip tendency analysis in understanding, first, the factors affecting the stability of the 2019 events and, second, in the mapping the susceptibility for seismicity over the area. This paper concludes with thoughts regarding the mechanisms triggering induced seismicity in this area.

## 6.2 Geological background and induced earthquakes

### *6.2.1 Regional seismicity: natural and induced*

Prior to 2014, this study area, and generally the Alberta Basin, has experienced low levels of seismicity. Only 35 cataloged events above $M_W$ 2.5 since 1960 [*USGS*, 2020] are reported within this area. Many of these are associated with a cluster occurring in the SW part of the study area (**Figure 6.2b**) possibly related to natural gas production during the 1980s, in a region that was consequently referred to as the Rocky Mountain House Seismic Zone (RMHSZ) [*Rebollar et al.*, 1982; *Wetmiller*, 1986]. Slightly to the west of our study area (~W116.20º, N52.75º), wastewater-injection-induced earthquakes have been reported at the Cordel Field [*R Schultz et al.*, 2014] with $M_L < 4$ in the early 2000s. It should be noted, however, that the RMHSZ and Cordel Field events are all located to the SW of the Cordilleran Deformation Front in a highly faulted and fractured rock masses thrust upwards during the orogeny that produced during the formation of the Rocky Mountains.

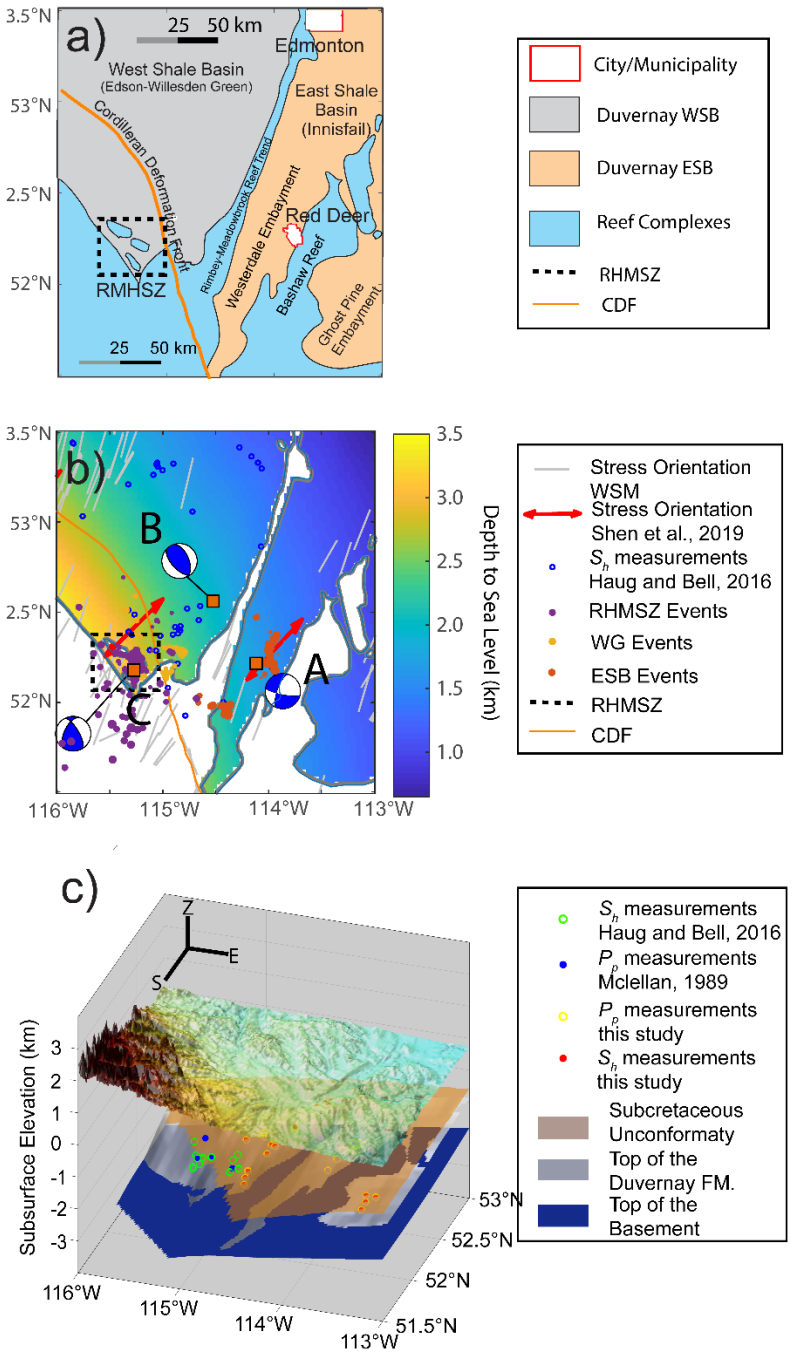


**Figure 6.2. a)** Map of major geographic features associated with the Duvernay Formation, including the WSB and the ESB. **b)** Detail map of epicenters within the study area, the background color indicates depths from sea level to the tops of the Duvernay Formation. Outlined brown squares: three major earthquakes

designated A, B, and C with FM resolved (details Table 6.1) **c)** 3D view of the study area, comprising in stratigraphically descending order, the surface topography, sub-Cretaceous unconformity

However, since 2010, in an area to near the town of Fox Creek to the north of this study area, a number of induced earthquakes have been linked to multistage hydraulic fracturing for hydrocarbons primarily within the high-organic bearing Devonian marine sedimentary formations. While only less than 2 percent [*Atkinson et al.*, 2016] of these wells are reportedly seismogenic (even less if vertical HF wells are to be included), a series of $2.5 < M_L < 4.7$ earthquakes occurred within a small area near the town of Fox Creek, Alberta including some felt by the local residents and triggered the *AER*'s [2015] traffic light protocal resulting in the shut-in of the responsible wells. These earthquakes also motivated an extensive analysis of borehole-logging and pressure-testing data [*Shen et al.*, 2018; 2019a], leading to the construction of a quantitative model for the stress tensor over the Fox Creek area that was then applied in understanding the conditions for stability/instability along the rupture planes for 11 of the largest induced events [*Shen et al.*, 2019b].

Since 2012, this study area also experienced high levels of the HF activities into the target Duvernay Formation [*BMO*, 2019]. However, the area near the city of Red Deer appeared to be seismically quiescent and was consequently mapped by *Pawley et al.* [2018] as low risk in comparison with the Fox Creek area to the north; this difference in seismic activities initially motived, for the purposes of comparison, development of the quantitative stress model described here. This quiescence ended, however, with two events felt by the local residents in March 2018 and March 2019.

The source parameters of the $M_L$ 3.1 (Mar 9, 2018) earthquake were poorly constrained – owing to the sparse seismometers network near the epicenter at the time. However, the larger *Event A* and later deployed dense seismometer array, deployed after the M 3.1 event [*Schultz and Wang*, 2020], allowed for accurate FM determination; subsequently, an intensified search in the area detected > 1200 additional earthquakes in the Westerdale Embayment from 2014 to 2019 with magnitudes of $M_L$ -0.7 - 4.3 [*Schultz and Wang*, 2020]. Temporal and spatial associations are highly correlated with HF activities in the ESB that commenced in 2012 [*BMO*, 2019]. Meanwhile, the other well-developed HF sites (i.e., north of the city of Red Deer, the Ghost Pine Embayment, and most of the WG, see Figure 6.2a) have remained quiescent.

The $M_L$ 4.2/$M_W$ *3.8* earthquake (Mar 4, 2019) near the city of Red Deer triggered a new traffic light protocol [*AER*, 2019], followed by the shut-in of the suspected seismogenic wells. Earthquakes with smaller magnitudes (< 2.5) are also reported in the nearby Willesden Green (WG) area of the Duvernay play in the West Shale Basin (WSB). More recently, intensive studies of existing seismic data revealed additional small clusters, some of which are likely natural but many associated with HF operations since 2014 [*Schultz and Wang*, 2020]. In contrast, HF wells in portions of the East Shale Basin (ESB, i.e., Ghost Pine Embayment and most of the WG) remain non-seismogenic up to the date of this writing.

It is also important to note the occurrence of an $M_W$ 3.9 ($M_L$ 4.3) earthquake (*Event B*) at a depth of 15 km in the NW corner of the study area on Mar 10, 2019 (see Figure 6.2b). This event's mid-crustal depth, its reverse fault FM, and its distances to any HF activity diagnosed it as a natural event [*Schultz and Wang*, 2020].

### *6.2.2 Regional geology*

HF activities occur within the Duvernay Formation that is bisected by the Rimbey-Meadowbrook Reef Trend (Figure 6.1a, 6.2a) into areas referred to as the WSB in gray and ESB in tan [*Preston et al.*, 2016]; the portions of the WSB and ESB are, respectively, within the Edson-Willesden Green (WG) and the Innisfail Regulatory Assessment Areas [*Preston et al.*, 2016]. The Bashaw Reef complex extends NE into the ESB, separating the Westerdale and Ghost Pine Embayments. The depth of the Duvernay Formation increases significantly from NE to SW (Figure 6.1c) due to its steep dip and increasing surface topography westward (Figure 6.2c). The Cordilleran Deformation Front is another important structural element (Figure 6.1a, 6.2a) that separates highly deformed lithologies in the SW from those more gently dipping to the NE.

The broad sedimentary stratigraphy (Figure 6.1b) is underlain by Paleoproterozoic metamorphic and igneous rocks and is comprised of: 1) a thick succession of Paleozoic to lower Mesozoic carbonates, shales, and evaporites deposited predominantly during tectonic quiescence, and 2) an upper succession of Mesozoic basin-filling siliciclastics that formed in response to orogenesis along the western margin of North America. Orogenesis initiated in the Late Jurassic (163 Ma) and continued through to the Eocene (52.1 Ma), punctuated by periods of tectonic quiescence [*Pană and van der Pluijm*, 2015]. Significant unconformities separate the sedimentary successions from the underlying crystalline rocks and within the sedimentary succession between phases 1 and 2. Here, we provide a brief overview of the local structure with a focus on those elements that possibly relate to faults in the study area.

Precambrian basement rocks in the WCSB comprise a number of Archean- to Paleoproterozoic-aged tectonic provinces [*Ross et al.*, 1991; *Ross and Eaton*, 1999, Figure 6.3].

The Archean portion of the basement represents the oldest and most stable part of the cratonic rocks that make up the core of North America. Younger rocks were welded to the Archean crust in the Paleoproterozoic during accretionary and collisional processes [*Hoffman*, 1988]. The Precambrian tectonic domains within the study area were delineated through potential field maps and U-Pb geochronology from basement samples taken from drill-cores [*Burwash et al.*, 1994; *Ross and Eaton*, 1999; *Ross et al.*, 1991]. A prominent feature in potential field data is the NE-trending Snowbird Tectonic Zone, which bisects the basement in the northwestern part of the study area (Figure 6.3). Another prominent basement feature can be seen on LITHOPROBE 2D seismic profiles that cut through the NE section of the study area, where they show a strong subhorizontal reflector interpreted as an abrupt change in metamorphic facies [*Bouzidi et al.*, 2002] or as regional sills at about 15 to 20 km depth. A series of reflectors with an apparent westward dip of about 45° are readily in the uppermost metamorphic crust. Interestingly, an abrupt 10 km change in the topography of the Mohorovičić discontinuity has also been interpreted [*Bouzidi et al.*, 2002] that hints at tectonic motions in the distant past.

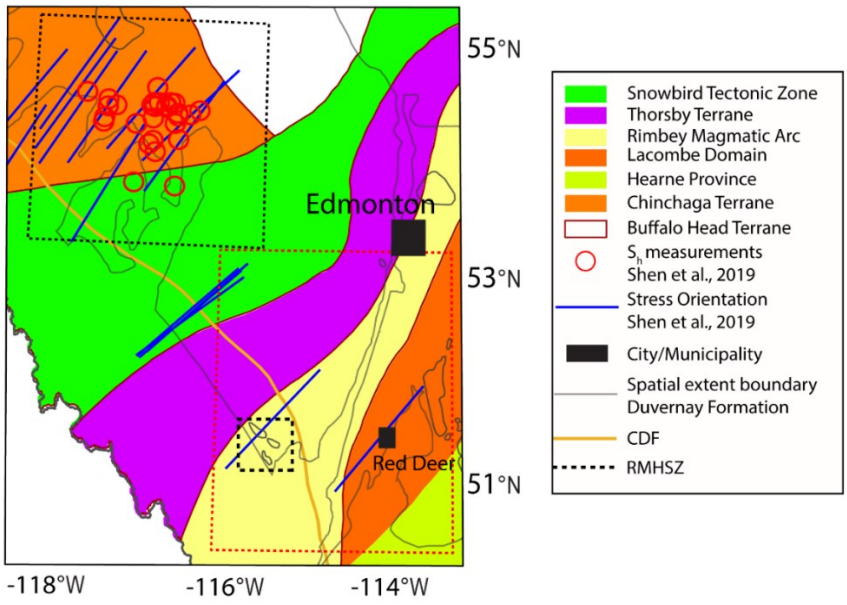


**Figure 6.3**. Geological features of our study are with a) map of the tectonic provinces mapped by *Ross et al.* [1991] with their boundary lines reproduced in *Gu and Shen* [2015].

Despite the clear features revealed in the crustal-scale seismic-reflection profiles, there is little clear evidence for any large-scale tectonic reactivation within the Precambrian basement. Nevertheless, numerous studies (see recent review in *Corlett et al.* [2018]) have used various lines of evidence suggesting that the modest fault displacements of the basement may have influenced the deposition of the Paleozoic sediments. If fault-related displacements of the basement exist in the study area, they remain below the limit of seismic resolution [*Ross and Eaton*, 1999]. For example, *Edwards and Brown* [1999] attempted to relate the 540 km long, suspiciously linear Rimbey-Meadowbrook Leduc Reef trend that runs through the study area to possible basement structure, but no relationship was observed. The debate of possible Precambrian basement fault control on the overlying Phanerozoic sediments, however, is longstanding (see *Moore* [1988]).

The top of the Precambrian basement in the study area marks a global event in the form of a nonconformity, known as the 'great unconformity' [*Peters and Gaines*, 2012]. In the study area, the basement (Figure 6.2c) is overlain by Middle Cambrian rocks, which are, in turn, overlain by Devonian strata, separated by the sub-Devonian unconformity. Within this assemblage, the Devonian succession comprises a middle Devonian package, of mostly siliciclastics and evaporites, and an Upper Devonian succession of mostly carbonate reefs and intervening basin-filling siliciclastic. The Upper Devonian Duvernay Formation consists mainly of bioturbated siliceous, calcareous, and argillaceous mudstones; it is the main target for HF because of its attractive organic content [*Rokosh et al.*, 2009] and mechanical stiffness. Presently, the Duvernay Formation still retains significant gas and condensate hydrocarbons that motivate exploitation with horizontal drilling and associated hydraulic fracturing.

The Devonian succession is overlain by late Paleozoic strata, the top of which is the sub-Cretaceous unconformity (Figure 6.1c, 6.2c). Early Cretaceous siliciclastic sediments overlie the Paleozoic succession in the study area, which were deposited in a foreland basin setting [*Beaumont*, 1981]. The foreland basin was created during flexure of the lithosphere induced from crustal loading initiated by convergent tectonics, commencing possibly as early as the late Jurassic, although the timing is debated [*Chen et al.*, 2019; *Pană and van der Pluijm*, 2015]. The flexure of the Precambrian basement surface and the Paleozoic strata is particularly apparent as an increasing structural dip toward the orogen in the west (Figure 6.1c). The easternmost edge of the deformation front falls within the SW corner of the study area.

To the best of our knowledge, there are no currently available reports of pre-existing faults to the east of the Cordilleran Deformation Front within the study area - in stark contrast to the

well-known sequence of major thrust faults and complex structures exposed in the fold and thrust belt [e.g., *Price*, 2001] to the south-west of this boundary. Within the subsurface, evidence from seismic-reflection profiles suggest faulting effecting successions from the Paleozoic to Mesozoic: both to the north associated with the Peace River Arch [e.g., *Weides et al.*, 2014] and to the south [e.g., *Galloway et al.*, 2018; *Lemieux*, 1999]. Additionally, to the north near Fox Creek, the existence of faults has been inferred from various interpretations of seismic reflection data and its attributes [e.g., *Chopra et al.*, 2017; *Corlett et al.*, 2018; *Eaton et al.*, 2018; *Ekpo et al.*, 2017; *Weir et al.*, 2018]. Sedimentation patterns and accommodation trends within the basin could also be indicative of differential vertical displacements. For example, to the north of our study area, syndepositional motion along faults related to the Snowbird Tectonic Zone may have resulted in anomalous localized thickening of the Albian Viking Formation [*Schultz et al.*, 2019].

### *6.2.3 Regional state of stress*

According to the Mohr-Coulomb static frictional criterion, slip occurs on a pre-existing plane of weakness will displace once the in-plane traction exceeds the clamping force that depends on the effective plane-normal traction, a static co-efficient of friction, and a cohesive strength. Once sliding commences, dynamic rate-state frictional relations may be invoked to describe subsequent behavior [e.g., see review in *Marone,* 1998]. We cannot rule out the possibility that the events described here occurred on planes of weakness that may have already been imperceptibly creeping at extremely small rates, but given the traditional absence of seismicity and the lack of evidence for large deformation within the sediment stack outside of the deformation front, it is not clear that a rate-state formulation, that would require accurate knowledge of actual long-term slip rates and material properties, is warranted. Hence, our stability analysis will rely

on the static frictional principles originated by Amontons and supported by *Byerlee's* [1978] finding that the static friction $\mu$, constrained between 0.6 to 0.85, can reasonably describe the rock's in-situ behavior.

Despite this straightforward principle, direct quantitative analysis of the slip-tendency of faults remains rare, largely owing to the difficulties in obtaining reliable quantitative stress magnitudes and fluid pressures [e.g., *Schwab et al.*, 2017]; those variables are required to revolve for the traction forces on the faulting planes. To obtain representative stress values, nearly all of the studies that attempt to quantitatively assess the stability on faults are forced to make numerous assumptions; these often include the use of estimates of stress and pore pressure gradients, reliance on frictional constraints along hypothetical optimally oriented, critically-stressed, faults, or application of the lateral constraint concept. The values provided by such methods may deviate significantly from those actually exist within the Earth's interior; particularly, the use of the lateral constraint assumption may mislead [e.g., *Ong et al.*, 2016]. More accurate stress field information can only be reliably obtained from deep boreholes. Consequently, the state of stress is best constrained by different but complementary measurements, and the economic costs associated with obtaining this information can be prohibitive. If stress field data are, however, available, it should be used as one component of a risk assessment in areas with low or nonexistent historical seismicity.

Earlier studies on the states of in-situ stress for the Alberta Basin started with the identification of borehole elongation measured with caliper logs [*Bell and Gough*, 1979] with a more recent review by *Reiter et al.* [2014] these data are incorporated in the latest version of the Word Stress Map [WSM, *Heidbach et al.*, 2016] and included in the *Haug and Bell* [2016]

compilation. In addition to the latest compilation of the WSM, 20 borehole images with identified borehole breakouts (BO) and drilling-induced tensile fractures (DITF) were recorded in a published dataset [*Shen et al.*, 2018]. These studies all broadly show a relatively uniform NE-SW compression across the Alberta Basin; as such the azimuth $\phi$ of the greatest horizontal compression $S_H$ is expected to be ~45° in our study area.

It is usually assumed that the minimum horizontal compression $S_h$ magnitudes can be measured directly in certain transient pressure tests by finding the borehole pressure $P_{fc}$ at which a small induced hydraulic fracture closes. These tests are variously called extended leak-off tests, micro-fracture tests, mini-fractures tests, and diagnostic fracture injection test (DFIT), with this latter term currently usually used for all such tests (see discussion of the methods in *Shen et al.* [2018]). *Bell and Caillet* [1994] compiled 106 $S_h$ measurements from tests in the Mesozoic hydrocarbon reservoirs. *Haug and Bell* [2016] have updated these data by incorporating results from later studies [*Bell and Bachu*, 2003; *Bell and Grasby*, 2012; *McLellan*, 1989; *Woodland and Bell*, 1989]; 39 of the reported results are within this study area (see Figure 6.2b, 6.2c). Their results are reported as average secant $S_h$ gradient of ~19 kPa/m. *McLellan* [1989] also reported 16 formation pore pressure $P_P$ measurements and 4 $S_h$ measurements, which had not been included in other published stress-data compilations (see Figure 6.2c). More recently, *Shen et al.* [2018] reported 38 $S_h$ measurements from recently conducted tests in the Duvernay Formation, including 12 measurements in our study region that provided an average secant gradient of ≈ 21 kPa/m, but if analyzed together as a set plotted with depth, indicated a tangent gradient $\Delta S_h(z)/\Delta z \approx 32$ kPa/m.

No reliable method to directly measure the $S_H$ magnitudes from deep boreholes yet exists; it can only be constrained. *Shen et al.* [2019a] attempted to overcome this limitation in the Fox

Creek area by combining the measured values of $S_h$ and $S_V$ with the 'shape factor' [*Bott*, 1959] derived by inverting the local FM to provide constrained $S_H$ distribution; efforts had also been expended with borehole failures identified by examining the image logs [*Shen et al.*, 2018]. These inversions, too, show $\sigma_2$ is close to vertical in agreement with the Andersonian assumptions and indicating a strike-slip faulting environment at least within the Duvernay Formation.

## 6.3 Stress measurements and fault stability

### *6.3.1 Data and Quantitative 3D Stress Model*

Here, we develop a model that quantitatively predicts the states of stress for a crustal volume that encompasses the Duvernay Formation within the study area. Similar to a previous study in the Fox Creek area to the north [see Figure 6.1, *Shen et al.*, 2019a], we provide a Matlab™ program [RD_stress.m, see *Shen and Schmitt*, 2020], allowing users to estimate the stress magnitudes within the Duvernay Formation beneath the desired surface position in the study area.

In alignment with most other geomechanical analysis, this work assumes an Andersonian [*Anderson*, 1951] state of stress that at a sufficient depth the vertical compression $S_V$ is the principal stress; and by default, the other two principal stresses are the maximum $S_H$ and minimum $S_h$ horizontal compressions. The azimuth direction $\phi$ of $S_H$ then provides enough information to complete the total stress tensor [e.g., *Schmitt et al.*, 2012]. When necessary to depart from the Andersonian assumption, the three principal compressions are denoted $\sigma_1 > \sigma_2 > \sigma_3$. Further determination of the formation rock's pore fluid pressure $P_P$ is necessary for calculating effective stresses and understanding potential rock failure. In this writing, fluid pressures and compressive stresses are assigned with positive signs following standard conventions in the geosciences.

Details of the analysis on ($S_h$, $S_V$, $P_P$ and $\phi$) employs methods similar to that used in the earlier study of the Fox Creek area [*Shen et al.*, 2018; 2019a]. Here, only a brief summary of the results are provided.

*Constraining $S_h$, $S_V$, $P_P$ and $\phi$*

Stress orientations azimuths $\phi$ (Figure 6.4a) are obtained from an analysis of breakout and drilling induced tensile fractures observed in one newly analyzed image log (Lat: 52.281062, Lon: -113.962146) near the city of Red Deer combined with earlier compilations [*Reiter et al.*, 2014; *Shen et al.*, 2019a]. In the study area, 54 measurements of $\phi$ reported by *Haug and Bell* [2016] and *Reiter et al.* [2014] are included in the current compilation of the WSM. Recently, *Shen et al.* [2019] constructed a detailed stress orientation map for the Kaybob assessment area with 20 image logs collected in the area near the foothills of the Alberta Basin (see Figure 6.1a). One of the image logs reported in *Shen et al.* [2019] is located within our study region, and several more image logs are located nearby. In this analysis, one new log (Lat: 52.281062, Lon: -113.962146) near Red Deer, is obtained and analyzed. Similar to observations made in the Kaybob area [*Shen et al.*, 2019], we do not observe a correlation between $\phi$ and depth. Some recent studies have been able to effectively use abundant natural fractures from image logs [e.g., *Ameen, 2019*], but this approach is not available to us as natural fractures appear only rarely within out set of image logs.

A map of relative confidence (Figure 6.4b) is also computed according to the distances and consistency/quality of nearby measurements [some included in *Shen et al.*, 2018, 2019a]. In essence, the normalized uncertainty $A \rightarrow 0$ if the prediction is made with at least three nearby measurements with high consistency. On the other hand, the uncertainty $A \rightarrow 1$ for locations that are either far away from observations and/or with multiple observations, in close proximity,

reporting different $\phi$. It is important to note that convention on the value of A here differs from that in *Shen et al.,* [2019a] and care needs to be taken when making comparisons. However, this does not affect in any way our findings. In general, confidence on the predicted stress orientation $\phi$ in the southwest of our study area is low, where the Duvernay Formation is absent where Leduc Formation reefs are present. Mathematically, this is due to a number of WSM observations, some from presumably the same boreholes, reporting different $\phi$ within a small distance.

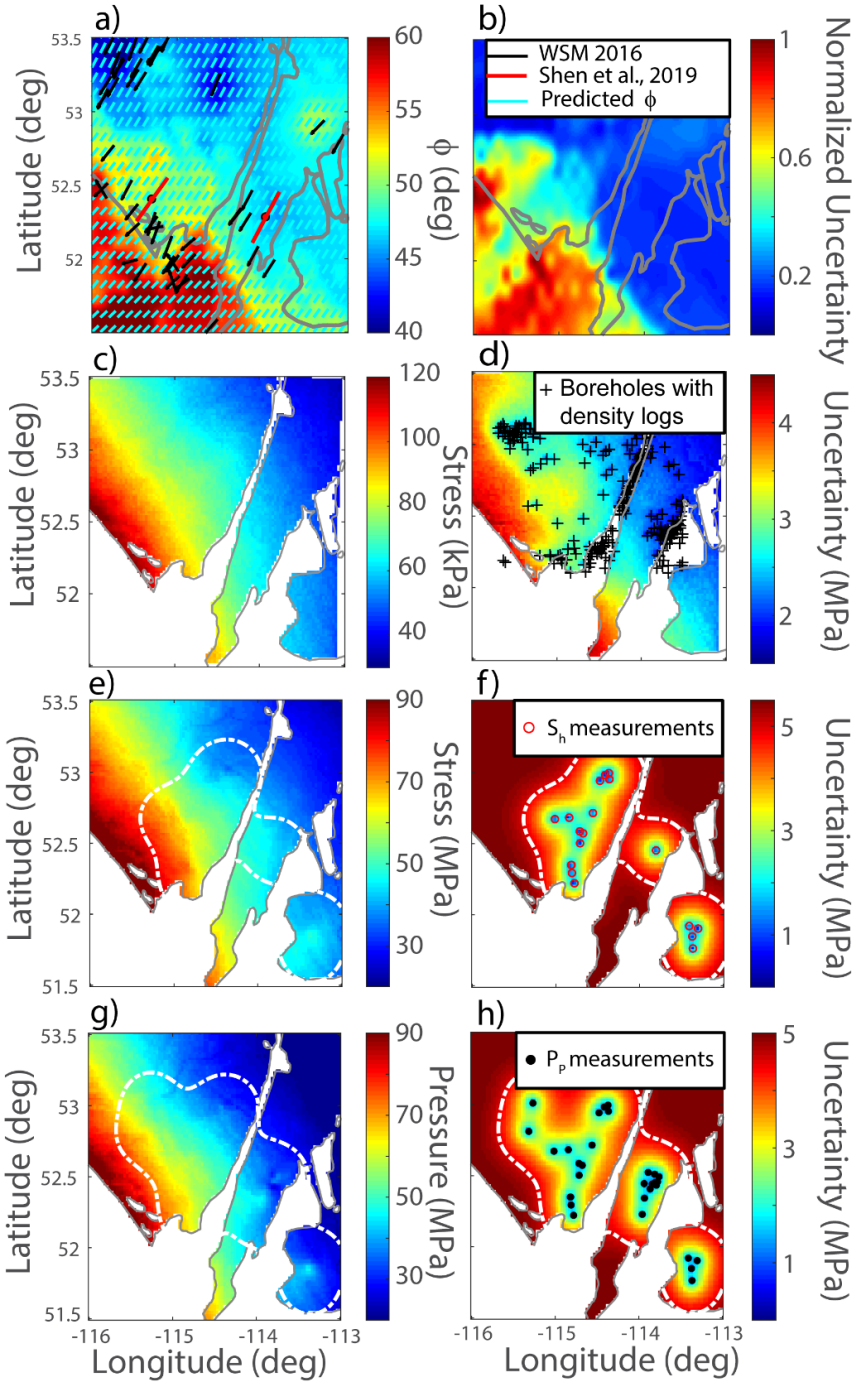


**Figure 6.4.** Spatial maps for the states of stress in the center of the Duvernay Formation of our study area. **a)** the orientation of $S_H$ and **b)** normalized uncertainty A (from 0 - 1). **c)** the magnitudes of $S_V$ and **d)** uncertainty. **e)** magnitudes of $S_h$ and **f)** the uncertainties. **g)** and **h)** shows the $P_P$ and the uncertainties.

White contours in e) to h) show the enclosed areas with uncertainties of less than 5 MPa for $S_h$ and 4.5 MPa for $P_P$. Gray lines enclose the areal extent of the Duvernay Formation engulfed by the Leduc reefs.

$S_V$ magnitudes are calculated by integration with the depth of the density logs while corrected using the Green's function method (GFM) of *Liu and Zoback* [1992] to account for variations in the surface topography. GFM is identical to a low-pass filter that removes the influences of short-wavelength topographic changes (e.g., valleys and mountain peaks) and preserves longer wave-length regional trends that impact $S_V$ at greater depth. We calculated the magnitudes of $S_V$ (Figure 6.4c) for the Duvernay Formation and its uncertainties (Figure 6.4d) by adapting the same GFM approach along with a 3D density model constructed from 681 density logs collected from Alberta Geological Survey's well log database, employing a kriging method documented in *Shen et al.* [2018].

$S_h$ magnitudes are determined from the analysis of transient pressure records that includes 8 new analyses and 12 from *Shen et al.* [2018]; and formation pore fluid pressures $P_P$ are determined with 22 records from *Shen et al.* [2018] and 20 newly collected ones. All of the available local $S_h$ and $P_P$ from measurements in the Mesozoic [*Haug and Bell*, 2016; *McLellan*, 1989] and more recent Duvernay [*Shen et al.*, 2018; 2019a] compilations are plotted versus depth (Figure 6.5) for comparison. Linear regression of $S_h$ vs. $z$ (see Figure 6.5a) gives

$$S_h(z) = 22.2\ (\pm 5.6)\ \frac{kPa}{m} z - 12.8(\pm 3.4)\ MPa \tag{6.1}$$

while a similar analysis for $P_P$ vs $z$ (see Figure 6.5b) yields

$$P_P(z) = 24.8\ (\pm 3.6)\ \frac{kPa}{m} z - 23.8(\pm 10.0)\ MPa \tag{6.2}$$

Further, to build a spatial map, we shifted measured $S_h$ and $P_p$ to the same depth using the tangent gradients $\Delta S_h(z)/\Delta z$ and $\Delta P_P(z)/\Delta z$ calculated through linear regression (Eqn. 6.1 and 6.2) to the depth of the Duvernay Formation. The uncertainties are updated with error propagation accordingly. Subsequently, simple kriging is performed with measurement points shifted into the same depth level. Maps for the magnitudes of $S_h$ (Figure 6.4e) and $P_P$ (Figure 6.4h) are constructed for the depths of the top of the Duvernay, with the uncertainty of the prediction (Figure 6.4f, 6.4h) calculated as the square root of the kriging variance. Such uncertainties are governed by two factors: 1) the uncertainties of the measurements: various interpretation techniques are adapted, reporting a range of results [see *Shen et al.,* 2018, for details] containing the values of $S_h$ and $P_p$ and their corresponding uncertainties, and 2) proximity to the observations. The uncertainties of the prediction generally rise at locations further away from observations. At sufficient distance, the prediction essentially becomes the average value of all observations, and the variances of the observations are considered as the uncertainty. In our model, the uncertainties of $S_h$ and $P_P$ near observations generally range from 0.5 MPa to 1 MPa, and rises to as high as 5.5 MPa for $S_h$ and 5 MPa for $P_P$ at distances further away. Generally, we consider the values predicted within the white contours in Figure 6.4e - h to be reliable, which mark the uncertainty of 5 MPa for $S_h$ and 4.5 MPa for $P_P$.

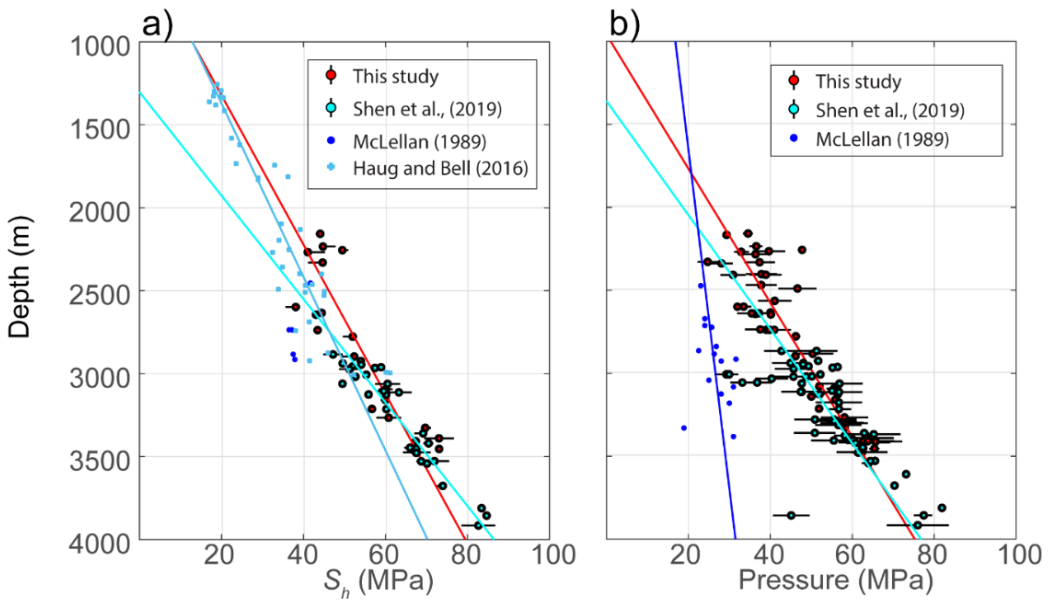


**Figure 6.5.** Reported measurements (with their respective uncertainties) and linear regression results for **a)** $S_h$ and **b)** $P_P$ from different sources. In **a)** cyan line shows the linear regression of the measurements of *Shen et al*. [2019]; azure line represents the linear regression of *Haug and Bell* [2016] data. Red line denotes the linear regression of the data utilized in this work. In b) blue line denotes the linear regression of *McLellan* [1989] data; cyan and red lines show the linear regression of *Shen et al*. [2019] measurements and data utilized in this work.

*Constraints on $S_H$*

As noted, the determination of $S_H$ is challenging; more efforts are necessary to describe its constraint using first, values obtained from the observed borehole breakout dimensions, and second, from inversion of the $M_W$ 3.8's FM solution (*Event* A). Our earlier attempts [*Shen et al.,* 2019a] on constraining $S_H$ through borehole images for the areas near Fox Creek was not successful; few borehole failures are observed in the Duvernay segments of the image logs and the knowledge of $P_P$ of other geological units was not available for analysis at that time. However, here we revist this method with 1. Earlier reported pore pressures [see *McLellen*, 1989, included

in *Shen and Schmitt*, 2020] on the geological formations more comparable to the segments of BO observation and 2. Newly acquired imagelog with continuous borehole failures on the segments overlap with the depths of the Duvernay Formation. Though the exact $P_P$ near the borehole is still up to debate, these newly found $P_P$ measurements and borehole images allow us to attempt constraining $S_H$ again.

Constraints of $S_H$ relies on the assumption that a borehole breakout is confined to those zones near the borehole, where the state of concentrated stress makes the material unstable to shear rupture. Consequently, the edge of the breakout delimits the zones of stability and instability from one another; the total angular width of the breakout $\beta$ can provide a constraint on the stress magnitudes. If a simple Mohr-Coulomb failure criterion is employed, $S_H$ may be expressed as [*Valley and Evans*, 2019]

$$S_H = \frac{C_o + \frac{2P_W}{1-sin\psi} - \frac{2P_p sin\psi}{1-sin\psi} - S_h(1-2\cos\beta)}{1+2\cos\beta} \tag{6.3}$$

where $\psi = \tan^{-1}(\mu)$ is the internal friction angle, $C_0$ is the unconfined compressive strength, and $P_w$ is the wellbore fluid (mud) pressure. If $P_P = P_{w,}$ this collapses to a form that excludes $\psi$

$$S_H = \frac{C_o + 2P_P - S_h(1-2\cos\beta)}{1+2\cos\beta} \tag{6.4}$$

that then, to account for the excess fluid pressure when $P_P$ is different from $P_W$, matches the values given in as the widely used form

$$S_H = \frac{C_o + 2P_P + \Delta P - S_h(1-2\cos\beta)}{1+2\cos\beta} \tag{6.5}$$

that $\Delta P = P_w - P_P$ [*Barton et al.*, 1988 ]; this equation only applies when $P_w$ is close to $P_P$.

Determination of the exact $\beta$ value from the image logs collected in this study is also hampered by the lack of access to the raw logs and poor image-scan resolution. Thus, we assigned considerable uncertainty (10 degrees) to the measured BO widths. For smaller or blurry BOs, which the widths are difficult to determine and thus not reported, a range of 0 - 45° is assumed. Further, we also tested a wide range of the rock's compressive strength unconfined compressional strength (UCS) from 60 to 160 MPa that represent broadly the range reported from a limited number of axial loading tests [*Ong et al.*, 2015]. The knowledge on the mechanical strength of the rocks from other geological units are unknown to the authors; hence here the same range is assumed as the Duvernay Shales.

Owing to the sparsity of the measurement points and large uncertainties, instead of constructing a map, we focused on providing a vertical profile of $S_H$ as a function of depth ($z$). Given the relatively high uncertainties associated with this method, we utilized a Monte Carlo (n = 5000) style analysis using randomly selected input parameters for Eqn. 6.5 and their corresponding uncertainties of: 1. $S_h$ predicted by Eqn. 6.1; 2. $P_W$ obtained from wells' drilling reports [see *Shen and Schmitt*, 2020]; 3 $P_P$ predicted by Eqn. 6.2 for the Duvernay Formation and other geological units by *McLellan* [1989]; 4. ranges of C and $\beta$ discussed in the paragraph above. A uniform distribution is assumed within the ranges of uncertainties. The median, $25^{th}$, and $75^{th}$ percentiles of the cumulative density function of the calculated $S_H$ distribution are shown in Figure 6.6. Despite the uncertainties, this analysis does give ranges of $S_H$ that are consistent with a strike-slip faulting environment.

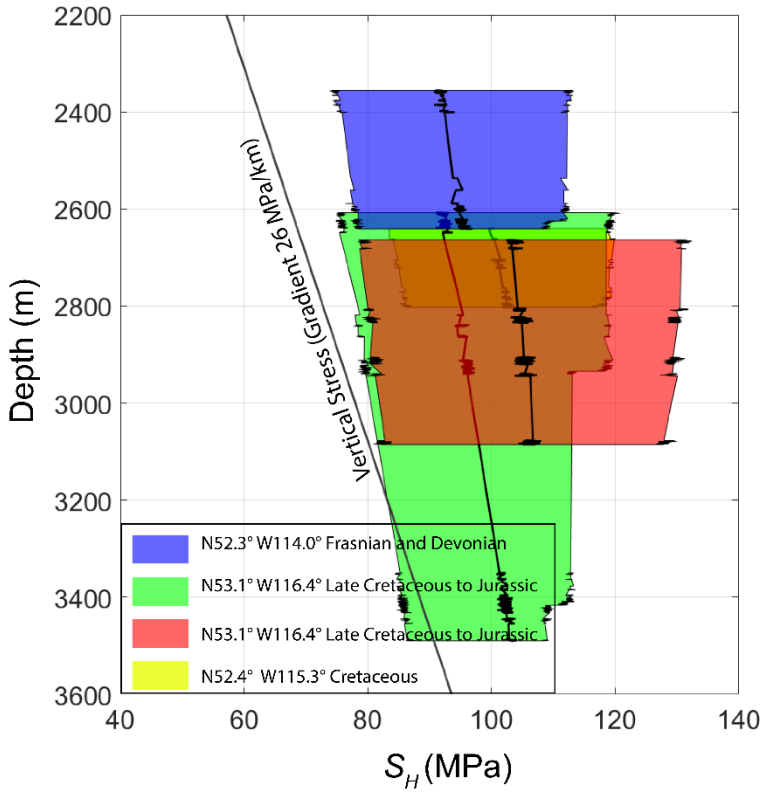


**Figure 6.6.** Estimated maximum stress $S_H$ from borehole breakouts. The width of the polygons mark the 25th to 75th percentile of the cumulative probability density functions for $S_H$, computed using Monte-Carlo methods, and the black lines stand for median values of $S_H$.

Eqn. 6.5 gives an estimate $S_H$ assuming the $P_w$ is reasonably close to $P_P$ [*Barton et al.*, 1988]. In practice, the validity of this assumption is challenged by a number of factors mostly revolving around the pressure difference between the $P_P$ and $P_w$. Here, we analyzed the borehole images that had also provided constraints on the stress orientation. Due to the limited available data, we also included two more sets of borehole images from locations slight to the west of our study area. Three of the image logs analyzed in this study report the segments of borehole BOs that are observed in the formations from the Cretaceous Glauconite to Cardium Formations (see Figure 6.6), with reported $P_P$ of ~24.6 MPa at 2.6 km (expected $P_w$ = ~30 MPa) to ~28.6 MPa at

3.9 km (expected $P_w$ = ~47 MPa) [*McLellan*, 1989]. From the segments of BOs within the Woodbend Group, including the Duvernay Formation, we observed $P_P$ overpressure of 38.2 MPa (2.5 km deep, expected $P_W$ ~= 30 MPa). It is also important to acknowledge the caveats that the reported $P_P$ from *McLellan* [1989] may not be representative of the virgin state of the reservoir as those measurements were made after extended periods of production. We also do not have knowledge of the $P_P$ in the Ireton Formation (Figure 6.1d) shales overlying the Duvernay Formation because it has not been of economic interest and there are no appropriate measurements within it.

Admittedly, there might exist more sophisticated method in identifications of fine details that might present in borehole images and account for secondary factors that are not considered here [e.g., chemical reaction, thermal effect, see review in *Schmitt et al.,* 2012]. Our constraints on the $S_H$ will unlikely be more robust through employment of such methodological improvement. The uncertainties caused by the lack of measurements on the rock's exact geomechanical properties. The question of whether $P_P = P_W$ remain unanswered

Despite all the caveats mentioned earlier, we calculated $S_H$ using the same approach for the other three wellbores (see Figure 6.6) for comparison with the results of stress inversion discussed below. It is worth noting that the $S_H$ values obtained from the depth of the Devonian Woodbend Group in the east part of our study area are shallower than those from the younger Cretaceous - Jurassic formations (e.g., Viking, Cardium, Glauconite) in the west because of the westward dipping trends owing to the elevated topography and isostasy within the foreland basin. Regardless, the constraints obtained through both borehole stability analysis, using observations

from the overpressured Duvernay Formation and less pressured Cretaceous -Jurassic geological units, reports that $S_H$ can be described roughly as a function of depth:

$$0.0143\ z\ \frac{MPa}{km} + 40MPa \leq S_H(z) \leq 0.0143\ z \frac{MPa}{km} + 80MPa \tag{6.6}$$

for z (depth) ranges between 2200 and 3200 m; the unit of stress is MPa; for 3200m < z < 3600m, owing to the constraint that $S_H > S_V$, we have:

$$S_V(z) < S_H(z) \leq 0.0143\ z \frac{MPa}{km} + 80MPa \tag{6.7}$$

An alternative way to constrain $S_H$ relies on the inversion of the FM solutions for the relative stress magnitudes represented by the shape factor $R$ in combination with knowledge of the other two components of the stress tensor. This starts with the assumption that a fault slip is parallel to the shear traction force on the faulting plane [*Wallace*, 1951]; consequently, such slip directions obtained from observed earthquake FM solutions may be inverted [*Michael*, 1984; *Vavryčuk*, 2014] for the relative deviatoric components of the stress tensor that may be used to construct the shape factor $R$ :

$$R = \frac{\sigma_1 - \sigma_2}{\sigma_1 - \sigma_3} \tag{6.8}$$

The $R$ determined in inversions gives only the relative deviatoric components of the stress tensor, but in a strike-slip faulting environment, it does allow $S_H$ to be calculated if $S_V$ and $S_h$ are independently found [e.g., *Hardebeck and Hauksson*, 2001; *Shen et al.*, 2019a]. One well-known complication, however, is that the FM solution for an arbitrary earthquake yields two possible conjugate slip planes: a true and an auxiliary fault plane; without additional complementary

geological observations, cannot be discriminated from one another. There are, however, numerous strategies that attempt to determine which plane may be preferred (e.g., *Vavryčuk* [2014]).

Here, the single FM is available from this *Event A* (see Table 6.1) is used first to determine *R,* assuming it occurs in or near the Duvernay. This was accomplished using modified inversion subroutines from *Vavryčuk*'s [2014] recently published code to each of the conjugate planes in isolation – it is worth noting that *Vavryčuk*'s [2014] subroutine automatically pick the conjugate plane that is more prone to slip, based on an Mohr-Coulomb style analysis, as the 'true' faulting plane. Here, we modify *Vavryčuk*'s [2014] program to not perform such discrimination two independent analysis are conducted for both conjugate planes from *Event A* and their results are compared. This is to account for the fact that we do not know which conjugate plane is the actual faulting plane. The distribution of possible *R* values (Figure 6.7a) was calculated in a 1000-realization Monte-Carlo approach; the orientation of each conjugate plane (see Table 6.1) randomly varied by up to ±5° to account for expected uncertainties in the FM solution.

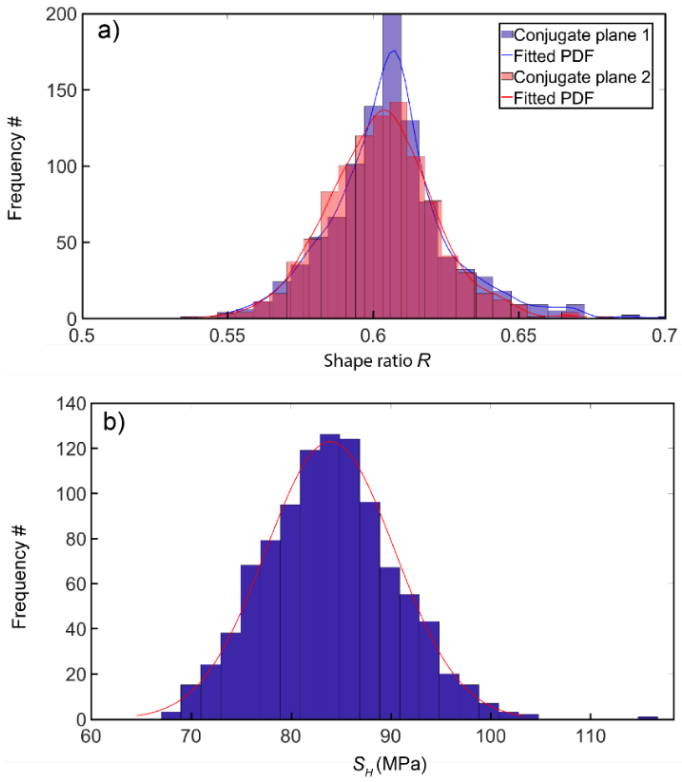


**Figure 6.7. a)** The distribution of shape factor $R$ computed for both conjugate fault planes from the earthquake's ($M_W$ 3.8/$M_L$ 4.2) focal mechanism solution, and **b)** inverted $S_H$ with the predicted $S_h$ and $S_V$ at the epicenter, using the $R$ distribution from conjugate plane 1, assuming an Andersonian strike-slip stress regime.

Without considering uncertainty, direct stress inversion performed on both planes report similar shape ratios (0.621 for plane 1 and 0.608 for plane 2); adding ranges of uncertainty to the FM solution for *Event A* (Table 6.1) produces similar distributions of $R$ between 0.55 and 0.67 (median 0.62, Figure 7a). Using the early constrained quantitative stress magnitudes of 40.3 MPa $\leq S_h \leq$ 50.9 MPa and 58.0 MPa $\leq S_V \leq$ 63.4 MPa together with the estimated range of values for $R$ via rearrangement of Eqn. 6.8 allows for the range 65 MPa $\leq S_H \leq$ 106 with median $S_H$ = 84 MPa (see Figure 6.7b). Considering the uncertainties and caveats associated with this approach, the

higher bounds of the uncertainty for $S_h$ (5.3 MPa, see section 6.3.3) are used; the uncertainty of $S_V$ (2.7 MPa) is selected from the regional average, given the abundant well logs used for the 3D density model. Using stress inversion results from either conjugate plane does not change the distributions of $S_H$ significantly. $S_H$ constrained through this approach is consistent with that $S_H$ of 75–116 MPa (see Figure 6.6) constrained from borehole failures.

### *6.3.2 Stability analysis for the $M_W$ 3.8 earthquake (Event A)*

As noted earlier, initiation of rupture along a plane of weakness is presumed to be governed by the Mohr-Coulomb frictional criterion that may be used to assess the stability or slip-tendency of an arbitrarily oriented plane of weakness [e.g., *Morris et al.*, 1996]. This is accomplished by resolving the stress tensor into its effective component tractions normal ($\sigma - P_f$) and tangential ($\tau$) to the plane of interest [see *Schmitt*, 2014, for a review] The criterion is expressed, adapting *Morris et al.* [1996], with a shear-to-normal ratio (*SNR*)- slip is expected once the friction on the surface is overcome

$$\mu < \frac{\tau - C}{\sigma - P_f} \equiv SNR \tag{6.9}$$

In Eqn. 6.9 we retain the cohesion $C$, which most authors dispense with, but as shown in *Shen et al.* [2019b], does noticeably influence the slip-tendency of the plane of weakness. Also, in this simplified form, a static frictional coefficient $\mu$ controls the ratio between shear friction and normal traction acting on the surface. $P_f$ should be considered as the fluid pressure active at the plane of weakness where slip occurs; it is sometimes omitted in many studies. For reasons discussed later, it is important to distinguish it from the ambient pore pressure $P_P$ measured from boreholes within the Duvernay Formation [see *Shen et al.* 2019b]. Admittedly, this simple friction

law may not adequately describe the rock's in-situ frictional behavior, particularly in a sense that the friction is impacted by the slip rate [e.g., *Marone*, 2021]. However, in this study we only attempt to investigate the incipient activation of the fault - we expect the slip rate is close to zero at this stage. Further, no information that is essential to describe a rate-dependent friction law is available for the studied geological units here.

We assess the ranges of fault *SNR* at *Event A's* focus by calculating the normal $\sigma$ and shear $\tau$ tractions resolved onto all possible planes [*Shen et al.* 2019b] using the stress model's predicted stress states (Table 6.1) with the most probable $S_H$ magnitude (84 MPa). The calculations were repeated with three different $P_f$ of i) absent $P_f = 0$ (Figure 6.8a), ii) $P_f = P_H$ of the normal hydrostatic pressure assuming a standard water pressure gradient of 10 MPa/km (Figure 6.8b), and iii) $P_f = P_P$ (Figure 6.8c) as found in our model interpolated from the transient borehole fluid tests in the Duvernay Formation. A previous meta-analysis of laboratory frictional measurements [*Shen et al.*, 2019b] suggested friction ranged $0.4 < \mu < 0.8$; these bounding values are shown for the sake of reference as contours in Figure 6.8. Although we do not know the actual frictional coefficients acting at *Event* A's focus, this is taken to be a reasonable range to assess stability. For example, one might expect that those planes subject to $SNR < 0.4$ will remain clamped while those with $SNR > 0.8$ will be increasingly prone to slip [*Shen et al.,* 2019b]. As such, Figure 6.8 demonstrates how $P_f$ controls fault stability.

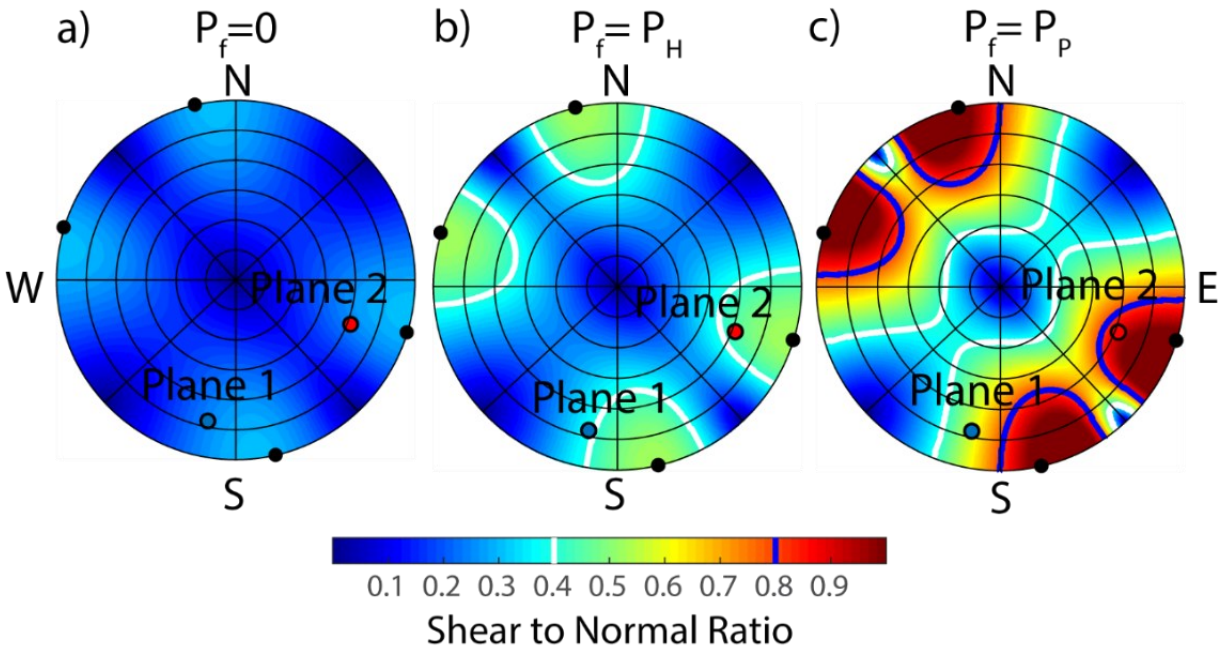


**Figure 6.8.** Stereonets of the *SNR* on all possible planes at *Event* A*'s* focus calculated assuming vanishing cohesion *C* with a) no fluid pressure $P_f = 0$, b) normal hydrostatic pressure $P_f = P_H$, and c) Duvernay Formation pore pressure $P_f = P_P$. Blue and red dots are the poles of the two conjugate planes of the event's FM. Black dots indicate the poles for hypothetical optimally oriented planes. Blue and white contours delineate *SNR* = 0.8 and 0.4.

The stereographic projections of Figure 6.8 show only three specific stress regimes but include uncertainties of the pressures and frictions. This allows for a broader range of possible stability conditions and more stochastic analysis, this is an approach that is now widely employed to assess the risk of seismicity through various derived metrics [e.g., *Seithel et al.*, 2019; *Shen et al.*, 2019b; *Walsh and Zoback*, 2016; *Yaghoubi et al.*, 2020]. To better explore these relationships, the critical values of $P_f^c$ required to induce slip [e.g., *Mukuhira et al.*, 2017; *Streit and Hillis*, 2004]

$$P_f^c = \frac{\mu\sigma - \tau + C}{\mu} \tag{6.10}$$

were calculated separately on each of *Event* A′s conjugate planes in a Monte Carlo simulation with 5000 *SNR* realizations that used values of friction $0.4 < \mu < 0.8$, of cohesion $0 < C < 5$ MPa, and ranges of the three principal stresses (Table 6.1). These realizations also accounted for uncertainties of the plane's strikes, dips, and rakes by varying these angles randomly by ±5° with the resulting distributions of the shear $\tau$ (Figure 6.9a) and normal (clamping) $\sigma$ (Figure 6.9b) tractions shown. The $\sigma$ distribution on Plane 2 is lower and distinct from that of Plane 1, suggesting that Plane 2 is more readily movable.

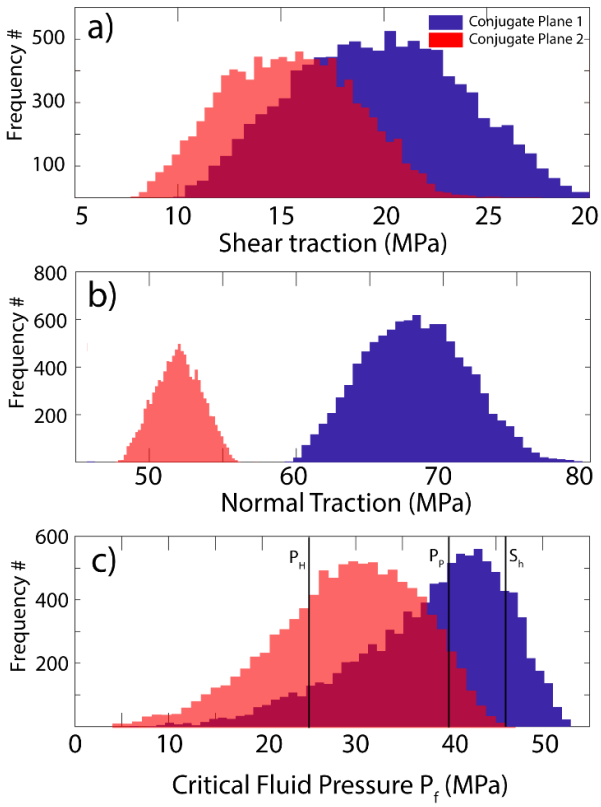


**Figure 6.9** Monte Carlo distributions of **a)** shear traction, **b)** normal clamping traction and **c)** critical $P_f^c$ required for slip on either *of Event* A′*s* conjugate planes.

### *6.3.3 Assess regional susceptibility*

In addition to assessing the stability of the induced event's fault planes, it is useful to further extend the stress model by using it to evaluate the susceptibility for induced seismicity more regionally. Here, we use the deviation of the critical fluid pressure $P_{fc}$ *(x,y)* on the fault plane from the expected ambient $P_P$*(x,y)*:

$$\Delta P(x, y) = P_P(x, y) - P_f^c(x, y) \tag{6.11}$$

Although the choice of $P_P$ is somewhat arbitrary, given its general trend with depth (see Figure 6.5), this measure does remove complications due to the variable Duvernay Formation depths while indicating how the level of pore fluid pressure perturbation necessary to induced slip. Progressively lower values of $\Delta P < 0$ indicates instability. Calculation of the fault's slip-tendency relies on the estimated value of $P_f^c$ that in turn, requires knowledge of the fault's orientation. *Schwab et al.* [2017] and *Stork et al.* [2018] provide examples of studies that estimate the stability on actual faults or lineaments imaged in 3D reflection seismic volumes but other studies have used seismicity to outline fault trends [e.g., *Eyre et al.*, 2019; *Jia*, 2019]. To overcome this limitation, here, we carry out the calculations over the study area by first assuming that at each mapped point planes of weakness have the same orientation as the most stable Plane 1 (Figure 6.10) for *Event* A and then, second, for the sake of comparison, with the orientation planes optimally oriented to slip; analysis on *Event* A's faulting plane 2 yields similar results to that for plane 1 and we do not repeat it here. For each orientation, the critical fluid pressure $P_f^c$ is first calculated (Figure 6.10a and b) followed by $\Delta P$ (Figure 6.10c and d) in which the lower the value of $\Delta P$, the greater the susceptibility. Though our earlier slip-tendency analysis suggests faults are unlikely to be oriented in these directions, this analysis does allow for a relative comparison.

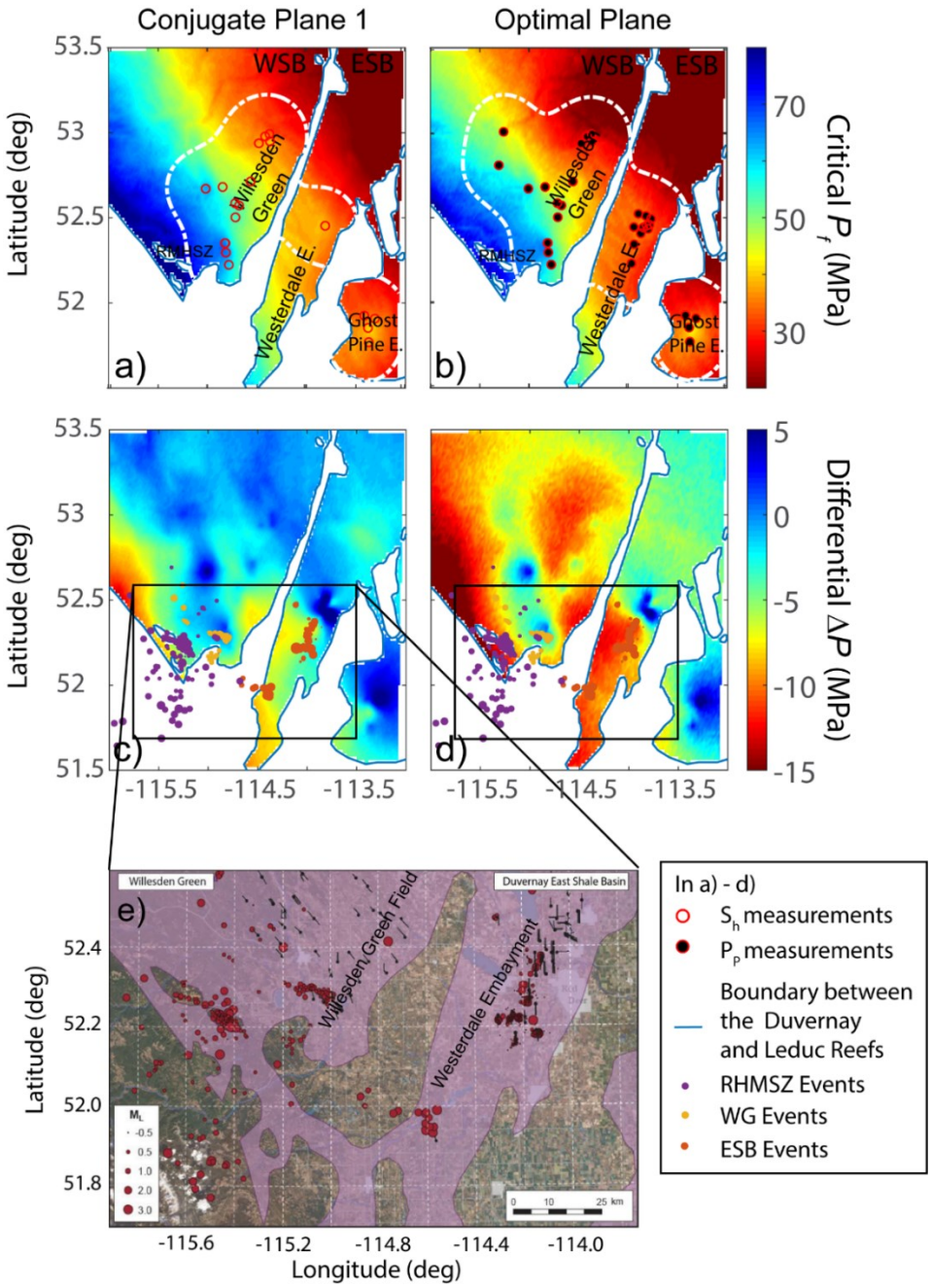


**Figure 6.10.** Required critical pressure $P_f^c$ to activate hypothetical faults across the study area for **a)** hypothetical faults across the region oriented parallel to the conjugate plane 1 for the Red Deer earthquake listed in Table 6.1, and **b)** assumed faults oriented optimally to slip. **c)** and **d)** are the corresponding pressure difference $\Delta P$ (= $P_f^c$ - $P_P$) shown in a) and b). **e)** The study area in *Schultz and Wang* [2020], with earthquake locations and nearby HF wells.

We note that many authors instead employ Coulomb failure stress [e.g., *King et al.*, 1994]. We avoid this measure because it necessitates calculation of $\Delta\sigma$ and $\Delta\tau$ that in turn requires specific knowledge of the perturbing load and its geometry relative to the vulnerable fault plane [*Catalli et al.*, 2013], information that we do not at this time have. These can often be small, too, relative to the changes in $P_f$ due to injection [e.g., *Segall*, 1985].

## 6.4 Discussion

### *6.4.1 Comparison of $S_h$ and $P_P$ with Fox Creek area.*

An early motivation for this study was to determine whether there are any substantive differences in the stress states in the Fox Creek region that had displayed significant induced seismicity to the current study area, which is largely aseismic. In both areas, at the depth of the Duvernay Formation, a strike-slip faulting regime is indicated by the observed $S_V > S_h$ and the FM.

Our confidence of the stress orientation $\phi$ in the areas within the extent of the Duvernay Formation is generally high with stress orientations to the northeast (average $\phi \sim 48°$), which agrees with previous studies at much larger scales [*Reiter et al.*, 2014]. Comparatively, the stress orientation to the north in the Fox Creek area of *Shen et al.* [2019a] shows a similar NE stress orientation averaging 45°.

The secant gradient, which is simply the stress magnitudes divided by the depth and commonly reported in industry borehole measurements [e.g., *Bell and Haug,* 2016], do not show significant variation between the two areas (Table 6.2). In contrast, however, some differences appear in the tangent gradients with that for the Fox Creek (32.1 ± 3.1 MPa/km) exceeding that for the current Red Deer Study area (22.2 ± 5.6 MPa/km). However, some care must be taken

before making a general interpretation as there are some geographic complications between the West Shale Basin and East Shale Basin. The five $S_h$ values from the East Shale Basin, all at shallower depths from 2157 m to 2331 m, bias the aggregate slope. Repeating the regression using only the Williston Green values from 2300 m to 3500 m gives an $S_h$ tangent gradient that agrees with that for the Fox Creek area - the reasons for this are not known. The Fox Creek and Willesden Green zones, although more than 200 km from each other, both lie within the West Shale Basin and may have similar behavior. Alternatively, this may be due to differences in the depths at which the measurements are made.

**Table 6.2**. Comparison of calculated stress and pore pressure gradients between the Fox Creek and Red Deer study areas.

| Area | Gradient type (see text for details) | Red Deer (MPa/km) | | | Fox Creek (MPa/km) |
|---|---|---|---|---|---|
| | | Mesozoic[1] | Duvernay Aggregate | Duvernay Willesden Green Only | Duvernay[2] |
| Range of Measurement Depths (km) | | 1.3-3.0 | 2.1-3.5 | 2.3-3.5 | 2.9-3.9 |
| $S_V$ | Secant | | 24.5 ± 0.5 | | 24.5 ± 1.0 |
| $S_h$ | Secant | 16.8 ±3.2 | 18.3 ± 3.6 | 18.0 ± 3.3 | 19.2 ± 2.8 |
| | Tangent | 19.1 ± 2.4 | 22.2 ± 5.6 | 34.2 ± 6.0 | 32.1 ± 3.1 |
| $P_P$ | tangent | | 24.8 ± 3.6 | | 29.1±7.2 |

[1] Reported in *Haug and Bell* [2016]

[2]Reported in *Shen et al.,* [2019a]

Taken together, there does not appear to be significant differences in the $S_h$ and $P_P$ trends between the two zones, although there are indications that the observed values of $S_h$ within the

East Shale Basin are elevated relative to the predicted trend (Eqn. 6.1). It is important to note that the stress model, which relies on kriging of the observed values, retains these local variations. However, it does not appear that the regional differences in $S_h$ and $P_p$ could explain the variations in levels of seismicity between the Fox Creek region and the current study areas.

### *6.4.2 Relation to other seismicity in the area*

It is useful to contrast this situation with that in the nearby RMHSZ (near 52º12.5'N, 115º15'W), which lies within the deformation belt and where, as noted earlier, events were likely associated with sour gas production from Leduc Formation reefs through the 1980s. The foci of these events are reported at depths around 5.2 km (3.2 kmbsl) [*Wetmiller*, 1986], with a modest $M_W$ 3.4 (*Event* C*)*; the FM solution indicates this earthquake happens on an oblique reverse fault contrasting with the primarily strike-slip FM for *Event* A.

Using nearby measurements from boreholes compiled by *McLellan* [1989], *Baranova et al.* [1999] provided estimates for the Andersonian stress magnitudes at the depth of *Event* C*'s* focus obtaining relative $S_V < S_h < S_H$ - an observation that disagrees with our model, which predicts, at this location, a significantly larger $S_V$ such that $S_h < S_V < S_H$. One component of this discrepancy appears to be due to confusion in the use of elevations in *Baranova et al.* [1999] instead of the correct depths reported by *McLellan* [1989], which differ by more than 1 km; as such, their stress model appears to have inadvertently underestimated the $S_V$ magnitudes. Regardless, our observed strike-slip stress state is less consistent with the largely reverse faulting mechanism FM for *Event* C; this may indicate that the stress regime within the disturbed belt differs from that outside of it.

### *6.4.3 What triggered the $M_W$ 3.8 earthquake (Event A)*

In section 2.2 we showed our calculation of the slip tendency of the fault responsible for the *Event* A at different level of fluid pressures. Examination of Figure 6.8a, b suggests that if $P_f \leq P_H$ both conjugate planes are likely to remain clamped (i.e., $SNR < 0.4$). *Eyre et al.* [2019], for example, in their study near Fox Creek, presume that $P_f = P_H$ within the Duvernay Formation and estimate $SNR \sim 0.29$; suggest this would preclude active seismic slip. However, if $P_f$ is at the expected ambient formation pore pressure $P_P$ as provided in this study, both conjugate planes are significantly destabilized with the *SNR* for Plane 2, which strikes at 201°, falling outside the *SNR* = 0.8 contour (Figure 6.8c).

One point arising from Figure 6.8 is that both of the possible conjugate planes do not match those that are optimally oriented for slip (i.e., 30° from $S_H$ azimuth, assuming = 0.6) within the stress field. These results are similar to the conclusions of *Shen et al.* [2019b] for eleven events in the Fox Creek area and a number of the events induced by long-term injection near Prague, Oklahoma, USA [*Cochran et al.*, 2020].

The corresponding critical $P_f^c$ distributions (Figure 6.9c), too, differ significantly. Both distributions are asymmetric, and their peaks are offset. Plane 2's distribution shifted to significantly lower pressures indicating that, again, Plane 2 may more easily slip. The most vulnerable plane is often presumed to be that actually responsible for the earthquake [e.g., *Alt and Zoback*, 2016; *Vavryčuk*, 2014]. This may suggest, but cannot prove, that *Event* A occurred on Plane 2; both distributions have long tails to low $P_f$, offering a, though improbable, possibility that slip could be triggered on Plane 2 by pressures as low as 4 MPa. It is useful to examine Figure 6.9c for some typical values of $P_f$. Significant fractions of both distributions lie below that expected

for the normal hydrostatic gradient $P_f = P_{H,}$ further indicating that slip could initiate even for relatively low fluid pressures.

More interestingly, the Duvernay Formation reservoir at $P_P$ is highly overpressured [*Cochran et al.*, 2020; *Eaton and Schultz*, 2018; *Shen et al.*, 2019b] - more than 90% of Plane 2's distribution lies below this $P_P$. This means that there is a high likelihood of it being unstable, particularly if the fluid pressures are of those expected naturally in the reservoir. About 50% of the situations available to Plane 1, in contrast, also lie below this pressure. This is the same situation, although shown through a more statistical analysis here, as that encountered to the north in the Fox Creek area [*Shen et al.*, 2019b] where the faults were expected to be unstable at the natural pore pressure; the lack of natural, historical seismicity in the area suggests that the fluid pressure acting along the planes of weakness are likely lower. The Plane 2 distribution in Figure 6.9c does admit stable cases when $P_f = P_{P,}$ but this is not likely. In contrast, about 50% of the cases for Plane 1 remain stable for this condition.

It is also useful to compare the case of $P_f = S_h$. This pressure is a useful reference because $S_h$ determined from the pressure at which the fracture, artificially created during a transient pressure test and whose plane is presumed to be perpendicular to the $S_h$ direction, is deemed to close (see review in *Schmitt and Haimson* [2017]). As such, it provides a lower bound to the fluid pressures transmitted into the formation along an artificial fracture and, subsequently, to the fault should a direct hydraulic connection be established. The peaks for both distributions, and indeed the entire distribution for Plane 2, falls below $S_{h,}$ indicating that fluid pressures this high would certainly destabilize the fault.

In summary, two points are raised by the analysis of the critical $P_f^c$ distributions in Figure 6.9c. First, the natural reservoir pressure $P_P$ alone is sufficient to destabilize a relatively wide range of appropriately oriented planes of weakness; and the question arises as to why the more natural seismic activity is not present. And second, production-based HF operations at this site that must extend fluid pressures, which must exceed $S_h$ to propagate fractures, will readily provide sufficient critical $P_f$ to induce slip on both of the FM's conjugate planes; this is similar to that from the Fox Creek area [*Shen et al.*, 2019b; *Yaghoubi et al.*, 2020].

These observations are reinforced in more direct comparative examinations of *SNR* as a function of $P_f$ for both conjugate planes along with a hypothetical fault plane optimally oriented to the stress field (i.e., 30° from $S_H$ azimuth, assuming $\mu = 0.6$). These results are displayed in Figure 6.11, which is intended to compare the critical $P_f^c$ to fault stabilities (see methods in *Shen et al.,* [2019b]). The red and green ribbons represent envelopes for the set of the *SNR* calculations that, respectively, assume cohesions of either $C = 0$ or C = 5 MPa. The green ribbon in Figure 6.11a, for example, encompasses possible values of $S_H$ constrained with both borehole failures and FM inversion with a maximum cohesion of 5 MPa employed. This envelope is superimposed on a gray background that simply highlights the likely range of friction coefficients $0.4 < \mu < 0.8$ to illustrate the $P_f$ for which $SNR > \mu$ such that the fault is most likely to be unstable. As such, the portions of the envelopes above $SNR = 0.8$ and below $SNR = 0.4$ respectively delineate conditions under which the faults are highly likely to be either unstable or stable.

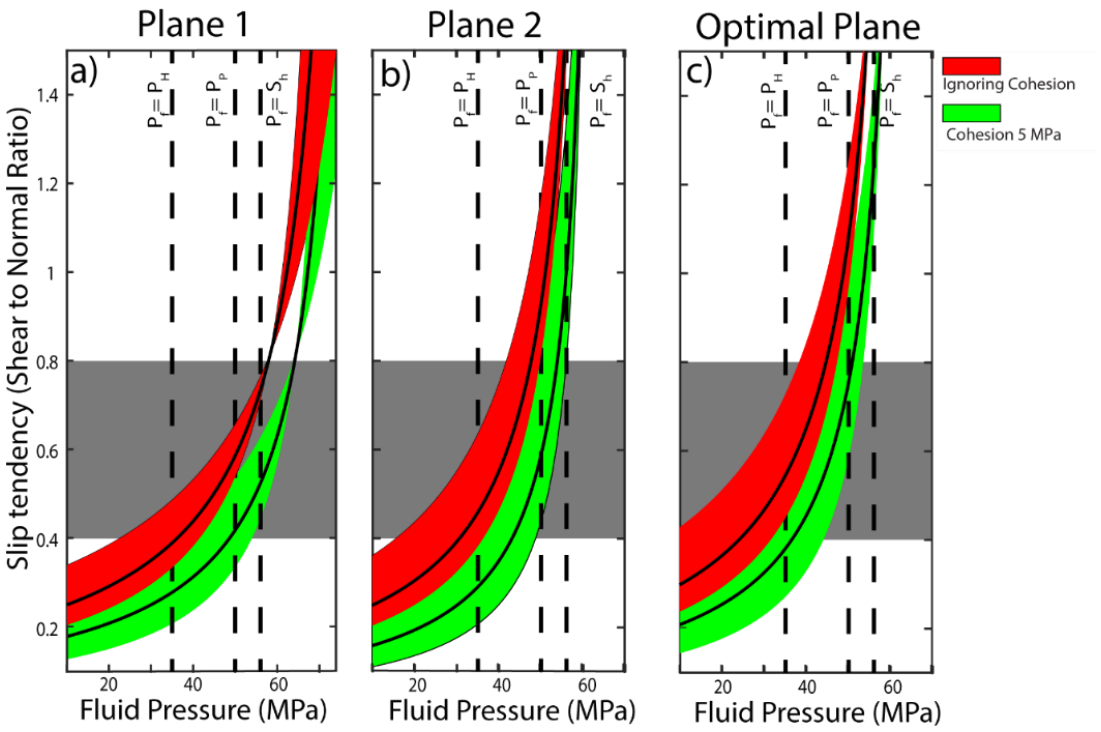


**Figure 6.11.** The slip tendency of the **a)** conjugate faulting plane 1, **b)** 2 of the FM solutions for the *Event* A, and **c)** a hypothetical fault oriented optimally (assuming $\mu = 0.6$) for slip initiation. Red and green stripes represent the range of values calculated for the constrained bounds of $S_H$ (75 – 106 MPa, median 84 MPa) account for either $C = 0$, or 5 MPa. Gray box denote the expected range of $\mu$ between 0.4 and 0.8.

Before we move on to the next section it is important to point out that the stereographic analysis of Figure 6.8 show that a wide range of faulting angles are susceptible to slip at $P_f$ that can be realistically achieved under the in-situ conditions. Without the incorporating stress measurements from various sources, inferring for the stress orientation solely on the basis of the P-T axis described in the earthquake's FM solution may be misleading; using changes in FM directions during microseismic clusters to claim large changes in stress magnitude and directions need to be carried out with particular care and should be supported by geomechanical constraints.

This particularly concerns studies that attempt to describe subtle stress variation over a relatively small volume of crust.

### *6.4.4 Areal constraints on stability and factors controlling IS*

One major motivation for this analysis is to investigate the correlation between our deterministic susceptibility map using $\Delta P$ (see Eqn. 6.11) as the metric with the geospatial locations of the reported seismic clusters.

Both sets of $\Delta P$ maps (Figure 6.10c - d) are mostly similar within the Westerdale Embayment's southern portion, displaying high values. In contrast, the immediately adjacent northern portions of the Westerdale Embayment and the Ghost Pine Embayment have positive $\Delta P$ indicating suggesting that these zones are relatively more stable. This observation may help to explain the clusters of induced events within the south Westerdale Embayment (see Figure 6.10c - e) and their absence in the Ghost Pine Embayment and north Westerdale Embayment despite significant hydraulic fracturing activity there [*Schultz and Wang*, 2020, see Figure 6.10e].

The good correlation between the $\Delta P$ susceptibility and seismicity just described is not as successful in the Willesden Green Field in the West Shale Basin immediately to the north on the other side of the Rimbey-Meadowbrook Reef Trend. Although the $\Delta P$ (Figure 6.10c - d) there is generally high, the Duvernay Formation seismicity observed in this area (orange dots) occurs within an area, though of only lower magnitudes [$M_W < 2$, *Schultz and Wang*, 2020], that on the basis of $\Delta P$, appears relatively more stable. This conflicts with the lack of events immediately to the east, where significantly less stable $\Delta P$ are seen regardless of the significant hydraulic fracturing activities.

There are several possible reasons for this discrepancy. First, to have an induced event, one presupposes the existence of an appropriate plane of weakness upon which sliding may occur. The aseismic zones may simply not have any vulnerable structures upon which sliding might occur. It may also be that such vulnerable structures do exist in these areas, but none of the hydraulic fracturing operations were within range to attain hydraulic connection [*Wilson et al.*, 2018]. Second, the stress and pore pressure model may not accurately predict the conditions everywhere within the study area. While we are generally confident in the results that lie within the white boundaries in Figures 6.4 and 6.10, there are some areas with fewer or no measurements that the extrapolations may not be valid due to geological complexity. This problem is particularly severe for $S_H$ - the values for which were not directly measured but constrained with a rather broader uncertainty. A third possibility is that vulnerable planes of weakness do exist, but stresses may have already been relieved by events prior to the historical record, aseismically, or via many smaller events that are not observed or cataloged.

As such, the relative susceptibility mapping of Figure 6.10 should not, without further information, be interpreted directly to indicate zones where induced earthquakes will/would occur, but rather provide additional constraints on the risks associated with a given perturbation in pressure. It would be useful to build on this model by comparing it against actual hydraulic fracturing pressure records. More specifically, how do the actual pressures attained during hydraulic fracture stimulations compare to the estimated $P_f^c$? Might the pressures employed in the aseismic eastern portion of the Willesden Green Field be lower than those used near the cluster of seismicity? Addressing these questions is beyond the scope of the current study; it is unknown whether the appropriate data even exists or could be accessed, but carrying out such an examination would test the validity of this stability analysis.

That human activities might initiate earthquakes has been known since the middle of the last century with a great deal of interest on earthquakes stimulated by deep fluid waste injections of the Denver earthquakes [e.g., *Healy et al.*, 1968], from crustal loading of large surface hydroelectric reservoirs [e.g., *Gough and Gough*, 1970; *Gupta*, 2018], due to stimulation and operation of geothermal reservoirs [e.g., *Zang et al.*, 2014], hydrocarbon energy production [e.g., *Suckale*, 2009; *Wetmiller*, 1986], long term disposal of water or greenhouse gases [e.g., *Ellsworth*, 2013] and hydraulic fracture stimulation [e.g., *Atkinson et al.*, 2016; *Fasola et al.*, 2019; *R Schultz et al.*, 2020].

An extensive literature supplying hypotheses have been developed to explain the mechanisms causing such induced earthquake; but virtually all of these require that the effective state of stress resolved on the vulnerable fault plane be sufficiently perturbed that Mohr-Coulomb frictional resistance, whether it be a static value or derived from a time-dependent rate-state model. This may be accomplished by either or both of locally modifying the state of total stress from the imposition of the new load nearby or by reducing the effective compressive traction normal traction $\sigma$ by increasing the fluid pressure $P_f$ [e.g., *Garagash and Germanovich*, 2012]. Recent experimental investigations also suggested that the effective initial stress also controls the rupture velocities and, thus, the earthquake types (i.e., seismic or aseismic; [*Passelègue et al.*, 2020]). Studies attempting to explain the responsible mechanism usually focus on one or the other as being primarily responsible, but changes in both should be expected to contribute to greater or lesser extents.

Different types of perturbing loads have been invoked. Some studies employ analytic elastic dislocation solutions [e.g., *Green and Sneddon*, 1950; *Pollard and Segall*, 1987; *Warpinski*,

2000] to calculate the stress field generated by a fluid-filled hydraulic fracture that is superposed to the existing stress field resolved onto a fracture plane [e.g., *Kettlety et al.*, 2020]. Other models have calculated the perturbing stresses using poroelastic analytic [e.g., *Baranova et al.*, 1999; *Goebel et al.*, 2017; *Segall*, 1985; *Segall and Lu*, 2015], or numerical [e.g., *Cueto-Felgueroso et al.*, 2018; *Deng et al.*, 2016] solutions. Depending on the availability of fluid pathways in the reservoir, fluid pressures changes due to fluid diffusion, too, are important [e.g., *Shapiro and Dinske*, 2009] and may explain some delays in seismicity in some cases [e.g., *Baisch et al.*, 2010].

Our fault stability analyses here show that the active fluid pressure $P_f$ is likely the most crucial factor, given that the expected natural pore pressures are already at ~90% of $S_h$. This indicates that even before anthropogenic disruption, the slip surface for *Event* A was already critically loaded. Consequently, the problem in trying to target the mechanisms ultimately responsible for triggering the slip, in this case, is that only small perturbations in $\sigma$, $\tau$, and $P_f$ might be required; this confounds clear discrimination of which factors are most important. Though various scenarios that might favor one or the other mechanisms can be modeled, during an HF stimulation, fluid pressures that often significantly in excess of $S_h$ are introduced to the system [e.g., *Kleiner and Aniekwe*, 2019]. The low matrix permeabilities of the rocks within and surrounding the Duvernay Formation, and many other unconventional shale oil/gas reservoirs, likely preclude diffusive fluid pressure transfers - fluid pressures need to be transmitted via more transmissive natural fractures systems [*Lele et al.*, 2017; *MacKay et al.*, 2018]. In contrast, induced poroelastic changes from a fracture are relatively modest in comparison [*Baranova et al.*, 1999; *Deng et al.*, 2016; *Goebel et al.*, 2017], suggesting that direct hydraulic connectivity may be the most important component in these cases [*Lele et al.*, 2017].

## 6.5 Conclusions

The current study area had, on the basis of the lack of seismicity, been assessed to have low seismic risk. Recent earthquakes that are related to hydraulic fracturing operations motivate further analysis. A more deterministic analysis that includes a geomechanical evaluation of fault slip-tendency is required to assist in explaining both the prior lack of seismicity and the recent events.

We developed a quantitative 3D model that estimates the quantitative absolute Andersonian stress tensor ($S_H$, $S_h$, $S_V$, and $\phi$) from borehole logs and transient pressure tests. This model incorporated information from both borehole breakouts and inversion of the limited focal mechanism solution available to provide ranges of $S_H$'s magnitudes. Despite the large uncertainties, an agreement is reached between the two methods, and our best estimation of $S_H$ falls between 75 MPa and 106 MPa at the epicenter of the $M_W$ 3.8/$M_L$ 4.2 (Red Deer, Alberta) earthquake.

We extended this model to further study the mechanical stability of the two possible conjugate fault planes associated with the Red Deer earthquake ($M_W$ 3.8). Both planes would remain stable if the fluid pressure acting on the fault $P_f$ is at the normal hydrostat. However, both are expected to be naturally unstable if $P_f$ is the same as the nominal pore fluid pressure $P_P$ measured from boreholes in the target Duvernay Formation. The historical lack of seismicity in the area may suggest that the high natural $P_P$ can only be dissipated on the faults, perhaps by leakage to overlying Mesozoic formations. Further, neither of the possible conjugate planes are optimally oriented to the stress field - a range of other planes of weakness are more susceptible to slippage. These findings suggest that the induced seismicity is triggered by elevating the fluid pressures on the fault via direct fluid pathways from the hydraulic fracture operations.

Motivated by such findings, we subsequently performed susceptibility analysis for the study area using both the critical $P_f^c$ needed to activate a fault and its difference to the expected ambient $P_P$ ($\Delta P = P_f^c - P_P$) as metrics. These suggest that the Ghost Pine Embayment to the southeast and the North Westerdale Embayment are generally stable (requires $P_f^c > P_P$ to be activated). This finding agrees with the general absence of earthquakes reported from seismological observations. The high-profile Red Deer $M_W$ 3.8/$M_L$ 4.2 earthquake happened in a zone we considered to be less stable owing to the high $P_P$ modeled with transient wellbore fluid tests.

Before concluding, it is worthwhile to reinforce that our analysis, both the stereographic projections analysis (see Figure 6.8) and the susceptibility maps (see Figure 6.10) are derived solely from the stress tensor. These analyses are not influenced by the study areas' past earthquake records or seismic quiescence that might be biased by the industry activities or regional seismometer station network's detection limit [*Schultz et al.*, 2015] – a fresh perspective on controlling factors of HF induced seismicity and seismic susceptibilities are provided here.

## References

Alberta Energy Regulator (AER, 2015), Subsurface order no. 2: Monitoring and reporting of seismicity in the vicinity of hydraulic fracturing operations in the Duvernay zone, Fox Creek, Alberta, *[Available at http://www.aer.ca/documents/bulletins/Bulletin-2015-07.pdf]. 3 pages*.

Alberta Energy Regulator (AER, 2019), Subsurface Order No. 7, *[Available at https://static.aer.ca/prd/documents/orders/subsurface-orders/SO7.pdf]. 4 pages*.

Alt, R. C., and M. D. Zoback (2016), In situ stress and active faulting in Oklahoma, *Bull. Seismol. Soc. Amer.*, *107*(1), 216-228.

Ameen, M.S., 2016. Fracture modes in the Silurian Qusaiba shale play, northern Saudi Arabia and their geomechanical implications. *Marine and Petroleum Geology*, 78, pp.312-355.

Ameen, M.S., 2019, April. Borehole imaging of natural fractures and stress indicators in the Jurassic Carbonate Shale Plays, Eastern Saudi Arabia. In Sixth EAGE Shale Workshop (Vol. 2019, No. 1, pp. 1-5). *European Association of Geoscientists & Engineers.*

Anderson, E. M. (1951), *The dynamics of faulting and dyke formation with applications to Britain*, Oliver and Boyd.

Atkinson, G. M., D. W. Eaton, H. Ghofrani, D. Walker, B. Cheadle, R. Schultz, R. Shcherbakov, K. Tiampo, J. Gu, and R. M. Harrington (2016), Hydraulic fracturing and seismicity in the Western Canada Sedimentary Basin, *Seismological Research Letters*, *87*(3), 631-647.

Atkinson, G. M., Eaton, D.W. and Igonin, N., 2020. Developments in understanding seismicity triggered by hydraulic fracturing. *Nature Reviews Earth & Environment*, 1(5), pp.264-277.

Baisch, S., R. Vörös, E. Rothert, H. Stang, R. Jung, and R. Schellschmidt (2010), A numerical model for fluid injection induced seismicity at Soultz-sous-Forêts, *International Journal of Rock Mechanics and Mining Sciences*, *47*(3), 405-413.

Baranova, V., A. Mustaqeem, and S. Bell (1999), A model for induced seismicity caused by hydrocarbon production in the Western Canada Sedimentary Basin, *Canadian Journal of Earth Sciences*, *36*(1), 47-64.

Barton, C. A., M. D. Zoback, and K. L. Burns (1988), In-situ stress orientation and magnitude at the Fenton Geothermal Site, New Mexico, determined from wellbore breakouts, *Geophysical Research Letters*, *15*(5), 467-470.

Beaumont, C. (1981), Foreland basins, *Geophysical Journal International*, *65*(2), 291-329.

Bell, J., and S. Bachu (2003), In situ stress magnitude and orientation estimates for Cretaceous coal-bearing strata beneath the plains area of central and southern Alberta, *Bulletin of Canadian Petroleum Geology*, *51*(1), 1-28.

Bell, J., and G. Caillet (1994), A reinterpretation of the stress regime of the Aquitaine basin, southwestern France, and implications for hydrocarbon recovery, in *Hydrocarbon and Petroleum Geology of France*, edited, pp. 209-219, Springer.

Bell, J., and D. Gough (1979), Northeast-southwest compressive stress in Alberta evidence from oil wells, *Earth and planetary science letters*, *45*(2), 475-482.

Bell, J., and S. Grasby (2012), The stress regime of the Western Canadian sedimentary basin, *Geofluids*, *12*(2), 150-165.

Bank of Montreal (BMO, 2019), East of the reef - Duvernay Oil Play, in *BMO Capital Markets - Energy - A & D Advisory*, edited.

Bott, M. H. P. (1959), The mechanics of oblique slip faulting, *Geological Magazine*, *96*(2), 109-117.

Bouzidi, Y., D. R. Schmitt, R. A. Burwash, and E. R. Kanasewich (2002), Depth migration of deep seismic reflection profiles: crustal thickness variations in Alberta, *Canadian Journal of Earth Sciences*, *39*(3), 331-350.

Burwash, R., C. McGregor, and J. Wilson (1994), Precambrian Basement Beneath the Western Canada Sedimentary Basin, Geological Atlas of the Western Canada sedimentary Basin, 49-56, *Alberta Research Council*.

Byerlee, J., 1978. Friction of rocks. In Rock friction and earthquake prediction (pp. 615-626). *Birkhäuser, Basel.*

Castaños, H., and C. Lomnitz (2002), PSHA: Is it science?, *Engineering Geology*, *66*(3-4), 315-317.

Catalli, F., M. A. Meier, and S. Wiemer (2013), The role of Coulomb stress changes for injection-induced seismicity: The Basel enhanced geothermal system, *Geophysical Research Letters*, *40*(1), 72-77.

Chen, Y., Y. J. Gu, C. A. Currie, S. T. Johnston, S.-H. Hung, A. J. Schaeffer, and P. Audet (2019), Seismic evidence for a mantle suture and implications for the origin of the Canadian Cordillera, *Nature communications*, *10*(1), 1-10.

Chopra, S., R. K. Sharma, A. K. Ray, H. Nemati, R. Morin, B. Schulte, and D. D'Amico (2017), Seismic reservoir characterization of Duvernay shale with quantitative interpretation and induced seismicity considerations—A case study, *Interpretation*, *5*(2), T185-T197.

Cochran, E. S., R. J. Skoumal, D. McPhillips, Z. E. Ross, and K. M. Keranen (2020), Activation of optimally and unfavourably oriented faults in a uniform local stress field during the 2011 Prague, Oklahoma, sequence, *Geophysical Journal International*, *222*(1), 153-168.

Corlett, H., R. Schultz, P. Branscombe, T. Hauck, K. Haug, K. MacCormack, and T. Shipman (2018), Subsurface faults inferred from reflection seismic, earthquakes, and sedimentological relationships: Implications for induced seismicity in Alberta, Canada, *Marine and Peroleum Geology*, *93*, 135-144.

Cueto-Felgueroso, L., C. Vila, D. Santillán, and J. C. Mosquera (2018), Numerical Modeling of Injection-Induced Earthquakes Using Laboratory-Derived Friction Laws, *Water Resources Research*, *54*(12), 9833-9859.

Deng, K., Y. Liu, and R. M. Harrington (2016), Poroelastic stress triggering of the December 2013 Crooked Lake, Alberta, induced seismicity sequence, *Geophysical Research Letters*, *43*(16), 8482-8491.

Eaton, D. W., N. Igonin, A. Poulin, R. Weir, H. Zhang, S. Pellegrino, and G. Rodriguez (2018), Induced Seismicity Characterization during Hydraulic-Fracture Monitoring with a Shallow-Wellbore Geophone Array and Broadband Sensors, *Seismological Research Letters*, *89*(5), 1641-1651.

Eaton, D. W., and R. Schultz (2018), Increased likelihood of induced seismicity in highly overpressured shale formations, *Geophysical Journal International*, *214*(1), 751-757.

Eberhart-Phillips, D., and D. H. Oppenheimer (1984), Induced seismicity in The Geysers geothermal area, California, *Journal of Geophysical Research: Solid Earth*, *89*(B2), 1191-1207.

Edwards, D. J., and R. J. Brown (1999), Understanding the influence of Precambrian crystalline basement on Upper Devonian carbonates in central Alberta from a geophysical perspective, *Bulletin of Canadian Petroleum Geology*, *47*(4), 412-438.

Ekpo, E., D. Eaton, and R. Weir (2017), Basement Tectonics and Fault Reactivation in Alberta Based on Seismic and Potential Field Data, in *Geophysics*, edited, IntechOpen.

Ellsworth, W. L. (2013), Injection-induced earthquakes, *Science*, *341*(6142), 1225942.

Ellsworth, W.L., Giardini, D., Townend, J., Ge, S. and Shimamoto, T., 2019. Triggering of the Pohang, Korea, earthquake (M w 5.5) by enhanced geothermal system stimulation. Seismological Research Letters, 90(5), pp.1844-1858.

Eyre, T. S., D. W. Eaton, M. Zecevic, D. D'Amico, and D. Kolos (2019), Microseismicity reveals fault activation before M w 4.1 hydraulic-fracturing induced earthquake, *Geophysical Journal International*, *218*(1), 534-546.

Fasola, S. L., M. R. Brudzinski, R. J. Skoumal, T. Langenkamp, B. S. Currie, and K. J. Smart (2019), Hydraulic fracture injection strategy influences the probability of earthquakes in the Eagle Ford shale play of South Texas, *Geophysical Research Letters*, *46*(22), 12958-12967.

Frankel, A. (2013), Comment on "Why earthquake hazard maps often fail and what to do about it" by S. Stein, R. Geller, and M. Liu, *Tectonophysics*, *592*, 200-206.

Galloway, E., T. Hauck, H. Corlett, D. Pană, and R. Schultz (2018), Faults and associated karst collapse suggest conduits for fluid flow that influence hydraulic fracturing-induced seismicity, *Proceedings of the National Academy of Sciences*, *115*(43), E10003-E10012.

Garagash, D. I., and L. N. Germanovich (2012), Nucleation and arrest of dynamic slip on a pressurized fault, *Journal of Geophysical Research: Solid Earth*, *117*(B10).

Goebel, T., M. Weingarten, X. Chen, J. Haffener, and E. Brodsky (2017), The 2016 Mw5. 1 Fairview, Oklahoma earthquakes: Evidence for long-range poroelastic triggering at> 40 km from fluid disposal wells, *Earth and Planetary Science Letters*, *472*, 50-61.

Gough, D., and W. Gough (1970), Load-induced earthquakes at Lake Kariba—II, *Geophysical Journal International*, *21*(1), 79-101.

Green, A., and I. Sneddon (1950), The distribution of stress in the neighbourhood of a flat elliptical crack in an elastic solid, paper presented at *Mathematical Proceedings of the Cambridge Philosophical Society*, Cambridge University Press.

Gu, Y. J., and L. Shen (2015), Noise correlation tomography of southwest western Canada sedimentary basin, *Geophysical Journal International*, *202*(1), 142-162.

Gupta, H. K. (2018), Reservoir triggered seismicity (RTS) at Koyna, India, over the past 50 yrs, *Bull. Seismol. Soc. Amer.*, *108*(5B), 2907-2918.

Hardebeck, J. L., and E. Hauksson (2001), Crustal stress field in southern California and its implications for fault mechanics, *Journal of Geophysical Research: Solid Earth*, *106*(B10), 21859-21882.

Haug, K., and J. S. Bell (2016), Compilation of In Situ Stress Data from Alberta and Northeastern British Columbia, edited, Alberta Geologcial Survey, Edmonton.

Healy, J., W. Rubey, D. Griggs, and C. Raleigh (1968), The denver earthquakes, *Science*, *161*(3848), 1301-1310.

Heidbach, O., M. Rajabi, K. Reiter, M. Ziegler, and W. team (2016), World stress map database release 2016, *GFZ Data Services*, *10*.

Hincks, T., W. Aspinall, R. Cooke, and T. Gernon (2018), Oklahoma's induced seismicity strongly linked to wastewater injection depth, *Science*, *359*(6381), 1251-1255.

Hoffman, P. F. (1988), United plates of America, the birth of a craton: Early Proterozoic assembly and growth of Laurentia, *Annual Review of Earth and Planetary Sciences*, *16*(1), 543-603.

Jia, S. Q. (2019), Stress Inversion and Damage Quantification in Tight Gas Shale with Application to Hydraulic Fracturing.

Kettlety, T., J. Verdon, M. Werner, and J. Kendall (2020), Stress transfer from opening hydraulic fractures controls the distribution of induced seismicity, *Journal of Geophysical Research: Solid Earth*, *125*(1), e2019JB018794.

King, G. C., R. S. Stein, and J. Lin (1994), Static stress changes and the triggering of earthquakes, *Bull. Seismol. Soc. Amer.*, *84*(3), 935-953.

Kleiner, S., and O. Aniekwe (2019), The Duvernay shale completion journey, paper presented at SPE Kuwait Oil & Gas Show and Conference, Society of Petroleum Engineers.

Lele, S., T. Tyrrell, and G. Dasari (2017), Geomechanical analysis of fault reactivation due to hydraulic fracturing, paper presented at 51st US Rock Mechanics/Geomechanics Symposium, American Rock Mechanics Association.

Lemieux, S. (1999), Seismic reflection expression and tectonic significance of Late Cretaceous extensional faulting of the Western Canada Sedimentary Basin in southern Alberta, *Bulletin of Canadian Petroleum Geology*, *47*(4), 375-390.

Liu, L., and M. D. Zoback (1992), The effect of topography on the state of stress in the crust: application to the site of the Cajon Pass Scientific Drilling Project, *Journal of Geophysical Research: Solid Earth*, *97*(B4), 5095-5108.

MacKay, M. K., D. W. Eaton, P. K. Pedersen, and C. R. Clarkson (2018), Integration of outcrop, subsurface, and microseismic interpretation for rock-mass characterization: An example from the Duvernay Formation, Western Canada, *Interpretation*, *6*(4), T919-T936.

Maury, V., J.-R. Grassob, and G. Wittlinger (1992), Monitoring of subsidence and induced seismicity in the Lacq gas field (France): the consequences on gas production and field operation, *Engineering Geology*, *32*(3), 123-135.

*Marone, C., 1998. Laboratory-derived friction laws and their application to seismic faulting. Annual Review of Earth and Planetary Sciences, 26(1), pp.643-696.*

McClure, M. W., and R. N. Horne (2011), Investigation of injection-induced seismicity using a coupled fluid flow and rate/state friction model, *Geophysics*, *76*(6), WC181-WC198.

McLellan, P. (1989), *In-situ stress magnitudes from hydraulic fracturing treatment records: a feasibility study*, Institute of Sedimentary and Petroleum Geology.

Michael, A. J. (1984), Determination of stress from slip data: faults and folds, *Journal of Geophysical Research: Solid Earth*, *89*(B13), 11517-11526.

Moore, P. F. (1988), Devonian reefs in Canada and some adjacent areas.

Morris, A., D. A. Ferrill, and D. B. Henderson (1996), Slip-tendency analysis and fault reactivation, *Geology*, *24*(3), 275-278.

Mukuhira, Y., C. Dinske, H. Asanuma, T. Ito, and M. Häring (2017), Pore pressure behavior at the shut-in phase and causality of large induced seismicity at Basel, Switzerland, *Journal of Geophysical Research: Solid Earth*, *122*(1), 411-435.

Ong, O. N., D. R. Schmitt, and R. S. Kofman (2015), Seismic anisotropy and uniaxial stress measurements on Duvernay sedimentary rocks in Alberta: Report submitted to AER Core Research Laboratory, 28 pp, Alberta Geological Survey, Edmonton.

Ong, O. N., D. R. Schmitt, R. S. Kofman, and K. Haug (2016), Static and dynamic pressure sensitivity anisotropy of a calcareous shale, *Geophys. Prospect.*, *64*(Advances in Rock Physics), 875-897.

Pană, D. I., and B. A. van der Pluijm (2015), Orogenic pulses in the Alberta Rocky Mountains: Radiometric dating of major faults and comparison with the regional tectono-stratigraphic record, *Bulletin*, *127*(3-4), 480-502.

Passelègue, F. X., M. Almakari, P. Dublanchet, F. Barras, J. Fortin, and M. Violay (2020), Initial effective stress controls the nature of earthquakes, *Nature Communications*, *11*(1), 1-8.

Pawley, S., R. Schultz, T. Playter, H. Corlett, T. Shipman, S. Lyster, and T. Hauck (2018), The geological susceptibility of induced earthquakes in the Duvernay play, *Geophysical Research Letters*, *45*(4), 1786-1793.

Peters, S. E., and R. R. Gaines (2012), Formation of the 'Great Unconformity' as a trigger for the Cambrian explosion, *Nature*, *484*(7394), 363-366, doi:10.1038/nature10969.

Pollard, D. D., and P. Segall (1987), Theoretical displacements and stresses near fractures in rock: with applications to faults, joints, veins, dikes, and solution surfaces, paper presented at Fracture mechanics of rock.

Preston, A., G. Garner, K. Beavis, O. Sadiq, and S. Stricker (2016), Duvernay reserves and resources report: A comprehensive analysis of Alberta's foremost liquids-rich shale resource, *Alberta Energy Regulator, Calgary*, 83.

Price, R. (2001), An evaluation of models for the kinematic evolution of thrust and fold belts: structural analysis of a transverse fault zone in the Front Ranges of the Canadian Rockies north of Banff, Alberta, *Journal of Structural Geology*, *23*(6-7), 1079-1088.

Rebollar, C., E. Kanasewich, and E. Nyland (1982), Source parameters from shallow events in the Rocky Mountain House earthquake swarm, *Canadian Journal of Earth Sciences*, *19*(5), 907-918.

Reiter, K., O. Heidbach, D. Schmitt, K. Haug, M. Ziegler, and I. Moeck (2014), A revised crustal stress orientation database for Canada, *Tectonophysics*, *636*, 111-124.

Rokosh, C., J. Pawlowicz, H. Berhane, S. Anderson, and A. Beaton (2009), What is shale gas? An introduction to shale-gas geology in Alberta, *Energy Resource Conservation Board (2008-08), available at: http://ags. gov. ab. ca/publications/abstracts/OFR_2008_08. html*.

Ross, G., and D. Eaton (1999), Basement reactivation in the Alberta Basin: Observational constraints and mechanical rationale, *Bulletin of Canadian Petroleum Geology*, *47*(4), 391-411.

Ross, G., R. Parrish, M. Villeneuve, and S. Bowring (1991), Geophysics and geochronology of the crystalline basement of the Alberta Basin, western Canada, *Canadian Journal of Earth Sciences*, *28*(4), 512-522.

Schmitt, D. R. (2014), Basic geomechanics for induced seismicity: A tutorial, *CSEG Recorder (Nov 2014)*, *39*(11), 20-27.

Schmitt, D. R., C. A. Currie, and L. Zhang (2012), Crustal stress determination from boreholes and rock cores: Fundamental principles, *Tectonophysics*, *580*, 1-26.

Schmitt, D. R., and B. Haimson (2017), Hydraulic fracturing stress measurements in deep holes, *Rock Mechanics and Engineering Volume 1: Principles*, 183.

Schultz, R., G. Atkinson, D. Eaton, Y. Gu, and H. Kao (2018), Hydraulic fracturing volume is associated with induced earthquake productivity in the Duvernay play, *Science*, *359*(6373), 304-308.

Schultz, R., R. J. Skoumal, M. R. Brudzinski, D. Eaton, B. Baptie, and W. Ellsworth (2020), Hydraulic Fracturing-Induced Seismicity, *Reviews of Geophysics*, *58*(3), e2019RG000695.

Schultz, R., V. Stern, and Y. J. Gu (2014), An investigation of seismicity clustered near the Cordel Field, west central Alberta, and its relation to a nearby disposal well, *Journal of Geophysical Research: Solid Earth*, *119*(4), 3410-3423.

Schultz, R., V. Stern, Y. J. Gu, and D. Eaton (2015), Detection threshold and location resolution of the Alberta Geological Survey earthquake catalogue, *Seismological Research Letters*, *86*(2A), 385-397.

Schultz, R., and R. Wang (2020), Newly emerging cases of hydraulic fracturing induced seismicity in the Duvernay East Shale Basin, *Tectonophysics*, 228393.

Schultz, R., R. Wang, Y. J. Gu, K. Haug, and G. Atkinson (2017), A seismological overview of the induced earthquakes in the Duvernay play near Fox Creek, Alberta, *Journal of Geophysical Research: Solid Earth*, *122*(1), 492-505.

Schultz, S., J. A. MacEachern, and H. D. Gibson (2019), Late Mesozoic reactivation of Precambrian basement structures and their resulting effects on the sequence stratigraphic architecture of the Viking Formation of east-central Alberta, Canada, *Lithosphere*, *11*(3), 308-321.

Schwab, D. R., T. S. Bidgoli, and M. H. Taylor (2017), Characterizing the Potential for Injection-Induced Fault Reactivation Through Subsurface Structural Mapping and Stress Field Analysis, Wellington Field, Sumner County, Kansas, *Journal of Geophysical Research: Solid Earth*, *122*(12).

Segall, P. (1985), Stress and subsidence resulting from subsurface fluid withdrawal in the epicentral region of the 1983 Coalinga earthquake, *Journal of Geophysical Research: Solid Earth*, *90*(B8), 6801-6816.

Segall, P., and S. Lu (2015), Injection-induced seismicity: Poroelastic and earthquake nucleation effects, *Journal of Geophysical Research: Solid Earth*, *120*(7), 5082-5103.

Seithel, R., E. Gaucher, B. Mueller, U. Steiner, and T. Kohl (2019), Probability of fault reactivation in the Bavarian Molasse Basin, *Geothermics*, *82*, 81-90.

Shapiro, S. A., and C. Dinske (2009), Fluid-induced seismicity: Pressure diffusion and hydraulic fracturing, *Geophys. Prospect.*, *57*(2), 301-310.

Shen, L., D. Schmitt, and K. Haug (2018), Measurements of the States of In Situ Stress for the Duvernay Formation near Fox Creek, West-Central Alberta*Rep.*, 29 pp, Alberta Energy Regulator / Alberta Geological Survey.

Shen, L., D. Schmitt, and K. Haug (2019a), Quantitative constraints to the complete state of stress from the combined borehole and focal mechanism inversions: Fox Creek, Alberta, *Tectonophysics*, *764*, 13, doi:https://doi.org/10.1016/j.tecto.2019.04.023.

Shen, L., D. Schmitt, and R. Schultz (2019b), Frictional Stabilities on Induced Earthquake Fault Planes at Fox Creek, Alberta: A Pore Fluid Pressure Dilemma, *Geophysical Research Letters*, *46*(15), 9, doi:10.1029/2019GL083566.

Shen, L., and D. Schmitt (2020), Data for: States of in-situ stress in the Duvernay East Shale Basin and Willesden Green of Alberta, Canada: variable in-situ stress states effect fault stability, Mendeley Data, V1, doi: 10.17632/tgmxx5vkjx.1

Shipman, T., R. MacDonald, and T. Byrnes (2018), Experiences and learnings from induced seismicity regulation in Alberta, *Interpretation*, *6*(2), SE15-SE21.

Stein, S., R. Geller, and M. Liu (2011), Bad assumptions or bad luck: Why earthquake hazard maps need objective testing, *Seismological Research Letters*, *82*(5), 623-626.

Stein, S., R. J. Geller, and M. Liu (2012), Why earthquake hazard maps often fail and what to do about it, *Tectonophysics*, *562*, 1-25.

Stork, A., C. Nixon, C. Hawkes, C. Birnie, D. White, D. Schmitt, and B. Roberts (2018), Is CO2 injection at Aquistore aseismic? A combined seismological and geomechanical study of early injection operations, *Int. J. Greenh. Gas Control*, *75*, 107-124.

Streit, J. E., and R. R. Hillis (2004), Estimating fault stability and sustainable fluid pressures for underground storage of CO2 in porous rock, *Energy*, *29*(9-10), 1445-1456.

Suckale, J. (2009), Induced seismicity in hydrocarbon fields, in *Advances in geophysics*, edited, pp. 55-106, Elsevier.

USGS (2020), Search Earthquake Catalog, edited, USGS.

Valley, B., and K. F. Evans (2019), Stress magnitudes in the Basel enhanced geothermal system, *International Journal of Rock Mechanics and Mining Sciences*, *118*, 1-20, doi:10.1016/j.ijrmms.2019.03.008.

van Thienen-Visser, K., and J. Breunese (2015), Induced seismicity of the Groningen gas field: History and recent developments, *The Leading Edge*, *34*(6), 664-671.

Vavryčuk, V. (2014), Iterative joint inversion for stress and fault orientations from focal mechanisms, *Geophysical Journal International*, *199*(1), 69-77.

Wallace, R. E. (1951), Geometry of shearing stress and relation to faulting, *The Journal of geology*, *59*(2), 118-130.

Walsh, F. R., and M. D. Zoback (2016), Probabilistic assessment of potential fault slip related to injection-induced earthquakes: Application to north-central Oklahoma, USA, *Geology*, *44*(12), 991-994.

Warpinski, N. R. (2000), Analytic crack solutions for tilt fields around hydraulic fractures, *Journal of Geophysical Research: Solid Earth*, *105*(B10), 23463-23478.

Weides, S. N., I. S. Moeck, D. R. Schmitt, and J. A. Majorowicz (2014), An integrative geothermal resource assessment study for the siliciclastic Granite Wash Unit, northwestern Alberta (Canada), *Environ. Earth Sci.*, *72*(10), 4141-4154.

Weir, R. M., D. W. Eaton, L. R. Lines, D. C. Lawton, and E. Ekpo (2018), Inversion and interpretation of seismic-derived rock properties in the Duvernay play, *Interpretation-a Journal of Subsurface Characterization*, *6*(2), SE1-SE14, doi:10.1190/int-2017-0149.1.

Wetmiller, R. J. (1986), Earthquakes near Rocky Mountain House, Alberta, and their relationship to gas production facilities, *Canadian Journal of Earth Sciences*, *23*(2), 172-181.

Wilson, M., F. Worrall, R. Davies, and S. Almond (2018), Fracking: How far from faults?, *Geomechanics and Geophysics for Geo-Energy and Geo-Resources*, *4*(2), 193-199.

Woodland, D., and J. Bell (1989), In situ stress magnitudes from mini-frac records in Western Canada, *Journal of Canadian Petroleum Technology*, *28*(05).

Yaghoubi, A., M. Dusseault, S. Mahbaz, and Y. Leonenko (2020), Probabilistic Injection-Induced Fault Slip Assessment in Fox Creek Alberta, paper presented at *54th US Rock Mechanics/Geomechanics Symposium*, American Rock Mechanics Association.

Zang, A., V. Oye, P. Jousset, N. Deichmann, R. Gritto, A. McGarr, E. Majer, and D. Bruhn (2014), Analysis of induced seismicity in geothermal reservoirs–An overview, *Geothermics*, *52*, 6-21.

# Chapter 7: Conclusions and directions for future research

## 7.1 Contributions of Work Described Here

Quantitative knowledge on the states of in-situ stress is an essential prerequisite for many geomechanical works. Here, motivated by the need for causational investigation on the hydraulic fracturing induced earthquakes in Alberta's Duvernay unconventional reservoir, geomechanical analysis is performed to investigate these earthquakes' triggering mechanism and seismic susceptibilities of the studied areas.

Our studies are uniquely different from other analyses that rely primarily on establishing a statistical spatial-temporal correlation between the HF/waste disposal schedules and observed earthquakes. This more deterministic approach departs from most studies that view induced seismicity from observed time- and space-dependent correlations between human activities and seismicity. These studies effectively established a causation link that confirmed these earthquakes are induced; however, questions including the physical triggering process can only be answered through geomechanical modeling. In this regard, it is worthwhile noting that even those studies that claim to rely on a ‘physics-based approach do not directly consider stability on individual susceptible fault planes directly, but examine only areas of increased or decreased stress, assuming that the most susceptible fault alignments are always ubiquitous.

In this thesis, we take an approach different from these seismological contributions and investigate the faults' slip-tendency by resolving the traction forces applied on them. We aggregated borehole in-situ stress measurements and built two fully quantitative 3D stress models for the areas near Fox Creek and Red Deer, where moderate induced earthquakes are reported and

felt by the local residents. This study does not rely on the areas' past earthquake history and therefore not impacted by the regional earthquake monitoring network's capability/incapability to detect earthquakes.

These quantitative stress models allow two unique studies that probe into the triggering mechanisms of these induced earthquakes and later to build a map of susceptibility on the basis of the slip-tendency along the faulting planes. We found that for both the Fox Creek and Red Deer earthquakes, faults cannot be stable at the presumed ambient high pore fluid pressures within the Duvernay Formation. Also, these faults do not need to be perfectly optimally oriented to the stress field to be activated. Elevated pore pressures, as the results of the HF operations that connect the overpressured unconventional reservoir to these faults, can sufficiently trigger these earthquakes. For the areas near the Red Deer, we also presented a susceptibility map built using our 3d stress-pore pressure model that is well correlated with most but not all, reported induced events. Further, these susceptibility maps also highlight an area, notably the Willesden Green Oil field, that would appear to be at higher risk but are not associated with any induced seismic events despite extensive hydraulic fracturing activity. This may suggest that susceptible planes of weakness may be absent from these areas.

### 7.2 Suggestions for future research

This study investigated the fault slip tendency in areas that HF-induced earthquakes are reported. Though we attempt to be as deterministic as possible, we do not take the poroelastic effect into account here. Though, this generally is believed to be secondary with stress perturbation less than 10 MPa. Future analysis can undoubtedly benefit from a fully coupled stress, pore fluid simulation that takes both fluid propagation and poroelastic deformation into account. However,

one problem with such analyses is that they require a large number of assumptions with regards to the physical properties of the materials and fluids and the structure, much of which is not well known.

Despite having the uncertainties accounted for, our analysis suffers from the large range of the constrained maximum horizontal stress $S_H$. We attempted to constrain this component of the stress tensor using combined borehole observation and earthquake focal mechanism solution inversion. Improvement on the accuracy of FM solutions can possibly help, but that requires collaboration with seismologists. Further, stress inversion might suffer from a philosophical deficiency that stress near the fault is inevitably disturbed and different from the far-field stress. We acknowledge this caveat in *Shen et al.,* [2019] but could not offer a method for mitigation.

That being said, a few techniques can be readily applied to improve the $S_H$ constrained through borehole images. First, in this study, only low-resolution scans of image logs are available for analysis. The width of borehole breakout and more subtle drilling-induced tensile fractures can be better identified and quantified should the actual logs are accessible to the author. $S_H$'s uncertainty also suffered from largely unknown rock's mechanical properties – rock's failure parameters are needed to assess the conditions the borehole fail and subsequently invert for $S_H$. We do not attempt to use the information of slanted boreholes; however, if the rock's elastic properties are measured with anisotropy properly accounted for, the method described in *Li et al.,* [2019] can be adapted for additional $S_H$ constraints.

A separate issue is that the location of the stress measurements made here are highly biased in that they all originate within a single formation that has received a great deal of attention because of the economic interest in the Duvernay Formation. We lack understanding of the true full

variations of stress and pore fluid pressures throughout the entire sedimentary column. Having this information would greatly improve our understanding of the entire system. One important question to ask is the degree to which the states of stress vary vertically through different formations. Might the Duvernay Formation, due to its higher stiffness, for example, relative at least to the overlying Ireton Formation, take up more of the tectonic load and concentrate the stresses? Other questions may revolve around how pore pressures might vary throughout the column. These variations in stress and fluid pressure could be important but ignored factors that might influence the location and distribution of seismicity. Ideally, a concerted scientific drilling campaign to make multiple measurements throughout the sedimentary strata and even into the basement would provide enormous insight into how these properties evolve.

Further, there exist questions on the states of pore pressure in the rocks near the wellbore. We observe that for some boreholes, the modeled $P_P$ of the Duvernay segment that approaches $S_h$, should result in the failure of borehole walls. However, for large segments of image logs of the Duvernay Formation, we do not observe such expected long, continuous borehole breakouts. In this work, the author did not attempt to study the cause for this unexpected phenomenon; this would be of interest for future investigations.

**References**

Li, W., Schmitt, D.R., Tibbo, M. and Zou, C., 2019. A program to calculate the state of stress in the vicinity of an inclined borehole through an anisotropic rock formation. *Geophysics*, *84*(5), pp.F103-F118.

Shen, L.W., Schmitt, D.R. and Haug, K., 2019. Quantitative constraints to the complete state of stress from the combined borehole and focal mechanism inversions: Fox Creek, Alberta. *Tectonophysics*, *764*, pp.110-123.

## Bibliography


Aadnoy, B.S., 1990. In-situ stress directions from borehole fracture traces. Journal of Petroleum Science and Engineering 4, 143-153.

Aadnoy, B.S., Bell, J.S., 1998. Classification of drilling induced fractures and their relationship to in situ stress directions. The Log Analyst, 27-42.

Adewole, E.O., Healy, D., 2017. Systematic assessment of fault stability in the Northern Niger Delta Basin, Nigeria: Implication for hydrocarbon prospects and increased seismicities. Tectonophysics 699, 227-243.

Ahmed, T. and McKinney, P. 2011. Advanced Reservoir Engineering (revised); Elsevier, 424 p.

Alberta Energy Regulator (AER, 2015), Subsurface order no. 2: Monitoring and reporting of seismicity in the vicinity of hydraulic fracturing operations in the Duvernay zone, Fox Creek, Alberta, *[Available at http://www.aer.ca/documents/bulletins/Bulletin-2015-07.pdf]. 3 pages*.

Alberta Energy Regulator (AER, 2019), Subsurface Order No. 7, *[Available at https://static.aer.ca/prd/documents/orders/subsurface-orders/SO7.pdf]. 4 pages*.

Alt, R. C., and Zoback M. D., 2016. In situ stress and active faulting in Oklahoma, *Bull. Seismol. Soc. Amer.*, *107*(1), 216-228.

Ameen, M.S., 2016. Fracture modes in the Silurian Qusaiba shale play, northern Saudi Arabia and their geomechanical implications. *Marine and Petroleum Geology*, 78, pp.312-355.

Ameen, M.S., 2019. April. Borehole imaging of natural fractures and stress indicators in the Jurassic Carbonate Shale Plays, Eastern Saudi Arabia. In Sixth EAGE Shale Workshop (Vol. 2019, No. 1, pp. 1-5). *European Association of Geoscientists & Engineers*.

Anderson, E.M., 1905. The dynamics of faulting; Transactions of the Edinburgh Geological Society, v. 8, no. 3, p. 387–402.

Anderson, E. M., 1942. The dynamics of faulting and dyke formation with applications to Britain, Oliver and Boyd.

Anderson, E.M., 1951. The Dynamics of Faulting and Dyke Formation with Applications to Britain, 2nd ed. Oliver and Boyd, London and Edinburgh.

Angelier, J., 1979. Determination of the mean principal directions of stresses for a given fault population. Tectonophysics 56, T17-T26.

Atkinson, G.M., Eaton, D.W., Ghofrani, H., Walker, D., Cheadle, B., Schultz, R., Shcherbakov, R., Tiampo, K., Gu, J., Harrington, R.M. and Liu, Y., 2016. Hydraulic fracturing and seismicity in the Western Canada Sedimentary Basin. *Seismological research letters*, *87*(3), pp.631-647.

Atkinson, G. M., Eaton, D.W. and Igonin, N., 2020. Developments in understanding seismicity triggered by hydraulic fracturing. *Nature Reviews Earth & Environment*, 1(5), pp.264-277.

Babcock, E.A., 1978. Measurement of subsurface fractures from dipmeter logs; AAPG Bulletin, v. 62, no. 7, p. 1111–1126.

Barree, R.D., Barree, V.L. and Craig, D., 2009. Holistic fracture diagnostics: consistent interpretation of prefrac injection tests using multiple analysis methods; SPE Production & Operations, v. 24, no. 3, p. 396–406.

Baranova, V., Mustaqeem, A., and Bell, S., 1999. A model for induced seismicity caused by hydrocarbon production in the Western Canada Sedimentary Basin, *Canadian Journal of Earth Sciences*, *36*(1), 47-64.

Bailey, A.H.E., King, R.C., Holford, S.P., Hand, M., 2016. Incompatible stress regimes from geological and geomechanical datasets: Can they be reconciled? An example from the Carnarvon Basin, Western Australia. Tectonophysics 683, 405-416.

Bao, X.W., Eaton, D.W., 2016. Fault activation by hydraulic fracturing in western Canada. Science 354, 1406-1409.

Barton, C.A., Zoback, M.D. and Burns, K.L. 1988. In-situ stress orientation and magnitude at the Fenton geothermal site, New Mexico, determined from wellbore breakouts; Geophysical Research Letters, v. 15, no. 5, p. 467–470.

Bell, J.S. and Babcock, E.A. 1986. The stress regime of the Western Canadian Basin and implications for hydrocarbon production; Bulletin of Canadian Petroleum Geology, v. 34, no. 3, p. 364–378.

Bell, J.S. and Bachu, S. 2003. In situ stress magnitude and orientation estimates for Cretaceous coal-bearing strata beneath the plains area of central and southern Alberta; Bulletin of Canadian Petroleum Geology, v. 51, no. 1, p. 1–28.

Bell, J.S. and Gough, D.I. 1979. Northeast-southwest compressive stress in Alberta evidence from oil wells; Earth and Planetary Science Letters, v. 45, no. 2, p. 475–482.

Bell, J.S. and Grasby, S.E. 2012. The stress regime of the Western Canadian Sedimentary Basin; Geofluids, v. 12, no. 2, p. 150–165.

Bell, J.S., Price, P. R., and McLellan, P.J. 1994. In-situ stress in the Western Canada Sedimentary Basin; Chapter 29 *in* Geological Atlas of the Western Canada Sedimentary Basin, G.D. Mossop and I. Shetsen (ed.), Canadian Society of Petroleum Geologists, Calgary, Alberta and Alberta Research Council, Edmonton, Alberta, p. 439–446.

Beaumont, C. 1981. Foreland basins, *Geophysical Journal International*, *65*(2), 291-329.

Bouzidi, Y., D. R. Schmitt, Burwash, R. A., and Kanasewich, E. R. 2002. Depth migration of deep seismic reflection profiles: crustal thickness variations in Alberta, *Canadian Journal of Earth Sciences*, *39*(3), 331-350.

Berens, P. 2009. CircStat: a Matlab Toolbox for circular statistics. Journal of Statistical Software, 31, 21.

Bott, M.H.P. 1959. The mechanics of oblique slip faulting. Geological Magazine 96, 109-117.

Bowman, A.W., Azzalini, A. 1997. Applied smoothing techniques for data analysis: the kernel approach with S-Plus illustrations. OUP Oxford.

Branscombe, P., MacCormack, K.E., Corlett, H., Hathway, B., Hauck, T.E., Peterson, J.T. 2018. 3D Provincial Geological Framework Model of Alberta, Version 1(dataset, multiple files). Alberta Energy Regulator, Edmonton, Alberta, Canada.

Brudy, M., Zoback, M.D. 1999. Drilling-induced tensile wall-fractures: implications for determination of in-situ stress orientation and magnitude. International Journal of Rock Mechanics and Mining Sciences 36, 191-215.

Byerlee, J. 1978. Friction of rocks, *Pure and Applied Geophysics PAGEOPH*, *116*(4-5), 615-626, doi:10.1007/BF00876528.

Castaños, H., and Lomnitz, C. 2002. PSHA: Is it science?, *Engineering Geology*, *66*(3-4), 315-317.

Catalli, F., M. A. Meier, and Wiemer, S. 2013. The role of Coulomb stress changes for injection-induced seismicity: The Basel enhanced geothermal system, *Geophysical Research Letters*, *40*(1), 72-77.

Chen, Y., Gu, Y. J., Currie, C. A., Johnston, S. T., Hung S.-H., Schaeffer A. J., and Audet, P. 2019. Seismic evidence for a mantle suture and implications for the origin of the Canadian Cordillera, *Nature communications*, *10*(1), 1-10.

Castillo, J.L. 1987. Modified fracture pressure decline analysis including pressure-dependent leakoff; Low-Permeability Reservoirs Symposium, Denver, Colorado, May 18–19, 1987, Paper SPE 16417, https://doi.org/10.2118/16417-MS.

Cinco-Ley, H. 1981. Transient pressure analysis for fractured wells; Journal of Petroleum Technology, v. 33, no. 9, p. 1–749.

Craig, D.P., Barree, R.D., Warpinski, N.R. and Blasingame, T.A. 2017. Fracture closure stress: re-examining field and laboratory experiments of fracture closure using modern interpretation methodologies; Society of Petroleum Engineers, Annual Technical Conference and Exhibition, October 9-11, San Antonio, Texas, Paper SPE-187038-MS, https://doi.org/10.2118/187038-MS.

Cant, D.J., Stockmal, G.S., 1989. The Alberta foreland basin: relationship between stratigraphy and Cordilleran terrane-accretion events. Canadian Journal of Earth Sciences 26, 1964-1975.

Célérier, B., Etchecopar, A., Bergerat, F., Vergely, P., Arthaud, F., Laurent, P., 2012. Inferring stress from faulting: From early concepts to inverse methods. Tectonophysics 581, 206-219.

Chang, C., Lee, J.B., Kang, T.-S., 2010. Interaction between regional stress state and faults: Complementary analysis of borehole in situ stress and earthquake focal mechanism in southeastern Korea. Tectonophysics 485, 164-177.

Chopra, S., Sharma, R.K., Ray, A.K., Nemati, H., Morin, R., Schulte, B., D'Amico, D., 2017. Seismic reservoir characterization of Duvernay shale with quantitative interpretation and induced seismicity considerations—A case study. Interpretation 5, T185-T197.

Chang, K. W., and Segall, P. 2016. Injection-induced seismicity on basement faults including poroelastic stressing, *Journal of Geophysical Research: Solid Earth*, *121*(4), 2708-2726, doi:10.1002/2015jb012561.

Çiftçi, N.B., 2013. In-situ stress field and mechanics of fault reactivation in the Gediz Graben, Western Turkey. J. Geodyn. 65, 136-147.

Crawford, B., Faulkner, D., and Rutter, E. 2008. Strength, porosity, and permeability development during hydrostatic and shear loading of synthetic quartz-clay fault gouge, Journal of Geophysical Research: Solid Earth, 113(B3).

Cochran, E. S., Skoumal, R. J., McPhillips, D., Ross, Z. E., and Keranen, K. M. 2020. Activation of optimally and unfavourably oriented faults in a uniform local stress field during the 2011 Prague, Oklahoma, sequence, *Geophysical Journal International*, *222*(1), 153-168.

Corlett, H., Schultz R., Branscombe, P., Hauck T., Haug K., MacCormack, K., and Shipman, T. 2018. Subsurface faults inferred from reflection seismic, earthquakes, and sedimentological relationships: Implications for induced seismicity in Alberta, Canada, *Marine and Peroleum Geology*, *93*, 135-144.

Cueto-Felgueroso, L., Vila, C., Santillán, D., and Mosquera, J. C. 2018. Numerical Modeling of Injection-Induced Earthquakes Using Laboratory-Derived Friction Laws, *Water Resources Research*, *54*(12), 9833-9859.

Day, R. W. 1992. Effective cohesion for compacted clay, Journal of geotechnical engineering, 118(4), 611-619.

Deng, K., Liu, Y., and Harrington, R. M. 2016. Poroelastic stress triggering of the december 2013 crooked lake, alberta, induced seismicity sequence, *Geophysical Research Letters*, *43*(16), 8482-8491, doi:10.1002/2016gl070421.

Davis, M. and Karlen, G. 2013. A regional assessment of the Duvernay Formation; a world-class liquids-rich shale play; extended abstract of presentation at CSPG/CSEG/CWLS GeoConvention 2013, (Integration: Geoscience Engineering Partnership), Calgary, Alberta, May 6-12, 2013, Search and Discovery Article #10638 (2014), URL <http://www.searchanddiscovery.com/pdfz/documents/2014/10638davis/ndx_davis.pdf.html> [August 2018].

Detournay, E., Cheng, A.D., Roegiers, J.C. and McLennan, J.D. 1989. Poroelasticity considerations in in situ stress determination by hydraulic fracturing; International Journal of Rock Mechanics and Mining Sciences & Geomechanics Abstracts, v. 26, no. 6, p. 507–513.

Doe, T., Ingevald, K., Strindell, L., Haimson, B. and Carlsson, H. 1981. Hydraulic fracturing and overcoring stress measurements in a deep borehole at the Stripa test mine, Sweden; American Rock Mechanics Association, 22nd U.S. Symposium on Rock Mechanics (USRMS), June 29–July 2, 1981, Cambridge, Massachusetts, Paper ARMA-81-0373, URL <https://www.onepetro.org/conference-paper/ARMA-81-0373> [August 2018].

Deichmann, N. and Giardini, D., 2009. Earthquakes induced by the stimulation of an enhanced geothermal system below Basel (Switzerland). *Seismological Research Letters*, *80*(5), pp.784-798.

Dieterich, J. H. 1972. Time-dependent friction in rocks, Journal of Geophysical Research, 77(20), 3690-3697.

Dieterich, J. H. 1978. Time-dependent friction and the mechanics of stick-slip, in Rock Friction and Earthquake Prediction, edited, pp. 790-806, Springer.

Eaton, D., 2017. Dynamics of fault activation from hydraulic fracturing in overpressured shales, 79th EAGE Conference and Exhibition 2017-Workshops Date. EAGE, Paris, p. 4.

Eaton, D., Schultz, R., 2018. Increased likelihood of induced seismicity in highly overpressured shale formations. Geophysical Journal International 214, 751-757.

Eaton, D.W., Igonin, N., Poulin, A., Weir, R., Zhang, H., Pellegrino, S., Rodriguez, G., 2018. Induced Seismicity Characterization during Hydraulic-Fracture Monitoring with a

Shallow-Wellbore Geophone Array and Broadband Sensors. Seismological Research Letters 89, 1641-1651.

Ellsworth, W.L., 2013. Injection-induced earthquakes. *Science*, *341*(6142).

Ellis, D.V. and Singer, J.M. 2007). Well Logging for Earth Scientists (Second Edition); Springer, Dordrecht, 692 p., https://doi.org/10.1007/978-1-4020-4602-5

Evans, D.M., 1966. The Denver area earthquakes and the Rocky Mountain Arsenal disposal well. *The Mountain Geologist*.

Eberhart-Phillips, D., and Oppenheimer, D. H. 1984. Induced seismicity in The Geysers geothermal area, California, *Journal of Geophysical Research: Solid Earth*, *89*(B2), 1191-1207.

Edwards, D. J., and Brown, R. J. 1999. Understanding the influence of Precambrian crystalline basement on Upper Devonian carbonates in central Alberta from a geophysical perspective, *Bulletin of Canadian Petroleum Geology*, *47*(4), 412-438.

Ekpo, E., Eaton, D., and Weir, R. 2017. Basement Tectonics and Fault Reactivation in Alberta Based on Seismic and Potential Field Data, in *Geophysics*, edited, IntechOpen.

Ellsworth, W.L., Giardini, D., Townend, J., Ge, S. and Shimamoto, T. 2019. Triggering of the Pohang, Korea, earthquake ($M_w$ 5.5) by enhanced geothermal system stimulation. Seismological Research Letters, 90(5), pp.1844-1858.

Eyre, T. S., Eaton D. W., Zecevic M., D'Amico, D., and Kolos, D. 2019. Microseismicity reveals fault activation before M w 4.1 hydraulic-fracturing induced earthquake, *Geophysical Journal International*, *218*(1), 534-546.

Fasola, S. L., Brudzinski, M. R., Skoumal, R. J., Langenkamp, T., Currie, B. S., and Smart, K. J. 2019. Hydraulic fracture injection strategy influences the probability of earthquakes in the Eagle Ford shale play of South Texas, *Geophysical Research Letters*, *46*(22), 12958-12967.

Frankel, A. 2013. Comment on "Why earthquake hazard maps often fail and what to do about it" by S. Stein, R. Geller, and M. Liu, *Tectonophysics*, *592*, 200-206.

Farahbod, A.M., Kao, H., Walker, D. M. and Cassidy, J. F. 2015. Investigation of regional seismicity before and after hydraulic fracturing in the Horn River Basin, northeast British Columbia. *Canadian Journal of Earth Sciences*, *52*(2), pp.112-122.

Faulkner, D., Mitchell, T., Healy, D., and Heap, M. 2006. Slip on'weak'faults by the rotation of regional stress in the fracture damage zone. Nature 444, 922.

Foulger, G. R., Wilson, M. P., Gluyas, J. G., Julian, B. R., and Davies, R. J. 2018. Global review of human induced earthquakes, *Earth-Science Reviews*, *178*, 438-514, doi:https://doi.org/10.1016/j.earscirev.2017.07.008.

Fordjor, C.K., Bell, J.S. and Gough, D.I. 1983. Breakouts in Alberta and stress in the North American plate; Canadian Journal of Earth Sciences, v. 20, no. 9, p. 1445–1455.

Fox, A. D. and Soltanzadeh, M. 2015. A regional geomechanical study of the Duvernay Formation in Alberta, Canada; paper presented at GeoConvention 2015, *Geoscience: New Horizons*, May 4–8, 2015, Calgary, Alberta.

Galloway, E., Hauck., T., Corlett., H., Pană, D., and Schultz, R. 2018. Faults and associated karst collapse suggest conduits for fluid flow that influence hydraulic fracturing-induced seismicity, *Proceedings of the National Academy of Sciences*, *115*(43), E10003-E10012.

Garagash, D. I., and Germanovich, L. N. 2012. Nucleation and arrest of dynamic slip on a pressurized fault, *Journal of Geophysical Research: Solid Earth*, *117*(B10).

Goebel, T., Weingarten., M., Chen, X., Haffener, J., and Brodsky, E. 2017. The 2016 Mw5. 1 Fairview, Oklahoma earthquakes: Evidence for long-range poroelastic triggering at> 40 km from fluid disposal wells, *Earth and Planetary Science Letters*, *472*, 50-61.

Gough, D., and Gough, W. 1970. Load-induced earthquakes at Lake Kariba—II, *Geophysical Journal International*, *21*(1), 79-101.

Gough, D.I. and Bell, J.S. 1981. Stress orientations from oil well fractures in Alberta and Texas; Canadian Journal of Earth Sciences, v. 18, p. 638–645.

Gough, D.I., and Bell, J.S. 1982. Stress orientation from borehole wall fractures with examples from Colorado, east Texas, and northern Canada; Canadian Journal of Earth Sciences, v. 19, p. 1358–1370.

Green, D.G. and Mountjoy, E.W. 2005. Fault and conduit controlled burial dolomitization of the Devonian west-central Alberta Deep Basin; Bulletin of Canadian Petroleum Geology, v. 53., no. 2, p. 101–129.

Gephart, J.W., 1990. Stress and the direction of slip on fault planes. Tectonics 9, 845-858.

Green, D.G., and Mountjoy, E.W. 2005. Fault and conduit controlled burial dolomitization of the Devonian west-central Alberta Deep Basin. Bulletin of Canadian Petroleum Geology 53, 101-129.

Giardini, D., 2009. Geothermal quake risks must be faced. *Nature*, *462*(7275), pp.848-849.

Gupta, H., Narain, H., Rastogi, B.K., and Mohan, I. 1969. A study of the Koyna earthquake of December 10, 1967. *Bulletin of the Seismological Society of America*, *59*(3), pp.1149-1162.

Gomberg, J. 2018. Unsettled earthquake nucleation, *Nature Geoscience*, *11*(7), 463-464, doi:10.1038/s41561-018-0149-x.

Gu, Y., and Wong, T.-f. 1994. Development of shear localization in simulated quartz gouge: Effect of cumulative slip and gouge particle size, pure and applied geophysics, 143(1-3), 387-423.

Gu, Y. J., and Shen, L. 2015. Noise correlation tomography of southwest western Canada sedimentary basin, *Geophysical Journal International*, *202*(1), 142-162.

Harris, R. A. 1998. Introduction to special section: Stress triggers, stress shadows, and implications for seismic hazard, *Journal of Geophysical Research: Solid Earth*, *103*(B10), 24347-24358, doi:10.1029/98jb01576.

Horner, R.B., Barclay, J.E. and MacRae, J.M. 1994. Earthquakes and hydrocarbon production in the Fort St. John area of northeastern British Columbia. *Can. J. Explor. Geophys.*, *30*(1), pp.39-50.

Healy, J.H., Rubey, W.W., Griggs, D.T. and Raleigh, C.B. 1968. The Denver earthquakes. *Science*, *161*(3848), pp.1301-1310.

Haimson, B.C. and Rummel, F. 1982. Hydrofracturing stress measurements in the Iceland research drilling project drill hole at Reydarfjordur, Iceland; Journal of Geophysical Research: Solid Earth, v. 87, no. B8, p. 6631–6649.

Hammermaster, K., Schmidt, G., Dunn, L., Brown, M., Bernard, R., Wen, E., Befus, R. and Gardiner, S. 2012. The Duvernay Formation (Devonian): an emerging shale liquids play in Alberta. In Canada: Expanded Abstracts, CSPG Conferences Abstract Archive.

Hardebeck, J.L., and Hauksson, E. 2001. Crustal stress field in southern California and its implications for fault mechanics. Journal of Geophysical Research-Solid Earth 106, 21859-21882.

Hardebeck, J.L., and Michael, A.J. 2006. Damped regional-scale stress inversions: Methodology and examples for southern California and the Coalinga aftershock sequence. Journal of Geophysical Research: Solid Earth 111.

Haug, K. and Bell, J.S. 2016. Compilation of in situ stress data from Alberta and northeastern British Columbia (tabular data, tab delimited); Alberta Energy Regulator, AER/AGS Digital Data 2016-0040, URL <https://ags.aer.ca/publications/DIG-2016-0040.html> [August 2018].

Heidbach, O., Rajabi, M., Reiter, K., Ziegler, M. and WSM Team. 2016. World Stress Map Database Release 2016; GFZ Data Services, http://doi.org/10.5880/WSM.2016.001.

Henton, J.A., Craymer, M.R., Dragert, H., Mazzotti, S., Ferland, R. and Forbes, D.L. 2006. Crustal motion and deformation monitoring of the Canadian landmass; Geomatica, v. 60, no. 2, p. 173–191.

Horner, D.R. 1951. Pressure build-up in wells; 3rd World Petroleum Congress, May 28–June 6, 1951, The Hague, Netherlands, Paper WPC-4135, URL <https://www.onepetro.org/conference-paper/WPC-4135> [August 2018].

Howard, G.C. and Fast, C.R. 1957. Optimum fluid characteristics for fracture extension; American Petroleum Institute, *Drilling and Production Practice*, January 1, 1957, New York, New York, Paper API-57-261, https://www.onepetro.org/conference-paper/API-57-261 [August 2018].

Hergert, T., Heidbach, O., Reiter, K., Giger, S., and Marschall, P. 2015. Stress field sensitivity analysis in a sedimentary sequence of the Alpine foreland, northern Switzerland. Solid Earth 6, 533.

Hicks, E.C., Bungum, H., and Lindholm, C.D. 2000. Stress inversion of earthquake focal mechanism solutions from onshore and offshore Norway. Norsk Geologisk Tidsskrift 80, 235-250.

Hubbert, M.K., and Rubey, W. W. 1959. Role of Fluid Pressure in Mechanics of Overthrust Faulting .1. Mechanics of Fluid-Filled Porous Solids and Its Application to Overthrust Faulting. Geol. Soc. Am. Bull. 70, 115-166.

Hincks, T., Aspinall, W., Cooke, R., and Gernon, T. 2018. Oklahoma's induced seismicity strongly linked to wastewater injection depth, *Science*, *359*(6381), 1251-1255.

Hoffman, P. F. 1988. United plates of America, the birth of a craton: Early Proterozoic assembly and growth of Laurentia, *Annual Review of Earth and Planetary Sciences*, *16*(1), 543-603.

Jia, S. Q. 2019. Stress Inversion and Damage Quantification in Tight Gas Shale with Application to Hydraulic Fracturing.

Kettlety, T., Verdon, J., Werner, M., and Kendall, J. 2020. Stress transfer from opening hydraulic fractures controls the distribution of induced seismicity, *Journal of Geophysical Research: Solid Earth*, *125*(1), e2019JB018794.

King, G. C., Stein, R. S., and Lin, J. 1994. Static stress changes and the triggering of earthquakes, *Bull. Seismol. Soc. Amer.*, *84*(3), 935-953.

Kleiner, S., and Aniekwe, O. 2019. The Duvernay shale completion journey, paper presented at SPE Kuwait Oil & Gas Show and Conference, Society of Petroleum Engineers.

Ikari, M. J., and Kopf A. J. 2017. Seismic potential of weak, near-surface faults revealed at plate tectonic slip rates, Science advances, 3(11), e1701269.

Ikari, M. J., D. M., and Marone C. (2007), Effect of hydration state on the frictional properties of montmorillonite-based fault gouge, Journal of Geophysical Research: Solid Earth, 112(B6).

Ikari, M. J., Marone C., and Saffer D. M. 2011. On the relation between fault strength and frictional stability, Geology, 39(1), 83-86.

Lopez-Comino, J.A., Cesca, S., Jarosławski, J., Montcoudiol, N., Heimann, S., Dahm, T., Lasocki, S., Gunning, A., Capuano, P. and Ellsworth, W.L. 2018. Induced seismicity response of

hydraulic fracturing: Results of a multidisciplinary monitoring at the Wysin site, Poland. Scientific reports, 8(1), pp.1-14.

Kohli, A. H., and Zoback, M. D. 2013. Frictional properties of shale reservoir rocks, Journal of geophysical research: solid earth, 118(9), 5109-5125.

Kastrup, U., Zoback, M.L., Deichmann, N., Evans, K.F., Giardini, D., Michael, A.J. 2004. Stress field variations in the Swiss Alps and the northern Alpine foreland derived from inversion of fault plane solutions. Journal of Geophysical Research: Solid Earth 109.

Konstantinovskaya, E., Malo, M., and Castillo, D.A. 2012. Present-day stress analysis of the St. Lawrence Lowlands sedimentary basin (Canada) and implications for caprock integrity during CO2 injection operations. Tectonophysics 518-521, 119-137.

Keranen, K.M., Savage, H.M., Abers, G.A. and Cochran, E.S., 2013. Potentially induced earthquakes in Oklahoma, USA: Links between wastewater injection and the 2011 Mw 5.7 earthquake sequence. *Geology*, *41*(6), pp.699-702.

Keranen, K.M., Weingarten, M., Abers, G.A., Bekins, B.A. and Ge, S., 2014. Sharp increase in central Oklahoma seismicity since 2008 induced by massive wastewater injection. *Science*, *345*(6195), pp.448-451.

Jaeger, J., Cook, N., Zimmerman, R., 2007. Fundamentals of rock mechanics. Wiley-Blackwell, New York.

Jones, L.M., 1988. Focal mechanisms and the state of stress on the San Andreas fault in southern California. Journal of Geophysical Research: Solid Earth 93, 8869-8891.

Logan, J. M., and Rauenzahn, K. A. 1987. Frictional dependence of gouge mixtures of quartz and montmorillonite on velocity, composition and fabric, Tectonophysics, 144(1-3), 87-108.

Levandowski, W., Herrmann, R.B., Briggs, R., Boyd, O., and Gold, R. 2018. An updated stress map of the continental United States reveals heterogeneous intraplate stress. Nature Geoscience, 1.

Liu, L., Zoback, M.D. 1992. The effect of topography on the state of stress in the crust: Application to the site of the Cajon Pass Scientific Drilling Project. Journal of Geophysical Research 97, 5095-5108.

Lund, B., Slunga, R. 1999. Stress tensor inversion using detailed microearthquake information and stability constraints: Application to Ölfus in southwest Iceland. Journal of Geophysical Research: Solid Earth 104, 14947-14964.

Lyster, S., Corlett, H., and Berhane, H. 2017. Hydrocarbon Resource Potential of the Duvernay Formation in Alberta – Update. Alberta Energy Regulator, Edmonton, p. 44.

Lele, S.P., Tyrrell, T., Dasari, G.R. and Symington, W.A. 2017. Geomechanical analysis of hydraulic fracturing induced seismicity at Duvernay field in western Canadian sedimentary basin. GeoConvention 2017, p.5.

Lele, S.P., Tyrrell, T. and Dasari, G.R. 2017, August. Geomechanical analysis of fault reactivation due to hydraulic fracturing. In 51st US Rock Mechanics/Geomechanics Symposium. American Rock Mechanics Association.

Li, L., Tan, J., Wood, D.A., Zhao, Z., Becker, D., Lyu, Q., Shu, B. and Chen, H. 2019. A review of the current status of induced seismicity monitoring for hydraulic fracturing in unconventional tight oil and gas reservoirs. Fuel, 242, pp.195-210.

Lemieux, S. 1999. Seismic reflection expression and tectonic significance of Late Cretaceous extensional faulting of the Western Canada Sedimentary Basin in southern Alberta, *Bulletin of Canadian Petroleum Geology*, *47*(4), 375-390.

Marone, C., Raleigh, C.B. and Scholz, C.H., 1990. Frictional behavior and constitutive modeling of simulated fault gouge. Journal of Geophysical Research: Solid Earth, 95(B5), pp.7007-7025.

Marone, C. 1998. Laboratory-derived friction laws and their application to seismic faulting, Annual Review of Earth and Planetary Sciences, 26(1), 643-696.

Marone, C., and Saffer, D. M. 2007. Fault friction and the upper transition from seismic to aseismic faulting, The Seismogenic Zone of Subduction Thrust Faults, 346-369.

Marone, C., Raleigh, C. B., and Scholz, C. 1990. Frictional behavior and constitutive modeling of simulated fault gouge, Journal of Geophysical Research: Solid Earth, 95(B5), 7007-7025.

Morris, A., Ferrill, D. A., and Henderson, D. B. 1996. Slip-tendency analysis and fault reactivation, Geology, 24(3), 275-278.

Morrow, C., Moore, D. E., and Lockner, D. 2000. The effect of mineral bond strength and adsorbed water on fault gouge frictional strength, Geophysical research letters, 27(6), 815-818.

Mardia, K., and Jupp, P. 1999. Directional Statistics. Wiley.

McGarr, A. 1988. On the State of Lithospheric Stress in the Absence of Applied Tectonic Forces. Journal of Geophysical Research: Solid Earth 93, 13609-13617.

McGarr, A., Gay, N.C. 1978. State of Stress in the Earth's Crust. Annual Review of Earth and Planetary Sciences 6, 405-436.

McTigue, D.F., Mei, C.C., 1981. Gravity-Induced Stresses near Topography of Small Slope. Journal of Geophysical Research 86, 9268-9278.

Michael, A.J., 1984. Determination of stress from slip data: faults and folds. Journal of Geophysical Research: Solid Earth 89, 11517-11526.

Miller, D.J., Dunne, T., 1996. Topographic perturbations of regional stresses and consequent bedrock fracturing. Journal of Geophysical Research: Solid Earth 101, 25523-25536.

Montone, P., Mariucci, M.T., Pondrelli, S., Amato, A., 2004. An improved stress map for Italy and surrounding regions (central Mediterranean). Journal of Geophysical Research: Solid Earth 109.

Morris, A.P., Ferrill, D.A., Walter, G.R., Price, A.M., Smart, K.J., Skoumal, R.J., Brudzinski, M.R., Currie, B.S., 2017. Lessons learned from the Youngstown, Ohio induced earthquake sequence from January 2011 to January 2012. Journal of Rock Mechanics and Geotechnical Engineering 9, 783-796.

Morin, M.L. 2017. Natural and drilling induced fractures in the Grosmont Formation, Alberta: implications for the state of stress; M.Sc. thesis, University of Alberta, Edmonton, Alberta, 108 p.

MacKay, M.K., Eaton, D.W., Pedersen, P.K. and Clarkson, C.R., 2018. Integration of outcrop, subsurface, and microseismic interpretation for rock-mass characterization: An example from the Duvernay Formation, Western Canada. Interpretation, 6(4), pp.T919-T936.

Maury, V.M.R., Grassob, J.R. and Wittlinger, G., 1992. Monitoring of subsidence and induced seismicity in the Lacq gas field (France): The consequences on gas production and field operation. Engineering Geology, 32(3), pp.123-135.

McClure, M.W. and Horne, R.N., 2011. Investigation of injection-induced seismicity using a coupled fluid flow and rate/state friction model. Geophysics, 76(6), pp.WC181-WC198.

McLellan, P., 1989. In-situ stress magnitudes from hydraulic fracturing treatment records: a feasibility study. Institute of Sedimentary and Petroleum Geology.

Moore, P. F. 1988. Devonian reefs in Canada and some adjacent areas.

Mukuhira, Y., Dinske, C., Asanuma, H., Ito, T. and Häring, M.O., 2017. Pore pressure behavior at the shut-in phase and causality of large induced seismicity at Basel, Switzerland. Journal of Geophysical Research: Solid Earth, 122(1), pp.411-435.

Nolte, K.G. 1979. Determination of fracture parameters from fracturing pressure decline; Society of Petroleum Engineers, Annual Technical Conference and Exhibition, September 23–26, Las Vegas, Nevada, Paper SPE-8341-MS, https://doi.org/10.2118/8341-MS.

Nakatani, M., and Scholz, C. H. 2004. Frictional healing of quartz gouge under hydrothermal conditions: 1. Experimental evidence for solution transfer healing mechanism, Journal of Geophysical Research: Solid Earth, 109(B7).

Nelson, E.J., Chipperfield, S.T., Hillis, R.R., Gilbert, J., McGowen, J., Mildren, S.D., 2007. The relationship between closure pressures from fluid injection tests and the minimum principal stress in strong rocks. International Journal of Rock Mechanics and Mining Sciences 44, 787-801.

Nolte, K.G. 1986. A general analysis of fracturing pressure decline with application to three models; SPE Formation Evaluation, v. 1, no. 6, p. 571–583.

Ong, O. N., Schmitt, D. R., and Kofman, R. S. 2015. Seismic anisotropy and uniaxial stress measurements on Duvernay sedimentary rocks in Alberta: Report submitted to AER Core Research Laboratory, 28 pp, Alberta Geological Survey, Edmonton.

Ong, O.N., Schmitt, D.R., Kofman, R.S., Haug, K., 2016. Static and dynamic pressure sensitivity anisotropy of a calcareous shale. Geophys. Prospect. 64, 875-897.

Pană, D. I., and van der Pluijm, B. A. 2015. Orogenic pulses in the Alberta Rocky Mountains: Radiometric dating of major faults and comparison with the regional tectono-stratigraphic record, *Bulletin*, *127*(3-4), 480-502.

Passelègue, F. X., M. Almakari, P. Dublanchet, F. Barras, J. Fortin, and M. Violay (2020), Initial effective stress controls the nature of earthquakes, *Nature Communications*, *11*(1), 1-8.

Pebesma, E.J., Wesseling, C.G., 1998. Gstat: a program for geostatistical modelling, prediction and simulation. Computers & Geosciences 24, 17-31.

Peška, P., Zoback, M.D., 1995. Compressive and tensile failure of inclined well bores and determination of in situ stress and rock strength. Journal of Geophysical Research: Solid Earth 100, 12791-12811.

Peterson, J., 2017. Subcrop extents of geological units at the sub-Cretaceous unconformity, west-central Alberta (gridded data, ASCII format), in: Regulator, A.E. (Ed.), AER/AGS Digital Data. Alberta Energy Regulator, Edmonton.

Pollard, D., Saltzer, S., Rubin, A.M., 1993. Stress inversion methods: are they based on faulty assumptions? Journal of Structural Geology 15, 1045-1054.

Pollard, D., Segall, P., 1987. Fracture mechanics of rock.

Pollard, D. D., and Segall, P. 1987. Theoretical displacements and stresses near fractures in rock: with applications to faults, joints, veins, dikes, and solution surfaces, paper presented at Fracture mechanics of rock.

Price, R. 2001. An evaluation of models for the kinematic evolution of thrust and fold belts: structural analysis of a transverse fault zone in the Front Ranges of the Canadian Rockies north of Banff, Alberta, *Journal of Structural Geology*, *23*(6-7), 1079-1088.

Pawley, S., Schultz, R., Playter, T., Corlett, H., Shipman, T., Lyster, S. and Hauck, T., 2018. The geological susceptibility of induced earthquakes in the Duvernay play. *Geophysical Research Letters*, *45*(4), pp.1786-1793.

Plumb, R.A., Evans, K.F. and Engelder, T., 1991. Geophysical log responses and their correlation with bed-to-bed stress contrasts in Paleozoic rocks, Appalachian Plateau, New York. Journal of Geophysical Research: Solid Earth, 96(B9), pp.14509-14528.

Preston, A., Garner, G., Beavis, K., Sadiq, O. and Stricker, S., 2016. Duvernay Reserves and Resources Report: A Comprehensive Analysis of Alberta's Foremost Liquids-Rich Shale Resource. Alberta Energy Regulator.

Raleigh, C.B., Healy, J.H. and Bredehoeft, J.D., 1976. An experiment in earthquake control at Rangely, Colorado. *Science*, *191*(4233), pp.1230-1237.

Rebollar, C.J., Kanasewich, E.R. and Nyland, E., 1982. Source parameters from shallow events in the Rocky Mountain House earthquake swarm. *Canadian Journal of Earth Sciences*, *19*(5), pp.907-918.

Reiter, K., Heidbach, O., Schmitt, D., Haug, K., Ziegler, M. and Moeck, I., 2014. A revised crustal stress orientation database for Canada. Tectonophysics, 636, pp.111-124.

Rokosh, C.D., Lyster, S., Anderson, S.D.A., Beaton, A.P., Berhane, H., Brazzoni, T., Chen, D., Cheng, Y., Mack, T., Pana, C. and Pawlowicz, J.G., 2012. Summary of Alberta's shale- and siltstone-hosted hydrocarbon resource potential. Energy Resources Conservation Board, ERCB/AGS Open File Report, 6, p.327.

Rebollar, C.J., Kanasewich, E.R. and Nyland, E., 1984. Focal depths and source parameters of the Rocky Mountain House earthquake swarm from digital data at Edmonton. *Canadian Journal of Earth Sciences*, *21*(10), pp.1105-1113.

Richards, B., Barclay, J., Bryan, D., Hartling, A., Henderson, C., Hinds, R., 1994. Carboniferous strata of the Western Canada sedimentary basin, in: Mossop, G.D., Shetsen, I. (Eds.), Geological atlas of the Western Canada Sedimentary Basin. Canadian Society of Petroleum Geologists and Alberta Research Council, Calgary.

Ross, G., and Eaton, D. 1999. Basement reactivation in the Alberta Basin: Observational constraints and mechanical rationale, *Bulletin of Canadian Petroleum Geology*, *47*(4), 391-411.

Ross, G.M., Parrish, R.R., Villeneuve, M.E. and Bowring, S.A., 1991. Geophysics and geochronology of the crystalline basement of the Alberta Basin, western Canada. Canadian Journal of Earth Sciences, 28(4), pp.512-522.

Ruina, A. 1983. Slip instability and state variable friction laws, *Journal of Geophysical Research: Solid Earth*, *88*(B12), 10359-10370, doi:10.1029/JB088iB12p10359.

Savage, W.Z., Swolfs, H.S., 1986. Tectonic and gravitational stress in long symmetric ridges and valleys. Journal of Geophysical Research: Solid Earth 91, 3677-3685.

Schmitt, D., Li, Y., 1993. Influence of a stress relief hole's depth on induced displacements: application in interferometric stress determinations, International journal of rock mechanics and mining sciences & geomechanics abstracts. Elsevier, pp. 985-988.

Schmitt, D.R. 2014. Basic geomechanics for induced seismicity: a tutorial, CSEG Recorder, v. 39, no. 11, p. 24–29.

Schmitt, D.R. and Haimson, B.C., 2017. Hydraulic fracturing stress measurements in deep holes. Rock Mechanics and Engineering, 1, pp.183-225.

Schmitt, D.R., Currie, C.A. and Zhang, L., 2012. Crustal stress determination from boreholes and rock cores: Fundamental principles. Tectonophysics, 580, pp.1-26.

Schultz, R., Stern, V. and Gu, Y.J., 2014. An investigation of seismicity clustered near the Cordel Field, west central Alberta, and its relation to a nearby disposal well. *Journal of Geophysical Research: Solid Earth*, *119*(4), pp.3410-3423.

Schultz, R., Stern, V., Gu, Y.J. and Eaton, D., 2015. Detection threshold and location resolution of the Alberta Geological Survey earthquake catalogue. Seismological Research Letters, 86(2A), pp.385-397.

Schultz, R., Atkinson, G., Eaton, D.W., Gu, Y.J., Kao, H., 2018. Hydraulic fracturing volume is associated with induced earthquake productivity in the Duvernay play. Science 359, 304-308.

Schultz, R., Wang, R., Gu, Y.J., Haug, K. and Atkinson, G., 2017. A seismological overview of the induced earthquakes in the Duvernay play near Fox Creek, Alberta. Journal of Geophysical Research: Solid Earth, 122(1), pp.492-505.

Schultz, R., Corlett, H., Haug, K., Kocon, K., MacCormack, K., Stern, V., Shipman, T., 2016. Linking fossil reefs with earthquakes: Geologic insight to where induced seismicity occurs in Alberta. Geophysical Research Letters 43, 2534-2542.

Schultz, R., Stern, V., Novakovic, M., Atkinson, G., Gu, Y.J., 2015. Hydraulic fracturing and the Crooked Lake Sequences: Insights gleaned from regional seismic networks. Geophysical Research Letters 42, 2750-2758.

Schultz, R., Wang, R., Gu, Y.J., Haug, K., Atkinson, G., 2017. A seismological overview of the induced earthquakes in the Duvernay play near Fox Creek, Alberta. Journal of Geophysical Research: Solid Earth 122, 492-505.

Schultz, R., and R. Wang (2020), Newly emerging cases of hydraulic fracturing induced seismicity in the Duvernay East Shale Basin, *Tectonophysics*, 228393.

Schultz, S., J. A. MacEachern, and H. D. Gibson (2019), Late Mesozoic reactivation of Precambrian basement structures and their resulting effects on the sequence stratigraphic architecture of the Viking Formation of east-central Alberta, Canada, *Lithosphere*, *11*(3), 308-321.

Schwab, D.R., Bidgoli, T.S., Taylor, M.H., 2017. Characterizing the Potential for Injection-Induced Fault Reactivation Through Subsurface Structural Mapping and Stress Field Analysis, Wellington Field, Sumner County, Kansas. Journal of Geophysical Research: Solid Earth 122, 10,132-110,154.

Schwanghard, W., 2010. variogramfit. Online web resource. URL https://www.mathworks.com/matlabcentral/fileexchange/25948-variogramfit. Last accessed Jan 2nd, 2018.

Shen, L., Schmitt, D.R., Haug, K., 2018a. Measurements of the states of in situ stress for the Duvernay Formation near Fox Creek, west-central Alberta; Alberta Energy Regulator / Alberta Geological Survey, AER/AGS Report 97, 29 p.

Shen, L., Schmitt, D.R., Haug, K. 2018b. In-Situ Stress Measurements for the Duvernay Formation, Alberta (tabular data, tab-delimited format); Alberta Energy Regulator / Alberta Geological Survey, AER/AGS Digital Data 2018-0013.

Sone, H., Zoback, M.D., 2013. Mechanical properties of shale-gas reservoir rocks—Part 2: Ductile creep, brittle strength, and their relation to the elastic modulus. Geophysics 78, D393-D402.

Sone, H., Zoback, M.D., 2014. Viscous relaxation model for predicting least principal stress magnitudes in sedimentary rocks. Journal of Petroleum Science and Engineering 124, 416-431.

Streit, E.E., Hillis, R.R., 2004. Estimating fault stability and sustainable fluid pressures for underground storage of CO2 in porous rock. Energy 29, 1445-1456.

Swarbrick, R.E., Osborne, M.J., 1998. Mechanisms that generate abnormal, pressures: An overview, in: Law, B.E., Ulmishek, G.F., Slavin, V.I. (Eds.), Abnormal Pressures in Hydrocarbon Environments. Amer Assoc Petroleum Geologists, Tulsa, pp. 13-34.

Samuelson, J., and Spiers, C. J. 2012. Fault friction and slip stability not affected by CO2 storage: Evidence from short-term laboratory experiments on North Sea reservoir sandstones and caprocks, Int. J. Greenh. Gas Control, 11, S78-S90.

Savage, H.M., Kirkpatrick, J.D., Mori, J.J., Brodsky, E.E., Ellsworth, W.L., Carpenter, B.M., Chen, X., Cappa, F. and Kano, Y., 2017. Scientific exploration of induced seismicity and stress (SEISMS). Scientific Drilling, 23, pp.57-63.

Scott, D. R., Marone, C. J., and Sammis, C. G. 1994. The apparent friction of granular fault gouge in sheared layers, Journal of Geophysical Research: Solid Earth, 99(B4), 7231-7246.

Scuderi, M., Collettini, C., and Marone, C., 2017, Frictional stability and earthquake triggering during fluid pressure stimulation of an experimental fault, Earth and Planetary Science Letters, 477, 84-96.

Segall, P. (1985), Stress and subsidence resulting from subsurface fluid withdrawal in the epicentral region of the 1983 Coalinga earthquake, *Journal of Geophysical Research: Solid Earth*, *90*(B8), 6801-6816.

Segall, P., and S. Lu (2015), Injection-induced seismicity: Poroelastic and earthquake nucleation effects, *Journal of Geophysical Research: Solid Earth*, *120*(7), 5082-5103.

Seithel, R., E. Gaucher, B. Mueller, U. Steiner, and T. Kohl (2019), Probability of fault reactivation in the Bavarian Molasse Basin, *Geothermics*, *82*, 81-90.

Shapiro, S. A., and C. Dinske (2009), Fluid-induced seismicity: Pressure diffusion and hydraulic fracturing, *Geophys. Prospect.*, *57*(2), 301-310.

Stein, S., R. Geller, and M. Liu (2011), Bad assumptions or bad luck: Why earthquake hazard maps need objective testing, *Seismological Research Letters*, *82*(5), 623-626.

Stein, S., R. J. Geller, and M. Liu (2012), Why earthquake hazard maps often fail and what to do about it, *Tectonophysics*, *562*, 1-25.

Stork, A., C. Nixon, C. Hawkes, C. Birnie, D. White, D. Schmitt, and B. Roberts (2018), Is CO2 injection at Aquistore aseismic? A combined seismological and geomechanical study of early injection operations, *Int. J. Greenh. Gas Control*, *75*, 107-124.

Schultz, R., Skoumal, R.J., Brudzinski, M.R., Eaton, D., Baptie, B. and Ellsworth, W., 2020. Hydraulic fracturing-induced seismicity. *Reviews of Geophysics*, *58*(3), p.e2019RG000695.

Shen, L., 2019. Data for: Quantitative constraints to the complete state of stress from the combined borehole and focal mechanism inversions: Fox Creek, Alberta, Mendeley Data, V1, doi: 10.17632/nxhs4ppcdf.1

Shen, L., and Schmitt, D., 2020. Data for: States of in-situ stress in the Duvernay East Shale Basin and Willesden Green of Alberta, Canada: variable in-situ stress states effect fault stability, Mendeley Data, V1, doi: 10.17632/tgmxx5vkjx.1

Stein, S., Geller, R.J. and Liu, M., 2012. Why earthquake hazard maps often fail and what to do about it. *Tectonophysics*, *562*, pp.1-25.

Suckale, J., 2009. Induced seismicity in hydrocarbon fields. In Advances in geophysics (Vol. 51, pp. 55-106). Elsevier.

Soliman, M.Y., Craig, D.P., Bartko, K.M., Rahim, Z. and Adams, D.M. (2005): Post-closure analysis to determine formation permeability, reservoir pressure, residual fracture properties; Society of Petroleum Engineers, Middle East Oil and Gas Show and Conference, March 12–15, 2005, Kingdom of Bahrain, Paper SPE-93419-MS, https://doi.org/10.2118/93419-MS.

Shapiro, S. A., and Dinske, C. 2009. Fluid-induced seismicity: Pressure diffusion and hydraulic fracturing, *Geophysical Prospecting*, *57*(2), 301-310, doi:10.1111/j.1365-2478.2008.00770.x.

Shipman, T., MacDonald, R., and Byrnes, T. 2018. Experiences and learnings from induced seismicity regulation in alberta, *Interpretation*, *6*(2), SE15-SE21, doi:10.1190/int-2017-0164.1.

Sibson, R. H. 1990. Conditions for fault-valve behaviour, *Geological Society, London, Special Publications*, *54*(1), 15-28, doi:10.1144/gsl.Sp.1990.054.01.02.

Sone, H., and Zoback, M. D. 2013. Mechanical properties of shale-gas reservoir rocks—Part 2: Ductile creep, brittle strength, and their relation to the elastic modulusMechanical properties of gas shale—Part 2, Geophysics, 78(5), D393-D402.

Stoakes, F. A., and Creaney, S. 1985. Sedimentology of a carbonate source rock: The duvernay formation of alberta, canada

Takahashi, M., Mizoguchi, K., Kitamura, K., and Masuda, K. 2007. Effects of clay content on the frictional strength and fluid transport property of faults, Journal of Geophysical Research: Solid Earth, 112(B8).

Tembe, S., Lockner, D. A., and Wong, T. -F. 2010. Effect of clay content and mineralogy on frictional sliding behavior of simulated gouges: Binary and ternary mixtures of quartz, illite, and montmorillonite, Journal of Geophysical Research: Solid Earth, 115(B3).

Tenthorey, E., and Cox, S. F. 2006. Cohesive strengthening of fault zones during the interseismic period: An experimental study, Journal of Geophysical Research: Solid Earth, 111(B9).

Terakawa, T., and Hauksson, E. 2018. Absolute Stress Fields in the Source Region of the 1992 Landers Earthquake, Journal of Geophysical Research: Solid Earth, 123(10), 8874-8890.

Townend, J., and Zoback, M. D. 2000. How faulting keeps the crust strong, *Geology*, *28*(5), 399-402, doi:10.1130/0091-7613(2000).

Terakawa, T. and E. Hauksson., 2018. Absolute Stress Fields in the Source Region of the 1992 Landers Earthquake. Journal of Geophysical Research: Solid Earth 123(10): 8874-8890.

USGS (2020), Search Earthquake Catalog, edited, USGS.

Valley, B. and Evans, K.F., 2019. Stress magnitudes in the Basel enhanced geothermal system. International Journal of Rock Mechanics and Mining Sciences, 118, pp.1-20.

Vavryčuk, V., 2014. Iterative joint inversion for stress and fault orientations from focal mechanisms. Geophysical Journal International 199, 69-77.

Vernik, L., Zoback, M.D., 1992. Estimation of Maximum Horizontal Principal Stress Magnitude from Stress-Induced Well Bore Breakouts in the Cajon Pass Scientific-Research Borehole. Journal of Geophysical Research-Solid Earth 97, 5109-5119.

Van der Baan, M. and Calixto, F.J., 2017. Human-induced seismicity and large-scale hydrocarbon production in the USA and C anada. *Geochemistry, Geophysics, Geosystems*, *18*(7), pp.2467-2485.

Wetmiller, R.J., 1986. Earthquakes near Rocky Mountain House, Alberta, and their relationship to gas production facilities. *Canadian Journal of Earth Sciences*, *23*(2), pp.172-181.

Wallace, R.E., 1951. Geometry of shearing stress and relation to faulting. The Journal of geology 59, 118-130.

Wang, R., Gu, Y.J., Schultz, R., Kim, A. and Atkinson, G., 2016. Source analysis of a potential hydraulic-fracturing-induced earthquake near Fox Creek, Alberta. Geophysical Research Letters, 43(2), pp.564-573.

Wang, R., Gu, Y.J., Schultz, R. and Chen, Y., 2018. Faults and non-double-couple components for induced earthquakes. Geophysical Research Letters, 45(17), pp.8966-8975.

Wang, R., Gu, Y.J., Schultz, R., Zhang, M. and Kim, A., 2017. Source characteristics and geological implications of the January 2016 induced earthquake swarm near Crooked Lake, Alberta. Geophysical Journal International, 210(2), pp.979-988.

Walsh, F. R., and Zoback, M. D. 2016. Probabilistic assessment of potential fault slip related to injection-induced earthquakes: Application to north-central Oklahoma, USA, *Geology*, *44*(12), 991-994.

Warpinski, N. R. 2000. Analytic crack solutions for tilt fields around hydraulic fractures, *Journal of Geophysical Research: Solid Earth*, *105*(B10), 23463-23478.

Weir, R.M., Eaton, D.W., Lines, L.R., Lawton, D.C. and Ekpo, E., 2018. Inversion and interpretation of seismic-derived rock properties in the Duvernay play. Interpretation, 6(2), pp.SE1-SE14.

Wetmiller, R. J. 1986. Earthquakes near Rocky Mountain House, Alberta, and their relationship to gas production facilities, *Canadian Journal of Earth Sciences*, *23*(2), 172-181.

Weeks, J. D., and Tullis, T. E. 1985. Frictional sliding of dolomite: A variation in constitutive behavior, Journal of Geophysical Research: Solid Earth, 90(B9), 7821-7826.

Weides, S.N., Moeck, I.S., Schmitt, D.R., Majorowicz, J.A., 2014. An integrative geothermal resource assessment study for the siliciclastic Granite Wash Unit, northwestern Alberta (Canada). Environ. Earth Sci. 72, 4141-4154.

Weiss, J., Pellissier, V., Marsan, D., Arnaud, L. and Renard, F., 2016. Cohesion versus friction in controlling the long-term strength of a self-healing experimental fault. Journal of Geophysical Research: Solid Earth, 121(12), pp.8523-8547.

White, J.A., Foxall, W., 2016. Assessing induced seismicity risk at CO 2 storage projects: Recent progress and remaining challenges. Int. J. Greenh. Gas Control 49, 413-424.

Williams, J.D.O., Fellgett, M.W., Quinn, M.F., 2016. Carbon dioxide storage in the Captain Sandstone aquifer: determination ofin situstresses and fault-stability analysis. Petrol. Geosci. 22, 211-222.

Wilson, M.P., Worrall, F., Davies, R.J. and Almond, S., 2018. Fracking: How far from faults?. Geomechanics and Geophysics for Geo-Energy and Geo-Resources, 4(2), pp.193-199.

Wu, P., 1991. Flexure of lithosphere beneath the Alberta Foreland Basin: Evidence of an eastward stiffening continental lithosphere. Geophysical Research Letters 18, 451-454.

Woodland, D.C. and Bell, J.S., 1989. In situ stress magnitudes from mini-frac records in Western Canada. Journal of Canadian Petroleum Technology, 28(5), pp.22-31.

Yerkes, R., Levine, P., Wentworth, C., 1990. Abnormally high fluid pressures in the region of the Coalinga earthquake sequence and their significance. United States Geological Survey Professional Paper 1487, 235.

Yaghoubi, A., Dusseault, M.B., Mahbaz, S.B. and Leonenko, Y., 2020, September. Probabilistic Injection-Induced Fault Slip Assessment in Fox Creek Alberta. In 54th US Rock Mechanics/Geomechanics Symposium. American Rock Mechanics Association.

Zang, A., Stephansson, O., 2010. Stress Field of the Earths Crust. Springer, Dordrecht.

Zanganeh, B., MacKay, M.K., Clarkson, C.R. and Jones, J.R. 2018. DFIT analysis in low leakoff formations: a Duvernay case study; Society of Petroleum Engineers, SPE Canada Unconventional Resources Conference, March 13–14, 2018, Calgary, Alberta, Paper SPE-189826-MS, https://doi.org/10.2118/189826-MS.

Zang, A., Oye, V., Jousset, P., Deichmann, N., Gritto, R., McGarr, A., Majer, E. and Bruhn, D., 2014. Analysis of induced seismicity in geothermal reservoirs–An overview. *Geothermics*, *52*, pp.6-21.

Zhang, H., Eaton, D.W., Li, G., Liu, Y., Harrington, R.M., 2016. Discriminating induced seismicity from natural earthquakes using moment tensors and source spectra. Journal of Geophysical Research: Solid Earth 121, 972-993.

Zoback, M.D., 2007. Reservoir Geomechanics; Cambridge University Press, Cambridge, United Kingdom, 489 p.

Zoback, M.D. and Zoback, M.L. 1991. Tectonic stress field of North America and relative plate motions; Neotectonics of North America, v. 1, p. 339–366.

Zoback, M.L., Zoback, M.D., Adams, J., Assumpcao, M., Bell, S., Bergman, E., Blümling, P., Brereton, N., Denham, D., Ding, J., 1989. Global patterns of tectonic stress. Nature 341,